OPTICALLY DETECTED NUCLEAR MAGNETIC RESONANCE ABOVE AND FAR BELOW EARTH'S MAGNETIC FIELD

Spin Dynamics and Relaxation in Unconventional Regimes

SVEN BODENSTEDT

Dissertation





Atomic Quantum Optics Group
The Institute of Photonic Sciences

Advisor: Prof. Dr. Morgan W. Mitchell Co-advisor: Dr. Michael C. D. Tayler

October 2023



This thesis describes the theoretical background, simulations, experimental apparatus, and measurements of nuclear spin dynamics via optically pumped magnetometers in unconventional magnetic field regimes. It is divided into four parts: Magnetometry, Nuclear Magnetic Resonance Spectroscopy, Nuclear Relaxation Dispersion, and Nuclear Spin Control, each looking at different aspects of this topic.

The magnetometry section describes how through integration of techniques from DC spin-exchange relaxation-free and rf magnetometers, a widely tunable magnetometer is developed that offers a nearly flat response from DC up to few kHz with a sensitivity of less than $20\,\mathrm{fT}\,\sqrt{\mathrm{Hz}}$. Within this range, it surpasses the capabilities of inductive detection methods and eliminates the necessity for cryogenic temperatures that are required for superconducting quantum interference devices (SQUIDs).

The subsequent part employs the magnetometer for conducting nuclear magnetic resonance spectroscopy experiments involving coupled nuclear spin systems. A comprehensive analysis is undertaken to ascertain the optimal magnetic field that yields the most precise determination of the J-coupling constant. It is shown that for some systems the ultralow field regime offers advantages compared to the zero- and high-field regime.

A key factor in choosing the optimal field is the nuclear spin relaxation's strong field dependency, explored in the thesis's third part. This section thoroughly examines this subject in the unconventional ultralow field range, discussing long-lived coherences and the impact of long correlations in molecular dynamics. The thesis experimentally investigates this by adapting the established fast-field cycling method to ultralow fields and combining it with optical detection.

The thesis's final part focuses on enhancing nuclear spin dynamics manipulation through advanced methods that ensure selective, efficient, accurate, and fault-tolerant spin control. ultralow fields possess unique attributes, making even basic techniques like spin-selective resonant pulses challenging to implement. To address this, novel concepts were devised, enabling effective spin control in the ultralow field range, rivaling or surpassing high-field counterparts.

The efficiency of these improved pulse sequences is demonstrated in dynamical decoupling, polarimetry, and spectral filtering experiments.

ZUSAMMENFASSUNG

Diese Arbeit beschreibt den theoretischen Hintergrund, Simulationen, Versuchsaufbauten und Messungen der Kernspindynamik mittels optisch gepumpter Magnetometer in unkonventionellen Magnetfeldregimen. Die Arbeit ist in vier Teile gegliedert: Magnetometrie, Magnetresonanyspektroskopie, Kernrelaxationsdispersion und die Kontrolle von Kernspins.

Im Abschnitt über Magnetometrie wird beschrieben, wie durch die Integration verschiedener Magnetometrietechniken ein weithin abstimmbares Magnetometer entwickelt wird, das eine nahezu flache Empfindlichkeitskurve von $20\,\mathrm{fT}\,\sqrt{\mathrm{Hz}}$ über weite Frequenzbereiche von wenigen Hz bis zu mehreren kHz aufweist. In diesem Bereich übertrifft es die Möglichkeiten alternativer Detektionsmethoden.

Im nächsten Teil wird das Magnetometer für die Durchführung von Experimenten zur kernmagnetischen Resonanzspektroskopie mit gekoppelten Kernspinsystemen eingesetzt. Es wird eine umfassende Analyse durchgeführt, um das optimale Magnetfeld zu ermitteln, das die genaueste Bestimmung der J-Kopplungskonstante ermöglicht. Es wird gezeigt, dass die vereinfachende Annahme, es handele sich um eines der beiden Extreme, entweder Hochfeld oder Nullfeld, nicht die allgemeinegültige Antwort ist.

Ein Schlüsselfaktor bei der Wahl des optimalen Feldes ist die Feldabhängigkeit der Kernspinrelaxation, die im dritten Teil der Arbeit untersucht wird. In diesem Abschnitt wird dieses Thema im unkonventionellen Bereich ultraniedriger Felder untersucht, wobei langlebige Kohärenzen und die Auswirkungen langzeitigen Korrelationen in der Molekulardynamik erörtert werden. Die Arbeit untersucht dies experimentell, indem sie die etablierte Fast-Field-Cycling-Methode an ultraniedrige Felder anpasst und mit optischer Detektion kombiniert.

Der letzte Teil der Arbeit konzentriert sich auf die Verbesserung der Manipulation der Kernspindynamik durch fortschrittliche Methoden, die eine selektive, effiziente, genaue und fehlertolerante Spin-Kontrolle gewährleisten. Ultra-niedrige Felder besitzen einzigartige Eigenschaften, die selbst grundlegende Techniken wie spinselektive Resonanzpulse zu einer Herausforderung machen. Deshalb wurden neuartige Konzepte entwickelt, die eine wirksame Spin-Kontrolle im Ultra-Niedrigfeldbereich ermöglichen, die mit den entsprechenden Verfahren im Hochfeldbereich konkurrieren oder diese sogar übertreffen. Die Wirksamkeit dieser verbesserten Pulssequenzen wird in Experimenten zur dynamischen Entkopplung, Polarimetrie und spektralen Filterung demonstriert.

RESUMEN

Esta tesis doctoral describe la teoría, simulaciones, aparato experimental y mediciones de dinámicas de spin nuclear por medio de magnetómetros de bombeo óptico en regímenes magnéticos no convencionales. Esta tesis está dividida en cuatro partes: magnetometría, espectroscopia de resonancia magnética nuclear, dispersión relajación nuclear y control de spin nuclear.

La sección de magnetometría describe cómo, mediante la integración de las técnicas de intercambio de spin DC libre de relajación y magnetómetros RF, se ha desarrollado un magnetómetro ampliamente ajustable que ofrece una respuesta casi plana desde DC hasta unos pocos kHz con una sensibilidad de menos de $20\,\mathrm{fT}\,\sqrt{\mathrm{Hz}}$. En este rango, sobrepasa las capacidades de métodos de detección inductiva y elimina la necesidad de temperaturas criogénicas que se necesitan para los aparatos superconductores de interferencia cuántica (SQUIDs).

En la siguiente parte se emplea el magnetómetro para realizar experimentos de espectroscopia de resonancia magnética nuclear en sistemas con spines nucleares acoplados. Se realiza exhaustivo análisis para encontrar el campo magnético que da la determinación más precisa de la constante J de acoplamiento. Se demuestra que la suposición de que este campo magnético es uno de los dos extremos, o algo o cero, no es la respuesta correcta para todos los sistemas.

Un factor clave para elegir el campo magnético es la fuerte dependencia de la relajación del spin nuclear con el campo. Esta dependencia se explora en la tercera parte de esta tesis en el rango no convencional de campos ultra bajos, con una discusión sobre coherencias persistentes de larga vida y el impacto de correlaciones extendidas en las dinámicas moleculares. Esto se estudia experimentalmente adaptando el método establecido de rotado rápido de campo (fast field cycling) a campos ultra bajos y combinándolo con detección óptica.

La parte final de esta tesis se enfoca en mejorar la manipulación de las dinámicas de espín nuclear mediante avanzados métodos que aseguran un control del espín selectivo, eficiente, exacto y a prueba de fallos. Los campos ultra bajos poseen atributos únicos que hacen que incluso las técnicas básicas como los pulsos resonantes selectivos de espín sean difíciles de implementar. Para solventar esto, se han desarrollado nuevos conceptos que permiten el control efectivo del espín en el rango de campos ultra bajos similares o incluso mejores que sus contrapartes de campos altos. La eficacia de estas secuencias de pulsos mejoradas se demuestra con experimentos de desacoplamiento dinámico, polarimetría y filtrado espectral.

RESUM

Aquesta tesi doctoral descriu la teoria, simulacions, aparell experimental i mesuraments de dinàmiques de espín nuclear per mitjà de magnetòmetres de bombeig òptic en règims magnètics no convencionals. Aquesta tesi està dividida en quatre parts: magnetometria, espectroscòpia de ressonància magnètica nuclear, dispersió relaxació nuclear i control de espín nuclear.

La secció de magnetometria descriu com, mitjançant la integració de les tècniques d'intercanvi de espín DC lliure de relaxació i magnetòmetres RF, s'ha desenvolupat un magnetòmetre àmpliament ajustable que ofereix una resposta gairebé plana des de DC fins a uns pocs kHz amb una sensibilitat de menys de $20\,\mathrm{fT}\,\sqrt{\mathrm{Hz}}$. En aquest rang, sobrepassa les capacitats de mètodes de detecció inductiva i elimina la necessitat de temperatures criogèniques necessàries en aparells superconductors d'interferència quàntica o SQUIDs (per les sigles en anglès).

A la següent part s'empra el magnetòmetre per realitzar experiments d'espectroscòpia de ressonància magnètica nuclear en sistemes amb espines nuclears acoblats. Es fa una anàlisi exhaustiva per trobar el camp magnètic que dóna la determinació més precisa de la constant J d'acoblament. Es demostra que alguns sistemes en règim de camps ultra baixos ofereixen avantatges quan es comparen amb els camps a zero y alt règim.

Un factor clau per triar el camp magnètic és la forta dependència de la relaxació de l'espín nuclear amb el camp. Aquesta dependència s'explora a la tercera part d'aquesta tesi al rang no convencional de camps ultra baixos, amb una discussió sobre coherències persistents de llarga vida i l'impacte de correlacions esteses a les dinàmiques moleculars. Aquest estudi es realitza experimentalment adaptant el mètode establert de rotació ràpida de camp (fast field cycling) a camps ultra baixos i combinant-ho amb detecció òptica.

La part final d'aquesta tesi s'enfoca a millorar la manipulació de les dinàmiques d'espín nuclear mitjançant mètodes avançats que asseguren un control de l'espín selectiu, eficient, exacte i a prova d'errors. Els camps ultra baixos tenen atributs únics que fan que fins i tot les tècniques bàsiques com els polsos ressonants selectius d'espín siguin difícils d'implementar. Per resoldre això, s'han desenvolupat nous conceptes que permeten el control efectiu de l'espín en el rang de camps ultra baixos similars o fins i tot millors que les contraparts de camps alts. L'eficàcia d'aquestes seqüències de polsos millorades es demostra amb experiments de desacoblament dinàmic, polarimetria i filtratge espectral.

This thesis includes material from the following published articles:

- Bodenstedt, S., Mitchell, M. W., Tayler, M. C. D., "Fast-field-cycling ultralow-field nuclear magnetic relaxation dispersion," Nature Communications 12, 4041 (2021)
- Bodenstedt, S., Moll, D., Glöggler, S., Mitchell, M. W., Tayler, M. C. D., "Decoupling of spin decoherence paths near zero magnetic field," The Journal of Physical Chemistry Letters 13, 98–104 (2021)
- Tayler, M. C. D., Mouloudakis, K., Zetter, R., Hunter, D., Lucivero, V. G., Bodenstedt, S., Parkkonen, L., Mitchell, M. W., "Miniature biplanar coils for alkali-metal-vapor magnetometry," Physical Review Applied 18, 014036 (2022)
- **Bodenstedt, S.**, Mitchell, M. W., Tayler, M. C. D., "Meridional composite pulses for low-field magnetic resonance," Physical Review A 106, 10.1103/physreva.106.033102 (2022)
- Mouloudakis, K., Bodenstedt, S., Azagra, M., Mitchell, M. W., Marco-Rius, I., Tayler, M. C. D., "Real-time polarimetry of hyperpolarized 13C nuclear spins using an atomic magnetometer," The Journal of Physical Chemistry Letters 14, 1192–1197 (2023)
- Chuchkova, L., Bodenstedt, S., Picazo-Frutos, R., Eills, J., Tretiak, O., Hu, Y., Barskiy, D. A., Santis, J., Tayler, M. C. D., Budker, D., Sheberstov, K. F., "Magnetometer-detected nuclear magnetic resonance of photochemically hyperpolarized molecules," The Journal of Physical Chemistry Letters, 6814–6822 (2023)

The thesis also includes materials from articles that are currently in manuscript form, which will be submitted shortly for peer review:

- **Bodenstedt, S.**, Mitchell, M. W., Tayler, M. C. D., "Resolution optimized NMR spectroscopy below Earth's field," In preparation. (2023)
- Tayler, M. C. D., **Bodenstedt**, **S.**, "NMRduino: a modular, opensource, low-field magnetic resonance platform," In review. (2023)
- **Bodenstedt, S.**, "DFTtools: a Python package for the analysis of low frequency free induction decays," In preparation. (2023)
- **Bodenstedt, S.**, Mitchell, M. W., Tayler, M. C. D., "Accounting for dq/dt in the Bloch equation," In preparation. (2023)

Finally, the work also includes materials from a peer-reviewed research proposal:

• **Bodenstedt, S.**, "Optical magnetometry of nuclear spin relaxation dispersion in ultra-low fields," Thesis Proposal (2020)

I am deeply grateful to my supervisor, Michael, for his comprehensive guidance, remarkable patience, and extensive expertise that have profoundly shaped my scientific journey. His openness to my persistent questioning and insightful responses fostered deep understanding and growth. My appreciation also extends to my group leader, Morgan, whose consistent guidance and invaluable assistance, regardless of subject alignment, have illuminated the path to success and refined my work.

I would like to convey my deep appreciation to office mates Kostas and Ola, who, despite busy schedules, consistently offered assistance. Kostas' guidance was instrumental in understanding spin-exchange collisions, a fundamental aspect of my research, while Ola's support alleviated internal pressures, ensuring a healthier journey.

I am also immensely grateful to the current members of the Atomic Quantum Optics group: Enes, Laura, María, Tomáš, Romain, Daniel, Ana, Diana, Rachel, Yanan, Gianvito, Yintao, Andrea, Harini, and Hana. Expressing my gratitude for the incredible memories we've shared would require far more space than I have here. From our times at ICFO to the beach, cinema, homes, bars, restaurants, and amidst nature, each moment has been an unforgettable chapter in our collective journey. I also hold dear the cherished memories shared with my former colleagues: Chiara, Hara, Vindhiya, Jia, Ricardo, Dominic, Fraser, Stuti, Pau, Natalia and Lorena.

I extend my acknowledgment to ICFO's administration, management, and workshops for their significant role in my achievements. Their meticulous attention to the behind-the-scenes operations and the seamless functioning of the institute has allowed me to fully dedicate myself to my projects.

My journey to this Ph.D. position began with invaluable support from my University of Stuttgart colleagues. Special thanks to Ilja for kickstarting this path by sending me to Barcelona. I am grateful to former supervisors Ingmar and Tobi, whose teachings formed my knowledge foundation. Thanks to past group leaders Jörg and Harald for an exceptional research environment. I also cherish the camaraderie and collaboration of former colleagues like Julia, Jakob, Stefan, and Philipp during my time in Stuttgart.

Gratitude extends to my colleagues of the ZULF ITN as well: Laurynas, Seyma, Vladimir, Kirill, James, Anjusha, Quentin, Aminata, Domingo, Oksana, and their supervisors. The few yet remarkable meetings were a treasure trove of knowledge, and the companionship of both scientific and non-scientific moments was equally appreciated. A heartfelt acknowledgment is reserved for my colleagues at the Helmholtz Institute in Mainz – John, Dmitry, and Teng – who generously hosted me in my initial PhD months, affording me a strong foundation in this new field. And to Roman, I extend special thanks; our discussions have profoundly challenged and refined my grasp of intricate physical nuances.

I am deeply grateful for the unwavering support and unconditional love provided by my grandmothers. Their emotional encouragement and genuine interest in my scientific journey have been a constant source of inspiration. My heartfelt appreciation also extends to my late grandpa, who not only shared his passion for science but also initiated me into the world of experimental physics from an early age. To my parents and sister, I owe immeasurable gratitude for their consistent support at every phase of my life, always offering a welcoming haven that I can call home.

I extend my heartfelt gratitude to both my current and former flatmates, Ediz, Fionnuala, Saskia, and Niall, whose presence in my life has made my home a truly welcoming and wonderful space. Their unwavering support were a constant comfort, and their willingness to stand by me when needed has been truly cherished.

My appreciation also extends to my circle of friends. I owe a special debt of thanks to Patrick, whose willingness to lend a listening ear provided solace whenever I sought it. Equally deserving of gratitude are Rüdi, whose weekly calls have added joy to my days, and Heike, who has brought warmth and positivity to our interactions. I am deeply thankful to Pedro for generously hosting me in Lanzarote, creating a unique environment for writing my thesis. Nat's kindness in lending me her pen during crucial moments by the beach and the memorable boat trips with Captain Alex are experiences I cherish. Enes, your travel magnets are a thoughtful reminder of your journeys and are greatly appreciated. My final appreciation goes to my caring girlfriend, whose unwavering support and belief in me provided the strength to persevere through challenges, always standing by my side during even the toughest times.

CONTENTS

Int	rodu	ction 1		
I	Mag	netometry		
1	_	nic Vapor Spin Physics Underlying Optical Magnetom-		
	etry	13		
	1.1	Fundamental Sensitivity Estimations 14		
	1.2	Density Matrix Equation 17		
	1.3	Numerical Calculations and Simulations 28		
	1.4	Accounting for dq/dt in the Bloch Equation 34		
2	-	able DC-RF Optical Pumped Magnetometer 41		
2.1 Motivation 41				
	2.2	Magnetometer Characteristics 42		
	2.3	State of the Art 46		
	2.4	Working Principle 49		
	2.5	Performance and Outlook 57		
II	Nuc	lear Magnetic Resonance Spectroscopy		
3	3.1	- to Ultralow Field Nuclear Magnetic Resonance 65 Quantum Mechanical Description 66		
	3.2	Differences Between Zero- and High-Field 68		
	3.3	Time-Dependent Signals 74		
	3·4	Initial State Preparation 80		
4		Solution Optimized J Spectroscopy 85		
4	4.1	Motivation for Ultralow Field Spectroscopy 86		
	4.2	Spectral Fitting via Least Squares Regression Analy-		
	4	sis 92		
	4.3	Experimental Results 97		
	4.4	Summary 101		
		•		
III	Nuc	lear Relaxation Dispersion		
5	Long	g-Lived Coherences 105		
	5.1	Quantum Master Equations 105		
	5.2	Liouville Bracket 108		
	5.3	Secular Approximation 109		
	5.4	Dipolar Relaxation 112		
	5.5	AX Spin Systems — e.g. Formic Acid-13C 113		
	5.6	A ₃ X Spin System — e.g. Methanol- ₁₃ C 117		

6	Nuclear Magnetic Relaxation Dispersion 121			
	6.1 Introduction to Fast-Field-Cycling Nuclear Relaxation			
		Dispersion 121		
	6.2	Brownian Motion, Relaxation and Correlation 122		
	6.3	Fast Field Cycling at ultralow Fields 127		
	6.4	FFC NMRD in Metal Containers 130		
	6.5	Liquids Confined in Porous Materials 131		
	6.6	Chemically Induced Dynamic Nuclear Polarization 135		
IV	Nuc	elear Spin Control		
7				
	7.1	Spin Inversion using Ordinary DC and AC Pulses 140		
	7.2	Composite 90x-180y-90x Inversion Pulses 144		
	<i>.</i> 7⋅3			
	7.4	Band-Selective, Uniform Response, Pure-Phase Pulses 149		
	7.5	Phase Alternating Composite Pulses 154		
	7.6	Outlook 156		
8 Decoupling of Spin Decoherence Paths 161				
	8.1	Coherent Averaging Theory 161		
	8.2	Zero-Field Implementation of the XY ₄ Pulse Sequence 167		
	8.3	Scalar Relaxation Effects due to Deuterium 173		
	8.4	Scalar Relaxation due to Nitrogen-14 175		
	8.5	Real-Time Polarimetry of Hyperpolarized Nuclear Spins 176		
Cc	nclu	sion 179		
Aŗ	pend	dix		
A	Mat	hematical Notation, Definitions and Derivations 187		
	A.1	Einstein Notation 187		
	A.2	Notation for Fields 187		
		Notation for Vector Spaces 187		
	A.4	Notation for Hilbert Spaces 188		
	A. 5	Notation for Product Spaces 191		
	A.6	Notation for Liouville Spaces 192		
	A.7	Reduced Density Operators 194		
	A.8	Commutators 196		
	A.9	Secular Approximations 197		
В	Rota	ation Algebra and Representation Theory 207		
	B.1	Algebraic Description of Rotations 207		
	B.2	Irreducible Representations of Lie Algebras 208		
	B.3	Spherical Basis States of Irreducible Representation 210		

	B.4	Product Space of Irreducible Representations 214
C	Nur	nerical Simulations and Calculations 221
	C.1	Spherical Operator Basis for 87Rb Ground Spin States 221
	C.2	Local Linearization of the Density Matrix Equation 222
	C.3	Numerical Integration of The Density Matrix Equa-
		tion 224
D	The	oretical Derivation of Zero Field NMR Spectra 227
	D.1	Hamiltonian 227
	D.2	Selection Rules 228
	D.3	Eigenenergies and Transition Frequencies 229
	D.4	Examples 229
	D.5	More Complex Systems 233
	D.6	Comparison to High Field 234
	D.7	J-Coupling Constant Sensitivity 235
E	Exp	erimental Setup — NMRduino 237
		NMRduino Hardware 237
	E.2	NMRduino Software 239
	-	Nuclear Spin Polarization 242
F	Data	a Analysis — DFTtools 245
	F.1	Motivation 245
	F.2	Fourier Analysis 248
	F.3	Examples 250
	F.4	Python Package 254
G	Mag	netometer Calibration and Sensitivity Estimation 261
	G.1	Power of a Time Domain Signal 261
	G.2	Amplitude Spectral Density 262
	G.3	<u>o</u>
	G.4	Sensitivity Calibration 268

Bibliography 269

ACRONYMS

3D three-dimensional AC alternating current

ASD amplitude spectral density BPP Bloembergen-Purcell-Pound

BQ 1,4-benzoquinone

BURP broadband uniform-rotation pure-phase CIDNP chemically induced dynamic nuclear po-

larization

Cs cesium

CSB bipolar current supply
DAC digital to analog converter

DC direct current

DFT discrete Fourier transform
DME density matrix equation

DTFT discrete-time Fourier transform

ELF extremely low frequency (3 Hz to 30 Hz)

EPR electron paramagnetic resonance

FFC fast field cycling
FID free induction decay
FT Fourier transform

FWHM full width at half maximum GNA Gauss-Newton algorithm

He helium
Hg mercury
K potassium

LDE linear differential equation

LF low frequency (30 kHz to 300 kHz)

LLC long-lived coherence

MCG magnetocardiography
MEG magnetoencephalography
MRI magnetic resonance imaging
NMR nuclear magnetic resonance

NMRD nuclear magnetic relaxation dispersion

NV nitrogen vacancy

OPM optically pumped magnetometer

PSD power spectral density

Rb rubidium

RF radio frequency RMS root mean square

SEOP spin exchange optical pumping SERF spin exchange relaxation free

SLF super low frequency (30 Hz to 300 Hz)

SNR signal-to-noise Ratio SO(3) 3D rotation group SPN spin projection noise

SQUID superconducting quantum interference de-

vice

SR2K scalar relaxation of the second kind

SU(2) special unitary group

TEMPOL 4-hydroxy-2,2,6,6-tetramethylpiperidin-1-

oxyl

ULF ultralow field

ULF ultra low frequency (0.3 kHz to 3 kHz)

USB universal serial bus VLF very low field

VLF very low frequency (3 kHz to 30 kHz)

ZULF zero- to ultralow field

TABLE OF VARIABLES

```
Hyperfine splitting
A_{\rm HF}
В
         Classical magnetic field vector
b
         Dipolar coupling constant
β
         Inverse spin temperature
         Classical electric field vector
\mathbf{E}
         Classical frequency
Ê
         Sum of spin operators
G(\tau)
        Auto-correlation function
         Landé g-factor
g
         Gyromagnetic ratio of an isolated electron
\gamma_{\rm e}
         (\approx -2\pi \times 28.03\,\mathrm{GHz}\,\mathrm{T}^{-1})
         Gyromagnetic ratio
\gamma
         Gyromagnetic ratio of a nuclear spin
\gamma_{\rm n}
Ĥ
         Hamiltonian
         Planck constant (\approx 6.626 \times 10^{-34} \,\mathrm{J\,Hz^{-1}})
ħ
Î
         Nuclear spin operator
         Spin-spin coupling constant
Î
         Sum of spin operators
Ê
         Liouville superoperator
         Classical magnetic moment vector
m
         Vacuum permeability
                                         (\approx
                                                  1.257 \times
\mu_0
         10^{-6} \,\mathrm{N}\,\mathrm{A}^{-2}
         Bohr magneton (\approx 9.274 \times 10^{-24} \, \mathrm{J \, T^{-1}})
\mu_{\rm B}
Ν
         Number of particles
         Resonance frequency
         Classical angular frequency
ω
Р
         Electron/nuclear spin polarization
         Slowing down factor
q
         Density operator
ô
```

- R_{OP} Optical pumping rate
- $\hat{\mathbf{R}}$ Rotation operator
- $R_{\rm SD}$ Spin-destruction collision rate
- *R*_{SE} Spin-exchange collision rate
- s Light polarization vector
- $\hat{\mathbf{S}}$ Electron spin operator
- T_1 Longitudinal relaxation time
- T_2 Transverse relaxation time
- au Classical torque vector
- au Correlation time
- $\hat{T}_{l,m}$ Spherical basis operator (see also Appendix B)

Further information about the mathematical notation can be found in Appendix A.

Magnetic fields represent a ubiquitous phenomenon in both our daily existence and throughout the universe. They manifest in diverse forms, encompassing static fields like the magnetosphere of the EARTH and alternating fields, as encountered in radio frequency (RF) transmission. Moreover, magnetic fields exhibit a wide range of strengths, from immensely intense fields, exceeding a billion tesla [1, 2], generated by neutron stars, to the more moderate fields exhibited by permanent magnets, as well as substantially weaker fields on the order of femto- to picotesla, stemming from biological events. At first, magnetic fields were primarily observed passively; however, contemporary advancements enable active engineering of these fields, both spatially and temporally. This manipulation is achieved through techniques such as shaping ferromagnetic materials or controlling electric current paths in coils.

Regardless of their source or form, magnetic fields are an essential aspect of modern technology, playing a crucial role in applications ranging from transportation (electric motors), energy (generators, fusion reactors), fundamental physics (particle accelerators), chemistry (nuclear magnetic resonance (NMR) spectroscopy), military/security (metal detectors), biology (muscle/plants), geology (rock magnetism) and archaeology to medical applications (magnetic resonance imaging (MRI), magnetoencephalography (MEG) and magnetocardiography (MCG)).

Due to the broad spectrum of these applications in the fields of technology, metrology, and basic science, there is a strong motivation to invent, develop, and improve techniques to study, manipulate, and create magnetic fields. This work will cover all three aspects of the field: The basic scientific interaction of magnetic fields with matter on the nanoscale will be studied in combination with demonstrating metrology techniques for its detection and outlining their technological applications.

SOURCES OF MAGNETIC FIELDS ON THE NANOSCALE

Magnetic fields are observed on a wide range of length scales. The magnetic field of the EARTH, which shields the surface from cosmic

radiation, is believed to originate from electric currents flowing in the EARTH's core. Magnetic fields are also produced by living creatures and organs (e.g. by the heart, brain, muscles), which creates an intrinsic interest in studying these (e.g. via MCG, MEG or Magnetomyography) to understand better how the body works or to apply in healthcare.

At the nanoscale, various phenomena contribute to spatial and temporal magnetic field variations which are graphically illustrated in Figure 0.1. Magnetic dipole fields are examples, which emerge when angular momentum, such as spin or orbital, is associated with a charged particle, thereby giving rise to a magnetic moment. This magnetic moment may still persist even for neutral particles, provided they are composed of charged constituents¹. The magnetic field strength at a specific position within a molecule depends upon the orientation of these magnetic moments and their relative positioning. Within non-paramagnetic molecules, permanent magnetic dipoles exist primarily in the form of spin-carrying nuclei. In the case of a molecule undergoing random rotational motion, the magnetic field produced by a dipole averages to zero, rendering direct measurements challenging when the field is averaged over timescales longer than the molecule's tumbling time.

In addition to nuclei, electrons also possess magnetic moments. Although they typically form pairs² within molecules through covalent bonds, their magnetic dipole fields, in combination with the magnetic Fermi³ contact interaction, indirectly give rise to a phenomenon known as *J-coupling* [3], which offers an additional path for nuclear spins couplings within molecules. Unlike dipolar fields, the Fermi contact interaction contributes a component that remains independent of the molecule's orientation. This unique characteristic enables the observation of this phenomenon even in systems undergoing random molecular tumbling.

Electrons can further influence the local magnetic field through induced electric currents that scale with externally applied macroscopic magnetic fields. This phenomenon, termed the *chemical shift*, demonstrates sensitivity to various factors, including the molecule's

¹ A notable example is the neutron, which consists of two "down" and one "up" quark, collectively contributing to its magnetic properties.

² Oxygen O_2 and nitrogen dioxide NO_2 are examples of paramagnetic molecules, where this is not true.

³ Enrico Fermi (1901-1954) was an Italian physicist who made significant contributions to quantum theory, nuclear physics, and the development of the first controlled nuclear chain reaction.

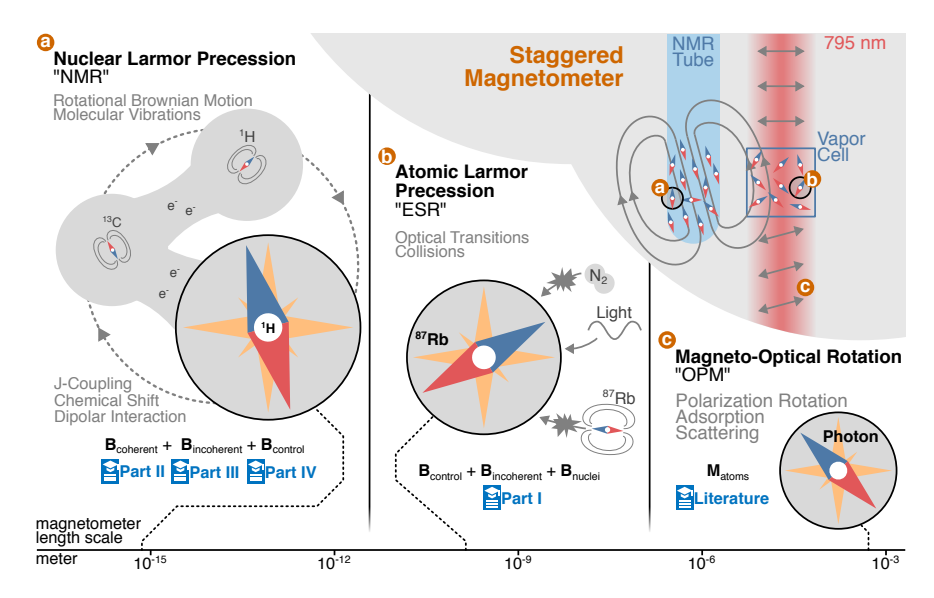


Figure 0.1: Graphical abstract of the thesis. An NMR experiment can be abstractly interpreted as a staggered magnetometer: Each stage is sensitive to certain magnetic interactions in its local environment. Whereas the lowest stage (a), the nuclear spins, are sensitive to external control field as well as (magnetic) spin-spin interactions, the second stage (b) monitors the impact of these local effects on the ensemble. In high-field NMR the second stage would be an inductive pick-up loop and also the last stage. In contrast, zero- to ultralow field (ZULF) NMR the second stage is made of a hot vapor of alkali atoms, that, similar to nuclear spins, are sensitive to control fields, local (magnetic) interactions, and the field generated by the nuclear spin ensemble. The last stage (c) transforms the previously gathered information which is encoded in the spin dynamics of the ensemble of alkali atoms via photons into a macroscopically measurable signal. During the whole process, magnetic field measurements are performed over several orders of length scale, allowing the translation of molecular dynamics to the macroscopic world.

orientation, its chemical structure, and the precise location of the nucleus within the molecule.

The ability to measure these magnetic fields provides valuable insights into the underlying determinants, encompassing aspects such as chemical structure, molecular orientation, and nuclear spin states. Moreover, any temporal variations in these parameters are intricately encoded within the magnetic field itself, offering a powerful means to explore dynamic molecular processes, including tumbling and vibrations. While conducting magnetometry at the subatomic level presents a considerable challenge, it can be accomplished using the very same particles responsible for some of these magnetic phenomena.

This is particularly significant since studying phenomena far below the diffraction limit of visible light poses exceptional challenges. In contrast to other forms of radiation, such as particle, gravitational, high-energy electromagnetic or acoustic radiation, magnetic fields form a unique set of features, such as their ability to penetrate many materials with minimal disturbance, while still being able to interact and being emitted by subatomic particles like nuclei.

SUBATOMIC MAGNETOMETRY

Historically, magnetometry traces its origins to the compass [4], a now everyday device. Over time, diverse types of magnetometers have been developed, each tailored to fulfill the requirements (size, field strength, sensitivity, frequency, etc.) of specific applications. At the nanoscale, magnetometers relying on nuclear spin precession emerge as promising tools for detecting localized and time-dependent magnetic field fluctuations within atoms and molecules. In the classical picture, if exposed to a magnetic field, a torque

$$\tau = \mathbf{m} \times \mathbf{B} \tag{0.1}$$

dependent on the magnetic field strength **B** and its relative orientation relative to the spin's magnetic moment **m**, leads to a rotation of the spin state. Thereby, by observing the magnetic moment's trajectory part of the magnetic field can be reconstructed.

Reading out the state of a single nuclear spin is not trivial and, so far, has only been achieved by atomic-like solid-state defects such as nitrogen vacancy (NV) centers in diamond [5, 6] or silicon vacancies in silicon carbide [7]. However, some of the nanoscale magnetic field

information is still encoded in the ensemble average of identical molecules which is one of the reasons for the success of NMR.

UNCONVENTIONAL REGIMES

Often, external magnetic fields $\mathbf{B}_{control}$ are applied in NMR to manipulate the nuclear spin states in a controlled manner. Constant fields cause the nuclear magnetic moments to undergo Larmor⁵ precession [8]

$$\omega_{\text{Larmor}} = 2\pi f_{\text{Larmor}} = |\gamma \mathbf{B}_{\text{local,avg.}}| , \qquad (0.2)$$

with the precession frequency f_{Larmor} depending on the local, time-averaged magnetic field $\mathbf{B}_{\text{local,avg.}} = \mathbf{B}_{\text{coherent}} + \mathbf{B}_{\text{control}}$ and the nuclear spin's gyromagnetic ratio γ . Many techniques of NMR are based on determining these fields indirectly at different spatial positions and spin configurations by measuring these oscillation frequencies.

By changing the bias magnetic field $\mathbf{B}_{control}$, the nuclear spin magnetometer can be tuned to be more or less sensitive to different types of interactions. Whereas traditionally, NMR is performed at high Larmor frequencies to profit from greatly increased sensitivity (due to higher thermal polarization and efficient RF-inductive-pickup detection) as well as spectral dispersion (through chemical shift),

⁴ Strictly speaking, control fields described by B_{control} also lead to coherent spin evolution.

⁵ Joseph Larmor (1857–1942) was a British physicist who made significant contributions to theoretical physics, especially in the areas of electromagnetism and the kinetic theory of gases, and is known for formulating the Larmor formula describing the rate at which an accelerated charged particle radiates energy.

this thesis focuses on a nuclear spin magnetometer operating in the ZULF[9-14] regime.

Whereas the zero-field regime, where the J-couplings dominate the coherent spin evolution, is already significantly less popular than conventional high-field NMR this thesis will focus on the even more unconventional ultralow field (ULF) regime, where the Zeeman⁶ term competes with the scalar coupling for dominance. The continuous transition of the nuclear spin being strongly coupled at zero-field up to the weak coupling limit reached at low/high fields offers a promising regime for high-resolution estimations of the J-coupling constants, due to the potential of combining the advantages (high transition moments, long-lived coherences, high J-sensitivity) by simultaneously avoiding the disadvantages (line broadening) of both regimes. This will be the main topic of Part ii, where Chapter 3 describes the theoretical foundation of the time-dependent observable signals and Chapter 4 describes how it can be used to estimate J-coupling constants with high resolution.

In the context of relaxometry, changing the magnetic field, and by that also the Larmor frequency ω_{Larmor} , allows probing different spectral regions [15, 16] of the Fourier⁷ transformed auto-correlation functions $G(\tau)$ that describe the time-correlation of molecular tumbling. These correlation functions can often be modeled with a single correlation time τ_{c} , leading to a spectrum with a zero-centered Lorentzian⁸ line shape

$$\mathcal{F}(G)(\omega) = J(\omega) \propto \frac{\tau_c}{1 + \omega^2 \tau_c^2}$$
 (0.3)

This curve tends to a plateau at low ($\omega \ll \tau_{\rm c}^{-1}$) and to a ω^{-2} power law at high ($\tau_{\rm c}^{-1} \ll \omega$) Larmor frequencies. Longitudinal relaxometry probes $J(\omega)$ at multiples of $\omega_{\rm Larmor}$. The transition from one regime to the other allows the accurate estimation of the correlation

⁶ Pieter Zeeman (1865–1943) was a Dutch physicist who discovered the Zeeman effect, providing crucial evidence for the existence of subatomic particles and advancing our understanding of atomic structure and magnetism.

⁷ Joseph Fourier (1768–1830) was a French mathematician and physicist who revolutionized the field of mathematical analysis and the understanding of heat transfer through his development of Fourier series and the Fourier transform, providing fundamental tools for studying periodic phenomena and signal processing.

⁸ Hendrik Lorentz (1853–1928) was a Dutch physicist who played a crucial role in the development of the theory of electromagnetism, particularly his formulation of the Lorentz transformation and his contributions to the understanding of the behavior of charged particles in electromagnetic fields. (Not to be confused with Ludvig Lorenz, a Danish physicist know for the Lorenz gauge condition.)

time τ_c and by that, getting insight into the underlying molecular dynamics. As a consequence, to investigate processes with very long correlation times the relaxation rates can be conveniently investigated at ZULF conditions⁹.

These conditions are also rather unconventional in the field of nuclear magnetic relaxation dispersion (NMRD) and the main topic of Part iii of the thesis, which is all about field-dependent relaxation rates, either caused by long-lived coherences (Chapter 5) in the strong coupling regime or slow molecular dynamics (see Chapter 6) observed in porous materials. The measurements were performed by extending the technique of fast field cycling (FFC) [17] to the ZULF regime.

Finally, the last part (Part iv) is all about using externally applied, carefully designed control fields to further tune the nuclear spin magnetometer. Different strategies for realizing selective/collective nuclear spin rotations at the unconventional ZULF conditions will be discussed in Chapter 7 and then applied in Chapter 8 to decouple nuclear spins, making the spins (in)sensitive to certain parts of (in)coherent magnetic fields.

ATOMIC SCALE MAGNETOMETRY

To perform these experiments, the evolution of the nuclear spin ensemble has to be observed. In contrast to atoms, even if nuclear isomers feature strong spin-orbit coupling¹⁰, the energy difference between nuclear isomers is often, with rare exceptions [18–20], too large for being addressable by optical transitions. Optical polarization (e.g. optical pumping) and read-out techniques that are available for atoms, are therefore not directly available for nuclear spins¹¹.

Nuclear spins, however, feature a magnetic moment whose dipole field may extend far beyond the molecule's size allowing a remote detection of the nucleus' spin state. Even if the nuclear magneton $5\times 10^{-27}\,\mathrm{J/T}$ is tiny, (about 50 orders of magnitude smaller than the Earth's dipole moment), the magnetic field of the ¹H nuclear spin

However, it is possible to optically polarize nuclear spins indirectly e.g. via SEOP.

⁹ Under some conditions, the spectral density function can also be studied in the rotating frame using spin-locking techniques [16].

¹⁰ The spin-orbit coupling scales linearly with γ/a_0^3 . Even if electrons may have a much higher gyromagnetic ratio, due to the drastically reduced characteristic distance a_0 (Bohr radius vs. nuclear radius), the energy splitting of nuclear isomers due to nuclear spin-orbit couplings is significantly higher.

¹¹ With some rare exceptions, e.g. optically detected nuclear magnetic resonance in mercury (Hg) [21]

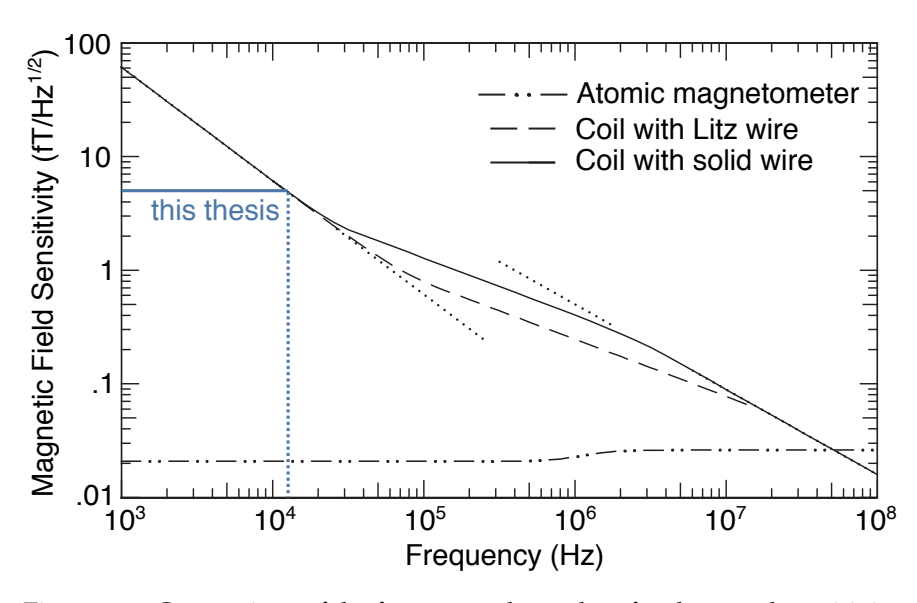


Figure o.2: Comparison of the frequency-dependent fundamental sensitivity of potassium-based optically pumped magnetometers (OPMs) and inductive detection using pick-up coils of comparable size (adapted from Savukov et al. [22] and Seltzer [23]). The blue line shows the performance of the OPM used in this thesis and the relevant frequency range. Improving the magnetometer's sensitivity by operating it closer to the fundamental sensitivity limits would extend the frequency region where the OPM outperform inductive detection.

in a fully polarized droplet of water (0.05 mL corresponds to 1×10^{22} 1H nuclei spins) measured at a distance of 1 cm is in the order of the Earth's magnetic field measured at the surface ($\approx6000\,\mathrm{km}$ distance from the core).

Whereas, in principle this suggests, that fully polarized liquids could be analyzed using a device as simple as a compass, in practice the achievable polarization levels are much lower. The thermal polarization at room temperature in a magnetic field of 1T is only in the order of 1×10^{-6} , resulting in a field of only a few picotesla, requiring more sophisticated sensing devices.

As can be seen in Figure 0.2, inductive detection based on the LORENTZ force on the electrons within conductors, is a great detector for nuclear spin precession at high-field where LARMOR frequencies are in the order of MHz and above. However, it becomes more and more inefficient as soon as the magnetic field and therefore the LARMOR frequency is reduced. For a long time, superconducting quantum interference devices (SQUIDs) which are also based on

electrons in the form of COOPER¹² pairs, were the only devices with sufficient sensitivity to detect NMR signals at much lower fields.

Even if electrons, similar to some nuclei, feature a magnetic moment, building a sensitive magnetometer based on electron spin precession is not trivial. One of the reasons is that dipolar relaxation between identical particles scales with γ^2 . With electrons, due to the significantly lower mass $m_e \approx m_n/2000$, having a much larger gyromagnetic ratio γ , electron spin precession experiences much higher relaxation rates due to dipole-dipole interaction compared to nuclei. In addition, atoms are also affected by collisions that affect the coherence of electron spin states¹³. Only when a mechanism that effectively eliminates the effect of spin-exchange collisions was discovered, did OPMs based on hot alkali vapor reach comparable sensitivities to SQUIDs (see Figure 0.2).

Similar to subatomic nuclear spin magnetometers, the individual atoms within a hot vapor base OPM can be interpreted as an atomic-sized magnetometer, that is sensitive to its local magnetic field environment. This is graphically illustrated in Figure 0.1b. In the same way, magnetic fields (and optical beams) are able to tune the magnetometer to be more or less sensitive to certain aspects of this magnetic environment, allowing the development of specialized magnetometers for different applications. This has been achieved with great success for different frequency regimes of the magnetic spectrum, leading to magnetometers being mostly sensitive to extremely low frequency (3 Hz to 30 Hz) (ELF) and super low frequency (30 Hz to 300 Hz) (SLF), such as spin exchange relaxation free (SERF) magnetometers, or alternatively to very low frequency (3 kHz to 30 kHz) (VLF) and low frequency (30 kHz to 300 kHz) (LF), such as RF magnetometers. Motivated by the special requirements of detecting NMRD in ultralow fields, this thesis investigates another unconventional regime, this time for OPMs.

In Part i of the thesis, a magnetometer will be described, that is capable of covering a broad range of frequencies from ELF and SLF via ultra low frequency (0.3 kHz to 3 kHz) (ULF) all the way to VLF while maintaining high sensitivity by effectively suppressing

¹² Leon Cooper (1930–present) is an American physicist who shared the Nobel Prize in Physics in 1972 for his work on the theory of superconductivity, specifically the formulation of the BCS theory alongside John Bardeen and Robert Schrieffer.

¹³ The reason for spin-exchange during atomic collisions is not dominated by dipoledipole interaction but an energy splitting between the singlet and triplet potentials of the alkali-alkali dimer, which may lead to a phase shift during the collisions that may exchange the electron spin states [23, 24].

relaxation caused by spin-exchange collisions. Chapter 1 discusses the limitations of optically pumped magnetometers with a special focus on relaxation caused by spin-exchange collisions and the strategies to effectively eliminate them. Chapter 2 will then discuss how these ideas can be exploited to build a tunable magnetometer for the detection of NMR at ZULF conditions.

MACROSCOPIC MAGNETOMETRY

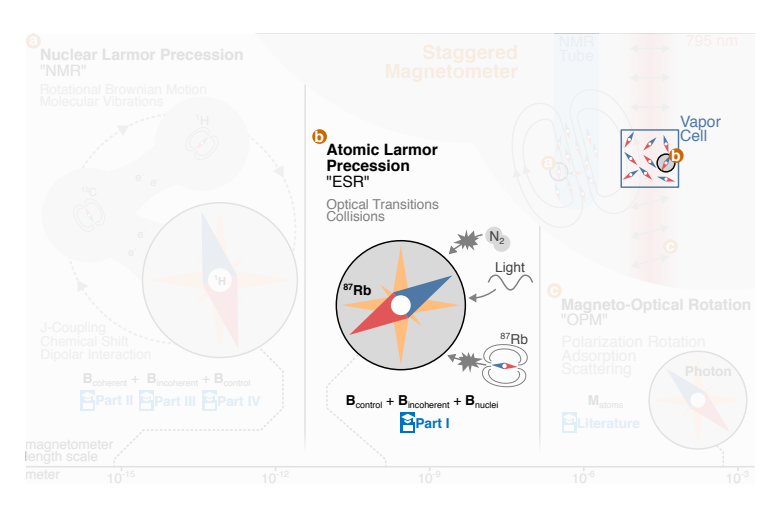
Finally, the last step of the staggered magnetometer in Figure 0.1c is about monitoring the electron spin. For high-electron spin precession frequencies again inductive detection could be an option which is often done in electron paramagnetic resonance (EPR) experiments. Other approaches such as electrically detected magnetic resonance [25] have been performed in solid, by probing the material's spin-state-dependent electrical properties (e.g. electrical resistance).

However, for alkali atoms, the availability of optical transitions can be exploited to efficiently measure the electronic spin state. Optically detected magnetic resonance [26] is a very common approach for other types of electron spin-based magnetometers like NV centers. In this thesis, optical rotation will be used to measure the projection of the magnetization of a hot vapor of ⁸⁷Rb.

All stages combined form a three-layer magnetometer system, comprising three magnetometer stages that perform magnetic field measurements from the subatomic to the macroscopic length scale. These measurements, realized in every ZULF NMR experiment, effectively bridge the gap of length scales to allow molecular dynamics and chemical structural information at the nanoscale to be observed on a macroscopic level.

Part I

MAGNETOMETRY



OPM are suitable for detecting NMR at zero field, offering high sensitivity and a sufficiently broad bandwidth that covers the range of common scalar coupling constants. However, when increasing the field to bridge the gap to conventional low-field NMR experiments, using an optical magnetometer raises several issues, including the need to compensate for the three orders of magnitude difference in atomic versus nuclear gyromagnetic ratio and the different operating conditions of DC and RF magnetometers.

In the first chapter of the thesis, the physical origin of these issues will be investigated (refer to Chapter 1). This knowledge will then be applied in Chapter 2 to design a magnetometer that can be instantly tuned to the nuclear LARMOR frequency over a broad range of frequencies.

These chapters follow closely the publication Bodenstedt et al. [27] with some additional results soon being published in Bodenstedt et al. [28].

1

ATOMIC VAPOR SPIN PHYSICS UNDERLYING OPTICAL MAGNETOMETRY

Magnetometers have a long and storied history, dating back to the discovery of the compass effect. For many years, sensitivity records in the low-frequency regime were held by SQUIDs, while inductive detectors held the record at high frequencies. However, in recent years, advancements in technology have allowed for the development of highly sensitive OPMs, which were previously limited by the short coherence times of atoms. Despite these earlier limitations, OPMs are now capable of achieving sensitivities that rival those of SQUIDs and inductive detectors, and they are becoming increasingly popular in a wide range of applications.

The best magnetic sensor strategy depends on many factors like bandwidth, operating conditions, energy consumption, weight, or sensing size. Only taking the latter into account, Figure 1.1 (adapted from [29]) provides an overview of different sensor strategies, their sensitivity, and their effective length. For detecting magnetic signals of NMR samples with a few milliliters in volume, the main topic of this thesis, OPMs, SQUIDs and inductive sensors are the most sensitive realized magnetometers so far.

The OPM revolution was triggered by the exploitation of a mechanism that can suppress efficiently relaxation caused by spin-exchange collisions, the dominant relaxation mechanism for dense alkali vapors. Even if the theory by Happer and Tam [30] from 1977 (based on previous work by Grossetête [31] from 1964) was known for decades, it was not until 2002 when Allred et al. [32] succeeded in exploiting this effect for magnetometry. Atomic magnetometers based on this principle are consequently called SERF magnetometers.

OPMs have been realized with several physical systems, including hot/cold thermal atomic vapors (based on potassium (K), rubid-

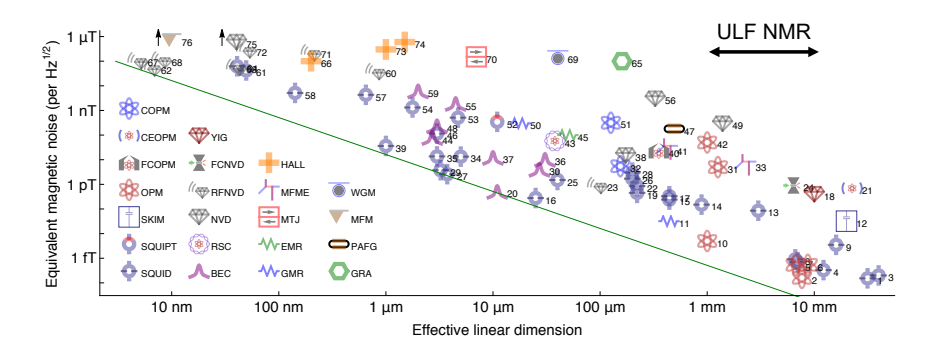


Figure 1.1: Reported magnetic sensitivity $\delta B\sqrt{T}$ for different sensor technologies (adapted from Mitchell and Palacios Alvarez [29]) as a function of their effective linear dimension. Except for RFNVD (= radio-frequency magnetometer based on a dense ensemble of NVs), the noise levels represent the lowest reported value at frequency $\leq 1\,\mathrm{kHz}$. References and numeric values can be found in [29].

ium (Rb), cesium (Cs), Hg¹ or helium (He)²) and solid-state defects (mostly dense ensembles of charged NVs).

This chapter will discuss the basics of the physics behind OPMs based on hot alkali vapors that are required to understand the limitations that existing implementations face and what ideas determined the choices that lead to designing the magnetometer used for most experiments of this thesis. This will not and cannot cover all the knowledge of the OPM community. The interested reader is referred to the book *Optical Magnetometry* by Budker and Kimball [35], the doctoral thesis by Seltzer [23], and the cited original publications.

1.1 FUNDAMENTAL SENSITIVITY ESTIMATIONS

In the classical description, the presence of a magnetic field ${\bf B}$ gives rise to a torque

$$\tau = \mu \times \mathbf{B} \tag{1.1}$$

perpendicular to both the magnetic moment μ and the field itself, which forces the magnetic moment to precess around the magnetic

¹ The ground state of Hg is an electronic singlet state. Some isotopes have a non-zero nuclear spin which allows magnetometry via the hyperfine levels [33].

² He has a singlet ground which is insensitive to magnetic fields. However, the first meta-stable triplet excited state can be efficiently populated and used for magnetometry [34].

field vector with angular precession frequency $\omega = \gamma \mathbf{B}$, where γ is spin system's gyromagnetic ratio. It is this precession that is eventually used for magnetometry. In the absence of any additional interactions, this precession would continue indefinitely.

Bloch Equations

However, in an ensemble, relaxation phenomena come into play, leading to the magnetization $\mathbf{M} = \frac{1}{V} \sum_i \mu_i$ relaxing towards its thermal equilibrium state \mathbf{M}_0 . Here, V is the ensemble's volume. A very simplified model that is often used in the context of spin precession, describes the temporal evolution of a magnetization vector $\mathbf{M} = (M_x, M_y, M_z)^{\mathsf{T}}$ in a magnetic field $\mathbf{B} = (B_x, B_y, B_z)^{\mathsf{T}}$ (with $B_z \gg B_x$, B_y) via the three phenomenological Bloch³ equations [36]

$$\frac{\mathrm{d}}{\mathrm{d}t}M_{x} = \gamma_{\mathrm{n}}\left(\mathbf{M} \times \mathbf{B}\right)_{x} - \frac{M_{x}}{T_{2}} \tag{1.2a}$$

$$\frac{\mathrm{d}}{\mathrm{d}t}M_{y} = \gamma_{\mathrm{n}} \left(\mathbf{M} \times \mathbf{B}\right)_{y} - \frac{M_{y}}{T_{2}} \tag{1.2b}$$

$$\frac{\mathrm{d}}{\mathrm{d}t}M_z = \gamma_{\mathrm{n}} \left(\mathbf{M} \times \mathbf{B}\right)_z - \frac{M_z - M_0}{T_1} \tag{1.2c}$$

These equations introduce two relaxation times⁴: The spin-spin relaxation time T_2 describes the dephasing phenomena of individual spins in an ensemble. During this process, the spin energy does not gain or lose energy. In contrast, the spin-lattice relaxation time T_1 describes a relaxation process leading the spin ensemble to approach its thermal equilibrium energy⁵. Using a random field model, it can be shown [37, 38] that in NMR for a single spin

$$T_1 \le T_2 \le 2T_1$$
 (1.3)

However, this inequality may not hold for all two levels systems at all time scales [39, 40].

- 3 Felix Bloch (1905–1983) was a Swiss-American physicist who made groundbreaking contributions to the field of solid-state physics, particularly his development of the Bloch theory, which explained the behavior of electrons in crystalline solids and laid the foundation for the understanding of phenomena such as electrical conductivity and magnetism.
- 4 Note that in the magnetometry community, there exist alternative definitions of relaxation times. For example, in Seltzer [23] the relaxation time $T_2^{(\text{Seltzer})} = 2\pi T_2$ are defined to fulfill $T_2^{(\text{Seltzer})} = 1/\Delta\omega$ with $\Delta\omega$ being the half width at half maximum of the magnetic resonance. This alternative convention will not be used within this thesis.
- 5 In NMR, the distinction between T_1 and T_2 is only meaningful in the presence of a strong magnetic field. At zero field ($\mathbf{B} = 0$ and $\mathbf{M}_0 = 0$) $T_1 = T_2$.

Equation 1.2a–1.2c are often sufficient to describe uncoupled systems with simple dynamics. However, in reality, non-linearities, cross-relaxation, and coupling between multiple spins often lead to non-exponential relaxation of multi-spin systems. For example, coupled spin states, like singlet states in a two-spin system, may decay significantly slower than each individual spin component, leading to the full system evolution being a superposition of long-lived and very unstable components that can no longer be described by Equation 1.2a–1.2c.

However, on short timescales, (sub-)systems may be still adequately described by a set of instantaneous relaxation times. This description will be used e.g. for describing the spin relaxation in a hot alkali vapor, that, when operated in the spin-exchange-dominated regime, features strongly non-exponential relaxation behavior.

Atomic Shot Noise Limit

Under these conditions and some additional assumptions⁶, Auzinsh et al. [43] derived an estimation

$$\delta B_{\rm SNL} pprox rac{1}{\gamma} rac{1}{\sqrt{N\tau T_2}}$$
 (1.4)

for the atomic shot noise limited (SNL) direct current (DC) sensitivity of a spin precession-based magnetic measurement. Here, N is the number of atoms, τ the is measurement time and γ is the atomic gyromagnetic ratio.

In reality, for an OPM based on hot alkali vapor, these assumptions are only partly fulfilled. For instance, the relaxation rate $\Gamma_{\rm rel} \equiv 1/T_2$ as well as the atomic gyromagnetic ratio γ depend on both the density (and therefore the number of atoms N) and the polarization level. The signal of interest is often not constant (i.e. non-DC signals). However, the equation can be interpreted as a kind of cost function in a multi-parameter optimization problem, being the minimum optimal operating condition where e.g. an increase of the number density would no longer lead to an improvement of sensitivity.

For OPMs based on alkali atoms, the parameter γ is in the order of the electron gyromagnetic ratio $\gamma_{\rm e}=-2\pi\times28\,{\rm GHz/T}$ and depends

Alternatively, often referred to as the spin projection noise (SPN) limit.

⁶ For example, the derivation assumes a system of N spins that are fully polarized. This state then precesses for the time T_2 . Afterward, the angular momentum is measured at an axis orthogonal to the current polarization with an accuracy given by Heisenberg uncertainty relation. This measurement is repeated for the measurement time τ . More details and derivations can be found in [41–43].

on the atomic species as well as the polarization and magnetic field. It is often convenient to define the precession slowing-down factor

$$q_{\text{Larmor}} \equiv \frac{\gamma_{\text{e}}}{\gamma} = \frac{\omega_0}{\omega} \stackrel{\text{in SERF}}{=} \frac{\left| \langle \hat{\mathbf{f}} \rangle \right|}{\left| \langle \hat{\mathbf{S}} \rangle \right|} , \qquad (1.5)$$

where ω_0 is the precession frequency of a free electron if placed in the same magnetic field as the atom.

The number of atoms N can be controlled by changing the temperature of the cell containing the vapor. The maximum measurement time τ is often limited by the lifetime of the signal of interest. In the context of NMR, this is usually given by the sample's nuclear spin relaxation time. Finally, the transverse relaxation rate $\Gamma_{\rm rel}$ depends on many factors, including the temperature, atomic density, buffer gas composition/pressure, magnetic field, and pumping rate.

Whereas there is literature discussing sensitivity optimization for specific applications [23, 44–47] little has been reported about rapidly tunable magnetometers spanning several orders of magnitude in bias field and center frequency. The latter operating conditions are needed for detecting the frequency dispersion of NMR relaxation rates, which is one of the goals of this thesis. In order to build a suitable magnetometer for this scenario, this chapter will investigate the magnetic field dependence of the parameters γ and $\Gamma_{\rm rel}$ and how they affect the magnetometer's sensitivity according to Equation 1.4.

1.2 DENSITY MATRIX EQUATION

In a general form, the time evolution of a quantum system described by a density operator $\hat{\rho}$ can be described by a density matrix equation (DME)

$$\frac{\mathrm{d}}{\mathrm{d}t}\hat{\rho}(t) = \mathcal{L}(\hat{\rho}(t), t) , \qquad (1.6)$$

where \mathcal{L} is a not necessarily linear function of $\hat{\rho}$ and t. In some scenarios, the time evolution can be expressed as a linear equation in the form of a master equation of LINDBLAD⁷ or REDFIELD⁸ form.

⁷ Göran Lindblad (1945–2020) was a Swedish mathematician and physicist known for his contributions to the field of open quantum systems, particularly his formulation of the Lindblad equation that describes the dynamics and evolution of quantum systems interacting with their environment.

⁸ Alfred G. Redfield (1890–1983) was an American chemist whose pioneering work in the field of nuclear magnetic resonance spectroscopy contributed significantly to the understanding of molecular structure and dynamics.

For alkali atoms, an approximate DME

$$\frac{\mathrm{d}}{\mathrm{d}t}\hat{\rho} = \mathcal{L}^{(\mathrm{coh})}(\hat{\rho}) + \mathcal{L}^{(\mathrm{SE})}(\hat{\rho}) + \mathcal{L}^{(\mathrm{SD})}(\hat{\rho}) + \mathcal{L}^{(\mathrm{OP})}(\hat{\rho}) + \mathcal{L}^{(\mathrm{diff})}(\hat{\rho}) \quad (1.7)$$

describing the time evolution of the ground state (including both hyperfine levels) was first derived by Happer and Tam [30] and can be roughly separated into five components, with the first one $\mathcal{L}^{(coh)}(\hat{\rho})$ summarizing the coherent, unitary evolution.

This chapter will briefly summarize the meaning of each term while highlighting the relevant implications for the magnetometer developed in this thesis.

Coherent Evolution

For a given Hamiltonian⁹ the coherent time-evolution of a quantum system can be described by the von Neumann¹⁰ equation

$$\mathcal{L}^{(\text{coh})}(\hat{\rho}) = \frac{1}{i\hbar} \left[\hat{H}, \hat{\rho} \right] . \tag{1.8}$$

For Alkali atoms in moderate fields a simple Hamiltonian

$$\hat{H}_0 = -\frac{A_{\text{HF}}}{\hbar^2} \hat{\mathbf{I}} \cdot \hat{\mathbf{S}} - \frac{\mu_{\text{B}} g_{\text{s}}}{\hbar} \mathbf{B} \cdot \hat{\mathbf{S}}$$
(1.9)

can be used to describe the coherent part of the evolution. Here, the nuclear spin's Zeeman interaction is ignored since it is orders of magnitude smaller¹² than the electron's and does not affect the analysis presented here significantly. For ^{87}Rb the hyperfine constant is $A_{\text{HF}}\approx 6.8\times 10^9\,\text{Hz}\cdot 2\pi\,\text{[48]}.$ The other fundamental constants are the Bohr magneton $\mu_{\text{B}}\approx 9.3\times 10^{-24}\,\text{J/T},$ the electron g-factor $g_{\text{e}}\approx 2.002$ and the reduced Planck¹⁴ constant $\hbar\approx 1.05\times 10^{-34}\,\text{Js}.$

- 9 William Rowan Hamilton (1805–1865) was an Irish mathematician and physicist who made important contributions to classical mechanics, optics, and algebra, including the development of quaternions, a mathematical system that extended complex numbers and found applications in various scientific and engineering fields.
- 10 John von Neumann (1903–1957) was a Hungarian–American mathematician and polymath who made significant contributions to various fields, including mathematics, physics, computer science, and economics, and is particularly known for his pioneering work in the fields of quantum mechanics and game theory.
- 12 The nuclear magneton $\mu_N \approx 5.1 \times 10^{-27}$ J/T is more than three orders of magnitude smaller than the Bohr¹³ magneton $\mu_B \approx 9.3 \times 10^{-24}$ J/T.
- 14 Max Planck (1858–1947) was a German physicist who revolutionized the field of quantum theory with his groundbreaking discovery of energy quantization, leading to the development of Planck's constant and laying the foundation for modern physics.

Also known as the LIOUVILLE¹¹-VON NEUMANN equation to highlight the analogy between classical HAMILTON mechanics and the quantum mechanical description

With this Hamiltonian the coherent time evolution is given by

$$\mathcal{L}^{(\text{coh})}(\hat{\rho}) = \frac{A_{\text{HF}}}{\hbar^2} \frac{\left[\hat{\mathbf{l}} \cdot \hat{\mathbf{S}}, \hat{\rho}\right]}{i\hbar} + \frac{\mu_{\text{B}}g_{\text{s}}}{\hbar} \frac{\left[\mathbf{B} \cdot \hat{\mathbf{S}}, \hat{\rho}\right]}{i\hbar} . \tag{1.10}$$

Secular Approximation

For absolute magnetic fields $|\mathbf{B}| \ll A_{\mathrm{HF}}/(\mu_{\mathrm{B}}g_{\mathrm{e}}) = 240\,\mathrm{mT}$, here called *moderate fields*, the hyperfine interaction is dominant and the Zeeman term only acts as a perturbation. In this case, an approximation (see Section A.9 for details) can be applied which leads to the neglection of certain off-diagonal terms in the system's Hamiltonian (see Figure 1.2) if it is expressed in an eigenbasis of the total angular momentum operator $\hat{\mathbf{F}}$ eigenstates. This approximation is very similar to the *secular approximation* applied to Hamiltonian in NMR and automatically leads to a decomposition of the Liouville space into subspaces (here labeled 1, 2, and 3), that are invariant under the time-evolution imposed by Equation 1.9.

The hyperfine coupling also causes an energy splitting between eigenstates with F = 1 and F = 1 which leads to fast oscillations of the elements of the subspace 2 and 3 (see Figure 1.2), that is much fast than any relaxation rate usually experienced by the atoms. For this reason, cross-relaxation between the subspaces is efficiently quenched leading to the independent time-evolution of the subspaces even under the influence of relaxation superoperators. The neglection of terms in the relaxation superoperators that cause cross-relaxation is also called *secular approximation* in NMR and is discussed in more detail in Section A.9.

The validity of these two approximations enables a completely separate analysis of the time evolution within the three subspaces. In the context of optical magnetometry, subspaces 2 and 3 produce time-dependent observables characterized by oscillations occurring at frequencies on the order of $A_{\rm HF}$, often surpassing the bandwidth limitations of typical photodiodes by several orders of magnitude. Consequently, it is often sufficient to focus on the analysis of subspace 1, denoted as the "secularized density" operator [47] given by

$$\hat{\rho}_{\text{sec}} = \hat{\rho}_{F=1} \oplus \hat{\rho}_{F=2} \quad , \tag{1.11}$$

where $\hat{\rho}_{F=1,2}$ represents block matrices containing the density operator for the subspaces of F=1 or F=2, respectively.

Sometimes only the last step is called the secular approximations in physics.

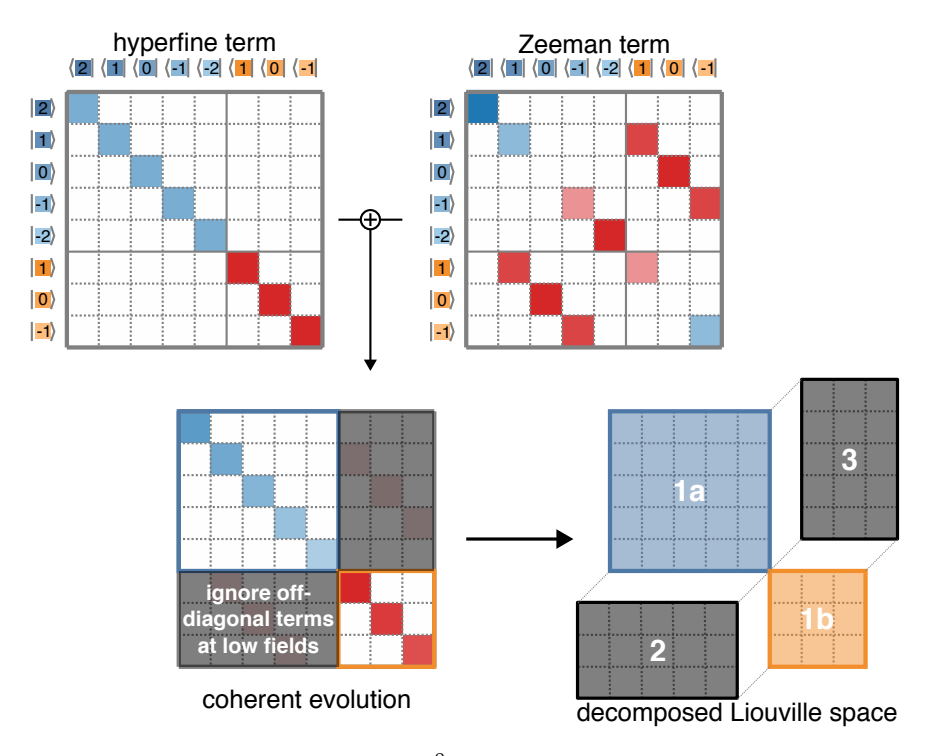


Figure 1.2: Approximation of the 87 Rb spin Hamiltonian leads to a decomposition of the system's Liouville space into subspaces that are invariant under coherent evolution. At moderate fields, the Zeeman term only acts as a perturbation to the dominant hyperfine term. As a consequence, off-diagonal terms outside the diagonal blocks can be ignored in the first order, which leads to a decomposition of the Liouville space into (at least) three invariant subspaces. Under coherent evolution the coherences in subspace (2) and (3) oscillate with a frequency in the order of the hyperfine splitting $A_{\rm HF}$. If this is significantly higher than the measurement bandwidth these coherences may not be observable and may be ignored. Red/blue squares indicate negative/positive terms whereas white represent zero.

For the rest of this chapter, the secular approximation is implicitly assumed without repetitive mention. This approach offers a distinct advantage: it compels the system to evolve as though the hyperfine coupling term were included, even when not explicitly integrated into the calculations. This proves particularly advantageous in numerical simulations, where the minimal time step is often constrained by the fastest dynamics within the system. Neglecting the hyperfine terms in such scenarios provides a substantial computational advantage while imparting minimal impact on result accuracy.

Spin-Exchange Collisions

The probabilistic nature of spin exchange/destruction collisions, optical pumping, or diffusion effects is not described in the form of a VON NEUMANN equation. Originally developed by Grossetête [31] and Happer and Tam [30] the following density matrix equation

$$\mathcal{L}^{(\text{SE})} = \frac{\hat{\rho}_I \otimes \hat{\rho}_S - \hat{\rho}}{T_{\text{SE}}} \tag{1.12}$$

describes the part of the time evolution of the density operator $\hat{\rho}$ that is caused by spin-exchange collisions with the spin-exchange collision time T_{SE} given by

$$\frac{1}{T_{\rm SE}} = R_{\rm SE} = n\overline{v}\sigma_{\rm SE} \tag{1.13}$$

with the atom density n, the mean velocity \overline{v} and σ_{SE} the spin-exchange collision cross-section.

$$\hat{\rho}_{I,S} = \text{Tr}_{I,S}(\rho) \tag{1.14}$$

are the reduced density operators in the subspace of the atom's nuclear spin *I* and *S* respectively.

Each reduced density operator is linear in $\hat{\rho}$. However, the tensor product $\hat{\rho}_I \otimes \hat{\rho}_S = \hat{\rho}_I \otimes \hat{\mathbb{1}}_S \cdot \hat{\mathbb{1}}_I \otimes \hat{\rho}_S$ is not. Analytical solutions exist for low polarization levels, where linear approximations can be applied. However, it is much harder to solve this equation analytically for arbitrary density operators.

Spin exchange collisions by themselves conserve both the ensemble's average nuclear $\langle \hat{S} \rangle$ and the electron spins $\langle \hat{I} \rangle$ (and by that also the average total angular momentum $\langle \hat{F} \rangle$), but relax the entanglement between the electron and nuclear spin subsystems towards a

Due to this non-linear term, 1.7 is not a classical quantum mechanical master equation of neither LINDBLAD or REDFIELD form.

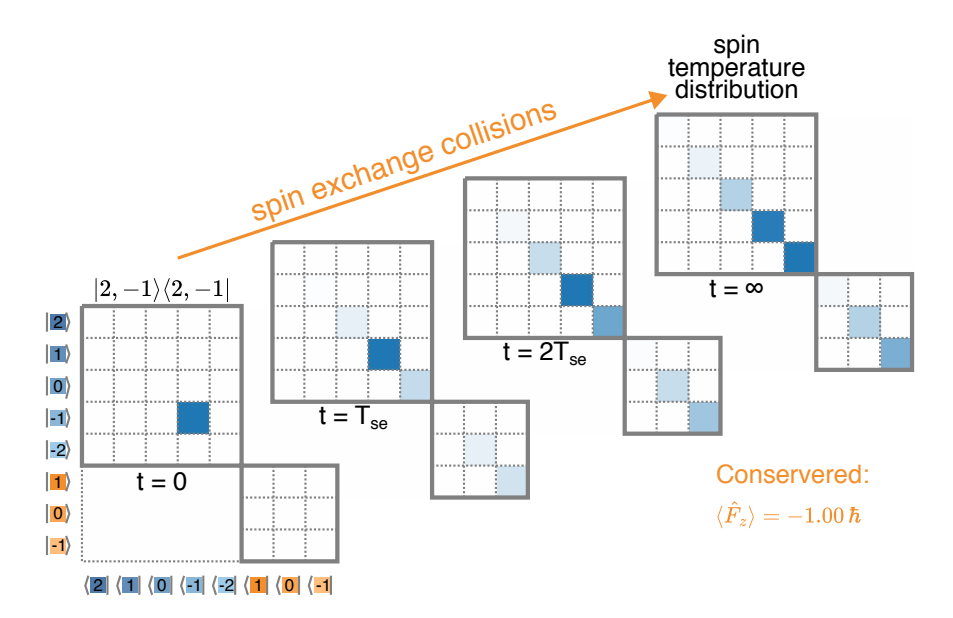


Figure 1.3: Graphical illustration of the effect of spin-exchange collisions (with a time constant $T_{\rm se}$) on an atomic ensemble of ⁸⁷Rb. Starting from a pure state $\hat{\rho}_0 = |2, -1\rangle \langle 2, -1|$ the system quickly relaxes towards a spin-temperature distribution while conserving the expectations values for each spin-operator. Dark blue indicates a high population (normalized to each graph's maximum value), whereas a white color represents zero population. The product basis of the hyperfine states $|Fm_F\rangle$ is chosen as the basis for the density matrix. Orange states represent F=1, whereas blue states represent F=2. Note that the secular approximation is applied (off-diagonal terms are neglected) which effectively introduces infinite hyperfine coupling.

product state. However, the product state quickly becomes entangled through the strong hyperfine interaction between the electron and nucleus. As a consequence, in contrast to spin-destruction collisions that will be discussed next, spin-exchange collisions only affect T_2 and do not cause any spin-lattice relaxation.

The effect of spin-exchange collisions is also illustrated in Figure 1.3. Starting from a pure state $\hat{\rho}_0 = |2, -1\rangle \langle 2, -1|$, the system quickly relaxes towards spin-temperature contribution (see Section 1.4) while conserving the expectations values of each spin operator.

The partial trace in Equation 1.14 can easily be calculated in the tensor product basis $|I m_I\rangle \otimes |S m_S\rangle$. However, since this is not the eigenbasis of the Hamiltonian it is sometimes useful to write the operators in a slightly different form [30]

$$\frac{\hat{\rho}_I \otimes \hat{\mathbb{1}}_S}{2} = \frac{\hat{\rho}}{4} + \frac{\hat{\mathbf{S}} \cdot \hat{\rho} \hat{\mathbf{S}}}{\hbar^2} \tag{1.15a}$$

$$2\hat{\mathbb{1}}_I \otimes \hat{
ho}_S = \hat{\mathbb{1}} + \frac{4\langle \hat{\mathbf{S}} \rangle \cdot \hat{\mathbf{S}}}{\hbar^2}$$
, (1.15b)

The right-hand side of Equation 1.15b can be calculated for any basis which may reduce the need for basis transformation and therefore speed up computation.

Spin Destruction Collisions

Spin destruction collisions completely depolarize the electron spin and can be mathematically described by

$$\mathcal{L}^{(\mathrm{SD})}(\hat{\rho}) = \frac{\hat{\rho}_I \otimes \frac{\hat{\mathbb{I}}_S}{2} - \hat{\rho}}{T_{\mathrm{SD}}} , \qquad (1.16)$$

where $T_{SD} \equiv 1/R_{SD}$ is the spin destruction time constant. The collisions may occur between alkali atoms but also include collisions with buffer gas atoms or quenching gas molecules.

Without hyperfine coupling, the nuclear spin would be unaffected by spin destruction collision and only the electron spin would relax with the inverse time constant $T_{\rm SD}$. However, the hyperfine coupling strongly couples the two spins and forces them to relax simultaneously. This phenomenon will be discussed in more detail in Section 1.3. In contrast to spin-exchange collisions, spin-destruction collisions cause both spin-lattice and spin-spin relaxation and there-

Derivation can be found in Section A.7 (Equation A.29 and Equation A.33).

This phenomenon is similar to SR₂K in NMR.

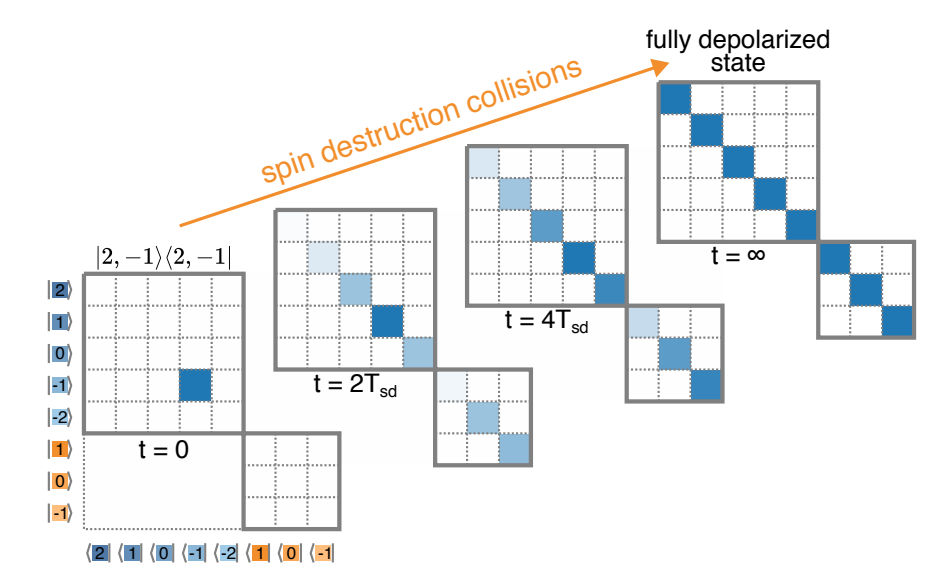


Figure 1.4: Graphical illustration of the effect of spin-destruction collisions (with time constant $T_{\rm SD}$) on an atomic ensemble of ⁸⁷Rb. Starting from a pure state $\hat{\rho}_0 = |2,-1\rangle \langle 2,-1|$ the system quickly relaxes towards a completely depolarized state. Dark blue indicates a high population (normalized to each graph's maximum value), whereas a white color represents zero population. The product basis of the hyperfine states $|Fm_F\rangle$ is chosen as the basis for the density matrix. Orange states represent F=1, whereas blue states represent F=2. Note that the secular approximation is applied (off-diagonal terms are neglected) which effectively introduces infinite hyperfine coupling. This leads to a fully depolarized state (even for the nuclear spin) even if the spin destruction term by itself would only relax the electron spin.

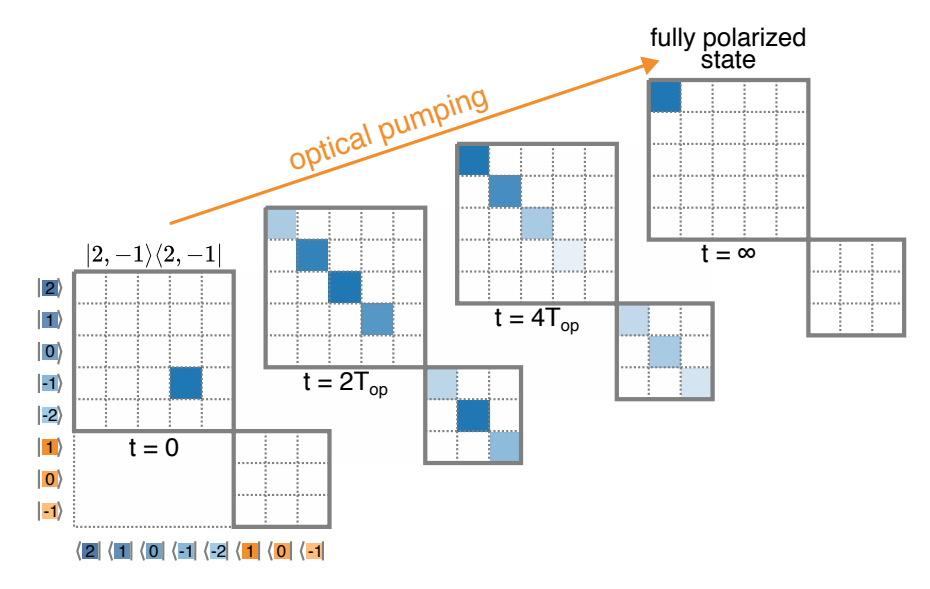


Figure 1.5: Graphical illustration of the effect of optical pumping with circularly polarized light (with time constant $T_{\rm op} \equiv 1/R_{\rm OP}$) on an atomic ensemble of $^{87}{\rm Rb}$. Starting from a pure state $\hat{\rho}_0 = |2,-1\rangle \langle 2,-1|$ the system evolves towards a completely polarized state $|2,2\rangle \langle 2,2|$. Dark blue indicates a high population (normalized to each graph's maximum value), whereas a white color represents zero population. The product basis of the hyperfine states $|Fm_F\rangle$ is chosen as the basis for the density matrix. Orange states represent F=1, whereas blue states represent F=2. Note that the secular approximation is applied (off-diagonal terms are neglected) which effectively introduces infinite hyperfine coupling. This leads to a fully polarized state (even for the nuclear spin) even if the optical pumping term by itself would only polarize the electron spin.

fore affect the longitudinal relaxation time T_1 as well as the transverse relaxation time T_2 . Figure 1.4 shows graphically the effect of spin-destruction collisions starting with the pure state $|2,-1\rangle \langle 2,-1|$ which relaxes towards the maximally mixed state 1/8.

Optical Pumping

The optical pumping term can be described

$$\mathcal{L}^{(\mathrm{OP})}(\hat{\rho}) = R_{\mathrm{OP}}\left(\hat{\rho}_{I} \otimes \left(\frac{\hat{1}_{S}}{2} + \mathbf{s} \cdot \frac{\hat{\mathbf{S}}_{S}}{\hbar}\right) - \hat{\rho}\right) \tag{1.17}$$

in a similar way. R_{OP} is the optical pumping rate and

For a $\sigma_{\mathbf{e}_z}^+$ polarized beam propagating along z it is $\mathbf{E} = \frac{|\mathbf{E}|}{\sqrt{2}} (\mathrm{e}^{-\mathrm{i}\omega t}, \mathrm{i}\mathrm{e}^{-\mathrm{i}\omega t}, 0)$ leading to $\mathbf{s} = (0,0,1)^{\mathsf{T}}$.

$$\mathbf{s} = \frac{\mathrm{i}}{|\mathbf{E}|^2} \mathbf{E} \times \mathbf{E}^* \tag{1.18}$$

the mean photon spin of a pump laser beam with a complex electric field vector **E**.

Just the optical pumping term by itself (Equation 1.17) would only polarize the electron spin, leaving the nuclear spin untouched. However, similar to the terms discussed in the previous sections, the hyperfine term links electron and nuclear polarization. This is graphically illustrated in Figure 1.5. Starting from the same pure state as $|2, -1\rangle \langle 2, -1|$ before, the optical pumping term transforms the system into the fully polarized (pure) state $|22\rangle \langle 22|$.

Spin Diffusion

Finally, spatial diffusion can be described by the following equation

$$\mathcal{L}^{(\text{diff})}\hat{\rho}) = D\boldsymbol{\nabla} \cdot \boldsymbol{\nabla}\hat{\rho} \quad , \tag{1.19}$$

where *D* is the diffusion coefficient. Spatial diffusion will be mostly ignored in this thesis. Diffusion is typically undesirable and can be partly suppressed by introducing a buffer gas at reasonably high pressure.

Avoiding spin diffusion not only prevents relaxation due to the diffusion itself, but it also prevents collisions with the cell walls that can significantly contribute to spin-destruction collisions. It also affects optical pumping by moving in or out of the beam profile.

Spin Temperature Distribution

For this section, the diffusion term is neglected. If there is no active optical pumping, the spin-destruction term (in combination with the spin-exchange and hyperfine terms) would relax the system to a completely mixed, unpolarized state. However, without spin destruction collisions there would exist a steady-state solution of the DME Equation 1.7 with non-zero polarization, called the *spin temperature distribution*

$$\hat{\rho}_{\text{steady-state}} = N_S N_I \cdot e^{\beta \cdot \hat{\mathbf{f}}} \tag{1.20}$$

which is defined by an inverse spin temperature β [30]. This density operator describes an ensemble with maximized entropy under

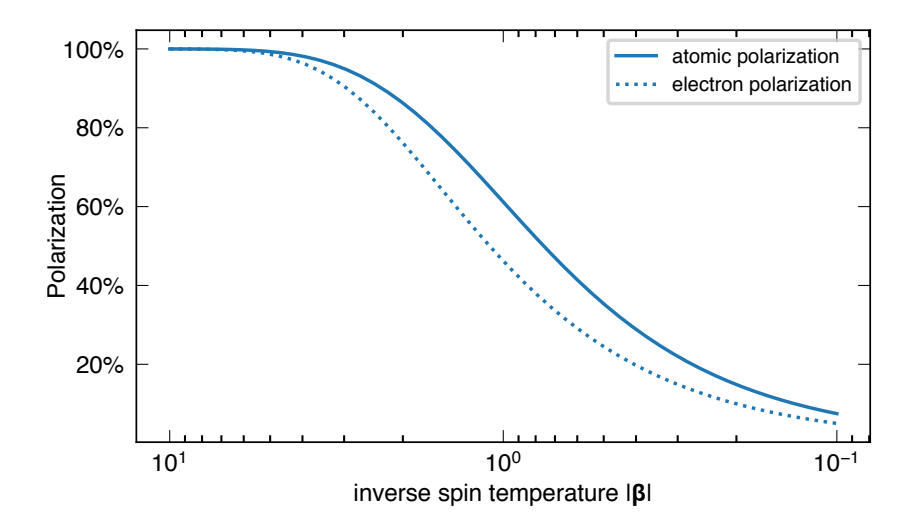


Figure 1.6: Electron (dotted) and atomic polarization (solid) as a function of the inverse spin temperature β .

the constraint of constant total angular momentum and number of atoms [49]. Here,

$$N_{\alpha} = \frac{\sinh(|\boldsymbol{\beta}|/2)}{\sinh(|\boldsymbol{\beta}|(\alpha+1/2))} \quad \text{for } \alpha \in \{S, I\}$$
 (1.21)

are normalization constants.

The fact alone, that a non-zero steady-state solution exists without active pumping highlights the important property of spin-exchange collisions that they do not necessarily lead to relaxation. More importantly, the solution also allows non-zero electron spin, which is important for magnetometry applications.

For the spin-temperature distribution, the absolute electronic and atomic polarization of an ⁸⁷Rb atomic ensemble

$$[0,1] \ni P_{S} = \frac{\left| \langle \hat{\mathbf{S}} \rangle \right|}{S\hbar} = \frac{2}{\hbar} \left| \langle \hat{\mathbf{S}} \rangle \right| = \frac{2}{\hbar} \frac{\left| \langle \hat{\mathbf{S}} \rangle \right|}{q_{\text{rel}}} \stackrel{87}{=} \frac{4P_{\text{F}}}{q_{\text{rel}}}$$
(1.22a)

$$[0,1] \ni P_{\mathrm{F}} = \frac{\left| \langle \hat{\mathbf{f}} \rangle \right|}{(I+S)\hbar} = \frac{q_{\mathrm{rel}} \left| \langle \hat{\mathbf{S}} \rangle \right|}{(I+S)\hbar} \stackrel{^{87}\mathrm{Rb}}{=} \frac{\left| \langle \hat{\mathbf{f}} \rangle \right|}{2\hbar} = \frac{q_{\mathrm{rel}} P_{\mathrm{S}}}{4} \quad (1.22b)$$

can be expressed as

$$P_{\rm F} = \tanh\left(\frac{|\beta|}{2}\right) \tag{1.23a}$$

$$P_{\rm S} \stackrel{\rm 87Rb}{=} \frac{4}{q_{\rm rel}} \tanh\left(\frac{|\beta|}{2}\right)$$
 (1.23b)

Even if $P_{\rm S}$ and $P_{\rm F}$ are different even for states described by a spin temperature, they are often not distinguished in the literature [35].

in terms of the inverse spin temperature β (see also Figure 1.6 and vice versa [23]

$$|\boldsymbol{\beta}| = \ln\left(\frac{1 + P_{\rm F}}{1 - P_{\rm F}}\right) \tag{1.24a}$$

$$|\boldsymbol{\beta}| \stackrel{^{87}\text{Rb}}{=} \ln \left(\frac{4 + q_{\text{rel}} P_{\text{S}}}{4 - q_{\text{rel}} P_{\text{S}}} \right) . \tag{1.24b}$$

Sometimes also called "paramagnetic factor" [50].

Here the longitudinal relaxation slowing down factor

$$q_{\text{rel}} = \frac{\left|\langle \hat{\mathbf{f}} \rangle \right|}{\left|\langle \hat{\mathbf{S}} \rangle \right|}$$

$$\stackrel{^{87\text{Rb}}[5^{1}]}{=} 4 + \frac{2}{\cosh(|\boldsymbol{\beta}|)}$$

$$\stackrel{^{87\text{Rb}}[5^{1}]}{=} 2 + \frac{4}{P_{S}^{2} + 1}$$

$$(1.25)$$

is introduced, which describes the slowed-down relaxation and optical pumping of the total angular momentum $\hat{\mathbf{F}}$ due to rapid spin-exchange collisions and hyperfine coupling. In the SERF regime it holds $q_{\rm rel} = q_{\rm Larmor}$.

If optical pumping (here assumed to be parallel with $\bf B$) and spin destruction are considered, the steady-state polarizations are given by

$$P_{\rm S} = \frac{|\mathbf{s}| R_{\rm OP}}{R_{\rm OP} + R_{\rm SD}} \tag{1.26a}$$

$$P_{\rm F} \stackrel{\rm 87Rb}{=} \frac{q_{\rm rel}}{4} \frac{|\mathbf{s}| R_{\rm OP}}{R_{\rm OP} + R_{\rm SD}} \tag{1.26b}$$

where again $R_{\rm OP}$ is the optical pumping rate, $R_{\rm SD} = 1/T_{\rm SD}$ the spin destruction rate and $q_{\rm rel}$ the slowing down factor.

1.3 NUMERICAL CALCULATIONS AND SIMULATIONS

The full DME Equation 1.7 is non-linear in $\hat{\rho}$ due to the spin-exchange collision term. Solving this ordinary differential equation analytically for a wide range of parameters is a difficult task unless extreme conditions (low polarization, SERF regime) are considered. Nonetheless, conducting numerical simulations and calculations can be relatively straightforward [30, 52, 53] and frequently provide a qualitatively sufficient understanding of the system.

This section will discuss the results of some of these calculations and simulations for ^{87}Rb . Some of these calculations are performed similarly to the theoretical analysis performed by Happer and Tam [30]. In contrast to their calculations, a local linearization of the spin-exchange term in the DME is employed to describe both low and high degrees of polarization. Further details are provided in Appendix C. For all results described in this chapter, a vapor temperature of 323.15 K (150 °C) and a buffer gas (N_2) pressure of 933 mbar (700 Torr) is assumed.

Transverse Relaxation, SERF Effect, and Light Narrowing

The first scenario explores the transverse relaxation rate $1/T_2$ as a function of the magnetic field B_z and atomic polarization/spin temperature β . It is assumed that the system is polarized along the z axis (parallel to B_z , i.e.

$$\hat{\rho}_0 \propto e^{\beta_z \hat{F}_z} \tag{1.27}$$

and that the overall polarization is kept constant (e.g. by constant optical pumping and only small angle excitation). This scenario is common for constantly pumped SERF/RF OPMs where the magnetic field and the pump beam are parallel.

Figure 1.7 shows the simulated slowest transverse relaxation rates as a function of the applied magnetic field B_z for various inverse spin temperatures β . The relaxation rates are obtained by taking the real part of an eigenvalue (λ_+) which is discussed in Appendix C. Even at high magnetic fields, due to the hyperfine coupling, the electronic spin decays significantly slower (top dashed red line) than the spin exchange rate (dashed grey line).

There are two common approaches to reduce the transverse relaxation rate even further:

Firstly, at low magnetic fields where the Larmor period $1/f_{\rm Larmor}$ is significantly longer than the spin-exchange collision time $T_{\rm SE}$, relaxation due to these collisions is strongly suppressed due to the SERF effect. Spin-exchange collisions by themselves do not cause the total angular momentum $\langle {\bf F} \rangle$ to relax. They do so only in combination with the Zeeman interaction, which leads to a dephasing of the two hyperfine subspaces. In the SERF regime, rapid spin-exchange collisions are constantly mixing the two hyperfine subspaces and preventing their dephasing.

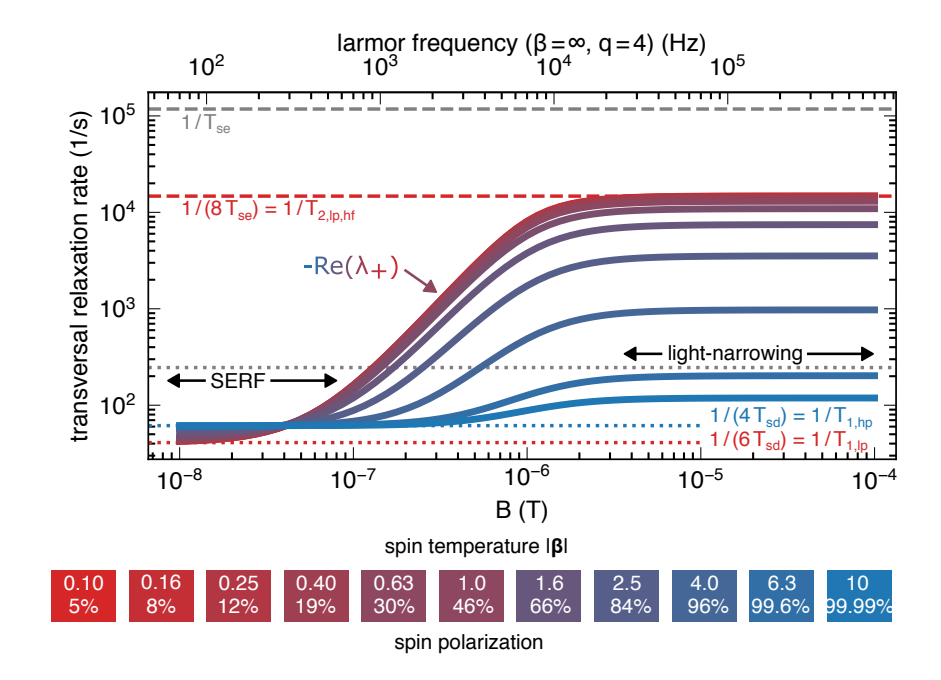


Figure 1.7: Numerical calculations of the transverse relaxation rate of ^{87}Rb for different inverse spin temperatures β (polarized along z and magnetic field (along z) under small angle excitation. Horizontal lines highlight relevant relaxation rates like the spin exchange rate $1/T_{\text{SE}}$ and the spin destruction rate $1/T_{\text{SD}}$. The values are obtained from extracting the real part of an eigenvalue λ_+ of the matrix elements defined via Equation C.12.

In the SERF regime, as long as the spin temperature is constant, the transverse relaxation is given by $T_2 = q_{\rm rel}T_{\rm SD}$. For ⁸⁷Rb the minimum is given by $q_{\rm LP}T_{\rm SD} = 6T_{\rm SD}$, where $q_{\rm LP} = 6$ is the low-polarization slowing down factor.

An alternative approach exploits highly polarized states. If most of the population is in the stretched $|F=2,m_F=2\rangle$ state, the F=1 hyperfine level is almost unpopulated and the dephasing has no significant impact on the ensemble magnetization. This regime is called the *light-narrowing* regime. Even if effective, at high magnetic fields, very high spin temperatures (and therefore optical pumping rates) are required to create a sufficiently stretched state to suppress the relaxation due to spin-exchange collisions. The relaxation also accelerates the more the polarization drops during the free induction decay (FID). The nonlinearity of the spin-exchange term leads to a massive increase of relaxation rates even for tiny changes in the polarization 15 .

Atomic Larmor Frequency and Precession Slowing Down Factor

Figure 1.8 shows the precession slowing down factor depending on the spin temperature as well as the magnetic field for the same conditions as above. In the SERF regime (LF = low field), where rapid spin-exchange collisions maintain the spin temperature equilibrium, the slowing down factor shows the strong polarization dependence and reaches the maximum values of $q_{\rm HP,LF} = 4$ and $q_{\rm LP,LF} = 6$ in the high (HP)/low polarization (LP) limit.

In contrast, at a high magnetic field, where the LARMOR precession is too fast to allow the spin-exchange collisions to maintain the equilibrium, the slowing-down factor tends to the constant, high-field maximum $q_{\rm HF}=4$.

Longitudinal Relaxation

In the last example, the longitudinal relaxation rate $1/T_1$ will be examined by numerically integrating the DME in Equation 1.7. The numerically simulated density operators $\hat{\rho}(t)$ can be used to calculate the expectations values $\langle \hat{S} \rangle (t)$, $\langle \hat{I} \rangle (t)$ and $\langle \hat{F} \rangle (t)$. By calculating the

Details in Appendix C.

¹⁵ The two most blueish lines in Figure 1.7 represent a polarization of $P=99\,99\%$ and $P=99\,6\%$. At Earth's magnetic fields, even this tiny difference leads to relaxation rates that differ by more than an order of magnitude.

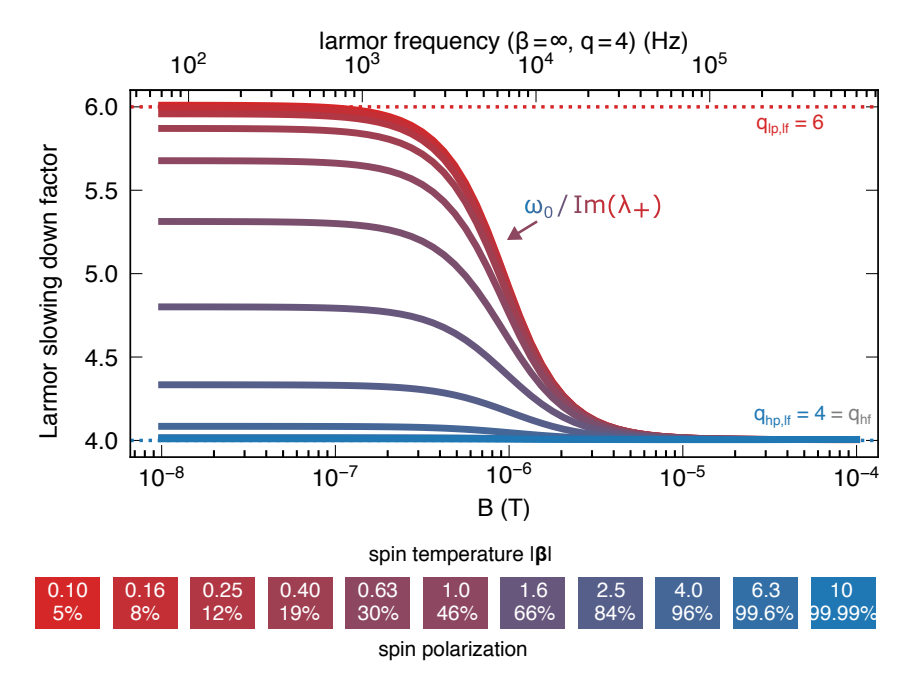


Figure 1.8: Numerical calculations of the precession slowing down factor $q_{\rm Larmor}=\omega_0/\omega$ of $^{87}{\rm Rb}$ for different inverse spin temperatures β (polarized along z and magnetic field (along z) under small angle excitation. At high magnetic fields it is $q_{\rm HF}\stackrel{87}{=}4$ independent of the inverse spin temperature. For low magnetic fields, $q_{\rm Larmor}$ depends on the polarization and can take values between $q_{\rm HP,LF}\stackrel{87}{=}4$ and $q_{\rm LP,LF}\stackrel{87}{=}6$. The values are obtained from extracting the imaginary part of an eigenvalue λ_+ of the matrix elements defined via Equation C.12.

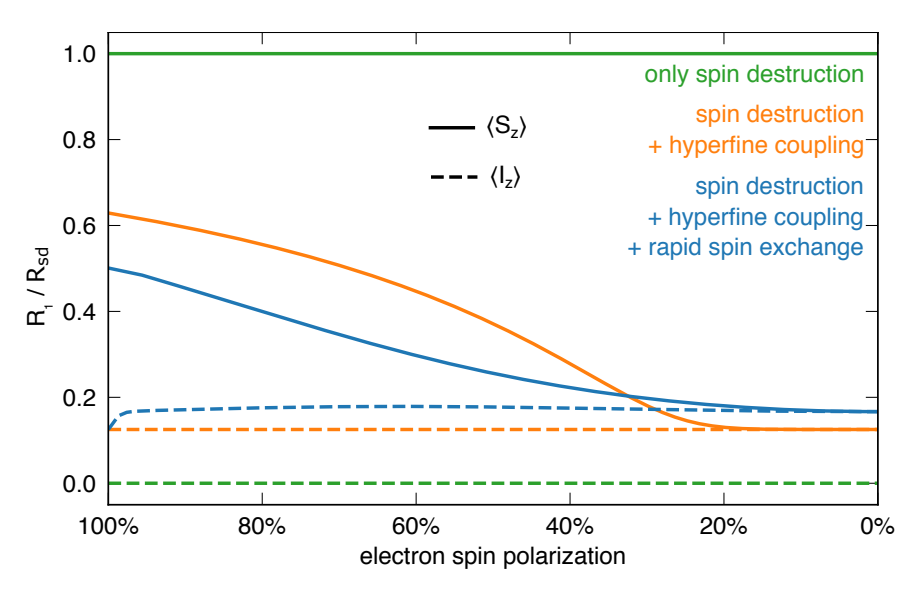


Figure 1.9: Simulation of the longitudinal relaxation of electron $\langle S_z \rangle$ and nuclear spin $\langle I_z \rangle$ for different combinations of interactions/couplings (spin destruction, spin exchange, and hyperfine coupling) as functions of the electron spin polarization. The state is polarized along z, parallel to the magnetic field B_z . As long as the fields are moderate, there is no field dependence.

slopes, e.g. $\frac{d\langle \hat{S} \rangle(t)}{dt}$ for short times the relaxation rates can be extracted for different polarization levels. The results of this analysis are plotted in Figure 1.9.

If there is no hyperfine interaction and no spin-exchange collisions, the electron and nuclear spins are completely decoupled. In this case, spin-destruction collisions only relax the electron spin at the rate $1/T_{\rm SD}$ whereas the nuclear spin is unaffected, which is shown by the green curves in Figure 1.9. However, as soon as the other interactions are considered (orange/blue curves), both spin systems relax at a reduced rate. This phenomenon is well known in the context of NMR as SR₂K if the electron spin is replaced by another, fast-relaxing nuclear spin (e.g. a quadrupolar nuclear spin). In this context, the hyperfine term is called J-coupling (or spin-spin coupling).

At high polarization levels, spin exchange collisions slow down the longitudinal relaxation, whereas they accelerate it at low polarization levels. In the latter regime, nuclear and electron spin relax at the same rate. In the case of rapid spin-exchange collisions, this is equal to $R_1 = q_{\rm rel}/T_{\rm SD}$. However, at high-polarization levels, the electron

spin relaxes significantly faster than this factor and the nuclear spin relaxation rate.

1.4 ACCOUNTING FOR DQ/DT IN THE BLOCH EQUATION

The last detail, the fact that electron and nuclear spin (and by that the total angular momentum) do not relax at the same rate at high polarization levels is not trivial. In fact, this effect does not show up (see Figure 1.10) if the spin system is modeled via the common BLOCH equation of the form [23, 35]

$$\frac{\mathrm{d}\mathbf{S}}{\mathrm{d}t} = \frac{1}{q} \left(\gamma_{\mathrm{e}} \mathbf{B} \times \mathbf{S} + R_{\mathrm{OP}} \left(\frac{\hbar s \mathbf{e}_{z}}{2} - \mathbf{S} \right) - R_{\mathrm{SD}} \mathbf{S} \right) , \qquad (1.28)$$

which holds for low polarization levels or scenarios where the spin temperature is constant. These requirements are often fulfilled in scenarios where small perturbations from steady-state solutions are simulated. However, for FIDs or measurements involving the longitudinal relaxation rates, the polarization may change in time which requires the introduction of correction terms.

A common approach to derive Equation 1.28, see e.g. [23] or [35], is to start from

$$\frac{\mathrm{d}\mathbf{F}}{\mathrm{d}t} = \gamma_{\mathrm{e}}\mathbf{B} \times \mathbf{S} + R_{\mathrm{OP}} \left(\frac{\hbar s \mathbf{e}_{z}}{2} - \mathbf{S} \right) - R_{\mathrm{SD}}\mathbf{S}$$
 (1.29)

which, in similar form, was originally derived by Happer and Tam [30] and further studied by Appelt et al. [50]. It can be transformed via $\mathbf{F} = q\mathbf{S}$ into

$$\frac{\mathrm{d}\mathbf{F}}{\mathrm{d}t} = \frac{1}{q} \left(\gamma_{\mathrm{e}} \mathbf{B} \times \mathbf{F} + R_{\mathrm{OP}} \left(\frac{\hbar q s \mathbf{e}_z}{2} - \mathbf{F} \right) - R_{\mathrm{SD}} \mathbf{F} \right) \tag{1.30}$$

which looks similar to Equation 1.28 except the electron **S** spin being replaced by the total angular momentum **F**. This equation may describe accurately the time evolution of the ensemble in the SERF regime, but it does not describe the accessible observable, i.e. the electron spin **S**.

It may therefore be convenient to transform it into an equation for the electron spin by using the same identity $\mathbf{F} = q\mathbf{S}$ leading to

$$\frac{d(q\mathbf{S})}{dt} = \gamma_{e}\mathbf{B} \times \mathbf{S} + R_{OP} \left(\frac{\hbar s \mathbf{e}_{z}}{2} - \mathbf{S}\right) - R_{SD}\mathbf{S} . \qquad (1.31)$$

It can be shown [35]
that rapid spin
exchange leads to $F \parallel S$ in the SERF
regime.

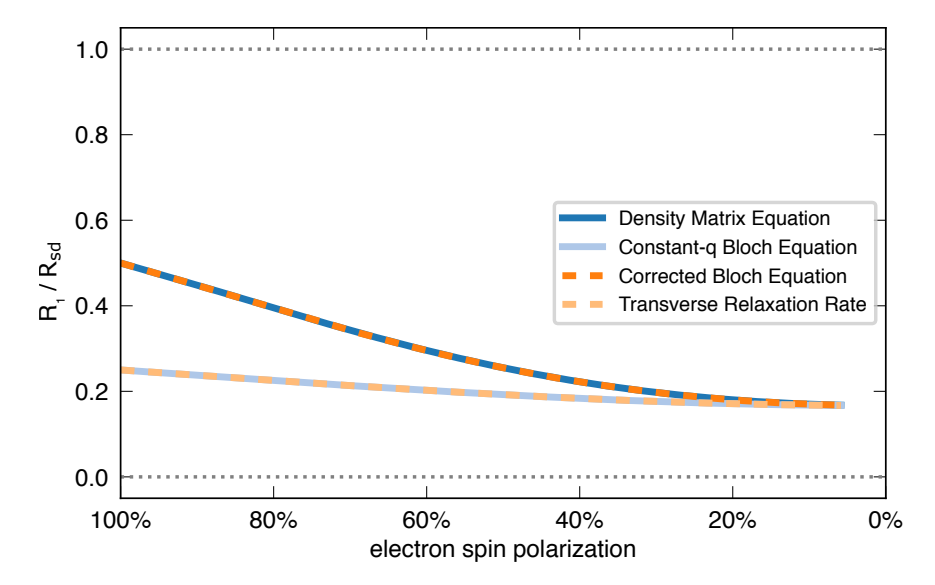


Figure 1.10: Simulated longitudinal relaxation rates using both the DME from Equation 1.7 and the BLOCH equation from Equation 1.28 for different levels of electron spin polarization. As can be seen, the Bloch equation (light blue) does not accurately describe longitudinal electron spin relaxation at high polarization levels due to neglecting the time dependence of the slowing-down factor q in its derivation. It only affects state evolution with time-dependent spin polarization (i.e. quasi-steady-state scenarios are not affected) or scenarios with high polarization. In other words, results that are based on the assumption of low spin polarizations are also not affected as well as transverse relaxation with constant spin polarization (bright orange). The corrected Bloch equation (see Equation 1.37 and Equation 1.39) match the DME simulations. In the extreme case of full polarization P = 100% the transverse relaxation time $T_2 = 2T_1$ is twice as long as the longitudinal relaxation time.

If q is constant in time, i.e. $\frac{dq}{dt} \approx 0$, it holds $\frac{d\mathbf{F}}{dt} = \frac{d(q\mathbf{S})}{dt} \approx q\frac{d\mathbf{S}}{dt}$, leading to Equation 1.28. Here, in contrast, the scenario of $\frac{dq}{dt}$ not being negligible is considered and q is assumed to change in time. To this end, the product rule

$$\frac{\mathrm{d}(q\mathbf{S})}{\mathrm{d}t} = \frac{\mathrm{d}q}{\mathrm{d}t}\mathbf{S} + \frac{\mathrm{d}\mathbf{S}}{\mathrm{d}t}q\tag{1.32}$$

is applied on the left-hand side of Equation 1.31. By applying the chain rule twice to the first term¹⁶, the total derivative

$$\frac{\mathrm{d}q}{\mathrm{d}t} = \frac{\mathrm{d}q(|\mathbf{S}(t)|)}{\mathrm{d}t} = \frac{\mathrm{d}q}{\mathrm{d}|\mathbf{S}|} \cdot \frac{\mathrm{d}|\mathbf{S}|}{\mathrm{d}\mathbf{S}} \cdot \frac{\mathrm{d}\mathbf{S}}{\mathrm{d}t}$$
(1.33)

can be split into three terms. In the SERF regime, by assuming perfect spin-temperature distributions, explicitly calculating and combining the first

$$\frac{\mathrm{d}q}{\mathrm{d}|\mathbf{S}|} \stackrel{1.22a}{=}_{1.25} - \frac{32|\mathbf{S}|}{(4|\mathbf{S}|^2 + 1)^2} , \tag{1.34}$$

and the second

$$\frac{\mathrm{d}\left|\mathbf{S}\right|}{\mathrm{d}\mathbf{S}} = \begin{pmatrix} \frac{\partial}{\partial S_x} \\ \frac{\partial}{\partial S_y} \\ \frac{\partial}{\partial S_z} \end{pmatrix} \sqrt{S_x^2 + S_y^2 + S_z^2} = \frac{1}{\left|\mathbf{S}\right|} \begin{pmatrix} S_x \\ S_y \\ S_z \end{pmatrix} = \frac{\mathbf{S}}{\left|\mathbf{S}\right|} \tag{1.35}$$

term leads to

$$\frac{\mathrm{d}q}{\mathrm{d}t} = -\frac{32}{(4|\mathbf{S}|^2 + 1)^2}\mathbf{S} \cdot \frac{\mathrm{d}\mathbf{S}}{\mathrm{d}t} , \qquad (1.36)$$

Inserting Equation 1.36 in Equation 1.32 and combining it with Equation 1.31 leads to the corrected Bloch equation 17

$$\frac{d\mathbf{S}}{dt}q - \frac{32}{(4|\mathbf{S}|^2 + 1)^2} \left(\mathbf{S} \cdot \frac{d\mathbf{S}}{dt}\right) \mathbf{S}$$

$$= \gamma_e \mathbf{B} \times \mathbf{S} + R_{\text{OP}} \left(\frac{\hbar s \mathbf{e}_z}{2} - \mathbf{S}\right) - R_{\text{SD}} \mathbf{S}$$
(1.37)

Here, $\frac{d|\mathbf{S}|}{d\mathbf{S}} = \left(\frac{\partial |\mathbf{S}|}{\partial S_x}, \frac{\partial |\mathbf{S}|}{\partial S_y}, \frac{\partial |\mathbf{S}|}{\partial S_z}\right)^\mathsf{T}$ is used as a short notation for the total derivative of the function $|\mathbf{S}| : \mathbb{R}^3 \to \mathbb{R} : \mathbf{S} = (S_x, S_y, S_z)^\mathsf{T} \mapsto |\mathbf{S}| = \sqrt{S_x^2 + S_y^2 + S_z^2}$ expressed as a Jacobian matrix (other maybe more familiar notations are $D|\mathbf{S}|$, $\mathbf{J}_{|\mathbf{S}|}$, $\frac{\partial |\mathbf{S}|}{\partial (S_x, S_y, S_z)}$ or $\nabla |\mathbf{S}|$) with \cdot representing matrix multiplication.

for the electron spin in the SERF regime¹⁸. For the special case of polarization ($\mathbf{S} = (0,0,S_z)$) and magnetic field ($\mathbf{B} = (0,0,B_z)$) being parallel to the z-axis, the Equation 1.37 can be further simplified

$$\frac{dS_z}{dt}q - \frac{32S_z^2}{(4S_z^2 + 1)^2} \frac{dS_z}{dt} = \frac{dS_z}{dt} \left(q - \frac{32S_z^2}{(4S_z^2 + 1)^2} \right)
= R_{OP} \left(\frac{\hbar s}{2} - S_z \right) - R_{SD}S_z$$
(1.38)

leading to

$$\frac{dS_z}{dt} = \left(q - \frac{32S_z^2}{(4S_z^2 + 1)^2}\right)^{-1} \left(R_{OP}\left(\frac{\hbar s}{2} - S_z\right) - R_{SD}S_z\right)$$
 (1.39)

which is of very similar form compared to Equation 1.28. The correction caused by dq/dt is responsible for the faster relaxation observed in Figure 1.9 and is now correctly predicted. For $|\mathbf{S}| = \text{const.}$ it follows dq/dt = 0 and the additional relaxation disappears which explains why this error does not affect quasi-steady-state solutions.

In the extreme limit of full polarization, i.e. $S_z = \frac{1}{2}$ and q = 4, and no optical pumping, the relaxation rate is given by

$$\frac{1}{T_1} = \left(4 - \frac{32(1/2)^2}{(4(1/2)^2 + 1)^2}\right)^{-1} R_{SD} = \frac{R_{SD}}{2} . \tag{1.40}$$

Under the same conditions, in the SERF regime the transverse relaxation time

$$T_2 = \frac{q}{R_{\rm SD}} = \frac{4}{R_{\rm SD}} = 2T_1 \tag{1.41}$$

is twice as long as the longitudinal relaxation time, which is identical to the thermodynamic limit for an uncoupled single spin system (compare Equation 1.3) and a phenomenon rarely observed for spin precession experiments.

The increased rate of relaxation stems from the characteristic of the spin temperature distribution that also influences the polarization-dependent deceleration factor q and the disparity between electron spin and atomic polarization. As can be seen in Figure 1.11a, for each hyperfine manifold (F = 1 and F = 2), there is a fixed ratio between the electron spin and the total angular momentum, which could be described by the constant slowing down factors $q_{F=1} = -4$ and $q_{F=2} = 4$.

¹⁸ Optical pumping is already assumed to be along z.

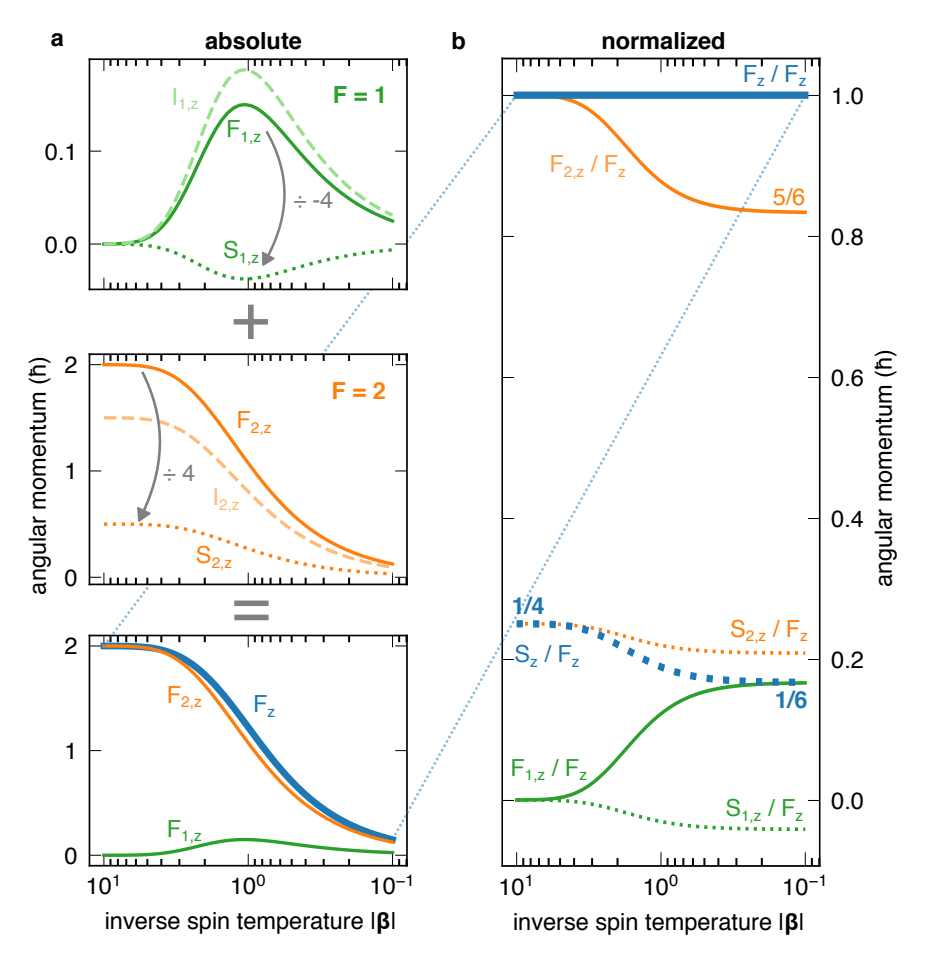


Figure 1.11: Contribution of the nuclear and electron spin of the two hyperfine states of ^{87}Rb to the total angular momentum as a function of the inverse spin temperature $|\pmb{\beta}|$. a) The two top plots show the expectation values $\langle \hat{S}_z \rangle, \langle \hat{I}_z \rangle$ and $\langle \hat{F}_z \rangle$ for the two hyperfine subspaces F=1 (top) and F=2 (middle). For each subspace, it shows that only 1/4 of the total angular momentum is carried by the electron spin, although the sign differs for both levels. At high spin temperatures $|\pmb{\beta}|\gg 1$ the total spin is carried by the F=2 states, whereas at low spin temperatures $|\pmb{\beta}|\ll 1$ it is distributed 5/6 (F=2) to 1/6 (F=1). This leads to a spin-dependent contribution of the proportion of the total spin, that is carried by the electron spin as can be seen in b). In the end, this is responsible for the spin temperature dependent slowing down factor as well as the faster electron spin relaxation compared to the total angular momentum.

What changes with the inverse spin temperature β or polarization is the ratio of how much each of the hyperfine manifolds contributes to the total state. As can be seen in Figure 1.11b, at high polarization levels, the state is almost completely given by states with F=2, explaining the high-polarization slowing down factor $q_{\text{HP,LF}}=4=q_{F=2}$. At low polarization levels, there is a 5/6 to 1/6 ratio, which explains the low polarization slowing down factor

$$\frac{1}{q_{\text{LP,LF}}} = \frac{\langle \hat{S}_z \rangle}{\langle \hat{F}_z \rangle} = \frac{\langle \hat{S}_{1,z} \rangle + \langle \hat{S}_{2,z} \rangle}{\langle \hat{F}_z \rangle} = \frac{\langle \hat{F}_{1,z} \rangle / q_{F=1} + \langle \hat{F}_{2,z} \rangle / q_{F=2}}{\langle \hat{F}_z \rangle}$$

$$= \frac{5/6 \cdot \langle \hat{F}_z \rangle / 4 - 1/6 \cdot \langle \hat{F}_z \rangle / 4}{\langle \hat{F}_z \rangle} = \frac{1}{6}, \tag{1.42}$$

i.e. $q_{LP,LF} = 6$.

As a consequence, the amount of angular momentum carried by the electron spin is lower at low-polarization than at high-polarization levels, as can be seen in Figure 1.11b. Therefore, the electron spin has to have a higher decay rate to maintain the spin-temperature distribution, which cannot be provided by the constant-q Bloch equation (1.28) for the electron spin.

TUNABLE DC-RF OPTICAL PUMPED MAGNETOMETER

The preceding chapter introduced some basic physics underlying the operating principle of OPMs. In this chapter, the magnetometer utilized for the experiments presented in this thesis is described. It bridges the frequency gap between SERF and RF magnetometers and allows studying field depending NMR phenomena. This chapter summarizes lots of results that are published in Bodenstedt et al. [27].

2.1 MOTIVATION

Similar to the field of OPMs, relaxation in NMR, caused by random fluctuations of microscopic physical processes, may strongly depend on the external magnetic field and the LARMOR frequency. By studying nuclear spin relaxation, valuable information about the nanoscale environment of molecules can be obtained. This method is employed in the field of NMRD to investigate the relaxation of nuclear spins at various magnetic fields (see Chapter 6). Typically, this technique involves either spatially moving the sample between different magnetic field environments or changing the magnetic field in situ via coils and rapid current switching, limiting this approach to magnetic fields close to Earth's field or samples with long relaxation times or

Combining this technique with OPM detection may solve both issues. However, to this end, a magnetometer that can operate across a broad range of magnetic fields while also being tunable to the nuclear LARMOR frequency is necessary. Moreover, it should be resilient to fast magnetic field changes (e.g., FFC or control pulses) and should have short recovery times after temporary saturation. The desired frequency range covers five decades of the RF spectrum, ranging from Extremely Low Frequency (ELF) through ELF, SLF, ULF, VLF to LF.

The challenge here is to find a design and operating conditions that allow rapid changes in the nuclear LARMOR frequency without sacrificing sensitivity. The desired time scale precludes changes in the vapor, temperature, laser current, or diode temperature. The entire

setup should also be compact enough to be portable for conducting experiments outside the laboratory.

2.2 MAGNETOMETER CHARACTERISTICS

This section summarizes some OPM specific characteristics and compares them to the requirements for the experiments described in this thesis.

Sensing Pattern

Scalar magnetometers measure the absolute magnitude of a magnetic field vector $|\mathbf{B}|$ without providing information about its orientation. In the context of OPMs based on alkali atoms, this is achieved through sensors that exclusively measure the frequency of an FID. Scalar magnetometers can achieve sub-femtotesla sensitivity $(0.54\,\mathrm{fT}/\sqrt{\mathrm{Hz}})\,[54])$ and can be employed for monitoring brain activity in a human brain [55]. However, in the context of nuclear spin precession, the detectable magnetic field

$$\mathbf{B}(t) = \begin{pmatrix} B_{\mathbf{x}}(t) \\ B_{\mathbf{y}}(t) \\ B_{\mathbf{z}}(t) \end{pmatrix} = \begin{pmatrix} B_{\mathbf{n}} \cos(\gamma_{\mathbf{n}} B_{0} t) \\ B_{\mathbf{n}} \sin(\gamma_{\mathbf{n}} B_{0} t) \\ B_{0} \end{pmatrix}$$
(2.1)

consists of a large component $\mathbf{B}_0 = (0,0,B_0)^\intercal$ along one axis (usually the z-axis), along with a relatively smaller, rotating field \mathbf{B}_n , where $|\mathbf{B}_n| = B_n \ll B_0$ and $\mathbf{B}_n \perp \mathbf{B}_0$. The absolute magnetic field

$$|\mathbf{B}(t)| = |\mathbf{B}_0 + \mathbf{B}_n| \approx B_0 + \mathcal{O}(B_x, B_y) \approx \text{const.}$$
 (2.2)

is almost independent (to a first-order approximation) of the field generated by nuclear spins. Consequently, scalar magnetometers are not ideal for detecting nuclear spin precession¹.

In contrast, vector magnetometers exhibit an orientation-dependent response². In this thesis, a vector magnetometer is chosen, with its

- 1 In principle, nuclear spin precession could be detected with a scalar magnetometer, for instance, by employing a solenoid to shield the \mathbf{B}_0 field from the magnetometer and applying an offset field to the sensor. At zero-field, scalar detection would also be possible, as the total magnetic field oscillates rather than precesses.
- 2 This does not imply that vector magnetometers always measure the projection of a magnetic field vector onto a specific axis. However, by employing additional techniques (e.g. field modulation), it is often feasible to extract the individual three-dimensional (3D) magnetic field components [23].

sensitive axis orthogonal to the \mathbf{B}_0 field and lying within the plane defined by the precessing nuclear spin vector.

Frequency Range

In comparison to SQUIDs, OPMs have a much narrower bandwidth, typically in the range of tens or hundreds of Hertz (Hz) for OPMs based on the SERF effect. While this narrow bandwidth is typically sufficient for detecting zero-field NMR spectra, as splittings due to scalar couplings rarely exceed a few hundred Hertz, NMRD requires the detection of nuclear spin precession over a much broader frequency range. Fortunately, it is often unnecessary to cover the entire frequency range in a single measurement, and the ability to tune the magnetometer's center frequency would suffice.

Although sub-femtotesla OPMs have been demonstrated for both DC signals [56] and RF signals [47] (even above MHz frequencies [57, 58]), achieving such high sensitivity continuously across a broad frequency range with a single, rapidly tunable sensor is not a straightforward task. This challenge primarily arises from the fact that DC and RF magnetometers operate in quite distinct regimes, involving different considerations for laser power, cell temperature, and gas pressure/composition. These parameters cannot be changed rapidly or, in some cases, not at all due to the long settling times of laser drivers or temperature controllers.

For this thesis, a rapidly tunable magnetometer was developed. This magnetometer combines the sensitivity-enhancing effects of DC, i.e. the SERF effect, and RF, i.e., the light-narrowing effect, to achieve nearly constant sensitivity across the ELF to VLF range without requiring adjustments to slowly changing variables such as cell temperature or laser power. This magnetometer meets the requirements for detecting NMRD signals at ultralow field strengths.

Magnetic Environment

Passive magnetic shielding, employing metals with high permeability (e.g., mu-metal), proves to be an effective means of reducing residual magnetic fields to a level suitable for SERF magnetometers, which are utilized in this context to detect nuclear spin precession signals. While this shielding assists in achieving the desired sensitivity of

the sensors, it imposes certain limitations on the NMR aspect of the experiment.

Magnetic shields not only restrict the potential size of NMR samples but also prohibit the application of high polarizing/control fields within the shield due to the risk of polarizing the shield itself. This is less of a concern for NMR detection applications but becomes more critical in the context of MRI. Additionally, the shield complicates sample handling by restricting the ways a sample can be placed, moved, or shuttled in and out if manually opening the shield is not an option.

While, for the experiments discussed in this thesis, the advantages of operating the magnetometer within the shield outweigh its disadvantages, shield-less NMR detection using OPM may offer certain advantages and has been demonstrated for e.g. nuclear quadrupole resonance at medium frequency (0.3 MHz to 3 MHz) RF frequencies [57, 59]. In principle, magnetometers with sufficient sensitivity (a few femtoteslas per square root of hertz, fT/ $\sqrt{\rm Hz}$) to detect NMR signals have been demonstrated in unshielded environments [60]. However, these magnetometers are often scalar magnetometers, making them less suitable for NMR detection and requiring differential or gradiometric operation to mitigate the impact of common mode noise.

Atomic Species

The choice of atomic species has a significant impact on the design and operation of an atomic magnetometer because the wavelength of the atomic transitions determines the requirements for the optics and lasers used. Additionally, different atomic species have varying vapor pressures, spin-exchange and spin-destruction collision cross-sections, nuclear spin, and isotopic compositions, all of which can affect the sensitivity and performance of the magnetometer.

The selection of ⁸⁷Rb as the atomic species for all the magnetometers used in this thesis was partly influenced by the availability of cells, lasers, and optics. However, this choice can be further justified. Among all alkali atoms, potassium (K) has the lowest spin exchange and spin destruction cross-sections, followed by rubidium (Rb) and cesium (Cs), making it the atomic species with the best expected (and achieved so far) sensitivity. However, at the same temperature, it also has the lowest vapor pressure among all stable alkali atoms. This could pose a significant challenge, especially for nuclear mag-

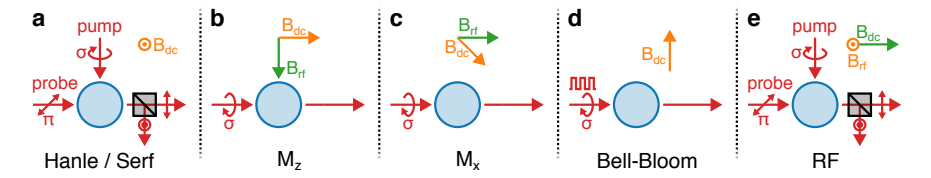


Figure 2.1: Overview of some magnetometer geometries (inspired by Fabricant et al. [42]) used to measure DC magnetic fields (**a**–**d**) in comparison to the most sensitive implementation of an RF magnetometer **e**. Red arrows indicate laser beams, orange arrows are measurable, target magnetic fields, and green arrows control fields. The SERF [56] **a**, the $M_{\rm Z}$ **b** [61], the $M_{\rm X}$ **c** [62] as well as the Bell-Bloom magnetometer **d** [63] have all been operated with sensitives in the order of 20 fT / $\sqrt{\rm Hz}$ and below. For this thesis, a combination of the SERF **a** and RF magnetometer **e** was used, due to their almost identical geometry.

netic resonance (NMR) samples with potential boiling points close to room temperature, where temperature isolation becomes a critical issue for K magnetometers. This challenge may become even more pronounced when dealing with biological samples that may have very limited temperature tolerance. Not only is temperature isolation a concern with K, but temperature stability is also a factor.

Rb appears to be a good compromise in this regard, offering lower collision cross-sections than Cs while achieving optimal densities at lower temperatures compared to K. For these reasons, this thesis will focus its discussion on magnetometers based on ⁸⁷Rb.

Geometry and Readout

The practically reachable sensitivity and performance of an OPM strongly depend on how the atomic state is controlled, how it evolves, and how it is read out. In an experiment, this is mostly determined by the number and geometry of the laser beams, their temporal and spatial profiles, polarization, and wavelength/detuning. Additionally, DC and RF/microwave control fields may be applied to further manipulate the system's evolution.

Figure 2.1 provides an overview of popular magnetometer geometries used for both DC and RF detection. Since the main objective of this thesis is to construct a combined DC/RF magnetometer, the chosen geometry should have operating conditions that work reasonably well for different frequency regimes. Ultimately, the SERF magne-

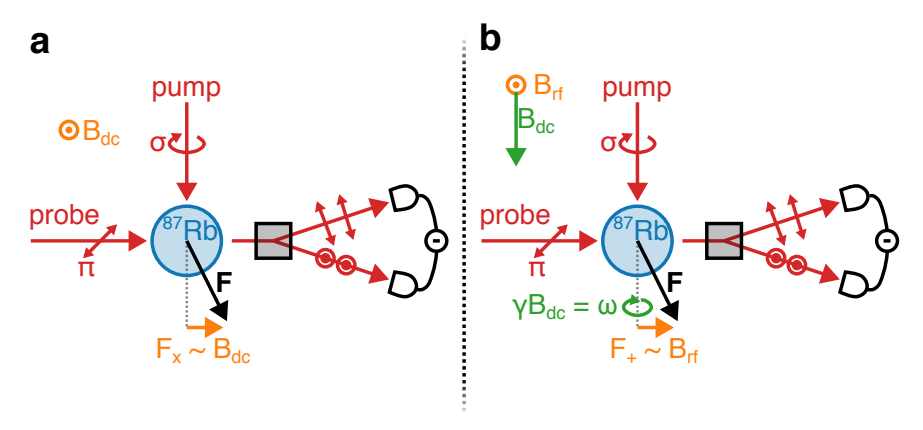


Figure 2.2: A more detailed schematic (in comparison to Figure 2.1a,e) for a typical two-beam SERF (a) and RF (b) OPM. The red arrows indicate the laser beams, with the pump beam being circularly polarized and the probe beam being linearly polarized. Optical rotation is measured using balanced detection. The orange arrows represent the target magnetic field, which is orthogonal to both the pump and probe beams. In b, the green arrow indicates a constant control magnetic field parallel to the pump beam.

tometer (a) and the RF magnetometer (e) meet these requirements by having nearly identical geometries.

Both magnetometers are based on a two-beam configuration, utilizing one resonant, circularly polarized laser beam for optical pumping, while incorporating a second, orthogonal, linearly polarized probe beam for non-destructive³ optical rotation measurements.

2.3 STATE OF THE ART

While specialized magnetometers tailored to specific operating conditions have been demonstrated, there has yet to be a setup encompassing the entire operating range necessary for the aforementioned experiments. This section elucidates the most relevant magnetometer strategies:

Spin-Exchange Relaxation Free Magnetometer

Magnetometers based on hot alkali vapors in the SERF regime have been reported [68] with sensitivities around $1\,\mathrm{fT}\,\sqrt{\mathrm{Hz}}^{-1}$. These types of magnetometers use two continuous wave beams: one for optical pumping employing on-resonant, circularly polarized light, while the other beam is linearly polarized and far off-resonant for non-destructive readout based on optical rotation (see Figure 2.2). The two beams are orthogonal to each other and the sensitive axis of the magnetometer.

These magnetometers exhibit sensitivity levels on par with SQUIDs, but they usually come with a significantly restricted bandwidth. For sufficiently slow spin precession ($\omega \ll 1/T_{\rm sd}$), the atomic state can be well described by a spin temperature distribution. In such cases, the spin evolution can often be described sufficiently with the phenomenological Bloch equation (see Equation 1.28).

$$\frac{\mathrm{d}\mathbf{S}}{\mathrm{d}t} = \frac{1}{q} \left(\gamma_{\mathrm{e}} \mathbf{B} \times \mathbf{S} + R_{\mathrm{OP}} \cdot \left(\frac{\hbar s \mathbf{e}_{z}}{2} - \mathbf{S} \right) - R_{\mathrm{SD}} \mathbf{S} \right) . \tag{2.3}$$

Here, $\mathbf{S} = \langle \hat{\mathbf{S}} \rangle$ represents the expectation value for the electron spin. In the following, it is assumed that the atoms are pumped along the z-axis and detected along the x-axis. Assuming a static magnetic field

$$\mathbf{B} = (B_{x}, B_{y}, B_{z})^{\mathsf{T}} , \tag{2.4}$$

the steady-state solution for the electron spin's x-component is given by:

$$S_x = S_0 \frac{(R_{\text{OP}} + R_{\text{SD}}) \gamma_e B_y + \gamma_e^2 B_x B_z}{(R_{\text{OP}} + R_{\text{SD}})^2 + \gamma_e^2 |\mathbf{B}|^2} .$$
 (2.5)

For $B_z = 0$ or $B_x = 0$, the magnetometer is only sensitive to magnetic fields along the y-axis, making it an ideal vector magnetometer. In other scenarios, the signal is a combination of all magnetic field components.

For an oscillating field along y with a constant field along z

$$\mathbf{B}(t) = (0, B_1 \cos(\omega t), B_0)^{\mathsf{T}} \tag{2.6}$$

This equation will only be used to discuss quasi-steady-state solutions, i.e., when dq/dt = 0, and the correction term derived in Section 1.4 can be ignored.

³ Typically, in an OPM, non-destructive readout does not fulfill the specific requirements of a quantum non-demolition measurement [64, 65] (with some exceptions [66, 67]). Here, the terms "non-destructive" or "dispersive" measurements will be used instead

the equation is solved by

$$S_{x}(t) = \frac{S_{0}\gamma_{e}B_{1}T_{2}}{2q} \left(\frac{\cos(\omega t) + (\omega - \omega_{0})T_{2}\sin(\omega t)}{1 + (\omega - \omega_{0})^{2}T_{2}^{2}} + \frac{\cos(\omega t) - (\omega + \omega_{0})T_{2}\sin(-\omega t)}{1 + (\omega + \omega_{0})^{2}T_{2}^{2}} \right)$$
(2.7)

with $\omega_0 = q \gamma_e B_0$ and $T_2 = q/(R_{OP} + R_{SD})$.

This equation suggests a clear method for converting a SERF magnetometer into an RF magnetometer by matching ω_0 with ω

$$S_x(t) = \frac{S_0 \gamma_e B_1 T_2}{2q} \left(\cos(\omega t) + \frac{\cos(\omega t) - 2\omega T_2 \sin(-\omega t)}{1 + 4\omega^2 T_2^2} \right)$$
 (2.8)

through the application of a magnetic field. However, the phenomenological Bloch equations do not accurately describe the spin evolution when spin precession surpasses the spin-destruction rate [23]. Furthermore, both T_2 and q are dependent on polarization (S_0) and the magnetic field (refer to Figure 1.7 and Figure 1.8). Notably, T_2 can vary significantly in magnitude when the magnetometer no longer operates in the SERF regime.

The SERF effect, which suppresses spin-exchange relaxation, relies on slow spin precession to maintain the distribution of spin temperatures. Therefore, extending an atomic magnetometer to the RF regime, where it experiences high frequencies and magnetic fields, necessitates a different approach to suppress relaxation caused by spin-exchange collisions.

Radio-Frequency Magnetometer

As demonstrated in Section 1.3, the SERF effect is not the sole phenomenon for suppressing transversal relaxation resulting from spin-exchange collisions. As long as a high spin polarization can be maintained, the light-narrowing effect proves to be nearly as effective and is the preferred method for highly sensitive RF magnetometers that rely on optically pumped atoms.

In the same scenario as previously described, i.e.,

$$\mathbf{B}(t) = (0, B_1 \cos(\omega t), B_0)^{\mathsf{T}},$$
 (2.9)

the expectation value [47]

$$\langle \hat{S}_x \rangle = \frac{S_0 \gamma_e B_1 T_2}{2q} \cos(\omega t)$$
 (2.10)

is almost identical to Equation 2.8. The resemblance between these equations implies that combining both of these approaches could be a promising strategy, provided that the relaxation time remains sufficiently long in both regimes. Furthermore, the field and polarization-dependent slowing-down factor, denoted as $q = q(P, |\mathbf{B}|)$, must be considered when attempting to maintain the magnetometer in resonance (via $\omega \stackrel{!}{=} \omega_0 = q \gamma_e B_0$) across a wide field range.

Integrated Sensors

There is a growing development of integrated, miniaturized [69, 70], mass-producible, and commercially available [71–73] magnetometers that are based on OPMs. The primary application driving these sensors is MEG, which measures the magnetic fields emitted by neural activity in the brain. For this reason, these sensors are optimized for detecting weak, low-frequency signals (less than 200Hz), specifically in the ELF and SLF frequency ranges. In contrast, NMRD requires a tunable magnetometer capable of detecting signals up to several kilohertz. Commercially available sensors are challenging to modify, both in terms of software and hardware, and therefore are not well-suited for the applications described in this thesis⁴.

2.4 WORKING PRINCIPLE

There are three significant challenges when operating the magnetometer across a wide range of RF frequencies (from ELF to low frequency LF bands):

As demonstrated in the previous section, the signal (in the linear regime) scales proportionally with the transverse relaxation rate T_2 . Spin-exchange collisions have the potential to significantly reduce T_2 . Therefore, to achieve a highly sensitive magnetometer, the a) suppression of spin-exchange collisions is of utmost importance. Keeping the magnetometer in resonance with the signal of interest poses another challenge, particularly due to the variable b) slowing-down factor. Lastly, in the context of NMRD, it is essential to maintain the magnetometer in resonance with the nuclear LARMOR frequency. Since both atomic and nuclear spins have LARMOR frequencies pri-

⁴ Savukov et al. [74] demonstrated the operation of a commercial QuSpin sensor at a few kHz, but this resulted in a significant loss in sensitivity (55 fT/ $\sqrt{\rm Hz}$ compared to 15 fT/ $\sqrt{\rm Hz}$).

marily determined by the magnetic field and a substantial difference in gyromagnetic ratios, c) *matching the atomic and nuclear* Larmor *frequencies* necessitates advanced magnetic field engineering.

Suppressing of Relaxation

In contrast to the SERF effect, light-narrowing operates effectively even in high magnetic field environments. However, optimal sensitivity for magnetometers operating in the SERF regime is typically achieved at lower pumping rates. If both operating modes are to be used simultaneously, an intermediate pumping rate will be required, which will not be optimal for either of these operating regimes.

Figure 2.3d illustrates how the transverse relaxation rate $(1/T_2)$ depends on the pumping rate and the bias field (brighter indicating slower relaxation). At low fields, thanks to the SERF effect, relaxation caused by spin-exchange collisions is efficiently suppressed across all spin polarization levels (see Figure 2.3b). In contrast, at high bias fields, only states with high pumping rates (and thus high spin polarization) benefit from light-narrowing, which reduces relaxation.

In both cases, an increase in the relaxation rate is noticeable at pumping rates exceeding $1 \times 10^4 \, 1/\mathrm{s}$. This is because the optical pumping rate itself contributes to the total relaxation via $1/T_2 = (R_{\mathrm{OP}} + R_{\mathrm{SD}})$. In other words, there exists an optimal pumping rate that minimizes the transverse relaxation rate, dependent on the temperature and magnetic field.

Slowing-Down Factor

Similar to the transverse relaxation rate T_2 , the slowing-down factor q also depends on both spin polarization and the bias field. To maintain resonance with the signal of interest in the magnetometer, it is essential to know the value of the slowing-down factor, or alternatively, employ a field-locking mechanism.

Thankfully, a prerequisite for operating the magnetometer in the light-narrowing regime is high spin polarization. As illustrated in the preceding chapter (refer to Figure 1.8), it becomes evident that for a high polarization (i.e., high spin temperatures), the slowing-down factor $q_{\rm HP}=4$ remains relatively constant. It is worth noting that for quantum noise-optimized SERF magnetometers, the optimal fundamental sensitivity is achieved at lower polarization levels, potentially

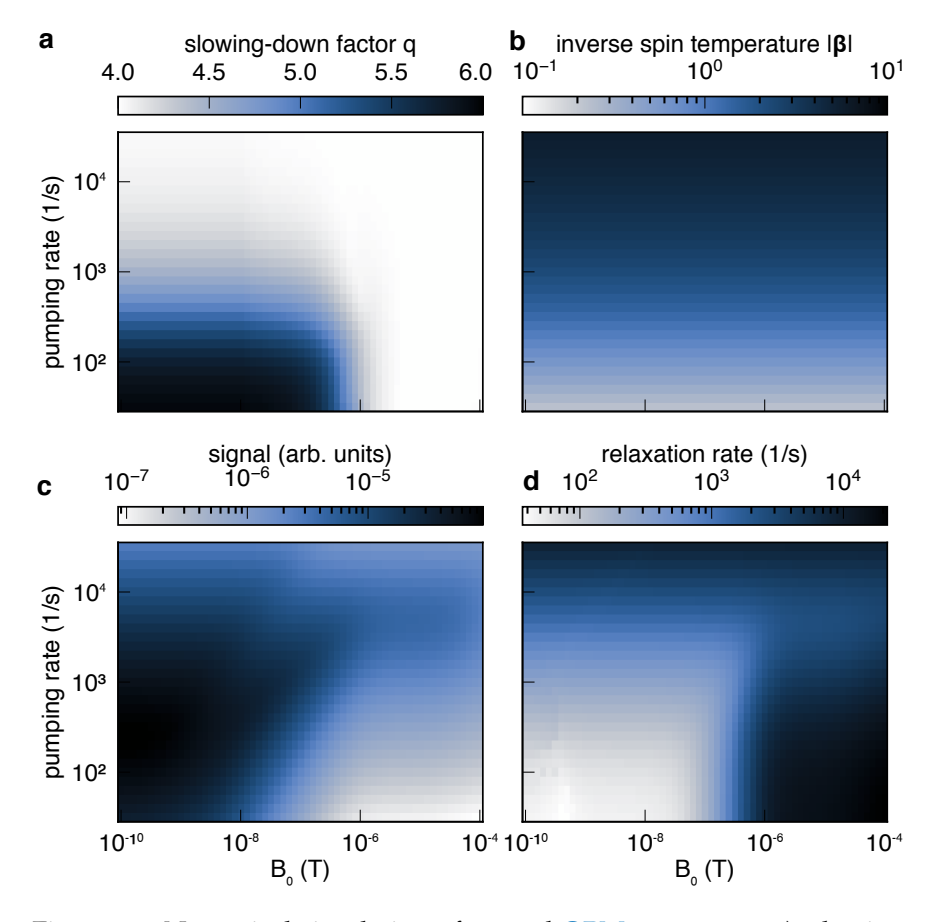


Figure 2.3: Numerical simulation of several OPM parameter: **a**), slowing-down factor (**b**), spin temperature (**c**), signal amplitude (**d**) and transversal relaxation rate T_2 (**e**) for various bias fields B_0 and pumping rates R_{OP} . As for the simulation in the previous chapter, a temperature of 323.15 K (150 °C) and a buffer gas (N₂) pressure of 933 mbar (700 Torr) are assumed.

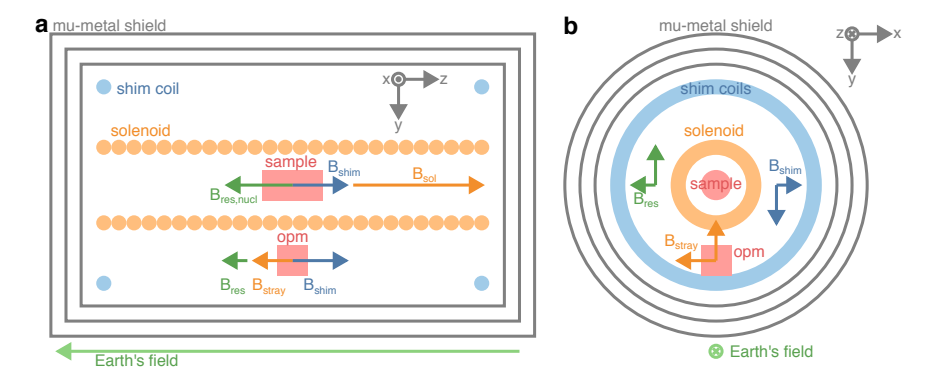


Figure 2.4: Schematic illustrating the coil arrangement and magnetic fields within the three-layer magnetic shield. The sample and the OPM are depicted as red boxes, while the light orange structure represents a long solenoid responsible for providing the bias field for nuclear spin precession. Orange arrows indicate the primary magnetic field $B_{\rm sol}$ inside the solenoid, as well as the stray field $B_{\rm stray}$ outside of it. Residual fields are denoted by green arrows, and the magnetic fields generated by shim coils are represented by blue arrows. Panel **a** shows a side view, while panel **b** displays the frontal cross-section of the shield.

resulting in a different slowing-down factor. Furthermore, any minor deviations at extremely low fields, where the bandwidth is narrower than the LARMOR frequency, are not a significant concern.

Hence, the variable slowing-down factor poses no issue, as long as the optical pumping rate is sufficiently high to uphold a strong spin polarization. Figure 2.3a presents the slowing-down factor for various pumping rates and bias fields. Notably, for the chosen optical pumping rate, the slowing-down factor exhibits almost no dependency on the bias field.

Matching Atomic and Nuclear Larmor Frequency

The gyromagnetic ratio of nuclear spins (e.g. hydrogen-1 with $\gamma_{^{1}H}=2\pi\times42\,\text{MHz/T}$) may differ significantly, by over two orders of magnitude, from that of rubidium-87 atoms ($\gamma_{e}/q_{Larmor}=2\pi\times5700\,\text{MHz/T}$ to $7000\,\text{MHz/T}$). Applying the same bias field to both spin species will not lead to the same Larmor frequency, which is crucial for efficient detection. Figure 2.4 presents a solution to this problem by employing a solenoid around the sample to provide the bias field for the nuclear spin species. A thin solenoid, combined with

magnetic shielding, produces only a small stray field. This arrangement allows the nuclear spin to experience a much higher magnetic field than the atoms used for the OPM.

The field experienced by the atoms is given by

$$\mathbf{B}_{\mathrm{opm}} = \begin{pmatrix} B_{\mathrm{opm,x}} \\ B_{\mathrm{opm,y}} \\ B_{\mathrm{opm,z}} \end{pmatrix} \approx \begin{pmatrix} B_{\mathrm{res,x}} + \mathbf{r}_{\mathrm{opm}} \boldsymbol{\nabla} B_{\mathrm{res,x}} + B_{\mathrm{shim,x}} + B_{\mathrm{stray,x}} \\ B_{\mathrm{res,y}} + \mathbf{r}_{\mathrm{opm}} \boldsymbol{\nabla} B_{\mathrm{res,y}} + B_{\mathrm{shim,y}} + B_{\mathrm{stray,y}} \\ B_{\mathrm{res,z}} + \mathbf{r}_{\mathrm{opm}} \boldsymbol{\nabla} B_{\mathrm{res,z}} + B_{\mathrm{shim,z}} + B_{\mathrm{stray,z}} \end{pmatrix},$$
(2.11)

whereas the nuclear spin experiences the field

$$\mathbf{B}_{n} = \begin{pmatrix} B_{n,x} \\ B_{n,y} \\ B_{n,z} \end{pmatrix} \approx \begin{pmatrix} B_{\text{res},x} + \mathbf{r}_{n} \nabla B_{\text{res},x} + B_{\text{shim},x} + B_{\text{sol},x} \\ B_{\text{res},y} + \mathbf{r}_{n} \nabla B_{\text{res},y} + B_{\text{shim},y} + B_{\text{sol},y} \\ B_{\text{res},z} + \mathbf{r}_{n} \nabla B_{\text{res},z} + B_{\text{shim},z} + B_{\text{sol},z} \end{pmatrix} . (2.12)$$

It is assumed that the OPM is placed in the origin (e.g. $\mathbf{r}_{\text{opm}} = (0,0,0)^{\intercal}$ and the sample is spatially shifted by the distance d along y (e.g. $\mathbf{r}_{\text{n}} = (0,d,0)^{\intercal}$).

It is further assumed that the field in the solenoid is predominantly along z (i.e. $B_{\text{sol,z}} \gg B_{\text{sol,x,y}}$) and that the field of the nuclei along z is much bigger than along the other two components, i.e.

$$B_{\rm n,z} \gg B_{\rm n,x}, B_{\rm n,y}$$
 (2.13)

The Larmor frequency

$$\omega_{0} = \gamma_{n} |\mathbf{B}_{n}|$$

$$= \pm \gamma_{n} \sqrt{B_{n,x}^{2} + B_{n,y}^{2} + B_{n,z}^{2}}$$

$$\stackrel{2.13}{=} \pm \gamma_{n} B_{n,z} + \mathcal{O}(B_{n,x}, B_{n,y})$$

$$\approx \pm \gamma_{n} \cdot \left(B_{\text{res},z} + d \frac{\partial B_{\text{res},z}}{\partial y} + B_{\text{shim},z} + B_{\text{sol},z}\right)$$

$$= \pm \gamma_{n} \cdot (B_{\text{res},n,z} + B_{\text{shim},z} + B_{\text{sol},z})$$

$$(2.14)$$

of the nuclei is determined by the absolute magnetic field $|\mathbf{B}_n|$. Using the previous assumption (Equation 2.13) the LARMOR frequency mainly depends on the z component.

In the last line the abbreviation

Brosp z =

 $\begin{array}{l} B_{\mathrm{res,n,z}} = \\ B_{\mathrm{res,z}} + d \frac{\partial B_{\mathrm{res,z}}}{\partial y} \ is \\ introduced. \end{array}$

For the OPM the bias field should be parallel to the pump beam. Assuming the atoms are pumped along the z the assumption of the previous sentence implies

$$B_{\text{opm,x}} \stackrel{!}{=} 0 \Longrightarrow B_{\text{res,x}} \stackrel{!}{=} -B_{\text{shim,x}} - B_{\text{stray,x}}$$
 (2.15a)

$$B_{\mathrm{opm,y}} \stackrel{!}{=} 0 \Longrightarrow B_{\mathrm{res,y}} \stackrel{!}{=} -B_{\mathrm{shim,y}} - B_{\mathrm{stray,y}}$$
 . (2.15b)

With the other x and y components being equal to zero, the atomic LARMOR frequency

$$\omega_{0} = \frac{\gamma_{e}}{q} |\mathbf{B}_{opm}|$$

$$= \pm \frac{\gamma_{e}}{q} \sqrt{B_{opm,x}^{2} + B_{opm,y}^{2} + B_{opm,z}^{2}}$$

$$= \pm \frac{\gamma_{e}}{q} B_{opm,z}$$

$$= \pm \frac{\gamma_{e}}{q} (B_{res,z} + B_{shim,z} + B_{stray,z})$$
(2.16)

is given by the *z* component of the magnetic field.

In practice, the fields produced by the four coils (solenoid, shim x, y and z) are controlled via four electric currents ($I_{\rm sol}$, $I_{\rm shim,x}$, $I_{\rm shim,y}$, $I_{\rm shim,z}$). All field are assumed to be linear in current

$$B_{\text{shim},x} = k_{\text{shim},x} I_{\text{shim},x} \tag{2.17a}$$

$$B_{\text{shim,y}} = k_{\text{shim,y}} I_{\text{shim,y}} \tag{2.17b}$$

$$B_{\text{shim,z}} = k_{\text{shim,z}} I_{\text{shim,z}} \tag{2.17c}$$

$$B_{\text{sol,z}} = k_{\text{sol,z}} I_{\text{sol}} \tag{2.17d}$$

$$B_{\text{stray,x}} = k_{\text{stray,x}} I_{\text{sol}} \tag{2.17e}$$

$$B_{\text{stray,y}} = k_{\text{stray,y}} I_{\text{sol}} \tag{2.17f}$$

$$B_{\text{stray,z}} = k_{\text{stray,z}} I_{\text{sol}} . {(2.17g)}$$

and the conversion factors k can be calibrated using the magnetometer and NMR.

Combining equations Equation 2.14–2.16 and using the identities Equation 2.17a–2.17g leads to set of linear equations that can be expressed as a matrix

$$\begin{pmatrix}
\pm \omega_{0} - \gamma_{n} B_{\text{res,n,z}} \\
\pm \omega_{0} - \frac{\gamma_{e}}{q} B_{\text{res,z}} \\
-B_{\text{res,x}} \\
-B_{\text{res,y}}
\end{pmatrix} = \begin{pmatrix}
0 & 0 & \gamma_{n} k_{\text{shim,z}} & \gamma_{n} k_{\text{sol,z}} \\
0 & 0 & \frac{\gamma_{e}}{q} k_{\text{shim,z}} & \frac{\gamma_{e}}{q} k_{\text{stray,z}} \\
k_{\text{shim,x}} & 0 & 0 & k_{\text{stray,x}} \\
0 & k_{\text{shim,y}} & 0 & k_{\text{stray,y}}
\end{pmatrix} \cdot \begin{pmatrix}
I_{\text{shim,x}} \\
I_{\text{shim,z}} \\
I_{\text{shim,z}} \\
I_{\text{sol}}
\end{pmatrix}$$
(2.18)

and be solved using standard linear algebra methods⁵.

Spin Noise Limited Sensitivity

Since the spin operators due not commute

$$\left[\hat{S}_{x},\hat{S}_{y}\right] = i\hbar\hat{S}_{z} \tag{2.19}$$

the uncertainty in measuring any component of a single spin is limited and given by ${\rm Heisenberg}^6$ uncertainty principle

$$\sigma_{\hat{S}_x}\sigma_{\hat{S}_y} \ge \frac{\hbar}{2} \left| \left\langle \hat{S}_z \right\rangle \right| ,$$
 (2.20)

with $\sigma_{\hat{O}}$ being the standard deviation of an operator \hat{O} . The standard deviation of N uncorrelated measurements of \hat{S}_x on atoms described by a density operator $\hat{\rho}$ can be calculated via [23]

$$\sigma_{\hat{S}_x}^{(N)} = \sqrt{\frac{\sigma_{\hat{S}_x}}{N}} \tag{2.21}$$

With this, the sensitivity (in Js/ $\sqrt{\text{Hz}}$)

$$\sigma_{\langle \hat{S}_x \rangle}^{(N)} \approx \sigma_{\hat{S}_x}^{(N)} \sqrt{4T_2}$$
 (2.22)

⁵ The two \pm symbols in the equation give actually rise to four independent solutions. Which one is the best, depends on the additional boundary conditions of the experiment (e.g. minimized gradient, minimized coil currents, etc.).

⁶ Werner Heisenberg (1901–1976) was a pioneering German physicist who formulated the uncertainty principle and made fundamental contributions to the development of quantum mechanics.

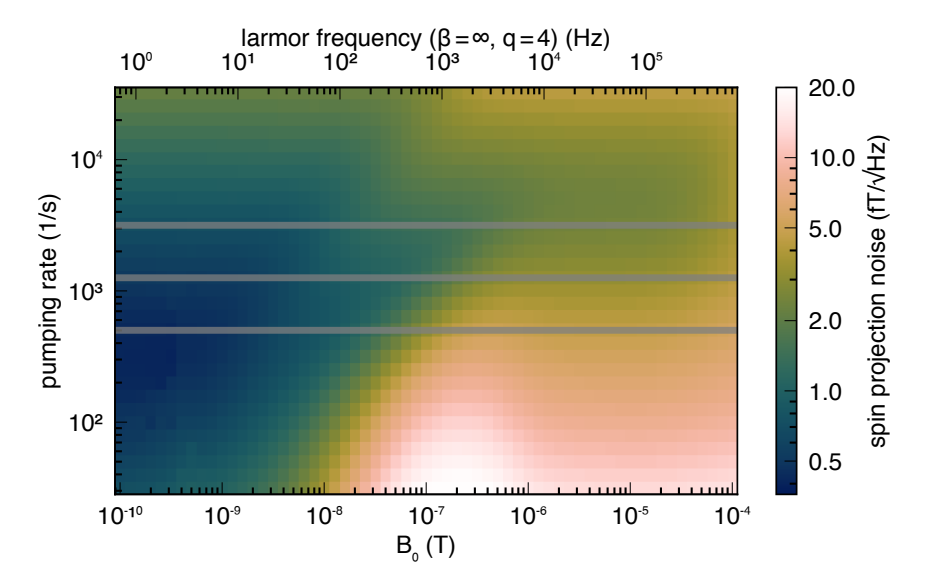


Figure 2.5: Spin projection noise limited sensitivity for various bias fields B_0 and pumping rates $R_{\rm OP}$. The bottom grey line shows the optimal pumping rate $R_{\rm OP} = 2R_{\rm SD}$ for a SERF magnetometer. The top grey line shows the optimal pumping rate for a magnetometer operating at $10\,\rm kHz$. Finally, the middle line indicates an intermediate pumping rate that offers good sensitivity over a broad range of frequencies.

for a continuous measurement of \hat{S}_x can be estimated⁷ by applying the Wiener⁸–Khinchin⁹ theorem and by assuming long measurement times t compared to the transverse relaxation time T_2 , i.e. $t \gg T_2$ (more details in Seltzer [23] and Budker and Kimball [35]).

⁷ This is only a rough estimation that uses several assumptions that may not be justified in the actual physical system. More sophisticated spin noise models (e.g. in Mouloudakis et al. [75]) are more accurate but, for now, only cover in the low-polarization limit. Especially the assumption of an exponential correlation function [23] may not be fully accurate. Further theoretical work on modeling the spin noise at various polarization levels is needed for more accurate results. The shape of the correlation function does not affect the total spin noise but its spectral distribution. Similar to the technique of *noise shaping* used in data processing, the signal-to-noise Ratio (SNR) of a magnetometer is not only affected by the total power of the noise but also its spectral distribution.

⁸ Norbert Wiener (1894–1964) was a pioneering American mathematician and philosopher known for his groundbreaking work in the development of cybernetics, a field that explored the interdisciplinary study of control and communication in living organisms and machines.

⁹ Aleksandr Khinchin (1894–1959) was a prominent Soviet mathematician known for his significant contributions to probability theory and his work on the law of the iterated logarithm.

For the simulations in Figure 2.5 the number density N = nV is estimated using a volume of $V = (3 \text{ mm})^3$ and the corresponding alkali density at $T = 323.15 \text{ K} (150 \,^{\circ}\text{C})$. An oscillating test field with a fixed amplitude of $B_1 = 1 \text{ pT}$ provides the proportionality factor

$$a(B_0, R_{\text{OP}}) = \frac{B_1}{\langle \hat{S}_x \rangle (B_0, R_{\text{OP}})}$$
(2.23)

between the magnetic field B_1 and the signal $\langle \hat{S}_x \rangle$ (see Figure 2.3c). By using this factor, the spin projection noise limited sensitivity

$$\sigma_B = a\sigma_{\hat{S}_\chi}^{(N)} \sqrt{4T_2} \tag{2.24}$$

can be estimated for various pumping rates $R_{\rm OP}$ and bias magnetic fields B_0 with the results shown in Figure 2.5. By choosing a pumping rate that is between the optimal value of the SERF and lightnarrowing regime the magnetometer can be operated over a broad range of frequencies by simultaneously maintaining high, almost constant sensitivity.

2.5 PERFORMANCE AND OUTLOOK

In this section, the performance of the tunable magnetometer will be discussed. It will be shown that a higher pumping rate when compared to a pure SERF magnetometer, not only enhances sensitivity at RF frequencies but also has a positive impact on the magnetometer's bandwidth and response time. Both of these characteristics are crucial within the context of NMR. The former allows for the simultaneous detection of widely separated NMR peaks (either due to large J-couplings or differences in nuclear gyromagnetic ratios), while the latter reduces the dead time of the magnetometer following a magnetic field pulse, which is necessary to initiate nuclear spin evolution. A 3D rendering of the setup can be observed in Figure 2.6.

Sensitivity and Bandwidth

Figure 2.7a illustrates the spectral sensitivity for various bias fields. At low frequencies, the magnetometer is constrained by technical 1/f noise. The peak sensitivity, approximately $10\,\mathrm{fT}/\sqrt{\mathrm{Hz}}$ is achieved at around 100 Hz and even at 3 kHz the sensitivity remains below 3 kHz. In comparison to the simulations, the sensitivity exceeds the simulated spin-projection noise-limited sensitivity by approximately

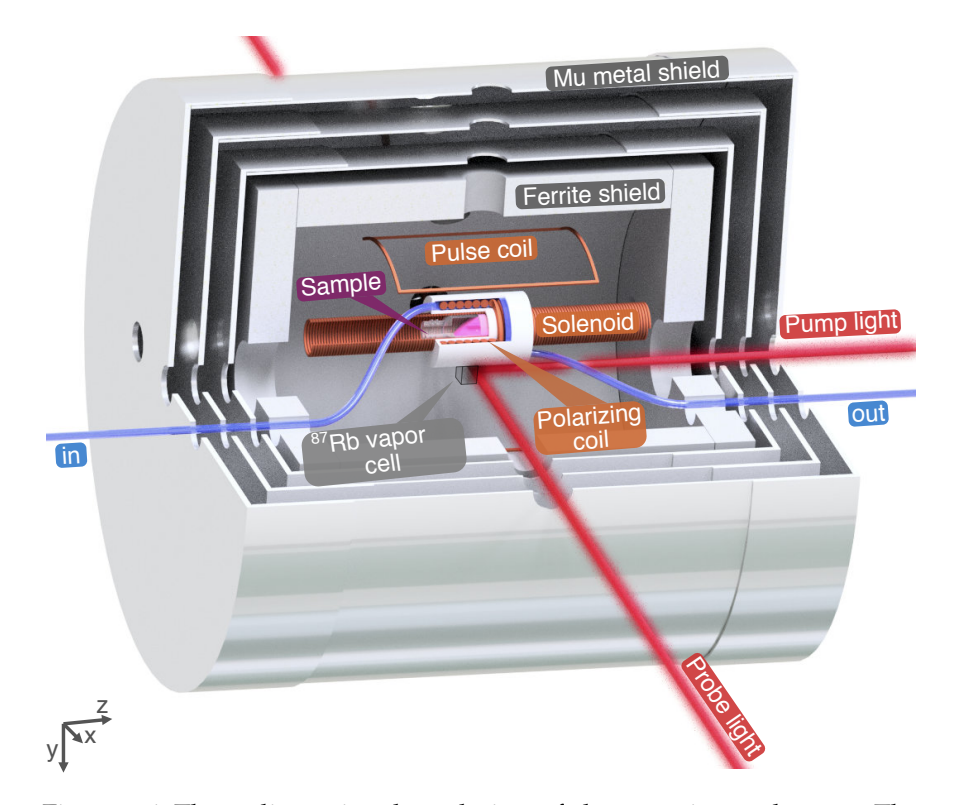


Figure 2.6: Three-dimensional rendering of the experimental setup. The vapor cell is positioned beneath a water-cooled coil system that houses the solenoid and the pre-polarizing coil. The circularly polarized pump beam and the linearly polarized probe beam are oriented orthogonal to each other. Saddle coils are employed to apply magnetic field pulses for the purpose of rotating the nuclear spin states. The entire setup is enclosed within a four-layer magnetic shielding system, consisting of three layers of mu-metal and one layer of ferrite.

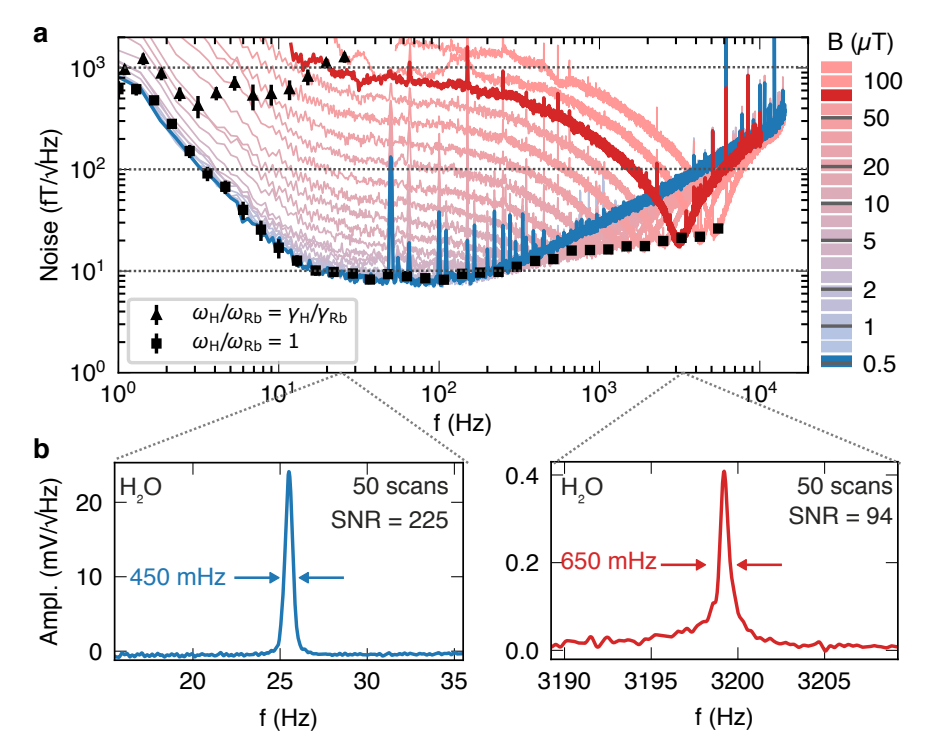


Figure 2.7: Performance of the tunable magnetometer. **a** sensitivity across a wide frequency range for various bias fields is depicted. The squares represent sensitivity when nuclear and atomic Larmor frequencies are matched. The triangles demonstrate sensitivity at the nuclear Larmor frequency when only a constant field exists along the z-axis. **b** NMR signal of a 1 ml sample of milli-Q water, measured after pre-polarization at 20 mT.

an order of magnitude. Calibration was carried out following the procedure detailed in Appendix G.

The bandwidth is on the order of several hundred hertz, which is sufficient even for ${}^1J_{^1H^{13}C}$ couplings that can be as high as 100 Hz. This bandwidth surpasses that of many SERF magnetometers, thanks to the higher pumping rate required for optimal RF performance. Further increasing the pumping rate could extend the bandwidth, but it would come with a trade-off involving reduced sensitivity at lower frequencies.

Gradient Broadening

In theory, an infinite solenoid produces a constant field profile inside. However, due to the finite length and potential winding inaccuracies,

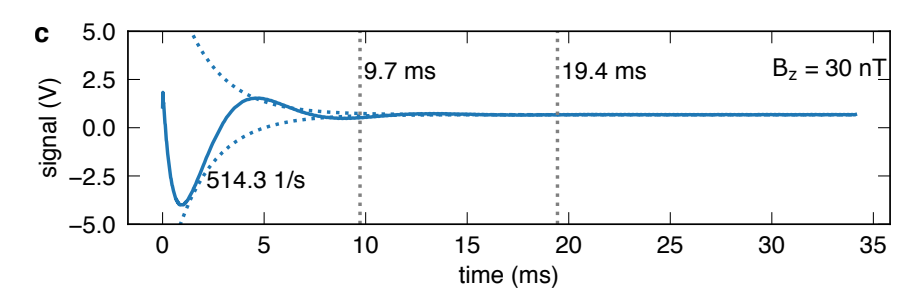


Figure 2.8: Typical magnetometer response at 30 nT after a magnetic field pulse. The relaxation rate is in the order of 500 1/s. The magnetometer has almost fully recovered after 5 to 10 transverse relaxation times, as indicated by the vertical dashed lines.

there may be gradients in the field profile. If the natural linewidth of an NMR signal is narrow enough, the broadening due to gradients provides a direct measure of the field homogeneity produced by the solenoid. Figure 2.7b illustrates a gradient broadening of only 200 mHz across the Larmor frequency range of 3200 Hz. This corresponds to a field inhomogeneity of 63 ppm, which is orders of magnitude worse when compared to commercial high-field systems. However, within the frequency range of interest, the gradient broadening is still narrower than the natural linewidth for many samples.

Response/Dead Time

Figure 2.8 illustrates the typical response behavior of the OPM at low magnetic fields ($B_z = 30\,\mathrm{nT}$) following a strong magnetic field pulse, which may occur during an NMR experiment. In this regime, the atomic transverse relaxation rate ($\approx R_{\mathrm{OP}}/4 \approx 500\,\mathrm{s}^{-1}$) is predominantly influenced by the pumping rate R_{OP} . The magnetometer requires approximately 5 to 10 times the transverse relaxation time to fully recover, which falls within the range of 10 ms to 20 ms. This recovery time is sufficient for studying most samples with relaxation rates of up to tens per second. However, challenges may arise when dealing with fast-relaxing samples having relaxation rates exceeding $100\,\mathrm{s}^{-1}$, as the initial decay cannot be easily observed by the magnetometer due to its overlap with the magnetometer's response at the same frequency.

At higher bias fields and atomic LARMOR frequencies, the transverse relaxation rate accelerates, resulting in a shorter recovery time

for the magnetometer. This recovery time could be further improved by increasing the pump rate, but this would come at the cost of reduced sensitivity at lower frequencies.

Temperature and Stability

The atomic vapor cell must be maintained at a constant temperature to ensure both the vapor density and kinetic energy of the atoms remain stable. Currently, this setup lacks a feedback-controlled stabilizer and relies solely on a constant amplitude alternating current (AC) heating current. Consequently, this situation may result in potential long-term temperature fluctuations.

The polarizing coil draws a substantial current in the order of several amperes. Due to the internal resistance of the coils, this can significantly elevate the temperature in the vicinity of the coil. Although a passive cooling system employing a siphon mechanism and water helps mitigate most of the heating, it lacks active stabilization, and the cooling capacity depends on the variable flow rate, leading to prolonged temperature variations.

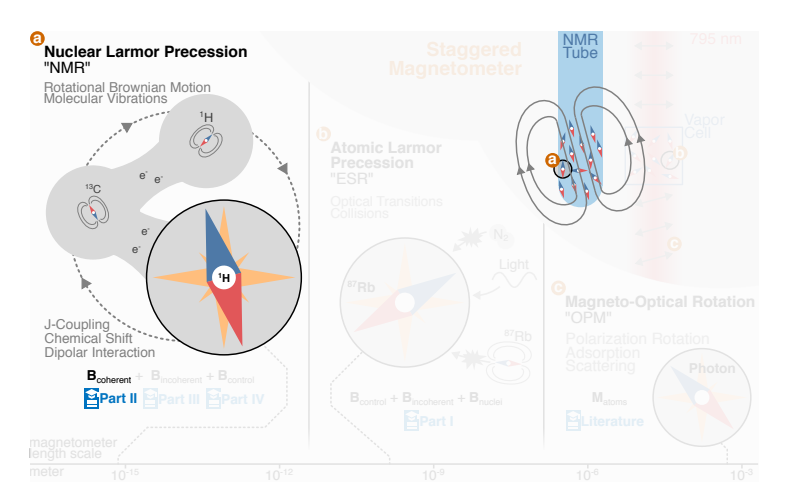
In the future, both issues could be addressed by implementing temperature monitoring and introducing active feedback loops for both the heating and cooling systems. In addition to temperature fluctuations, mechanical vibrations, and technical noise also impact the overall system stability, particularly at low frequencies. Other sources of noise include fluctuations in the lasers (intensity, polarization, wavelength), as they are not actively locked.

Tunability

The maximum tuning range is presently restricted by the current driver responsible for generating the magnetic field for the NMR sample, and it is approximately 5 kHz. Atomic RF magnetometers have demonstrated the ability to operate at frequencies in the hundreds of kHz, and it is anticipated that the magnetometer will perform effectively with only minor adjustments. Nevertheless, gradient broadening will also become more prominent at these frequencies, leading to a decrease in the SNR.

Part II

NUCLEAR MAGNETIC RESONANCE SPECTROSCOPY



OPM fulfill the requirements for detecting the magnetization of nuclear spins in terms of sensitivity and bandwidth. However, predicting and interpreting the time-dependent signals that arise at ultralow field conditions is not straightforward.

In this part of the thesis, Chapter 3 explains the origin of zero-field NMR spectra and how they continuously evolve towards their high-field counterparts with increasing field strength. In Chapter 4, this knowledge will be applied to extract scalar coupling constants with unprecedented accuracy. The discussion will also explore whether the distinct differences between ZULF and high-field NMR could lead to advantages or disadvantages in certain scenarios.

The results of these chapters will soon be published in Bodenstedt et al. [76] and Bodenstedt et al. [77].

ZERO- TO ULTRALOW FIELD NUCLEAR MAGNETIC RESONANCE

The nuclear shell model, which was developed in 1949 and honored with the Nobel¹ Prize in Physics awarded to Maria Goeppert Mayer² and J. Hans D. Jensen³, predicts a nonzero nuclear spin I for the ground state of any nucleus with an odd number of protons and/or neutrons. This nuclear spin is connected to a magnetic moment

$$\mathbf{m} = \gamma_{\mathbf{n}} \mathbf{I} \tag{3.1}$$

through the gyromagnetic ratio γ_n . The dipole magnetic field generated by a single nuclear spin or an ensemble of them can be externally detected to read out the ensemble's average spin state. When placed within an external magnetic field $\bf B$, an isolated nuclear spin undergoes Larmor precession, where the exact precession frequency

$$f_{\text{Larmor}} = \frac{\omega_{\text{Larmor}}}{2\pi} = \frac{\gamma_{\text{n}} |\mathbf{B}|}{2\pi},$$
 (3.2)

is linear to the magnetic field strength. This particular frequency, specific to both the magnetic field and the nuclear species, is commonly known as the resonance frequency in the context of NMR.

Conventional NMR is arguably one of the applications that benefited the most from the improvements in generating and controlling high magnetic fields using superconducting magnets allowing up to GHz resonance frequencies. Most of its various applications in chemistry, physics, and life science would benefit from even higher

¹ Alfred Nobel (1833–1896) was a Swedish inventor, engineer, and industrialist best known for inventing dynamite and for establishing the Nobel Prizes through his will, which recognize outstanding contributions to humanity in the fields of physics, chemistry, medicine, literature, and peace.

² Maria Goeppert Mayer (1906–1972) was a German-American physicist who was awarded the Nobel Prize in Physics in 1963 for her development of the nuclear shell model, which explained the structure of atomic nuclei.

³ J. Hans D. Jensen (1907—1973) was a German physicist awarded the Nobel Prize in Physics in 1963 for his contributions to the understanding of the nuclear structure, particularly his work on the nuclear shell model.

magnetic fields if they were stable, controllable, and homogeneous. Therefore, detecting the evolution of the states of nuclear spin ensembles in environments where the strength of magnetic fields is drastically reduced seems counter-intuitive at first.

Yet, the influence of the bias magnetic field extends beyond the determination of the nuclear LARMOR frequency. Conceptually, a nuclear spin can be seen as a subatomic-scale magnetometer. By changing the bias magnetic field, the nuclear spin magnetometer can be tuned to be more or less sensitive to certain aspects of spin-spin couplings and frequency bands in the magnetic (noise) spectrum.

As an example, at ZULF, in contrast to high-field conditions, heteronuclear spins are sensitive to the secular components of the J-coupling, potentially resulting in spectra that are more responsive to J-coupling constants (refer to Chapter 4). In Chapter 5, it will be investigated how the sensitivity of spin systems to fluctuating magnetic fields caused by other nuclei varies with changes in the external magnetic field. This transition between the strong and weak coupling limits facilitates the formation of long-lived coherence (LLC) [78, 79], which are less influenced by relaxation due to magnetic dipole-dipole interactions. Finally, in NMRD, nuclear spins can be tuned to detect parts of the magnetic noise spectrum associated with molecular processes characterized by very long coherence times resulting from slow molecular motion (see Chapter 6).

This chapter focuses on the theoretical background of the spectroscopy [80–84] aspect of ZULF NMR. The time evolution of the nuclear spin state is encoded in the externally detected magnetic field. However, the fact alone that there is a non-trivial (i.e. a nonconstant) magnetically detectable time evolution even in the complete absence of externally applied bias fields, is not obvious and requires studying the quantum mechanical model of the nuclear spin system. This chapter will delve into the prerequisites for the existence of such non-trivial time evolution, explore its derivation, and quantify its characteristics.

3.1 QUANTUM MECHANICAL DESCRIPTION

The LARMOR precession of an individual spin can be effectively described by a classical model, but when considering spin-spin couplings among multiple spins, a quantum mechanical treatment becomes necessary due to the limitations of the classical approach.

Hamiltonian

Nuclear spins can engage with magnetic and electric fields through diverse mechanisms, encompassing the Zeeman effect, chemical shifts, electric quadrupole moments, direct magnetic dipole-dipole interactions with other nuclei, and indirect interactions mediated by electrons in the form of J-coupling. These interactions collectively form a Hamiltonian

$$\hat{H} = -\sum_{i} \gamma_{i} \hat{\mathbf{I}}_{i} \cdot \mathbf{B} + \sum_{i} \gamma_{i} \sigma_{i} \hat{\mathbf{I}}_{i} \cdot \mathbf{B} + \underbrace{\frac{2\pi}{\hbar} \sum_{i,j>i} J_{ij} \hat{\mathbf{I}}_{i} \cdot \hat{\mathbf{I}}_{j}}_{\hat{H}_{J}} + \hat{H}_{\text{quadrupolar}} + \hat{H}_{\text{dipole-dipole}}$$

$$(3.3)$$

for a nuclear spin system composed of nuclear spins denoted as $\hat{\mathbf{l}}_i$.

In liquids undergoing rapid molecular tumbling, the Hamiltonian is averaged across all rotational orientations, resulting in the elimination of the last two terms (describing dipole-dipole and quadrupolar interactions). Consequently, only the Zeeman, chemical shift, and J-coupling terms remain as the primary factors influencing resonance frequencies. Moreover, the quadrupolar term becomes negligible for nuclei with I < 1. Nevertheless, despite not being directly observable in the spectrum, both dipole-dipole and quadrupolar terms play an important role in the relaxation mechanism of the system.

Origin of J-Coupling

At zero field ($\mathbf{B} = \mathbf{0}$), the J-coupling is the only interaction determining the resonance frequency in liquids. First observed in 1952 by Hahn and Maxwell [85] and in the same year theoretically described by Ramsey and Purcell [3], the J-coupling describes an interaction of nuclear spins that arises from direct dipolar coupling

$$\hat{H}_{2} = \frac{g\mu_{\mathrm{B}}\mu_{0}}{4\pi\hbar} \sum_{k,l} \gamma_{\mathrm{L}l} \frac{3(\hat{\mathbf{S}}_{k} \cdot \mathbf{r}_{kl})(\hat{\mathbf{I}}_{l} \cdot \mathbf{r}_{kl})}{|\mathbf{r}_{kl}|^{5}} - \frac{\hat{\mathbf{I}}_{l} \cdot \hat{\mathbf{S}}_{k}}{|\mathbf{r}_{kl}|^{3}}$$
(3.4)

of the nuclear spins $\hat{\mathbf{I}}_l$ with the electron spins $\hat{\mathbf{S}}_k$, in combination with the Fermi contact interaction

$$\hat{H}_3 = \frac{2}{3} \frac{g \mu_B \mu_0}{\hbar} \sum_{k,l} \gamma_{I,l} \delta(\mathbf{r}_{kl}) \hat{\mathbf{I}}_l \cdot \hat{\mathbf{S}}_k . \tag{3.5}$$

Here, $g \approx 2$ is the electron spin g-factor, μ_B the Bohr magneton, μ_0 the magnetic permeability constant, $\gamma_{I,l}$ the gyromagnetic ratio of nuclear spin l, $\hat{\mathbf{S}}_k$ the spin operator of electron spin k, $\hat{\mathbf{I}}_l$ the spin operator of nuclear spin l and $\mathbf{r}_{kl} = \mathbf{r}_k - \mathbf{r}_l$ relative location between the k-th electron and l-th nuclear spin.

If these terms are treated as a perturbation to the "nuclear-free" molecular Hamiltonian they give rise to energy corrections of the form

$$\hat{H}_{J} = \frac{2\pi}{\hbar} \begin{pmatrix} \hat{I}_{x}^{(1)} & \hat{I}_{y}^{(1)} & \hat{I}_{z}^{(1)} \end{pmatrix} \cdot \begin{pmatrix} J_{xx} & J_{xy} & J_{xz} \\ J_{yx} & J_{yy} & J_{yz} \\ J_{zx} & J_{zy} & J_{zz} \end{pmatrix} \cdot \begin{pmatrix} \hat{I}_{x}^{(2)} \\ \hat{I}_{y}^{(2)} \\ \hat{I}_{z}^{(2)} \end{pmatrix}$$
(3.6)

that are nowadays known under the term J-coupling and are typically anisotropic. For liquid samples that experience rapid molecular tumbling, the energy corrections can be averaged over all molecular rotational states. In this case, Ramsey⁴ [3] correctly identified that especially the last term \hat{H}_3 contributes to what nowadays is known as the scalar J-coupling, describing an energy correction of the form

$$\hat{H}_{J} = \frac{2\pi}{\hbar} \sum_{i,j>i} J_{ij} \hat{\mathbf{I}}_{i} \cdot \hat{\mathbf{I}}_{j} , \qquad (3.7)$$

with
$$J = (J_{xx} + J_{yy} + J_{zz})/3$$
.

The J-coupling can be motivated by considering the hydrogen molecule ${}^{1}\text{H}_{2}$ in its electronic ground state, where the two electron spins are anti-parallel (Figure 3.1). The Fermi contact interaction, which remains unaffected by molecular tumbling, favors each nuclear spin aligning with its corresponding electron spin rather than being antialigned. The energy difference between these states is proportional to the J coupling constant J_{HH} .

3.2 DIFFERENCES BETWEEN ZERO- AND HIGH-FIELD

There are fundamental differences between zero-field and high-field NMR. Some are readily apparent, such as the lack of chemical shift information in zero-field NMR due to the absence of external magnetic fields. However, this section delves into more profound disparities,

⁴ Nathaniel Foster Ramsey (1915–2011) was a prominent American physicist and Nobel laureate, recognized for his groundbreaking contributions to the field of atomic and molecular physics, particularly his development of the molecular beam technique.

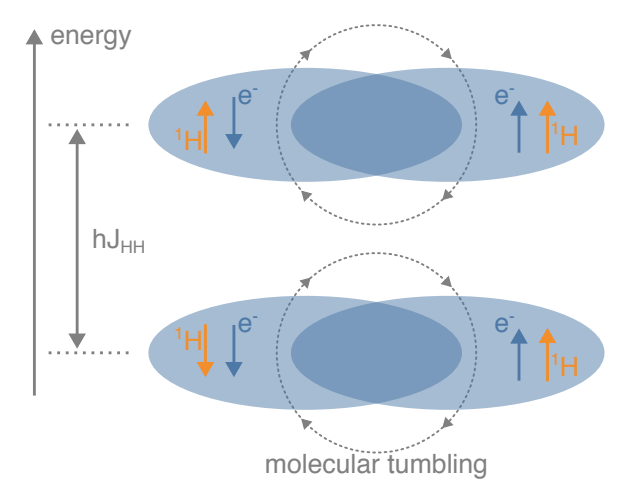


Figure 3.1: Illustrative explanation of the J-coupling. The figure shows the nuclear and electron spin of a hydrogen molecule in its electronic ground state. The electron's non-vanishing probability at one of the nuclei results in an energetically favored alignment of the electron and nuclear spins. Since the Fermi contact interaction remains unaffected by molecular tumbling, this energy difference persists even in liquids, leading to the scalar J-coupling $J_{\rm HH}$.

particularly the alteration in the system's symmetry. In the case of liquid samples undergoing rapid molecular tumbling, the zero-field Hamiltonian exhibits complete rotational symmetry under both spatial and spin rotations, whereas this symmetry is broken in high-field NMR. The implications of this symmetry violation will be explored in the following section, following a brief explanation of field terminology.

Field Regime Terminology

Various subfields within the realm of NMR have formulated their distinct and at times conflicting definitions of magnetic field regimes. In this thesis, unless explicitly stated otherwise, the definitions outlined in Figure 3.2 will be used. These definitions are based on the terms described in Equation 3.3.

Within this framework, *high* field designates the field regime where the absolute chemical shift difference between two homonuclear spins significantly surpasses the homonuclear J-coupling. In contrast, *low* field extends from this point downwards to the threshold where the

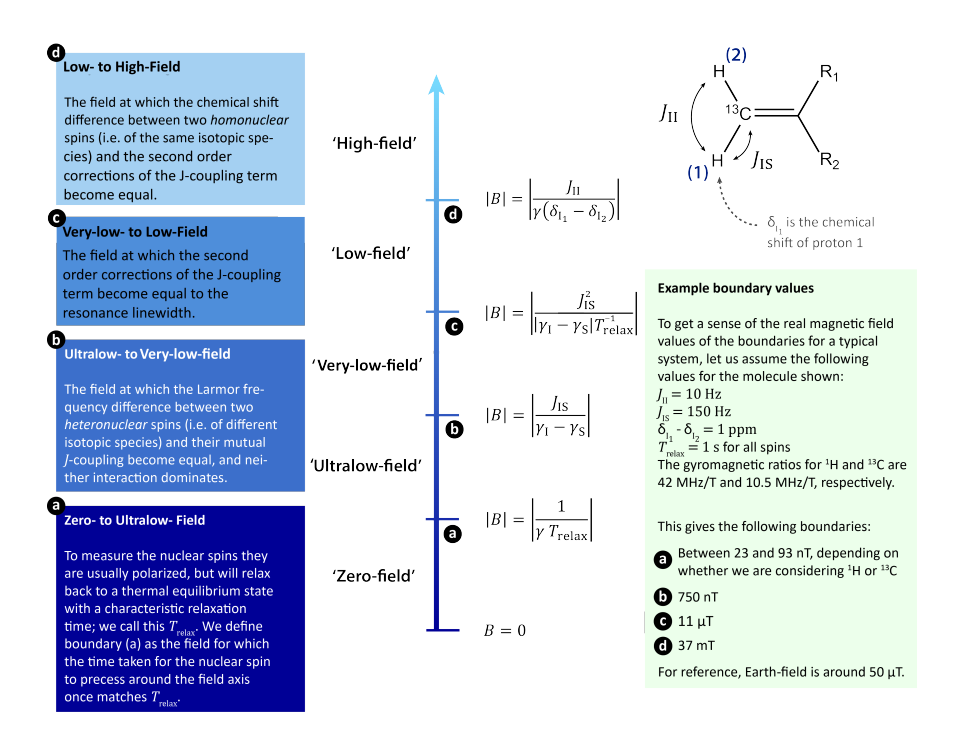


Figure 3.2: Schematic for the definitions of the field regimes used in this thesis. The calculated boundaries vary considerably depending on the specific system being studied. (Modified from Eills [86]; inspired by Appelt et al. [87].)

second-order corrections of the J-coupling term become comparable to the relaxation rate. *very-low* field encompasses the range from there down to the field level at which the difference in Larmor frequencies between two heteronuclear spins equals their J-coupling constant. *ultralow* field takes over from this point and extends downward to the field at which the Larmor frequency becomes comparable to the relaxation rate. Any magnetic field strength below this threshold is categorized as *zero* field.

Symmetry and Conservation

NOETHER⁵'s theorem [88]

"If a system has a continuous symmetry property, then there are corresponding quantities whose values are conserved in time."

establishes a connection between symmetries inherent in a physical system and corresponding conservation laws. Specifically, time-translation invariance results in the conservation of mass-energy, while space-translation invariance ensures the conservation of linear momentum.

In zero-field NMR, assuming liquid samples where the rotational Brownian⁶ motion averages out any spatial anisotropy, the Hamiltonian is completely invariant under both spatial and spin rotations. This complete rotational symmetry leads to the commutators

$$[\hat{H}, \hat{\mathbf{F}}] = \mathbf{0} \tag{3.8a}$$

$$[\hat{H}, \hat{\mathbf{F}}^2] = 0 \tag{3.8b}$$

of the rotation generators (i.e. the total angular momentum operator $\hat{\mathbf{F}} = \sum_i \hat{\mathbf{I}}_i$) being zero. By applying the Ehrenfest⁷ theorem [89]

$$\frac{\mathrm{d}}{\mathrm{d}t} \langle \hat{\mathbf{f}} \rangle = \frac{1}{\mathrm{i}\hbar} [\hat{\mathbf{f}}, \hat{H}] + \langle \frac{\partial \mathbf{F}}{\partial t} \rangle = \mathbf{0}$$
(3.9)

- 5 Emmy Noether (1882–1935) was a pioneering German mathematician known for her groundbreaking contributions to abstract algebra and for establishing Noether's theorem, which relates symmetries in physical systems to conserved quantities.
- 6 Robert Brown (1773–1858) was a Scottish botanist who discovered and described the random motion of microscopic particles suspended in a fluid, now known as Brownian motion, which provided crucial evidence for the existence of atoms and molecules.
- 7 Paul Ehrenfest (1880-1933) was an influential Austrian-Dutch physicist known for his significant contributions to statistical mechanics and quantum theory.

 $[\hat{A}, \hat{\mathbf{B}}] \equiv$ $[\hat{A}, \hat{B}_x], \dots, [\hat{A}, \hat{B}_z].$ Proof of 3.8a-3.8b in Section A.8. it can be shown that the expectation value of the total spin $\hat{\mathbf{F}}$ is constant 8 .

The consideration of this symmetry alone demonstrates that non-zero frequency resonances in ZULF NMR can solely be detected within heteronuclear spin systems. This arises from the fact that the physically measurable quantity is the total magnetic moment

$$\langle \hat{\mathbf{m}} \rangle = \sum_{i} \langle \hat{\mathbf{m}}_{i} \rangle = \sum_{i} \gamma_{i} \langle \hat{\mathbf{I}}_{i} \rangle$$
 (3.10)

In the case of homonuclear spin systems, where all gyromagnetic ratios are equal, i.e., $\gamma_i = \gamma \, \forall i$, it holds that

$$\frac{\mathrm{d}}{\mathrm{d}t} \langle \hat{\mathbf{m}} \rangle = \gamma \frac{\mathrm{d}}{\mathrm{d}t} \langle \sum_{i} \hat{\mathbf{I}}_{i} \rangle = \gamma \frac{\mathrm{d}}{\mathrm{d}t} \langle \hat{\mathbf{F}} \rangle \stackrel{3.9}{\underset{ZULF}{\rightleftharpoons}} \mathbf{0}$$
(3.11)

or $\langle \hat{\mathbf{m}} \rangle = \text{const.}$, resulting in an absence of observable time-varying signals. Only when there are at least two nuclear spins, denoted as i and j, with $\gamma_i \neq \gamma_j$, can the total angular momentum be conserved even if the magnetic moment itself is not, thereby giving rise to an oscillating signal.

Furthermore, this symmetry facilitates the decomposition of the HILBERT⁹ space (as well as the LIOUVILLE space) into rational invariant subspaces, establishing a connection between nuclear spin dynamics in zero-field and the extensively researched characteristics of rotational LIE¹⁰ groups and algebras (see Appendix D).

In contrast, at a high field, this symmetry is broken. The only remaining symmetry is rotational symmetry around the axis parallel to the magnetic field. Assuming that the magnetic field aligns with the z-axis, the Hamiltonian

$$[\hat{H}, \hat{F}_z] = 0 \tag{3.12}$$

still commutes with the z-component of the total angular momentum, denoted as \hat{F}_z , resulting in the conservation of $\langle \hat{F}_z \rangle = \text{const.}$

⁸ For a similar reason spin-exchange collisions conserve the ensemble's average electron angular momentum.

⁹ David Hilbert (1862–1943) was a German mathematician who made significant contributions to a wide range of mathematical disciplines, including algebra, number theory, geometry, and mathematical physics, and is renowned for his influential list of 23 unsolved problems that shaped the course of 20th–century mathematics.

¹⁰ Marius Sophus Lie (1842–1899) was a Norwegian mathematician who revolutionized the field of symmetry and group theory, providing the foundation for the development of modern differential geometry and Lie theory, with wide–ranging applications in physics and mathematics.

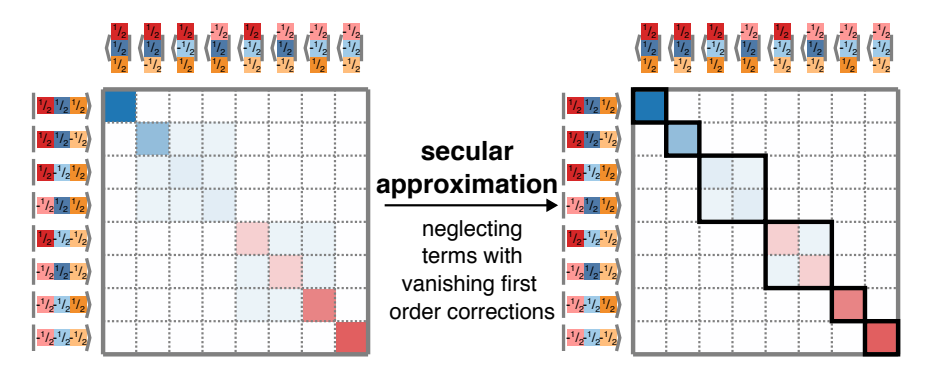


Figure 3.3: Schematic illustration of the secular approximation of a three A₂X spin system (A: red/blue; X: orange) that is pairwise coupled via a single coupling constant J. The matrix represents the Hamiltonian from Equation 3.13 in the Zeeman basis, where blue/red squares indicate positive/negative elements. If the secular approximation is applied, all terms with vanishing first-order energy corrections are neglected. In this specific scenario, this applies to terms of the form $\hat{I}_{i,\pm}^{(A)}\hat{I}_{\mp}^{(X)}$ that originate from the J-coupling Hamiltonian.

Similar to ZULF NMR, this, in principle, would allow longitudinal J-spectroscopy for heteronuclear spin systems. However, as will be demonstrated later, these transitions possess a vanishing transition moment, permitting the detection of high-field NMR resonance only in the transverse plane.

It is essential to note that these symmetry considerations are only valid for the coherent aspect of the system's time evolution, as described by the Hamiltonian. Incoherent processes, such as relaxation mechanisms, can significantly validate these conservation laws.

Secular Approximation

Whenever a parameter within a physical model undergoes a drastic change or completely disappears, as is the case with the magnetic field in zero-field NMR, the applicability of approximations used in the model must be reassessed. One such approximation that greatly simplifies a Hamiltonian in high-field NMR is the *secular approximation*, whose simple derivation can be found in Section A.9. In essence, when assuming a perturbed Hamiltonian, the secular approximation permits the neglect of terms with vanishing first-order energy corrections.

For instance, in a simple three-spin system

$$\hat{H} = B_z \gamma_A (I_{1,z}^{(A)} + I_{2,z}^{(A)}) + B_z \gamma_X I_z^{(X)} + \frac{2\pi J}{\hbar} (\hat{\mathbf{I}}_1^{(A)} \cdot \hat{\mathbf{I}}_2^{(A)} + \hat{\mathbf{I}}_1^{(A)} \cdot \hat{\mathbf{I}}_2^{(X)} + \hat{\mathbf{I}}_2^{(A)} \cdot \hat{\mathbf{I}}_2^{(X)})$$
(3.13)

at high field, where the ZEEMAN term predominates and the J-coupling serves as a perturbation, examining the last terms of Equation 3.13

$$\hat{l}_x = (\hat{l}_+ + \hat{l}_-)/2 \\ and \hat{l}_y = \\ (\hat{l}_+ - \hat{l}_-)/(2i).$$

$$\hat{\mathbf{I}}_{i}^{(A)} \cdot \hat{\mathbf{I}}^{(X)} = \hat{I}_{i,x}^{(A)} \cdot \hat{I}_{x}^{(X)} + \hat{I}_{i,y}^{(A)} \cdot \hat{I}_{y}^{(X)} + \hat{I}_{i,z}^{(A)} \cdot \hat{I}_{z}^{(X)}
= \frac{\hat{I}_{i,+}^{(A)} \hat{I}_{-}^{(I)}}{2} + \frac{\hat{I}_{i,-}^{(A)} \hat{I}_{+}^{(I)}}{2} + \hat{I}_{i,z}^{(A)} \cdot \hat{I}_{z}^{(X)}$$
(3.14)

and computing the first-order energy corrections

$$\langle m_{I,1} m_{I,2}, m_A | \hat{I}_{i,\pm}^{(A)} \hat{I}_{\mp}^{(I)} | m_{I,1} m_{I,2}, m_A \rangle = 0$$
 (3.15a)

$$\langle m_{I,1} m_{I,2}, m_A | \hat{I}_{i,z}^{(A)} \hat{I}_{z}^{(I)} | m_{I,1} m_{I,2}, m_A \rangle = m_{I,i} m_A \hbar^2$$
 (3.15b)

indicates that terms like $\hat{I}_{i,\pm}^{(A)} \hat{I}_{\mp}^{(I)}$ can be disregarded under the secular approximation¹¹. It is important to note that this approximation is not applicable at zero field, where the J-coupling Hamiltonian is dominant, and the Zeeman term acts as a perturbation. In Chapter 4, it will be demonstrated that this difference may result in ZULF NMR spectra being more responsive to variations in the coupling constant J.

3.3 TIME-DEPENDENT SIGNALS

For a given time-independent Hamiltonian \hat{H} let $|i\rangle$ represent an orthonormal basis of its eigenstates with corresponding eigenenergies E_i . The system's time evolution is described by the time-dependent density operator

$$\hat{\rho}(t) = e^{-i\hat{H}t/\hbar}\hat{\rho}(0)e^{i\hat{H}t/\hbar} . \tag{3.16}$$

This section aims to examine the criteria that must be met by an observable \hat{A} , the Hamiltonian \hat{H} , and the initial density operator $\hat{\rho}(0)$ to enable the measurement of time-dependent signals.

¹¹ Note that in the Zeeman basis the same would be true for the $\hat{l}_{1,\pm}^{(A)}\hat{l}_{2,\mp}^{(A)}$ operator. However, due to the degeneracy, the pure Zeeman basis would not be the first-order eigenbasis used in perturbation theory. Instead for the A_2 subsystem, the singlet-triplet basis would be used, which features non-zero first-order energy corrections.

Observables

For an observable \hat{A} the time-dependent expectation value is given by

$$\langle \hat{A} \rangle (t) = \operatorname{tr}(\hat{\rho}(t)\hat{A}) \ .$$
 (3.17)

Inserting Equation 3.16 and using the identity $\operatorname{tr}(\cdot) = \sum_{i} \langle i | \cdot | i \rangle$ the expectation value in Equation 3.17 can be expressed as

$$\langle \hat{A} \rangle (t) = \sum_{i} \langle i | e^{-i\hat{H}t/\hbar} \hat{\rho}(0) e^{i\hat{H}t/\hbar} \hat{A} | i \rangle$$
 (3.18)

and further expanded using the two identities $\sum_{j} |j\rangle \langle j|$, $\langle j| e^{-i\hat{H}t} = \langle j| e^{-iE_{j}t}$ and $e^{i\hat{H}t} |j\rangle = e^{iE_{j}t} |j\rangle$

$$\langle \hat{A} \rangle (t) = \sum_{i} \langle i | e^{-i\hat{H}t/\hbar} \hat{\rho}(0) \sum_{j} |j\rangle \langle j | e^{i\hat{H}t/\hbar} \hat{A} |i\rangle$$

$$= \sum_{i,j} \langle i | e^{-i\hat{H}t/\hbar} \hat{\rho}(0) |j\rangle \langle j | e^{i\hat{H}t/\hbar} \hat{A} |i\rangle$$

$$= \sum_{i,j} \langle i | e^{-iE_{i}t/\hbar} \hat{\rho}(0) |j\rangle \langle j | e^{iE_{j}t/\hbar} \hat{A} |i\rangle$$

$$= \sum_{i,j} \langle i | \hat{\rho}(0) |j\rangle \langle j | \hat{A} |i\rangle e^{i(E_{j} - E_{i})t/\hbar} .$$
(3.19)

In that way, the expectation value of \hat{A} can be expressed as the sum of a product of two matrix elements $\langle i|\hat{\rho}(0)|j\rangle$ and $\langle j|\hat{A}|i\rangle$.

The latter includes the measurable observable \hat{A} and is called the *transition moment*. For a system of nuclear spins $\{\hat{\mathbf{l}}_i\}$ with gyromagnetic ratios γ_i it is usually proportional the projection of the total magnetization $\mathbf{n} \cdot \hat{\mathbf{M}} = \sum_i \mathbf{n} \cdot \hat{\mathbf{M}}_i = \sum_i \gamma_i \mathbf{n} \cdot \hat{\mathbf{l}}_i$ of the spin ensemble along an axis represented by \mathbf{n} .

The former matrix element

$$\langle i|\hat{\rho}(0)|j\rangle = \sum_{k} \langle k|j\rangle \langle i|\hat{\rho}(0)|k\rangle = \operatorname{Tr}|j\rangle \langle i|\hat{\rho}(0) = \operatorname{Tr}\left((|i\rangle \langle j|)^{\dagger}\hat{\rho}(0)\right)$$
$$= \langle ij|\hat{\rho}(0)\rangle_{\mathcal{L}}$$

(3.20)

calculates the component of the Liouville space vector $|\hat{\rho}(0)\rangle_{\mathcal{L}} = \hat{\rho}(0)$ with respect to the basis vector $\langle ij|_{\mathcal{L}} = |i\rangle \langle j|$ using the Frobenius¹² inner product (see Equation A.21).

In the context of dipole transition it is called the transition dipole moment.

See Equation A.20 for more details about the notation $|\cdot\rangle_{\mathcal{L}}$ of vectors in the LIOUVILLE space.

¹² Georg Frobenius (1849–1917) was a German mathematician who made significant contributions to the fields of group theory, representation theory, and matrix theory, including the development of the Frobenius method for solving linear differential equations.

In other words, a coherence $|i\rangle\langle j|$ can only be observed if both its transition moment $\langle j|\hat{A}|i\rangle$ and its projection of $\hat{\rho}(0)$ are non-zero. If both requirements are fulfilled, an oscillating signal with the frequency $(E_j-E_i)/h$ could potentially be observed.



Eigenstates of a Two Spin-1/2 System

As an example, the dynamics of a system of two J-coupled heteronuclear ($\gamma_1 \neq \gamma_2$) spin-1/2 nuclei (e.g. formic acid-¹³C) will be investigated to highlight the key difference between high- and zero-field NMR phenomena. The corresponding product HILBERT space

$$\mathcal{H}_1 \otimes \mathcal{H}_2$$
 (3.21)

 $|\downarrow\rangle_{\alpha} \stackrel{\text{def}}{=} |-\frac{1}{2}\rangle_{\alpha} \text{ and}$ $|\uparrow\rangle_{\alpha} \stackrel{\text{def}}{=} |\frac{1}{2}\rangle_{\alpha} \text{ with}$ $\hat{I}_{z}^{(\alpha)} |m_{\alpha}\rangle_{\alpha} =$ $\hbar m_{\alpha} |m_{\alpha}\rangle_{\alpha} \text{ for}$ $\alpha \in \{1, 2\}$

is spanned by the basis vectors

$$|\downarrow\rangle_1 \otimes |\downarrow\rangle_2$$
, $|\downarrow\rangle_1 \otimes |\uparrow\rangle_2$, $|\uparrow\rangle_1 \otimes |\downarrow\rangle_2$, $|\uparrow\rangle_1 \otimes |\uparrow\rangle_2$, (3.22)

which are eigenstates of the Zeeman operator $-\sum_i \gamma_i (1 - \sigma_i) \hat{\mathbf{l}}_i \cdot \mathbf{B}$ and are referred to as the Zeeman basis. The following short notation

$$|\cdot\cdot\rangle \stackrel{\text{def}}{=} |\cdot\rangle_1 \otimes |\cdot\rangle_2$$
 (3.23)

will be used as an abbreviation to refer to these basis vectors.

In high-field, the Hamiltonian in Equation 3.3 can be simplified

$$\hat{H}_{hf} = -\gamma_1 \hbar B_z \hat{I}_z^{(1)} - \gamma_2 \hbar B_z \hat{I}_z^{(2)} + \frac{2\pi}{\hbar} J \hat{I}_z^{(1)} \hat{I}_z^{(2)}$$
(3.24)

by applying a secular approximation to the J-coupling term (chemical shift and other interactions are ignored for this example). The Hamiltonian commutes with both $\hat{I}_z^{(1)}$ and $\hat{I}_z^{(2)}$, justifying the selection of the Zeeman basis for this Hilbert space, which is also an eigenbasis of the Hamiltonian.

In contrast, the zero-field Hamiltonian

$$\hat{H}_{zf} = \frac{2\pi}{\hbar} J \hat{\mathbf{I}}_1 \cdot \hat{\mathbf{I}}_2 = \frac{2\pi}{\hbar} J \left(\hat{\mathbf{F}}^2 - \hat{\mathbf{I}}_1^2 - \hat{\mathbf{I}}_2^2 \right)$$
(3.25)

commutes with the total angular momentum $\hat{\mathbf{F}}^2$ (with $\hat{\mathbf{F}} = \hat{\mathbf{I}}_1 + \hat{\mathbf{I}}_2$) and its z-component $\hat{F}_z \stackrel{\text{def}}{=} \hat{I}_z^{(1)} + \hat{I}_z^{(2)}$, but not with $I_z^{(1)}$ and $I_z^{(2)}$ individually and the Zeeman basis not an eigenbasis of this Hamiltonian. Instead, the states

 $\hat{\mathbf{F}}^2 | F, m_{\mathrm{F}} \rangle = \hbar^2 F(F+1) | F, m_{\mathrm{F}} \rangle$ and $\hat{F}_z | F, m_{\mathrm{F}} \rangle = \hbar m_{\mathrm{F}} | F, m_{\mathrm{F}} \rangle$

$$|S_0\rangle \stackrel{\mathrm{def}}{=} |0,0\rangle \equiv \frac{|\uparrow\downarrow\rangle - |\downarrow\uparrow\rangle}{\sqrt{2}}, \ |T_0\rangle \stackrel{\mathrm{def}}{=} |1,0\rangle \equiv \frac{|\uparrow\downarrow\rangle + |\downarrow\uparrow\rangle}{\sqrt{2}},$$
(3.26a)

$$|T_{-}\rangle \stackrel{\text{def}}{=} |1, -1\rangle \equiv |\downarrow\downarrow\rangle, \ |T_{+}\rangle \stackrel{\text{def}}{=} |1, 1\rangle \equiv |\uparrow\uparrow\rangle$$
 (3.26b)

form an eigenbasis of $\hat{\mathbf{F}}^2$, \hat{F}_z and the zero-field Hamiltonian and will be referred to as the singlet-triplet basis.

Figure 3.4a shows the energy level diagram for both scenarios, labeled with the corresponding eigenbasis. By starting at zero-field and gradually increasing the B_z field along the z axis the diagrams can be transformed into each other.

Transition Moments

Given the eigenbasis $\{|i\rangle\}$ of the corresponding Hamiltonians, the observable coherences can be determined by calculating the transition matrix elements

$$\langle j | \hat{M}_{0,\pm} | i \rangle$$
 (3.27)

from Equation 3.18 with $\hat{M}_{0,\pm}$ being the components of the magnetic moment operators in the spherical basis. Analogous to the polarization of light, $\hat{M}_0 = \hat{M}_z$ represents magnetic moments that are linearly polarized along z, whereas $\hat{M}_{\pm} = \hat{M}_x \pm i \hat{M}_y$ describes rotating magnetic moments about the z-axis. Figure 3.4a shows an overview of the observable coherences with respect to the detection axis.

At high-field, assuming purely positive gyromagnetic ratios, i.e. $\gamma_1, \gamma_2 > 0$,

$$\langle\downarrow\downarrow|\hat{M}_{-}|\uparrow\downarrow\rangle = \langle\downarrow\uparrow|\hat{M}_{-}|\uparrow\uparrow\rangle \propto \gamma_1$$
 (3.28a)

$$\langle \downarrow \downarrow | \hat{M}_{-} | \downarrow \uparrow \rangle = \langle \uparrow \downarrow | \hat{M}_{-} | \uparrow \uparrow \rangle \propto \gamma_2 \tag{3.28b}$$

are the only allowed transitions with positive energy difference¹³ (i.e. $E_j > E_i$) which can be summarized by the two transitions rules $\{\Delta m_1 = -1, \Delta m_2 = 0\}$ or $\{\Delta m_1 = 0, \Delta m_2 = -1\}$ which are called *single quantum transitions*.

In contrast, at zero-field, there is an allowed transition for every operator

$$\langle T_{0,\pm} | \hat{M}_{0,\pm} | S_0 \rangle \propto (\gamma_1 - \gamma_2) \hbar$$
 (3.29)

For $\langle m'_1, m'_2 | \cdot | m_1, m_2 \rangle$ it is $\Delta m_1 = m'_1 - m_1$ and $\Delta m_2 = m'_2 - m_2$

¹³ Note that, in contrast to $\hat{M}_{x,y,z}$, \hat{M}_{\pm} are no longer Hermitian operators. However, due to $\hat{M}_{\pm}^{\dagger} = \hat{M}_{\mp}$, without loss of generality, only matrix elements with $E_j > E_i$ have to be considered and $\langle i | \hat{M}_{\pm} | j \rangle = \langle j | \hat{M}_{\mp} | i \rangle$. Similarly, it is $\langle i | \hat{M}_{0} | j \rangle = \langle j | \hat{M}_{0} | i \rangle^*$.

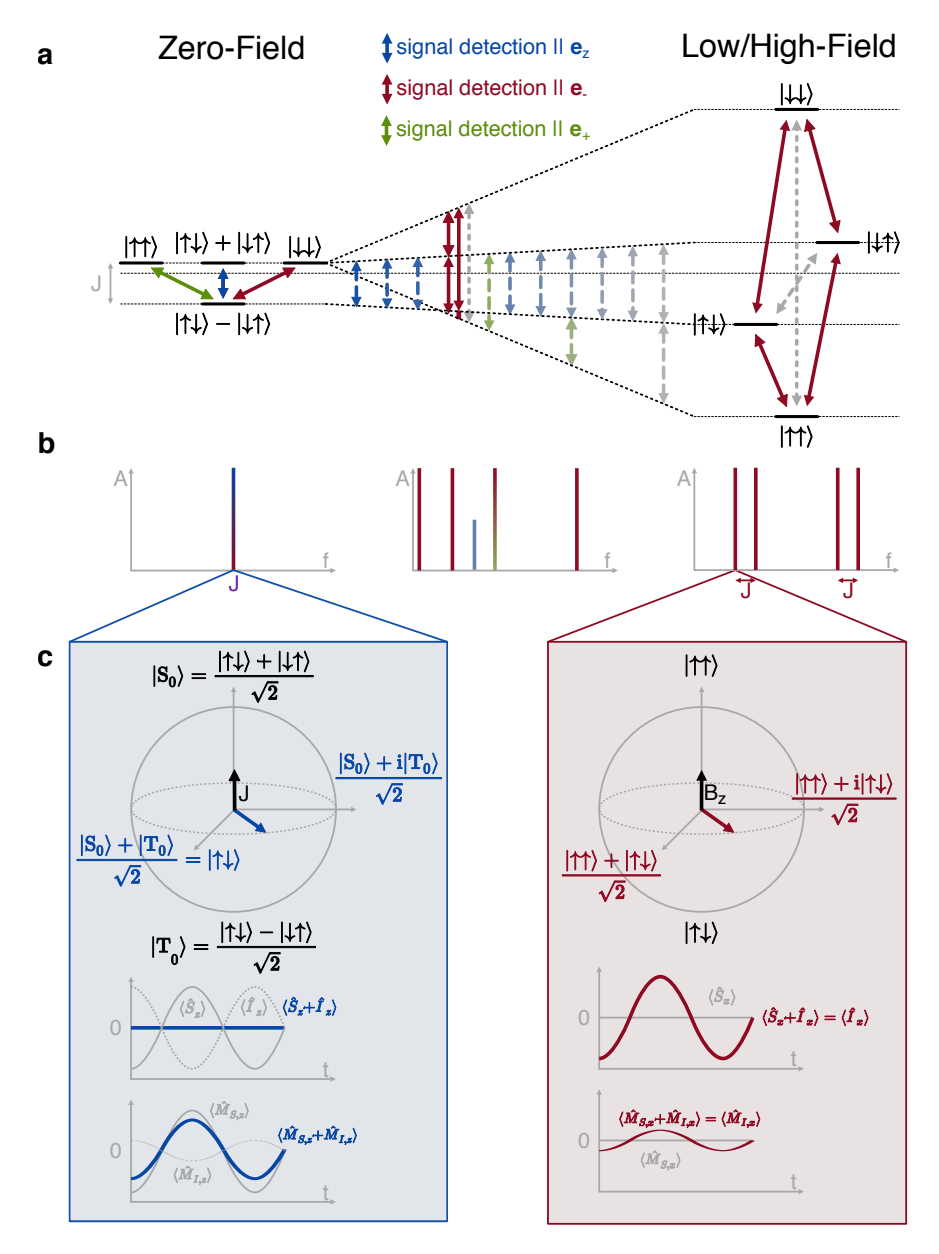


Figure 3.4: Schematic representation of the differences between zero and high-field NMR. **a**, energy level diagram of a coupled two-spin system. Arrows represent magnetic dipole transitions with the saturation representing the transition moment (grey = forbidden). Colors represent the axis of detection with the magnetic field being parallel to the z-axis. **b** and **c** show the observable NMR spectra with only one resonance line at zero field. **d** and **e** sketch the detailed dynamics of a single coherence/resonance showing the Bloch sphere, total angular momentum, and magnetization.

Here the selection rules are $\{\Delta F = 1, \Delta m_{\rm F} = 0, \pm 1\}$. Other transitions are allowed, i.e. between different $|T_{0,\pm}\rangle$ states with $\Delta F = 0$, but only with zero-frequency $(E_i = E_i)$ at zero-field.

In Figure 3.4a, the continuous evolution of transition moments is depicted as the system transitions from zero to high-field. Correspondingly, Figure 3.4b displays the associated spectrum. Within the intermediate regime, where the spins are neither strongly coupled (as in zero-field) nor weakly coupled (as in high-field), the number of transitions reaches its maximum, resulting in nearly all transitions being observable, except for the $|\uparrow\uparrow\rangle\leftrightarrow|\downarrow\downarrow\rangle$ transition, which remains forbidden. The potential of this increased number of transitions will be explored in Chapter 4 to reduce uncertainty in J-coupling estimations. It should be noted that the impact of the increased number of transitions in the intermediate coupling regime will be more pronounced for larger spin systems.

Relation Between Spin and Magnetization

While the occurrence of an oscillating signal in NMR from low to high field can be adequately explained using semiclassical models describing spin precession, the emergence of resonance at zero-field presents a more intricate challenge. Figure 3.4c endeavors to shed light on the underlying dynamics, with a specific focus on the exemplary transition $|S_0\rangle \leftrightarrow |T_0\rangle$. As discussed in Section 3.2, the spherical symmetry mandates the conservation of the total nuclear angular momentum. Consequently, a direct measurement of the total nuclear angular momentum would not yield an oscillating signal, marking a noteworthy distinction from high-field NMR (as depicted on the right side of the figure), where the signal arises directly due to the precession of the nuclear angular momentum.

In contrast, the origin of the NMR signal at zero-field is rooted in the oscillation of the relative contributions of each spin's nuclear angular momentum to the total nuclear spin angular momentum. This oscillation, coupled with the presence of different gyromagnetic ratios, eventually results in oscillating magnetization that can be detected. In essence, even if a homonuclear spin system were to display identical spin dynamics, it would not produce a non-trivial zero-field spectrum.

Whereas the total angular momentum $\hat{\mathbf{F}} = \text{const}$ does not precess or oscillate for any of the allowed transitions, this is not necessarily

true for the magnetic moment. Here, simple oscillations ($|S_0\rangle \leftrightarrow |T_0\rangle$) as well as precession ($|S_0\rangle \leftrightarrow |T_\pm\rangle$) may be possible.

3.4 INITIAL STATE PREPARATION

A non-zero transition element, which implies an allowed transition, is just one of the prerequisites necessary to observe a coherence $|i\rangle\langle j|=|ij\rangle\mathcal{L}$ (as outlined in Equation 3.19). Moreover, it is essential that the energy difference $E_j-E_i>0$ is positive, and the inner product

$$\langle ij|\hat{\rho}(0)\rangle_{\mathcal{L}} \stackrel{!}{\neq} 0$$
 (3.30)

of the coherence $|ij\rangle \mathcal{L}$ with the initial density operator $|\hat{\rho}\rangle_{\mathcal{L}}$ must also be non-zero (as illustrated in Equation 3.20).

Thermally Polarized State

Given an ensemble of *N* identical particles, the number

$$\langle N_i \rangle = \frac{N}{Z} g_i e^{-E_i/(k_B T)} \tag{3.31}$$

of them that are expected to be found with an energy E_i can be described by the Maxwell¹⁴-Boltzmann¹⁵ statistics. Here, $k_{\rm B}$ is the Boltzmann constant, T the temperature, g_i the degeneracy, and Z the partition function necessary for normalization. For a nuclear spin I, the expression

$$p_{i} = \frac{\langle N_{i} \rangle}{N} = \frac{e^{m_{i}\hbar\gamma B_{z}/(k_{B}T)}}{Z} \stackrel{\hbar\gamma B_{z} \ll k_{B}T}{\approx} \frac{1 + m_{i}\hbar\gamma B_{z}/(k_{B}T)}{2I + 1}$$
(3.32)

¹⁴ James Clerk Maxwell (1831–1879) was a Scottish physicist whose groundbreaking work in electromagnetism formulated Maxwell's equations, unifying electricity, magnetism, and light into a single coherent theory and laying the foundation for modern physics.

¹⁵ Ludwig Boltzmann (1844–1906) was an Austrian physicist and mathematician who made significant contributions to the field of statistical mechanics, developing the statistical interpretation of entropy and providing fundamental insights into the behavior of atoms and molecules.

describes the probability of finding a single particle in the spin state m_i leading to the nuclear spin polarization

$$p = \frac{\langle I_z \rangle}{\max \langle I_z \rangle} = \frac{\sum_i p_i \hbar m_i}{I \hbar}$$

$$= \frac{\sum_i m_i \cdot (1 + m_i \hbar \gamma B_z / (k_B T))}{I \cdot (2I + 1)}$$

$$= \frac{\hbar \gamma B_z}{k_B T \cdot I \cdot (2I + 1)} \sum_i m_i^2$$

$$= \frac{\hbar \gamma B_z}{k_B T} \frac{(1 + I) / 3 \cdot I \cdot (2I + 1)}{I \cdot (2I + 1)}$$

$$= \frac{\hbar \gamma B_z}{k_B T} \frac{(1 + I)}{3}$$

$$I = \frac{\hbar \gamma B_z}{2k_B T} \frac{(1 + I)}{3}$$

$$I = \frac{1}{2} \frac{\hbar \gamma B_z}{2k_B T}$$
(3.33)

where in the last line a particle with I = 1/2 is assumed.

The density operator of a single nuclear spin species is then given by [38]

$$\hat{\rho}_{\text{thermal}} = \sum_{i} p_{i} |m_{i}\rangle \langle m_{i}|$$

$$= \sum_{i} \frac{1 + 2pm_{i}}{2I + 1} |m_{i}\rangle \langle m_{i}|$$

$$= \frac{1}{2I + 1} + \frac{2p\hat{I}_{z}}{\hbar(2I + 1)}$$

$$\stackrel{I=1/2}{=} \frac{1}{2} + \frac{p\hat{I}_{z}}{\hbar} .$$

$$(3.34)$$

The combined density operator for two spin-1/2 particles

$$\hat{\rho}_{\text{thermal}} = \hat{\rho}_{\text{thermal}}^{(1)} \otimes \hat{\rho}_{\text{thermal}}^{(2)} \\
= \frac{\hat{\mathbb{I}}}{4} + p_1 \frac{\hat{I}_z^{(1)}}{2\hbar} + p_2 \frac{\hat{I}_z^{(2)}}{2\hbar} + \frac{2p_1 p_2}{\hbar^2} \hat{I}_z^{(1)} \hat{I}_z^{(2)} \\
\stackrel{p_1, p_2 \ll 1}{=} \frac{\hat{\mathbb{I}}}{4} + p_1 \frac{\hat{I}_z^{(1)}}{2\hbar} + p_2 \frac{\hat{I}_z^{(2)}}{2\hbar}$$
(3.35)

is given by the product of the two single spin density operators $\hat{\rho}_{\text{thermal}}^{(1)}$ and $\hat{\rho}_{\text{thermal}}^{(2)}$. It may be worth noting that $\mathbb{1} \cong \hat{T}_{00}$, $\hat{I}_{1,z} \cong \hat{T}_{10}$ and $\hat{I}_{2,z} \cong \hat{T}_{10}$ are congruent to spherical basis operators of spherical rank o and 1.

Non-Adiabatic Shuttling to Zero Field

At high-field, the allowed transitions in Equation 3.28a-3.28b

$$\left|\downarrow\right\rangle\left\langle\uparrow\right|=\hat{I}_{-}$$
 (3.36)

 $\hat{I}_{-}^{(\alpha)}\hat{I}_{x}^{(\alpha)} - \mathrm{i}\hat{I}_{y}^{(\alpha)}$ for can be linked to the ladder operators $\hat{I}_{-}^{(1)}$ and $\hat{I}_{-}^{(2)}$. Giving the thermal state in Equation 3.35 a coherence can be generated simply by mal state in Equation 3.35 a coherence can be generated simply by applying a $\pi/2$ spin rotation about any axis orthogonal to z, e.g. $\hat{I}_{z}^{(1)} \to \hat{I}_{x}^{(1)} \text{ or } \hat{I}_{z}^{(2)} \to \hat{I}_{x}^{(2)}.$

The zero-field coherence

$$|T_0\rangle\langle S_0| = \frac{\hat{I}_z^{(1)}}{2\hbar} - \frac{\hat{I}_z^{(2)}}{2\hbar} + \frac{\hat{I}_-^{(1)}\hat{I}_+^{(2)}}{\hbar^2} - \frac{\hat{I}_+^{(1)}\hat{I}_-^{(2)}}{\hbar^2}$$
(3.37)

at low field from Equation 3.29 can also be expressed in terms of nuclear spin operators. 16. Assuming the state from Equation 3.35 was shuttled non-adiabatically to zero field the inner product (see Equation 3.20)

$$\operatorname{Tr}\left(\left(\left|T_{0}\right\rangle\left\langle S_{0}\right|\right)^{\dagger}\hat{\rho}_{\text{thermal}}\right) = \frac{p1 - p2}{4} \tag{3.38}$$

of $|T_0\rangle\langle S_0|$ with $\hat{\rho}_{thermal}$ can be calculated. It could even be enhanced by flipping one of the spins, e.g. $\hat{l}_z^{(2)} \rightarrow -\hat{l}_z^{(2)}$,

$$\hat{\rho}_{\text{thermal}} \to \frac{\hat{1}}{4} + p_1 \frac{\hat{I}_z^{(1)}}{2\hbar} - p_2 \frac{\hat{I}_z^{(2)}}{2\hbar}$$
 (3.39)

resulting in the inner product being (p1 + p2)/4. For an exemplary spin system of $I_1 = {}^{1}H$ and $I_2 = {}^{13}C$ with $\gamma_{^{1}H} \approx 4\gamma_{^{13}C}$ this would lead to a signal enhancement of

$$\frac{(p_1 + p_2)/4}{(p_1 - p_2)/4} = \frac{(\gamma_{1_H} + \gamma_{1_{3_C}})}{(\gamma_{1_H} - \gamma_{1_{3_C}})} \approx \frac{5}{3} .$$
 (3.40)

¹⁶ Even if the combination of the last two operators $(\hat{I}_{+}^{(1)}\hat{I}_{+}^{(2)} - \hat{I}_{+}^{(1)}\hat{I}_{-}^{(2)})/\hbar^2 \cong \hat{T}_{10}$ is also a spherical basis operator of spherical rank 1, it is inaccessible from the thermal state via simple spin rotations. However, the full J-coupling term can access it.

Adiabatic Shuttling to Zero Field

Alternatively, starting from the state of thermal polarization, it is possible to perform an adiabatic transfer to zero-field. The resultant density operator

$$\rho_{\text{adiabatic}} = \frac{\hat{1}}{4} + \frac{p_1 + p_2}{8\hbar} \left(\hat{I}_z^{(1)} + \hat{I}_z^{(2)} \right) \\
- \frac{p_1 + p_2}{8\hbar^2} \left(\hat{I}_-^{(1)} \hat{I}_+^{(2)} + \hat{I}_+^{(1)} \hat{I}_-^{(2)} + 4 \hat{I}_z^{(1)} \hat{I}_z^{(2)} \right)$$
(3.41)

commutes with the zero-field Hamiltonian. The third term cannot be transformed into observable coherences through straightforward spin rotations. However, the second term can be, simply by flipping one of the spins, leading to the inner product being $\frac{p_1+p_2}{8\hbar^2}$. In comparison to non-adiabatic shuttling, the signal obtained through this method is reduced by a factor of two, thus rendering non-adiabatic shuttling the preferred polarization technique.

RESOLUTION OPTIMIZED J SPECTROSCOPY

Nuclear spins expose the information they gather from their direct, local environment in two different ways: On the one hand, the coherent evolution of an ensemble spin state reveals the average (in time and space) energy level structure of the nuclear spin states. On the other hand, relaxation provides insight into the nature of the non-coherent, random interactions.

While Chapter 5 and Chapter 6 will delve into the latter aspect, this chapter is dedicated to the examination of the nuclear spin's coherent environment across various field regimes. In the case of liquid samples undergoing rapid molecular tumbling, at ZULF) conditions, only the J-coupling, and the ZEEMAN term persist after averaging over all rotational states. The origin of the J-coupling was discussed in Chapter 3. Given that it represents a nuclear spin-spin coupling mediated by electrons, it serves as a valuable tool for probing electron properties using nuclear spin. The capacity to measure J-coupling constants with exceptional precision endows the nuclear spin sensor with sensitivity to even the slightest variations in this constant. These variations could arise from solvent effects [90], temperature fluctuations, isotope shifts, or even the search for dark matter [91]. However, as an initial step, this chapter primarily focuses on establishing the boundaries of a novel and unknown technique, without specific application objectives at this stage.

In the context of the field regimes defined in Figure 3.2, zero-field spectroscopy has been employed for numerous molecules, achieving record precision in the measurement of J-coupling constants [83]. However, these accomplishments represent only a fraction of what has been attained at high-field. EARTH's field NMR has also been utilized for certain molecules to explore the ULF/very low field (VLF) regime [92, 93]. Nevertheless, EARTH's field is not low enough to reach ULF/VLF regime for spin systems with small coupling constants, resulting in limited studies focused on the ULF/VLF regime below EARTH's magnetic field [87, 94, 95].

4.1 MOTIVATION FOR ULTRALOW FIELD SPECTROSCOPY

One factor that may have prevented ULF/VLF NMR spectroscopy from reaching its full potential may be the historical unavailability of cost-effective sensors. Because inductive detection at low field levels is not feasible, only SQUIDs offered the necessary sensitivity for detecting NMR signals in such conditions for many years. It is only in recent times, thanks to advancements in OPM technology, that these experiments have become more accessible to a wider audience.

Now, with suitable OPM solutions becoming increasingly available, this section will explore the potential advantages of utilizing the ULF/VLF regime for spectroscopy. It aims to investigate how various spectrum properties, such as *J-coupling response*, *amplitude*, *number of resonances*, *line width*, *magnetic field uncertainty* and *complexity*, vary across different field regimes. Furthermore, it will delve into the field-dependent sensitivity of a prospective sensor and address common sources of noise.

In this chapter, a liquid sample of 2,2,2-trifluoroethanol will serve as an illustrative spin system. Due to the relatively similar gyromagnetic ratios of fluorine and hydrogen nuclear spins

$$\frac{\gamma_{19\,\mathrm{F}}}{\gamma_{1\,\mathrm{H}}} = \frac{40.08 \times 10^6\,\mathrm{Hz/T}}{42.58 \times 10^6\,\mathrm{Hz/T}} = 94.1\,\% \ , \tag{4.1}$$

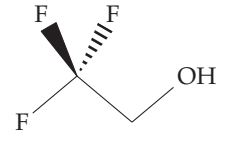
fluorine-hydrogen spin systems are not well-suited for zero-field spectroscopy, making 2,2,2-trifluoroethanol a potential candidate for spectroscopy in ULF/VLF. This compound represents an A_3X_2 spin system, disregarding the 1H nuclear spin of the -OH group, which is a reasonable assumption due to frequent chemical exchange rendering it effectively decoupled from the rest of the system. In Figure 4.1, an overview of the NMR spectra simulated across all three field regimes and the crossover regions is presented.

J-Coupling Response

Assuming a single resonance frequency v_i , its dependence on the J-coupling constant, i.e. the derivative

$$\frac{\partial v_i}{\partial I} \tag{4.2}$$

can vary among different field regimes, which will be referred to as the *J-response* in this context. For instance, the single zero-field



2,2,2-trifluoroethanol

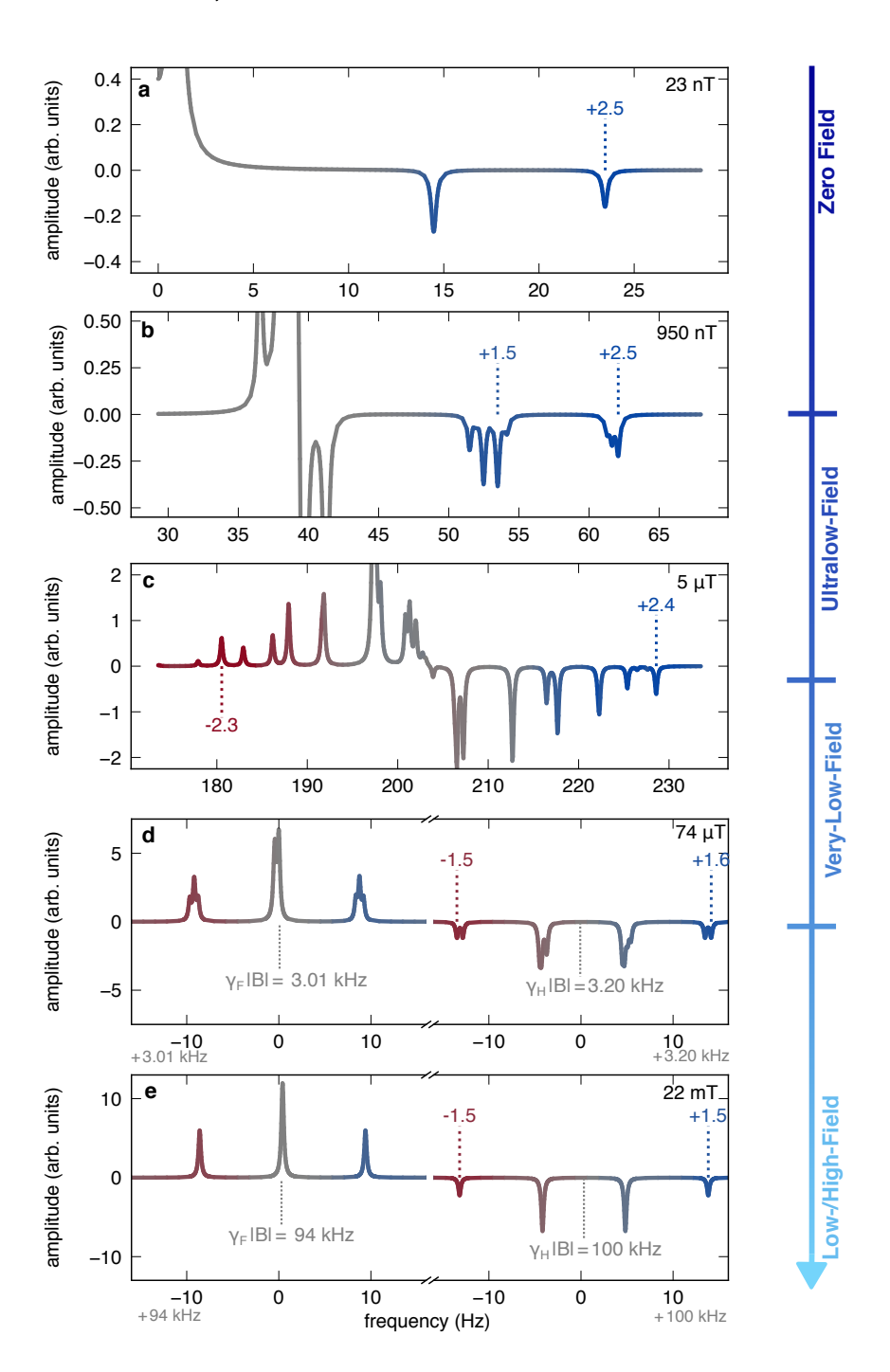


Figure 4.1: Simulated NMR spectra of CF₃CH₂OH at different field regimes. All spectra are simulated with the same initial thermal polarization with the hydrogen spins being flipped before acquisition to enhance the ZULF spectra. The colors indicate the sign of the J-response and the saturation indicates its magnitude.

($|\mathbf{B}| = 0$ T) resonance at $\nu = J$ for an AX spin system, as discussed in the previous chapter, would lead to a J-response of

$$\frac{\partial}{\partial J} \nu_i^{(AX)} \Big|_{|\mathbf{B}|=0} = \frac{\partial J}{\partial J} = 1$$
 (4.3)

and is twice as large

$$\frac{\partial}{\partial J} \nu_i^{(AX)} \Big|_{|\mathbf{B}| \gg 0} = \frac{\partial}{\partial J} \left(\frac{\gamma_{A,X}}{2\pi} |\mathbf{B}| \pm \frac{J}{2} \right) = \pm \frac{1}{2} . \tag{4.4}$$

as the value observed at high-field ($|\mathbf{B}|\gg 0$). When considering only a single resonance and assuming that all other parameters, such as SNR, linewidth, etc., remain constant and known, the uncertainty in estimating the J-coupling is directly proportional to the J-response. Focusing solely on the J-coupling response, zero-field spectroscopy holds the promise of delivering the most accurate results.

The precise enhancement, however, depends on the spin system. In the example provided in this chapter (2,2,2-trifluoroethanol), the highest detectable zero-field resonance exhibits a response of 2.5, as opposed to only 1.5 at high-field. This contrast is also illustrated in Figure 4.1, where the color-coding and labels represent the J-coupling response. The high J-coupling response remains consistent even at moderate fields in the ULF and VLF regimes, which serves as one of the motivations for spectroscopy. Figure 4.2a displays the J-responses for the detectable resonances of 2,2,2-trifluoroethanol. The largest responses are obtained at zero field. On the other hand, more observable resonances are present at high fields.

Complexity

The ULF/VLF regime has the highest amount of allowed transitions, which can also be seen Figure 4.1c. Assuming all other parameters remain unchanged, a greater number of transitions is expected to yield a more precise estimation of the coupling constant as long as the estimation is limited by SNR.

However, one mostly benefits from more resonances as long as they are spectrally resolved. Many resonances that are separated by less than their linewidth may actually increase the uncertainty. This can be seen in Figure 4.1b and Figure 4.1d that represent the intermediate regime between zero-field and ULF, or VLF and high-field respectively. These regions are expected to perform worse compared to the clearly resolvable spectra in the other three regimes.

In this context, limited by SNR means, that the uncertainty $\sigma_J \propto \sigma_{noise}$ in estimating J is proportional to the standard deviation of the noise in the spectrum σ_{noise} (see 4.2).

The substantial multitude of resonances implicates a challenge in extracting J-coupling constants from spectra, particularly in the case of complex molecules. One approach entails fitting the spectrum to a theoretical model, which restricts the technique's applicability to smaller molecules. Conversely, at both zero and high magnetic field strengths, the J-coupling constants can often be more easily determined by measuring the splitting and resonance frequency.

More resonances are also only better if their appearance does not come at the cost of a reduced resonance amplitude. In the case where two resonances are the results of a single resonance being split (e.g. by a small perturbation), the single resonance may perform better if the estimation is limited by SNR.

Amplitude

Even if it is assumed that the initial thermal polarization is independent of the detection field, the conversion of this thermal polarization into detectable coherences is more effective at high fields, as discussed in the previous chapter (see Chapter 3). Moreover, transition moments at high fields may also be greater ($\propto \gamma_i$) compared to zero field ($\propto \gamma_1 - \gamma_2$). Figure 4.1 and Figure 4.2b illustrate how the amplitudes of the resonances change with different magnetic fields. This is particularly significant for the system under discussion, CF₃CH₂OH, due to the very similar gyromagnetic ratios of ¹H and ¹⁹F. The amplitudes of the relevant resonances may change by more than an order of magnitude. As long as the decrease in amplitude is compensated, for example, by a narrower line or a larger J-response, there is a chance that the ULF/VLF regime may be more sensitive to the J coupling constants, provided that the estimation is limited by the SNR.

Magnetic Field Uncertainty

It is generally assumed that the magnetic field is known, with the only unknown variable being the J-coupling constant. However, this assumption is often inaccurate, at least in terms of the required accuracy and precision for fitting the spectra. Consequently, the magnetic field also becomes a freely adjustable parameter that must be considered, potentially influencing the uncertainty in the estimation of the J-coupling.

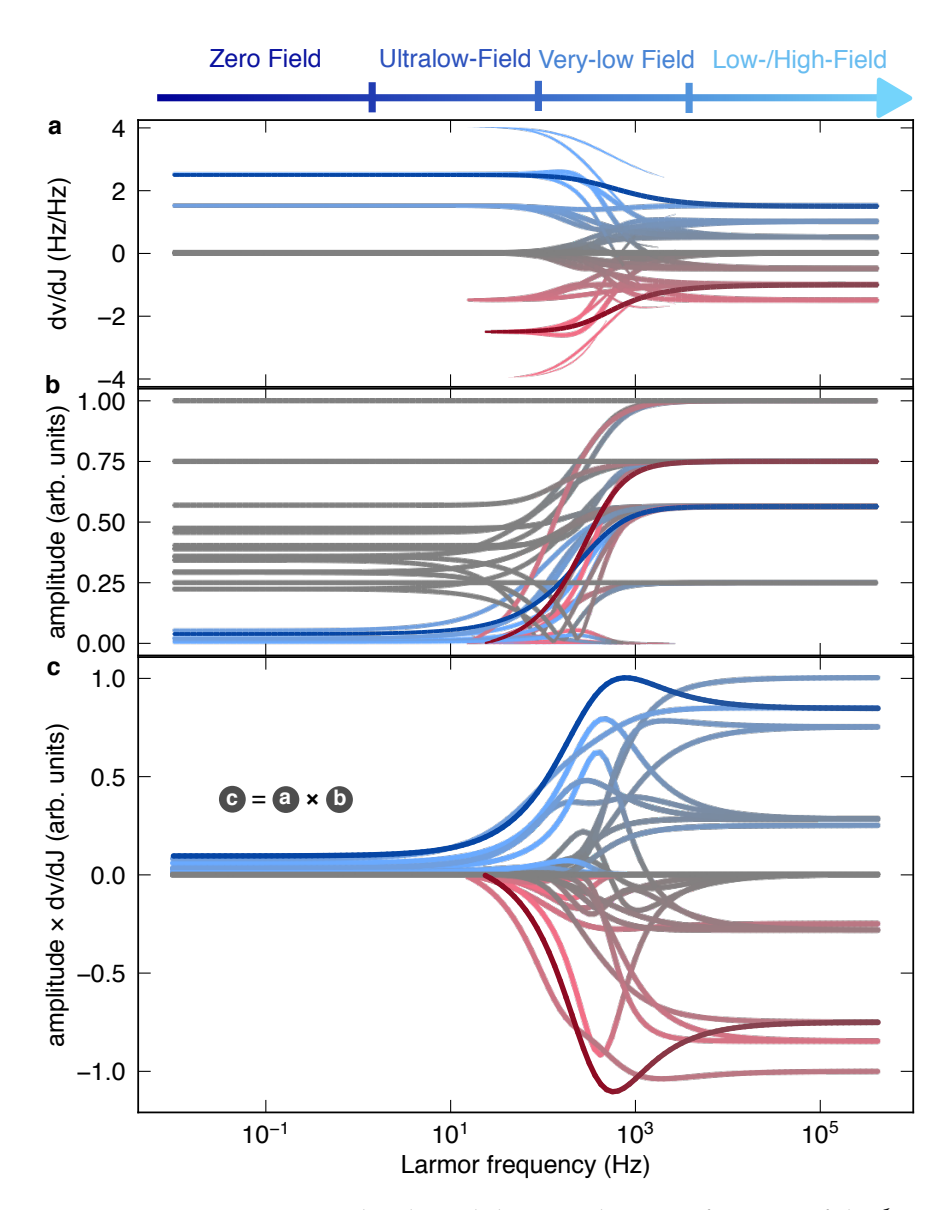


Figure 4.2: J-response, amplitude and their product as a function of the ¹H-LARMOR frequency for CF₃CH₂OH. Each line represents a single resonance while the colors represent the J-response. The two resonances highlighted in Figure 4.1 are also highlighted here (dark red and dark blue curve). Assuming all other parameters being constant, the product (c) of the J-response a and amplitude (b) is proportional to the inverse fit uncertainty (i.e. the higher the better).

However, it will be shown that in the specific case chosen for this example, involving the molecule CF_3CH_2OH , there is minimal dependence on the uncertainty of the magnetic field for J-coupling uncertainty, thanks to the nearly identical gyromagnetic ratios ($\gamma_{^{19}F}/\gamma_{^{1}H}=94$ %). In contrast, for the molecule to be studied in the upcoming chapter (see Chapter 5), the uncertainty in the magnetic field will play a more significant role.

Linewidth

The linewidth of a magnetic resonance may vary depending on the applied magnetic field. This variation can occur due to inhomogeneous broadening effects resulting from gradients parallel to the applied field or changes in the intrinsic relaxation rates. These factors will be the primary focus of the next two chapters. In Chapter 5 LLCs in the ZULF regime will be discussed, while Chapter 6 will investigate field-dependent relaxation rates in the ZULF regime, primarily caused by uncommonly slow molecular dynamics.

However, for the analysis in this chapter, the linewidth is assumed to be independent of the magnetic field, a hypothesis that aligns with experimental data except for some gradient-broadening effects occurring at magnetic fields exceeding 1 kHz. Subsequent chapters (see Chapter 5 and Chapter 6) will explore scenarios where the linewidth exhibits field-dependent behavior.

Limitations of the Experimental Apparatus

In this chapter, it is assumed that the sensitivity of the spectrometer does not depend on the magnetic field. However, this assumption is not accurate for inductive detectors and is also not entirely valid for OPMs. Particularly, at the time when the data presented here was recorded, the magnetometer did not perform optimally at frequencies above 1 kHz, resulting in reduced sensitivity at higher fields. Furthermore, due to technical noise, the low-frequency sensitivity (less than 50 Hz) of the OPM described here is orders of magnitude worse than in the optimal frequency range between 100 Hz to 300 Hz (refer to Figure 2.7).

Another source of systematic uncertainty pertains to the stability of the integrated oscillator employed within the microcontroller's data acquisition unit. Given its stability is merely 50 ppm, the detection In contrast, SQUIDs may have a bandwidth of a few MHz.

of a J-coupling of 10 Hz is subject to an uncertainty of 0.5 mHz, a magnitude considerably less than the experimentally obtained results typically in the range of a few mHz.

SNR vs. Broadening Limited Estimations

In the analysis presented in this chapter, the assumption is made that the estimation is constrained by the SNR. This assumption implies that the uncertainty, denoted as σ_J , in estimating the parameter J, is directly proportional to the standard deviation of the noise within the spectrum, denoted as σ_{noise} . To satisfy this assumption, it is necessary for the shape of the resonance to be well-known and is herein presumed to be a perfect Lorentzian shape. This presupposes that the resonance exhibits a pure exponential decay, devoid of any line-broadening or Fourier artifacts. While the latter requirement can be mitigated through more intricate data-processing techniques (see Appendix F), the presence of line broadening, for instance, due to magnetic field gradients, necessitates precise knowledge of the gradient and sample diffusion.

In other words, particularly in high fields where these assumptions are not guaranteed to hold, the estimation may be less accurate than what is projected in this chapter's analysis. A higher SNR does not automatically result in a more precise estimate of parameter J. In contrast, at ZULF/VLF, the gradient-induced broadening is typically negligible when compared to the resonance linewidth, and the spectra are almost invariably limited by the Signal-to-Noise Ratio (SNR).

4.2 SPECTRAL FITTING VIA LEAST SQUARES REGRESSION ANAL-YSIS

Given a function

$$\mathbf{f}: \mathbb{R}^n \to \mathbb{R}^m: \mathbf{x} \mapsto \mathbf{f}(\mathbf{x})$$
, (4.5)

with $n \le m$ the method of *least squares* is an approach to find the vector **x** that minimizes

$$\min_{\mathbf{x} \in \mathbb{R}^n} \frac{1}{2} \sum_{i=1}^m |f_i(\mathbf{x})|^2 \equiv \min_{\mathbf{x} \in \mathbb{R}^n} c(\mathbf{x})$$
(4.6)

the cost function $c(\mathbf{x}) = \frac{1}{2} \sum_{i=1}^{m} |f_i(\mathbf{x})|^2$. It is a standard approach in regression analysis and is often used in physics to find a model's parameters that fit best to a set of data.

Least Squares for Spectral Fitting

In NMR, a sampled spectrum s at frequencies $\mathbf{f} = (f_1, \dots, f_m)^{\mathsf{T}}$ can be often be approximated

$$s(\mathbf{x}) = \sum_{i=1}^{n} \mathcal{L}(\mathbf{f}, a_i(\mathbf{x}), \nu_i(\mathbf{x}), \Gamma_i(\mathbf{x}))$$
(4.7)

as the sum of Lorentzian functions

$$\mathcal{L}(f, a, \nu, \Gamma) = \frac{a\Gamma}{\Gamma^2 + 4\pi^2 (f - \nu)^2}$$
(4.8)

with amplitudes a_i , center frequencies v_i and decay rates Γ_i . The vector $\mathbf{x} = (J_i, \sigma_i, |\mathbf{B}|, \dots)^{\mathsf{T}}$ represents the unknown parameters of the model, i.e. the coupling constants J_i , chemical shifts σ_i or magnetic field $|\mathbf{B}|$.

Given a measured spectrum $\mathbf{y} = (y_1, \dots, y_m)$ the function $f(\mathbf{x})$ in Equation 4.5 can be defined as

$$\mathbf{f}(\mathbf{x}) = s(\mathbf{x}) - \mathbf{y} . \tag{4.9}$$

Several algorithms try to find the global minimum of Equation 4.6, with the Gauss¹-Newton² [96] and the *gradient decent* algorithm [97] (developed by Cauchy³) being the most popular ones. Here, the Levenberg-Marquardt algorithm is used, which can be seen as an interpolation between the previous two, by benefiting from the efficiency of the Gauss-Newton algorithm (GNA) and the robustness of the gradient descent algorithm.

¹ Carl Friedrich Gauss (1777–1855) was a German mathematician and physicist who made significant contributions to a wide range of mathematical disciplines, including number theory, geometry, and celestial mechanics, and is often referred to as the "Prince of Mathematicians."

² Isaac Newton (1643–1727) was a renowned English mathematician, physicist, and astronomer, recognized for formulating the laws of motion, universal gravitation, and his groundbreaking work in calculus.

³ Augustin-Louis Cauchy (1789–1857) was a prominent French mathematician known for his foundational contributions to analysis, complex function theory, and mathematical rigor.

Covariance Matrix Estimation

At the global minimum x_0 the covariance matrix [98]

$$\hat{K} = \sigma^2 \left(\left. \nabla^2 c \right|_{\mathbf{x}_0} \right)^{-1} \tag{4.10}$$

estimates the variance (K_{ii}) and co-variances (K_{ij}) of the parameters x_i and x_j via the Hessian⁴ matrix $\nabla^2 c$. Here σ^2 describes the variance of the (assumed) normal distribution of the residuals $f_i(\mathbf{x}_0)$. If σ^2 is not known it may be estimated

$$\sigma^2 \approx \frac{1}{m-n} \sum_{i=1}^{m} |f_i(\mathbf{x}_0)|^2$$
 (4.11)

and describes the noise in the system. For the analysis described here, it is assumed to be field-independent and will therefore be ignored in this chapter. However, in reality, the magnetometer's sensitivity is not perfectly flat and the residuals will not follow a normal distribution and also may be field-dependent.

The Hessian matrix

$$\nabla^{2} c(\mathbf{x}_{0}) \stackrel{\text{def}}{=} \begin{pmatrix} \frac{\partial^{2} c}{\partial x_{1}^{2}} & \cdots & \frac{\partial^{2} c}{\partial x_{1} \partial x_{n}} \\ \vdots & \ddots & \vdots \\ \frac{\partial^{2} c}{\partial x_{n} \partial x_{1}} & \cdots & \frac{\partial^{2} c}{\partial x_{n} \partial x_{n}} \end{pmatrix} \stackrel{GNA}{\approx} \mathbf{J}(\mathbf{x}_{0})^{\mathsf{T}} \cdot \mathbf{J}(\mathbf{x}_{0})$$
(4.12)

is often approximated using the function's Jacobian⁵

$$\mathbf{J} = \begin{pmatrix} \frac{\partial f_1}{\partial x_1} & \cdots & \frac{\partial f_1}{\partial x_n} \\ \vdots & \ddots & \vdots \\ \frac{\partial f_m}{\partial x_1} & \cdots & \frac{\partial f_m}{\partial x_n} \end{pmatrix} . \tag{4.13}$$

May ind(J) be the index of the J-coupling parameter in the vector \mathbf{x} . The value

$$u = \frac{1}{\sqrt{((\mathbf{J}(\mathbf{x}_0)^{\mathsf{T}} \cdot \mathbf{J}(\mathbf{x}_0))^{-1})_{\operatorname{ind}(J),\operatorname{ind}(J)}}} \propto \frac{1}{\sigma_J}$$
(4.14)

is inversely proportional to the uncertainty of the J-coupling constant, and will be referred to as the *J-score* in this thesis.

⁴ Ludwig Otto Hesse (1811–1874) was a German mathematician known for his contributions to algebraic geometry and his work on invariant theory.

⁵ Carl Gustav Jacob Jacobi (1804–1851) was a significant German mathematician celebrated for his groundbreaking work in elliptic functions, number theory, and mathematical physics.

Example: Single Resonance

To get some intuition about the scaling of the uncertainties, only a single Lorentzian resonance is considered. It is also assumed that the model's only unknown parameter is a single J-coupling constant (i.e. $\mathbf{x} = (J)^{\mathsf{T}}$ and $\mathrm{ind}(J) = 1$). In this case, the model spectrum is given by

Here, where x has only one element it is simply equal to 1.

$$\mathbf{s}: \mathbb{R} \to \mathbb{R}^m: J \mapsto \mathbf{s}(J) = \mathcal{L}(\mathbf{f}, a, \nu(J), \Gamma)$$
 (4.15)

The estimated standard deviation of *J*

$$\sqrt{\sigma_J} = \sqrt{\hat{K}_{\operatorname{ind}(J),\operatorname{ind}(J)}} \propto \sqrt{((\mathbf{J}(\mathbf{x}_0)^\intercal \cdot \mathbf{J}(\mathbf{x}_0))^{-1})_{\operatorname{ind}(J),\operatorname{ind}(J)}} \quad (4.16)$$

may be estimated using the model's JACOBIAN

$$J = \frac{d\mathbf{f}}{\partial J} = \frac{\partial \mathbf{s}}{\partial J}$$

$$= \frac{\partial}{\partial J} \mathcal{L}(\mathbf{f}, a, \nu(J), \Gamma)$$

$$= \frac{\partial \nu}{\partial J} \frac{\partial}{\partial \nu} \mathcal{L}(\mathbf{f}, a, \nu(J), \Gamma)$$
(4.17)

with the above definition of the J-response and the derivative of the LORENTZIAN

$$\frac{\partial}{\partial \nu} \mathcal{L}(f, a, \nu, \Gamma) = \frac{-16\pi^2 a \Gamma(f - \nu)}{(\Gamma^2 + 4\pi^2 (f - \nu)^2)^2} . \tag{4.18}$$

The standard deviation of *J*

$$\sqrt{\sigma_{J}} \propto \left(\sum_{i=1}^{m} \left(\frac{\partial \nu}{\partial J}\right)^{2} \left(\frac{\partial}{\partial \nu} \mathcal{L}(f_{i}, a, \nu, \Gamma)\right)^{2}\right)^{-\frac{1}{2}}$$

$$= \frac{\partial \nu}{\partial J} \left(\sum_{i=1}^{m} \left(\frac{\partial}{\partial \nu} \mathcal{L}(f_{i}, a, \nu, \Gamma)\right)^{2}\right)^{-\frac{1}{2}}$$
(4.19)

can be explicitly calculated. For small sample spacing $\Delta f = f_{i+1} - f_i$ the sum

$$\sum_{i=1}^{m} \left(\frac{\partial}{\partial \nu} \mathcal{L}(f_i, a, \nu, \Gamma) \right)^2 \approx \Delta f \int_{-\infty}^{\infty} \left(\frac{\partial}{\partial \nu} \mathcal{L}(f_i, a, \nu, \Gamma) \right)^2 = \Delta_f \frac{2\pi^2 a^2}{\Gamma^3}$$
(4.20)

may be replaced by an integral. In this case, the uncertainty of J is given by

$$\sqrt{\sigma_J} \propto \left(\frac{\partial \nu}{\partial J}\right)^{-1} \frac{\Gamma^{3/2}}{a} .$$
(4.21)

As can be seen, for a single resonance the uncertainty

$$\sqrt{\sigma_I} \propto \left(\frac{\partial \nu}{\partial I}\right)^{-1}$$
 (4.22)

scales linearly with the inverse J-response and the amplitude

$$\sqrt{\sigma_J} \propto \frac{1}{a}$$
 (4.23)

The decay rate Γ which is proportional to the linewidth scales the uncertainty

$$\sqrt{\sigma_J} \propto \Gamma^{\frac{3}{2}}$$
 (4.24)

with the power of 3/2.

Example: Double Resonance

As discussed in Figure 4.1, one would intuitively assume that the estimation for *J* is lower for resonances that are separated by a spectral distance similar to their linewidth. Figure 4.3 investigates the J-score for a pair of identical resonances as a function of their spectral separation. Indeed, it shows that there is a minimum in the J-score when the spectral separation is similar to the linewidth.

In contrast, for perfectly overlapping resonances (i.e. zero separation), the scenario is identical to a single resonance with twice the amplitude. Since the J-score scales linearly with the amplitude, the combined J-score is larger by a factor of 2. For infinitely separated resonances, the J-score increases by a factor of $\sqrt{2}$ compared to a single resonance.

Example: Whole Spectrum

The same can be done for the whole spectrum that is given by a finite sum of LORENTZIANS. In this context, here the J-score (see Equation 4.14) provides a measure of how well the J-coupling constant can be estimated for a given spectrum and a set of unknown parameters $\mathbf{x} = (J x_2 \dots x_n)^{\mathsf{T}}$ Figure 4.4 shows the normalized J-score for the molecule CF₃CH₂OH.

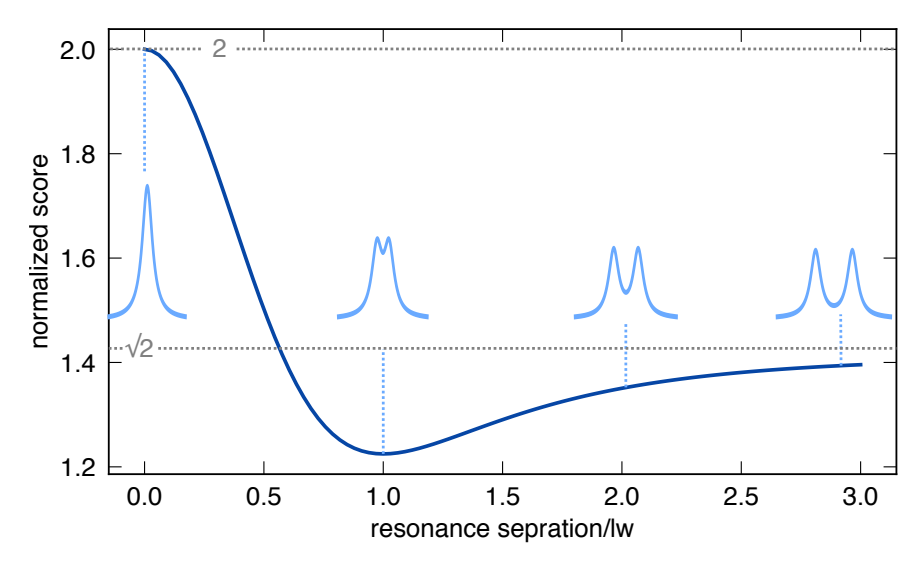


Figure 4.3: Normalized (to a single resonance) J-score function for a pair of identical resonances as a function of the center peak separation. For a perfect overlap, the J-score is twice as large whereas it is only bigger by a factor of $\sqrt{2}$ for the case of infinite separation. In between there is a minimum when the separation is similar to the linewidth.

4.3 EXPERIMENTAL RESULTS

The spectra presented in this chapter were obtained using the OPM system described in Chapter 2. The samples were externally polarized using a 1T to 2T HALBACH⁶ magnet (as detailed in Section E.3) and then hydraulically shuttled to a zero-field condition. Approximately 32 scans were recorded for each field point. In contrast to the simulations, the ¹H spins were not inverted before the acquisition process.

Figure 4.5 presents example spectra obtained at three distinct field points. The black curve represents the measured spectrum, with the grey line depicting the best fit. Vertical blue lines indicate the center frequency of the fitted resonances, while the width represents the fitting uncertainty. As anticipated by the simulations, the region spanning a few hundred hertz (as seen in Figure 4.5b) appears to be the most promising due to the presence of numerous non-overlapping

⁶ Klaus Halbach (1925–2000) was a German–American physicist known for his pioneering work in magnetic field engineering and the development of the "Halbach array," a unique arrangement of magnets with applications in various scientific and engineering fields.

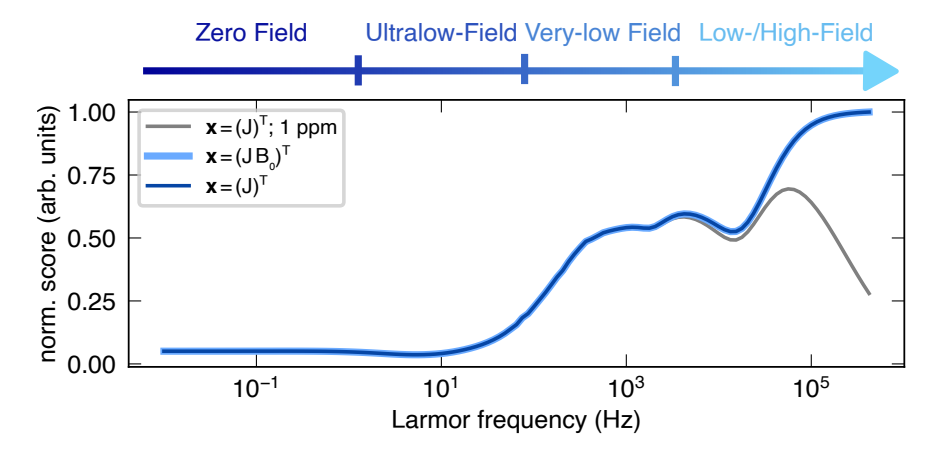


Figure 4.4: Field dependent J-score as a function of the ¹H Larmor frequency for CF_3CH_2OH with an assumed linewidth of $100 \, \text{mHz}$. There is almost no difference between the dark blue $(\mathbf{x} = (J)^\intercal)$ and light blue $(\mathbf{x} = (JB_0)^\intercal)$ due to the similar gyromagnetic ratios. In other words, knowing the magnetic field with perfect accuracy and precision does not improve the uncertainty in the J-estimation. Without gradient broadening (and assuming constant sensitivity, polarization, and perfect Lorentzian line shapes), as long as the estimation is limited by the SNR, the lowest uncertainty is at high field. However, this optimum shifts to lower fields as soon as gradient broadening is considered. Here, the grey curve simulates a field inhomogeneity of 1 ppm.

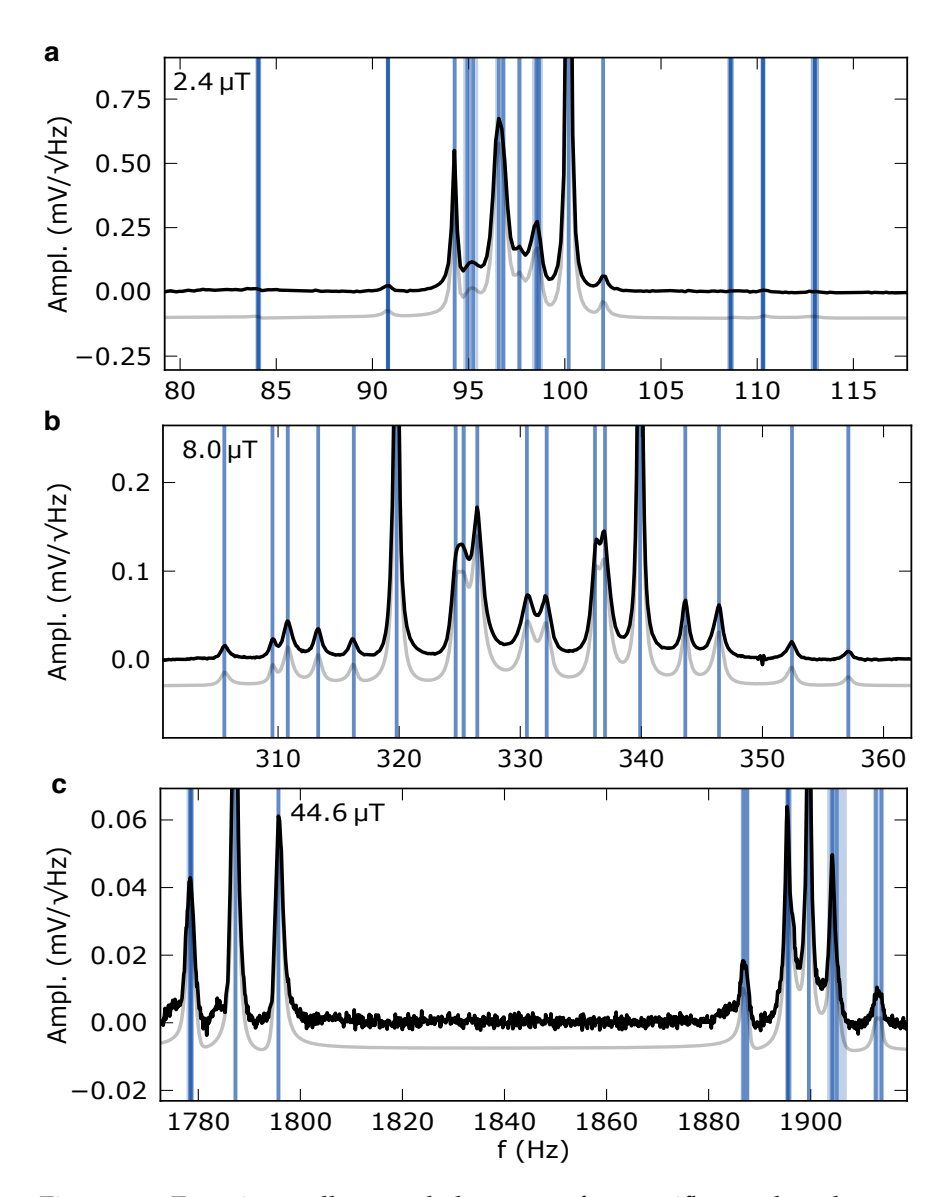


Figure 4.5: Experimentally recorded spectra of 2,2,2-trifluoroethanol, externally polarized at 1 T to 2 T and hydraulically shuttled to the ZULF regime. The black curve represents the FOURIER transformed, experimentally acquired time-domain data. The grey line represents the best-fitted spectrum. Blue vertical lines represent fitted resonances with the linewidth indicating their fitvariance. As expected from the previous theoretical discussion, the best results are expected from the transitions of the ULF to the VLF regime (b). At the transition to high-field (c) the spectral overlap of resonances drastically worsens the fit results. The same is true for lower fields (a) but due to the small transition moments.

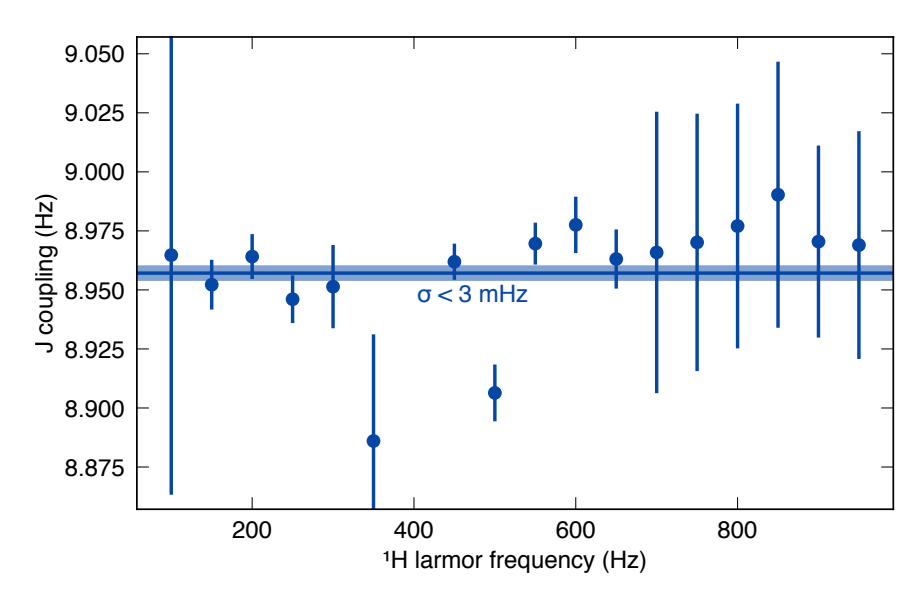


Figure 4.6: Results of the J-coupling estimation for different 1H Larmor frequencies. The lowest uncertainties can be found in the transition from the ULF to the VLF regime (150 Hz to 700 Hz). Above 700 Hz the spectral overlap during the transition to high fields leads to drastically increased fit uncertainties. In contrast, at lower fields, the small transition moment of the resonance with high J-response also leads to large uncertainties. In addition to the individual fits, all spectra can also be fitted simultaneously in one single least-squares optimization loop. The result is shown in the form of a blue vertical line with the width indicating the uncertainty. The result is estimated to be $J_{\rm HF} = 8.957(3)$ Hz.

resonances with substantial amplitudes. In contrast, the lowest magnetic field (Figure 4.5a) features well-separated resonances at the spectrum's edge; however, as predicted, their low amplitude results in poor SNR, translating to high fit uncertainties. At high magnetic fields (Figure 4.5c), the resonances become broader and overlap, contributing to increased uncertainty. Additionally, the sensitivity of the OPM is inferior in comparison to the optimal region.

The spectra are fitted using the DFTTOOLS PYTHON package (see Appendix F with Figure 4.6 showing the fit results. As predicted by the J-score discussion in the previous section, the lowest uncertainties can be found in the VLF regime, which benefits from higher resonance amplitudes but still features high J-responses. As soon as the resonances start to overlap during the transition to the high-field regime, the uncertainties drastically increase. At low fields, the uncertainties are huge due to the low transition amplitudes of the relevant



Figure 4.7: Which magnetic field gives the spectra with the lowest uncertainty for J-estimations? It depends. However, ZULF NMR may be the best option for systems that feature narrower lines at low fields. If, in addition, the zero-field resonance has a low transition moment, the optimal choice might be ULF/VLF NMR.

transitions due to the unfavorable similarity of gyromagnetic rations of ¹⁹F and ¹H.

In addition to individual fits for each magnetic field, all spectra can also be fitted simultaneously using the DFTToOLS package. Figure 4.6 shows the result of that fit, estimating the J-coupling constant $J_{\rm HF} = 8.957(3)$ Hz with an estimated fit-uncertainty of only 3 mHz. However, further experiments have to verify the accuracy of that fit and uncertainty estimation. As can be seen from the figure, there is a huge variation, with some data being separated from the global fit by several sigma. However, the experimental data confirms the results of the theoretical analysis at the beginning of this chapter defining possible scenarios for ULF/VLF spectroscopy as an addition to their zero- and high-field counterparts.

One argument for measuring spectra at different fields rather than a single one is the fact that this allows reducing the effect of technical noise peaks, which are very common in the ELF, SLF, ULF part of the magnetic noise spectrum. Due to the huge number of resonances, it can barely be avoided to have at least one resonance near a technical noise peak, which increases the uncertainty of the fit. However, by measuring at different fields this overlap will most likely affect different resonances every time, increasing the chance of having good estimates for every resonance at least one field.

4.4 SUMMARY

What is the best field to obtain the most accurate estimates for the J-coupling constant? Unsurprisingly, the answer is "it depends'.' An attempt to address this question is outlined in Figure 4.7. For zero-field, ULF, and VLF, the spectra rapidly become very complex as soon as the number of involved spins increases. For this reason, the

technique described here and zero-field NMR only work well with reasonably small molecules. If large molecules are involved, high-field NMR is most likely the best technique for estimating J-coupling constants.

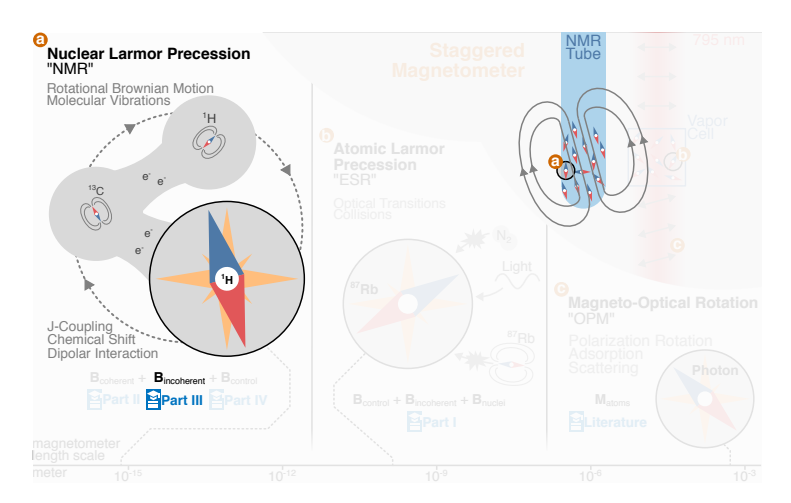
The superiority of high-field can be observed by examining how the uncertainty or the J-score scales with different parameters. High-field offers higher transition moments, leading to higher peak amplitudes that scale linearly with the J-score. Additionally, the number of resonances is lower due to many resonances perfectly overlapping. As seen from the previous discussion, n identical, perfectly overlapping resonances scale the J-score by n due to the n times increased amplitude. In contrast, n perfectly separated resonances only scale the J-score with only \sqrt{n} .

These are two compelling arguments in favor of high-field NMR spectroscopy, arguments that typically cannot be compensated solely by the higher J-response. The primary advantage of lower magnetic fields may be the narrower line widths Γ that scale the J-score by $\Gamma^{-3/2}$. If the line width remains more or less the same, high-field may be the best field to perform precise J-spectroscopy.

However, for systems exhibiting narrower resonance lines at zero ultralow field (ZULF), either due to long-lived coherence (as discussed in Chapter 5), effects originating from molecular dynamics (as detailed in Chapter 6), or simply due to inhomogeneous broadening, both zero-field and very low-field (ULF) and very low-field (VLF) NMR may offer superior means of estimating the J-coupling constant. This is particularly true for spin systems with an extremely low transition moment at zero-field, such as the ¹H-¹⁹F systems used as an example in this chapter. In such cases, ULF/VLF NMR techniques may indeed prove to be the most effective approach.

Part III

NUCLEAR RELAXATION DISPERSION



NMRD is a technique used to investigate field-dependent relaxation rates in NMR. The line widths of the NMR resonances discussed in this thesis so far have mostly not shown any field dependence beyond potential gradient broadening. This can be partially explained by exclusively operating within the extreme narrowing limit $\omega \tau_{\rm c} \ll 1$. For coupled spins, operating exclusively in either the weak or strong coupling regime or having many relaxation pathways may also prevent the detection of potential field-dependent coherence times (see Chapter 4).

In the next two chapters, spin systems will be studied at ultralow fields that do not satisfy the above criteria and, therefore, may exhibit field-dependent relaxation rates. While in Chapter 5, the field dependence arises due to long-lived coherences appearing in the strong-coupling regime, the systems in Chapter 6 deviate from the requirements of the extreme narrowing regime by featuring extremely slow molecular surface dynamics.

These chapters follow closely the two publications Bodenstedt et al. [27] and Chuchkova et al. [99].

In the previous chapter, the resonance linewidth was assumed to be constant which aligned well with the experimental data and simplified the numerical simulations and data analysis. However, this is not a good assumption for all scenarios. Magnetic field gradients can broaden resonance lines, increasing the line width at higher fields. Spectral overlap, i.e. resonances being too close to be resolved, appear to broaden resonances as well.

Furthermore, it is important to note that the natural linewidth of various resonances can vary and may exhibit a strong dependence on the magnetic field. This field-dependent behavior may stem from alterations in the system's eigenbasis leading to coherences and populations, which are more or less susceptible to relaxation mechanisms. Alternatively, the field dependence may arise from probing distinct spectral regions within the correlation function. While the latter subject will be extensively examined in the forthcoming chapter (see Chapter 6), this chapter exclusively concentrates on the field-dependent relaxation rates resulting from changes in the system's eigenbasis and their impact on the precision of J-coupling estimations.

To this end, the theory will first be discussed theoretically using a simple AX spin system, e.g. Formic Acid- 13 C. Subsequently, this insight will be extended to an A_3X spin system and compared against experimental data concerning 13 C-Methanol.

formic acid-13C

5.1 QUANTUM MASTER EQUATIONS

The (LIOUVILLE)-von Neumann equation

$$\frac{\mathrm{d}\hat{\rho}}{\mathrm{d}t} = -\frac{\mathrm{i}}{\hbar} \left[\hat{H}, \hat{\rho} \right] \tag{5.1}$$

describes how the density operator $\hat{\rho}$ of a quantum mechanical system evolves in time under the coherent evolution of a Hamiltonian. In many scenarios, it provides a good description of quantum mechanical systems if the Hamiltonian is deterministic and the system is not coupled to the environment.

However, in reality, these assumptions are often not fulfilled: In solution, molecules experience rapid molecular motion and tumbling which leads to orientation-dependent interactions to be modulated in time. Whereas this often does not affect energy levels on average and therefore the resonance frequencies, it can lead to relaxation.

Systems that are coupled to the environment can be described by quantum master equations¹. One form of a quantum master equation is the LINDBLADIAN [100]

$$\frac{\mathrm{d}\hat{\rho}}{\mathrm{d}t} = -\frac{\mathrm{i}}{\hbar}[\hat{H},\hat{\rho}] + \sum_{n,m=1}^{N^2} h_{nm} \left(\hat{A}_n \rho \hat{A}_m^{\dagger} - \frac{1}{2} \left\{ \hat{A}_m^{\dagger} \hat{A}_n, \hat{\rho} \right\} \right) \tag{5.2}$$

with the density operator $\hat{\rho}$, the Hamiltonian \hat{H} , an arbitrary orthonormal basis of Hilbert-Schmidt² operators A_n and the coefficient matrix h_{ij} . This master equation is both trace-conserving and completely positive which ensures a reasonable meaning of the physical interpretation of the density operator. The Lindbladian is often used to describe phenomenological processes.

However, sometimes it is desired to derive the master equation from a more fundamental physics perspective to relate relaxation processes to its microscopic origin in combination with noise-power spectral densities. For this reason, in NMR, a different approach is often used based on the REDFIELD equation [101]

$$\frac{\mathrm{d}\hat{\rho}}{\mathrm{d}t} = -\frac{\mathrm{i}}{\hbar}[\hat{H},\hat{\rho}] - \int_{0}^{t} \overline{\hat{H}_{1}(t), [\mathrm{e}^{-\mathrm{i}\hat{H}\tau}\hat{H}_{1}(t-\tau)\mathrm{e}^{\mathrm{i}\hat{H}\tau},\hat{\rho} - \hat{\rho}_{0}]} \mathrm{d}\tau$$

$$= -\frac{\mathrm{i}}{\hbar}[\hat{H},\hat{\rho}(t)] - \hat{\hat{\Gamma}}(\hat{\rho} - \hat{\rho}_{0})$$
(5.3)

is actually an ensemble average of an ensemble.

 $\{\hat{A},\hat{B}\} = \hat{A}\hat{B} + \hat{B}\hat{A}$

anticommutator.

is the

with $\hat{H}_1(t)$ describing a stochastic Hamiltonian and $\bar{\cdot}$ the ensemble average³. $\hat{\Gamma}$ is called the *relaxation superoperator*.

Some approximations went into deriving the Redfield equation. One of them requires that the correlation times τ are much shorter

- 1 It is called a master equation in analogy to a classical master equation that describes the time evolution of a system, that is always in a probabilistic combination of states with a transition matrix defining the transition rates between these states. Compare also to Equation 1.6.
- 2 Erhard Schmidt (1876–1959) was a German mathematician known for his pioneering work in the field of functional analysis, including the development of the Schmidt decomposition and his contributions to the theory of integral equations and orthogonal polynomials.
- 3 Note that in NMR the equilibrium density operator $\hat{\rho}_0$ is introduced ad hoc. This is done purely phenomenologically and is not a result of the derivation of the Redfield equation.

compared to the relaxation times⁴ T_2 . This so-called Markovian⁵ approximation⁶ is usually fulfilled for NMR but often not fulfilled for EPR experiments [101, 102].

By defining a spherical basis $\{\hat{T}_{l,m}^{(\mu)}\}$ for the Hilbert space, the stochastic Hamiltonian

$$\hat{H}_1 = \sum_{u,l,m} (-1)^m A_{l,-m}^{(\mu)} \hat{T}_{l,m}^{(\mu)}$$
(5.4)

can be expressed in this alternative basis, where $A_{l,-m}^{(\mu)}$ describe the components of \hat{H}_1 with respect to the spherical basis operator $\hat{T}_{l,m}^{(\mu)}$. It can be shown [101] that the relaxation superoperator $\hat{\Gamma}$ from Equation 5.3 can be transformed into a form

$$\hat{\hat{\Gamma}}(\cdot) = \sum_{\substack{\mu,\mu'\\l,l'\\m,m'}} (-1)^{m+m'} \int_0^t \left[\hat{T}_{l,m}^{(\mu)}, \left[e^{-i\hat{H}\tau} \left(\hat{T}_{l',m'}^{(\mu')} \right)^{\dagger} e^{i\hat{H}\tau}, \cdot \right] \right] C_{l,l',-m,-m'}^{\mu,\mu'} d\tau$$
(5.5)

where the time-correlation functions

$$C_{l,l',m,m'}^{\mu,\mu'} = \overline{A_{l,m}^{\mu} \left(A_{l',m'}^{(\mu')} \right)^* (t-\tau)}$$
(5.6)

were introduced.

The eigenbasis $\{\hat{V}_n\}$ of the commutator $[\hat{H},\cdot]$, i.e. $[\hat{H},\hat{V}_n]=\omega_n\hat{V}_n$ is another basis of the Hilbert space. The spherical basis operators can be expanded

$$\hat{T}_{l,m}^{(\mu)} = \sum_{n} v_{l,m,n}^{(\mu)} \hat{V}_n \stackrel{\text{def}}{=} \sum_{m=(n,l,m)} \hat{V}_m^{(\mu)}$$
(5.7)

in the new basis.

- 4 This circular reasoning might cause some problems if there is no prior knowledge about the system since the relaxation time must be known (at least the order of magnitude) to be able to evaluate if the REDFIELD approach can be used to calculate it.
- 5 Andrey Markov (1856–1922) was a Russian mathematician known for his pioneering work in probability theory and stochastic processes, particularly his development of the concept of Markov chains, which have applications in various fields including physics, computer science, and economics.
- 6 Also known as the REDFIELD limit, weak collision limit, or short-memory batch. It means that the random fluctuations happen on a much shorter time scale than the relaxation itself.

With these definitions, it can be shown [101] that Equation 5.5 can be transformed into a form

$$\hat{\hat{\Gamma}}(\cdot) = \frac{1}{2} \sum_{\mu,\mu'l,m,n} J_{l,l,-m,-m}^{\mu,\mu'}(\omega_n) \left[\hat{T}_{l,m}^{(\mu)}, \left[\left(\hat{V}_n^{(\mu')} \right)^{\dagger}, \cdot \right] \right]$$
 (5.8)

containing spectral-density functions

$$J_{l,l,m,m'}^{\mu,\mu'}(\omega) = 2 \int_0^\infty C_{l,l',m,m'}^{\mu,\mu'}(\tau) e^{i\omega\tau} . \tag{5.9}$$

Information about the molecular dynamics of a spin system is encoded in these spectral-density functions. Modifying the system Hamiltonian \hat{H} , changes the eigenbasis $\{\hat{V}_n\}$ as well as the eigenvalues ω_n . This allows probing the spectral density function by modifying the system's Hamiltonian, e.g. by changing the externally applied magnetic field. In practice, the explicit form of the relaxation superoperator $\hat{\Gamma}$ depends on the spin systems and their microscopic dynamics. In Section 5.4 an explicit expression will be given for dipolar relaxation in the extreme narrowing limit.

5.2 LIOUVILLE BRACKET

If $\dim_{\mathcal{H}}$ is the dimension of a system's Hilbert space, the matrix of a superoperator (e.g. $\hat{\Gamma}$) has $\dim_{\mathcal{H}}^4$ elements. This scaling quickly becomes analytically unmanageable as soon as the number of magnetically active nuclei is increased. However, often this matrix is sparse, leading to only a small fraction of the matrix elements being non-zero.

Assuming $\{\hat{A}_i\}$ being an orthonormal operator basis of the Liou-VILLE space, a single matrix element of a superoperator \hat{B} in this basis can be calculated using a so called Liouville bracket

$$\hat{B}_{ij} = \langle \hat{A}_i | \hat{B} | \hat{A}_j \rangle_{\mathcal{L}} , \qquad (5.10)$$

where $\langle \hat{A} | \hat{B} \rangle_{\mathcal{L}} = \operatorname{Tr} \hat{A}^{\dagger} \hat{B}$ is the Frobenius/Hilbert-Schmidt inner product (see Equation A.21). Assuming $\{|i\rangle\}$ is an orthonormal basis of the Hilbert space, $\{|ij\rangle_{\mathcal{L}} = |i\rangle\langle j|\}$ is often a suitable basis for the Liouville space.

In this basis, the density operator has the form

$$\hat{\rho}(t) = \sum_{ij} a_{ij}(t) |i\rangle \langle j| = \sum_{ij} a_{ij}(t) |ij\rangle_{\mathcal{L}} . \qquad (5.11)$$

If all cross-correlated terms are zero, i.e. the $\hat{\Gamma}$ is diagonal ($\hat{\Gamma}_{i\neq j}=0$) if expressed in this basis, the Liouville bracket

$$\langle ii|\,\hat{\hat{\Gamma}}\,|ii\rangle_{\mathcal{L}} \equiv 1/T_1$$
 (5.12)

describes the T_1 relaxation rate of the population of state $|i\rangle$, in other words the term

$$a_{ii}(t) = a_{ii}(0) \left(1 - e^{-t/T_1}\right) + a_{ii}(\infty)$$
 (5.13)

will exponentially decay withe rate $1/T_1$ towards its equilibrium value $a_{ii}(\infty)$.

Analogously, terms of the form $a_{ij}(t)|i\rangle\langle j|$ describe coherences. The corresponding Liouville bracket

$$\langle ij|\,\hat{\hat{\Gamma}}\,|ij\rangle_{\mathcal{L}} \equiv 1/T_2$$
 (5.14)

describes T_2 relaxation and the term

$$a_{ij}(t) = a_{ij}(0) \left(1 - e^{-t/T_2}\right) + a_{ij}(\infty)$$
 (5.15)

will decay exponentially towards its equilibrium value.

However, this is only true if the superoperator $\hat{\Gamma}$ is diagonal in this basis. Applying the secular approximation, which is discussed in the next section, is often a huge step towards this goal, bringing the relaxation operator at least in a block-diagonal form. From there, the density matrix equation (see Equation 5.3) can be interpreted as a system of linear differential equations (LDEs)7.

For solving this equation, the matrix of the superoperator can be diagonalized. Completely analogous to the OPM simulations/calculations discussed in Chapter 1 and Appendix C, the imaginary part of the eigenvalues can be interpreted as the resonance frequency whereas the real part describes relaxation.

5.3 SECULAR APPROXIMATION

Similar to other secular approximations, when applied to the relaxation superoperator, it allows for the neglect of certain matrix

⁷ Because the equation described here is completely linear in $\hat{\rho}$ makes solving this system of LDEs a much easier task compared to the OPM DME (see Equation 1.7), if the challenges of the potential enormous dimension is ignored.

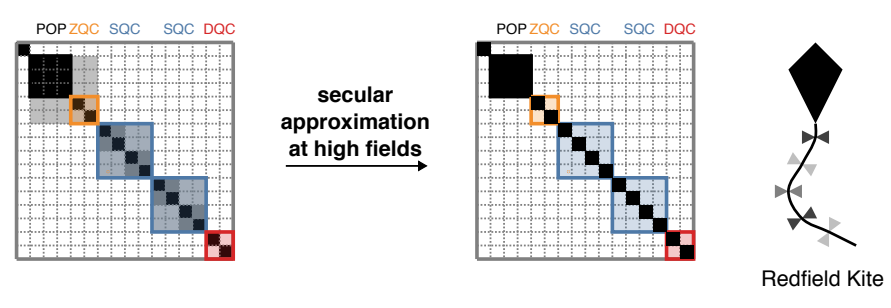


Figure 5.1: Sketch of the effect of the secular approximation to the relaxation superoperator at high field (inspired by [101, 102]). Neglecting secular terms leads to the characteristic block-diagonal shape which inspired the nickname *Redfield kite*. The terms are ordered by populations (POP), zero-quantum coherences (ZQC), single-quantum coherences (SQC) and double-quantum coherences (DQC).

elements that do not affect the outcome of the simulation or calculation on long time scales. A derivation and justification can be found in Section A.9.

The eigenstates $|i\rangle$ of the coherent Hamiltonian \hat{H} , i.e., \hat{H} $|i\rangle = E_i |i\rangle$ with eigenenergies E_i , form a basis of the system's Hilbert space. These states can be used to construct a basis $|i\rangle \langle j| \stackrel{\text{def}}{=} |ij\rangle \mathcal{L}$ of the corresponding Liouville space by forming all possible products between these basis states $|i\rangle$ and the corresponding dual basis $\langle j|$. Each of these basis operators, $|i\rangle \langle j| = |ij\rangle_{\mathcal{L}}$, can be assigned an oscillating frequency $\omega_{ij} = (E_j - E_i)/\hbar$, where \hbar represents the reduced Planck constant. According to the criteria of the secular approximation (see Section A.9), a matrix element $\hat{\Gamma}_{ij}$ can be neglected if the condition

$$|\hat{\hat{\Gamma}}_{ij}| \ll |\omega_i - \omega_j| \tag{5.16}$$

is met.

At high field, this approximation may apply to many elements due to the broad spread of resonance frequencies due to different gyromagnetic ratios, chemical shift differences, and resonance split to due to the J-coupling constant. For example, even in 40 MHz (1T) NMR spectrometer the resonance of ¹H and ¹³C are separated by 30 MHz which is several orders of magnitude above typically expected relaxation rate. Cross-relaxation terms between these two types of resonances are damped and can be neglected.

The typical block-diagonal form of the relaxation superoperator (see Figure 5.1), which is a consequence of the application of secu-

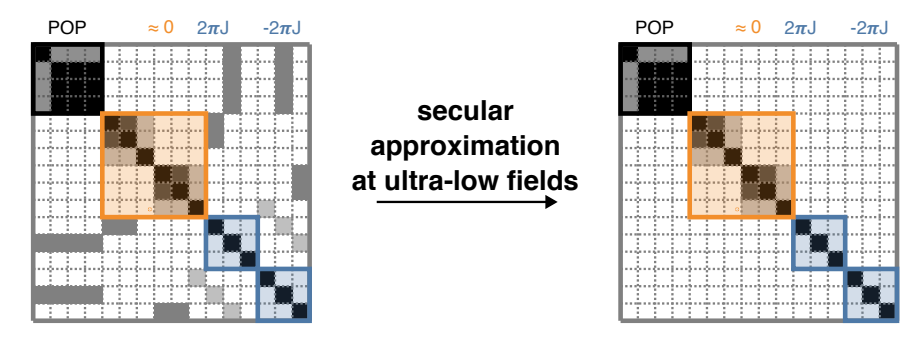


Figure 5.2: Sketch of the effect of secular approximations for an AX spin system close to zero-field. Applying the secular approximation will lead to fewer terms being neglected compared to the high-field scenario due to many oscillation frequencies being of similar value (\approx 0). Terms labeled with POP represent populations.

lar approximations results in the matrix being given the nickname *Redfield kite*, due to large block at the top left describing populations and the diagonal terms describing well-separated, non-degenerate resonances.

The secular approximation may also be applied at ZULF conditions. However, due to the much lower resonance frequencies, the reduced absolute difference in LARMOR frequencies of different spin species, and the insignificance of chemical shifts, the chance of the distance of oscillations frequencies of operators being comparable to the relaxation term is significantly increased. Relaxation superoperators may therefore contain more relevant terms (see Figure 5.2), allowing more relaxation pathways and may be more difficult to analyze. This is true zero-field, but even more at ULF/VLF, especially for molecules with numerous magnetically active, coupled spins.

Nevertheless, as the molecules discussed in this chapter are all sufficiently small and possess reasonably high J-couplings, the resonances become well-separated for most parameters, allowing for the application of the secular approximation. In combination with the nature of dipolar relaxation, which stands as one of the dominant relaxation mechanisms for liquid samples (as discussed in the next section), this results in nearly diagonal matrices. These matrices facilitate the extraction of relaxation rates using the LIOUVILLE bracket. However, for more complex molecules in future studies, such a luxury may not be provided. Given the unfavorable scaling of the superoperator space's dimension, brute-force diagonalization

For populations it is $\omega_i = 0 \Rightarrow \Delta \omega = 0$ and therefore the criteria of the secular approximation are never fulfilled

might prove prohibitively expensive, necessitating the development of new approaches.

5.4 DIPOLAR RELAXATION

Dipolar relaxation is one of the most effective relaxation mechanisms for liquid samples with more than one magnetically active nucleus. If two or more nuclear spins $\hat{\mathbf{I}}_j$ and $\hat{\mathbf{I}}_j$ are present within the same molecule, their two magnetic dipoles interact with each other

$$\hat{H}_{\text{dipole}} = -\frac{\gamma_1 \gamma_2 \hbar^2}{\left|\mathbf{r}_{jk}\right|^3} \frac{\mu_0}{4\pi} \left(\frac{3}{\left|\mathbf{r}_{(jk)}\right|^2} (\hat{\mathbf{I}}_j \cdot \mathbf{r}_{(jk)}) (\hat{\mathbf{I}}_k \cdot \mathbf{r}_{jk}) - \hat{\mathbf{I}}_j \cdot \hat{\mathbf{I}}_k \right) \tag{5.17}$$

depending on their relative orientation in space \mathbf{r}_{jk} . For molecules within a liquid solution, the relative orientation is modulated by Brownian motion. For small molecules, the incoherent variation of the dipolar interaction is the main contributor to relaxation at room temperature.

The spectral density function $J(\omega)$ introduced above contains the statistical information about this random Brownian motion and depends on the frequencies ω and the correlation times τ_c . If $\omega \tau_c \ll 1$ the spectral density function can be assumed to be constant $J(\omega) = J(0)$. This situation is called the *extreme narrowing* or fast motion limit. It is usually valid in the ZULF regime unless systems with extremely slow dynamics (see Chapter 6) are investigated.

If this assumption is valid, the relaxation superoperator for dipolar coupling of two spins has the simple form of [38]

$$\hat{\hat{\Gamma}}_{DD}(\cdot) = -\frac{6}{5}b_{jk}^2 \tau_c \sum_{q=-2}^{2} (-1)^q [\hat{T}_{2,-q'}^{jk} [\hat{T}_{2,q'}^{jk} \cdot]]$$
 (5.18)

with

$$b_{jk} = -\frac{\mu_0}{4\pi} \frac{\gamma_j \gamma_k \hbar}{\left|\mathbf{r}_{jk}\right|^3} \tag{5.19}$$

depending only on the (assumed to be constant) distance $|\mathbf{r}_{jk}|$ of the two spins. The spherical operators are defined as

$$\hat{T}_{2,-2}^{(jk)} = \frac{\hat{I}_{-}^{(j)} \hat{I}_{-}^{(k)}}{2\hbar^2}$$
 (5.20a)

$$\hat{T}_{2,-1}^{(jk)} = \frac{\hat{I}_{-}^{(j)} \hat{I}_{z}^{(k)} + \hat{I}_{z}^{(j)} \hat{I}_{-}^{(k)}}{2\hbar^{2}}$$
(5.20b)

$$\hat{T}_{2,\pm 0}^{(jk)} = \frac{4\hat{I}_z^{(j)}\hat{I}_z^{(k)} - \hat{I}_-^{(j)}\hat{I}_+^{(k)} - \hat{I}_+^{(j)}\hat{I}_-^{(k)}}{2\hbar^2\sqrt{6}}$$
(5.20c)

$$\hat{T}_{2,+1}^{(jk)} = -\frac{\hat{I}_{+}^{(j)}\hat{I}_{z}^{(k)} + \hat{I}_{z}^{(j)}\hat{I}_{+}^{(k)}}{2\hbar^{2}}$$
(5.20d)

$$\hat{T}_{2,+2}^{(jk)} = \frac{\hat{I}_{+}^{(j)} \hat{I}_{+}^{(k)}}{2\hbar^2} \ . \tag{5.20e}$$

The more general form

$$\hat{\hat{\Gamma}}_{DD}(\cdot) = -\frac{6}{5}\tau_{c}\sum_{i\neq j}b_{jk}\sum_{m\neq n}b_{mn}\sum_{q=-2}^{2}(-1)^{q}[\hat{T}_{2,-q'}^{jk}[\hat{T}_{2,q'}^{mn},\cdot]]$$
(5.21)

can be used to describe spin systems with more than two spins. Terms with i, j = m, n lead to *auto-correlated relaxation* whereas terms with $i, j \neq m, n$ lead to *cross-correlated relaxation*⁸.

5.5 AX SPIN SYSTEMS — E.G. FORMIC ACID-13C

In contrast to high field, even a heteronuclear spin system of the form AX can have long-lived coherences. In this section, the basic theoretical description is discussed for ¹³C-formic acid. Since only two spins are involved, the relaxation superoperator has the simple form

$$\hat{\hat{\Gamma}}_{DD}(\cdot) = -\frac{6}{5}\tau_c b_{HC}^2 \sum_{q=-2}^2 (-1)^q [\hat{T}_{2,-q}^{(HC)}, [\hat{T}_{2,q}^{(HC)}, \cdot]] .$$
 (5.22)

The correlation time is assumed to be $\tau_{\rm c}\approx 10\times 10^{-12}\,{\rm s}$ and the coupling constant $b_{\rm HC}\approx -147\times 10^3\,{\rm s}^{-1}$ depends on the distant $|{\bf r}_{\rm HC}|\approx 109\times 10^{-12}\,{\rm m}$ and the gyromagnetic ratios $\gamma_{\rm H}\approx 42.6\times 10^6\,{\rm Hz/T}$ and $\gamma_{\rm C}\approx 10.7\times 10^6\,{\rm Hz/T}$.

⁸ Note to be confused with auto- and cross-relaxation that describe diagonal and off-diagonal terms in the relaxation superoperator if expressed as a matrix in the eigenbasis of $[\hat{H}, \cdot]$.

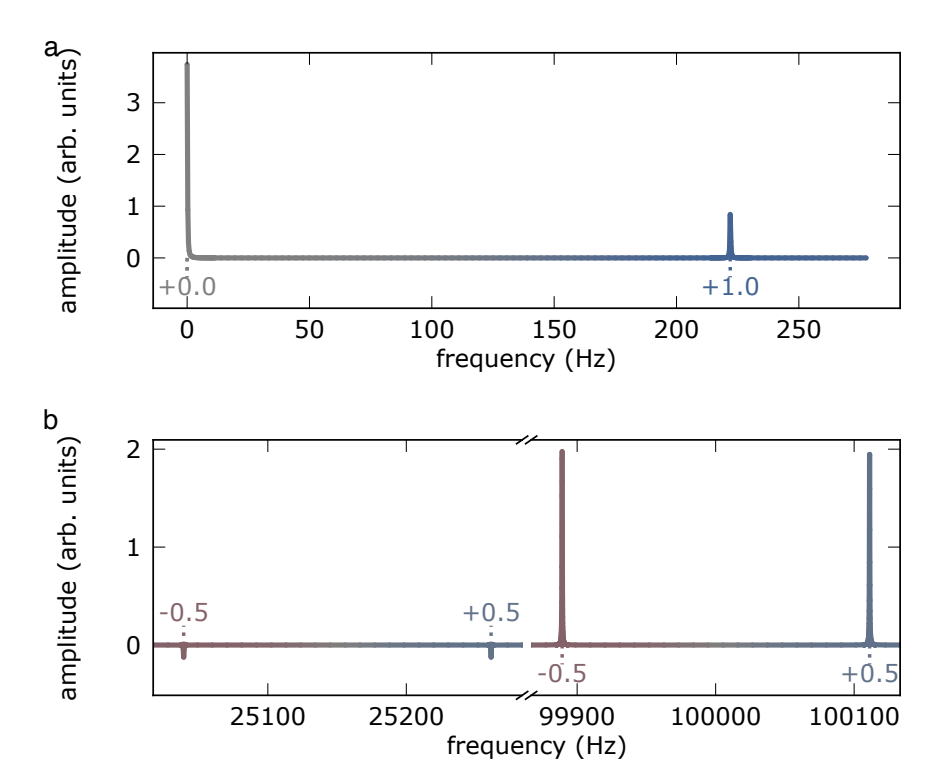


Figure 5.3: Simulated zero-field (a) and high-field (b) spectrum of an AX spin system such as formic acid-¹³C. As in the previous chapter, the colors indicate the sign of the J-response and the saturation indicates its magnitude.

The Hilbert space for two 1/2-spins has the dimension $4 = 2 \times 2$. The corresponding Liouville space (i.e. the space of operators on the Hilbert space) has therefore $16 = 4 \times 4$ dimensions. At zero field, the singlet-triplet states (see Equation 3.26b) are eigenstates of the zero-field Hamiltonian. If the signal is detected along the quantization axis (here z), the detectable signal (see Figure 5.3a) is proportional to matrix elements

$$|\hat{A}_{zf}\rangle_{\mathcal{L}} = |T_0\rangle\langle S_0| \quad . \tag{5.23}$$

The corresponding Liouville bracket

$$\hat{\hat{\Gamma}}_{zf} = \langle \hat{A}_{zf} | \hat{\hat{\Gamma}}_{DD} | \hat{A}_{zf} \rangle_{\mathcal{L}} = -\frac{1}{2} \tau_c b_{HC}^2$$
(5.24)

for this transition can be calculated.

In contrast, the ZEEMAN states form the eigenstates at high-field. The four detectable coherences (see Figure 5.3b) are of the form (see Equation 3.28a-3.28b)

$$|\hat{A}_{\mathrm{HF}}\rangle_{\mathcal{L}} = \begin{cases} |\downarrow\downarrow\rangle \langle\uparrow\downarrow| \\ |\downarrow\uparrow\rangle \langle\uparrow\uparrow| \\ |\downarrow\downarrow\rangle \langle\downarrow\uparrow| \\ |\uparrow\downarrow\rangle \langle\uparrow\uparrow| \end{cases} . \tag{5.25}$$

The corresponding LIOUVILLE

$$\hat{\hat{\Gamma}}_{HF} = \langle \hat{A}_{HF} | \hat{\hat{\Gamma}}_{DD} | \hat{A}_{HF} \rangle_{\mathcal{L}} = -\frac{17}{20} \tau_{c} b_{HC}^{2}$$
(5.26)

for this transition can be calculated. In other words, the relaxation rate at zero field is lower by a factor of 1.7 compared to high-field. The detectable signal at zero field lives significantly longer than at high field if the correlation time is assumed to be field-independent (extreme narrowing limit). Such a coherence can be called *long-lived coherence*.

In Figure 5.4a the value of the LIOUVILLE bracket for every resonance is plotted as a function of the applied magnetic field. In addition, the same analysis as in Chapter 4 is performed, showing the J-response in part Figure 5.4b, the amplitude in Figure 5.4c and finally the J-score in Figure 5.4d that now takes the linewidth into account. Surprisingly, both the J-response and the linewidth worsen

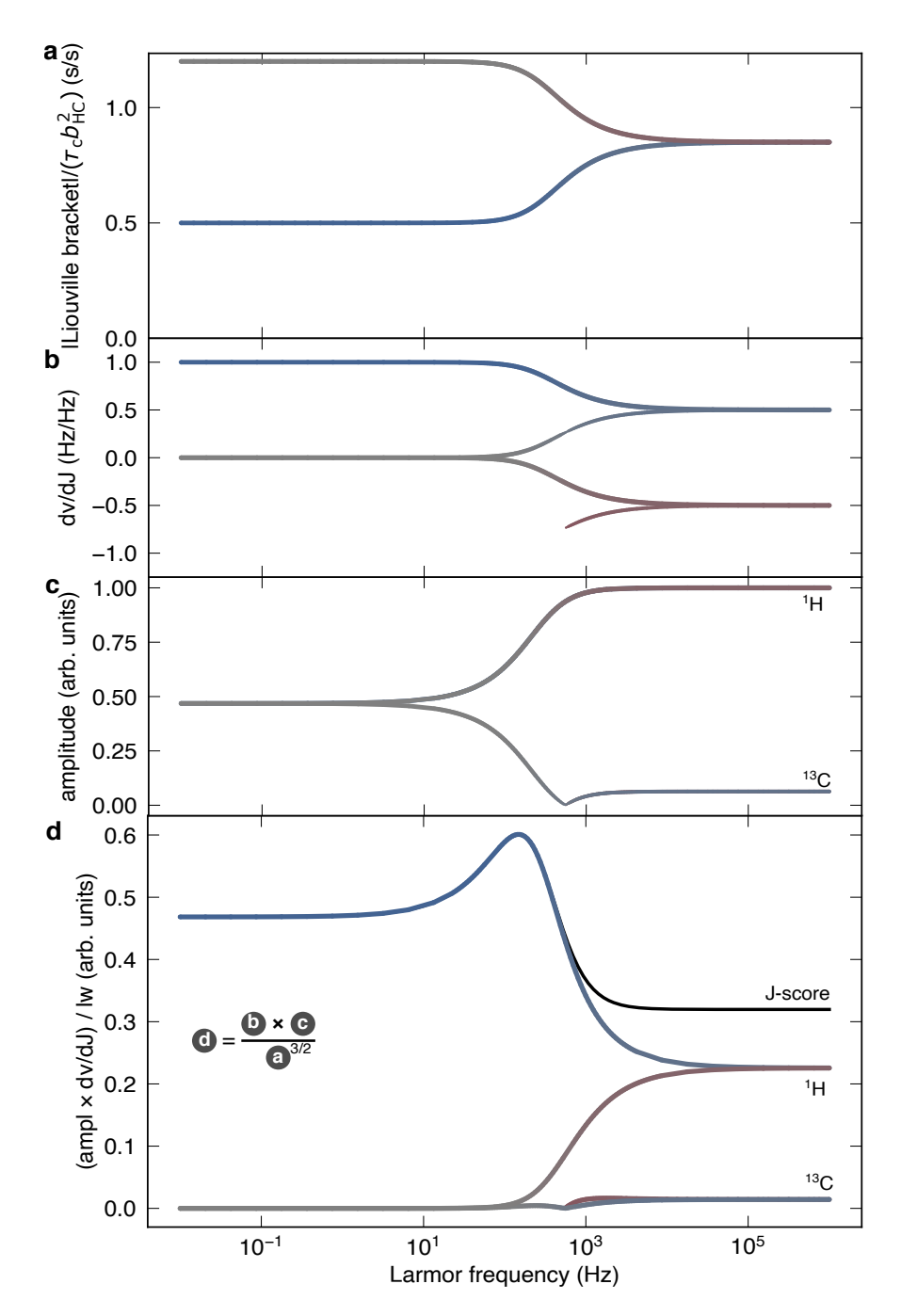


Figure 5.4: Simulated Liouville bracket (a), J-response (b), amplitude (c) and J-score (d) for the AX spin system formic acid- 13 C. The plateau of the Liouville bracket and the J-response extends to much higher fields compared to the amplitude, which leads to the optimal J-score being neither at zero- nor high-field but at the transition between ULF and VLF regime, if B_0 is known.

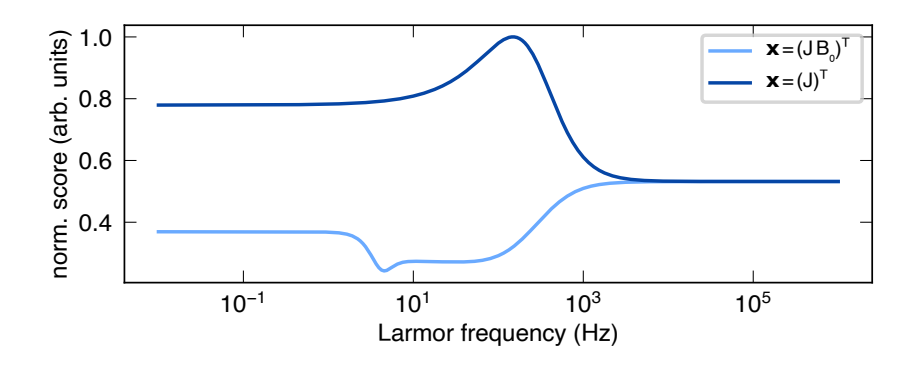


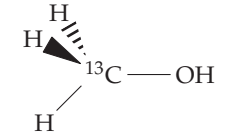
Figure 5.5: Field dependent J-score as a function of the ^1H Larmor frequency for $^{13}\text{CHOOH}$. In contrast to the example (CF₃CH₂OH) in the previous chapter, there is a significant difference depending on whether B_0 is a free fitting parameter at VLFs and below, which vanishes only at high fields. Assuming B_0 is known (e.g. by fitting the resonance of the ^1H nuclei of the carboxyl group), the highest J-score is reached in the VLF to low-field regime, even in the absence of inhomogeneous broadening.

much later than the amplitude, leading to an optimal J-score neither at zero- nor at high-field but at the transition between ULF and VLF.

However, this is only true in case the magnetic field is determined separately. Figure 5.5 shows the same J-score but compares it with the scenario of the magnetic field B_0 being an independent fit variable. In contrast to the previous chapter, due to the much larger difference in gyromagnetic ratio, the two variables are much more correlated and uncertainty in the magnetic field directly translates to a worse estimate in the J-coupling constant for field below the VLF regime.

5.6 A3X SPIN SYSTEM — E.G. METHANOL-13C

The existence of the long-lived coherences at zero-field was also experimentally confirmed by measuring the field-dependent spectrum of methanol- 13 C (see Figure 5.6 from Bodenstedt et al. [27]). The linewidth of resonance at $J=140.1\,\mathrm{Hz}$ appeared to be significantly narrower than the other, which is also predicted by the simulation. Figure 5.7 shows the field-dependent J-score for this molecule. It again performs better in the ULF to VLF regime.



methanol-13C

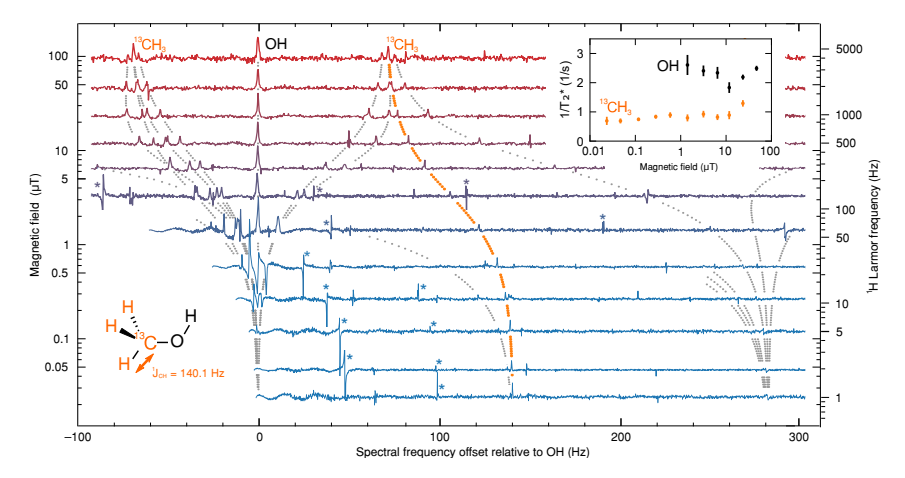


Figure 5.6: NMR spectra of ¹³CH₃OH versus field strength in the range 25 nT-100 T. Horizontal lines show NMR spectra, offset vertically by the field at which they were acquired (left scale), and horizontally to place the uncoupled OH resonance at zero. Individual resonances for the chemically distinct CH₃ and OH spin groups are clearly visible and demonstrate relative frequency shifts due to the transition between strong and weak heteronuclear coupling regimes corresponding to low and high field, respectively. The different peaks correspond to different spin combinations; in high field the peaks correspond to single-spin transitions of ${}^{1}H$, while at zero field peaks at ${}^{1}J_{CH} = 140.1 \,\mathrm{Hz}$ and $2 \times {}^{1}J_{CH} = 280.2 \, \text{Hz}$ correspond, respectively, to singlet-totriplet and triplet-to-quintet transitions of the ¹³CH₃. Features marked with an asterisk (*), e.g. $50 \, \text{nT}$ and $\approx 48 \, \text{Hz} + \approx 98 \, \text{Hz}$, are artefacts due to 50 Hz line noise and harmonics. The dotted curves show the predicted resonance frequencies as a result of the heteronuclear coupling. Inset shows transverse decay rate $1/T_{2,I}$ for the CH₃ signal peak (dotted orange curve) and OH signal peak (at 0 Hz) versus field strength. Error bars represent estimated standard deviation errors obtained from least-squares regression analysis.

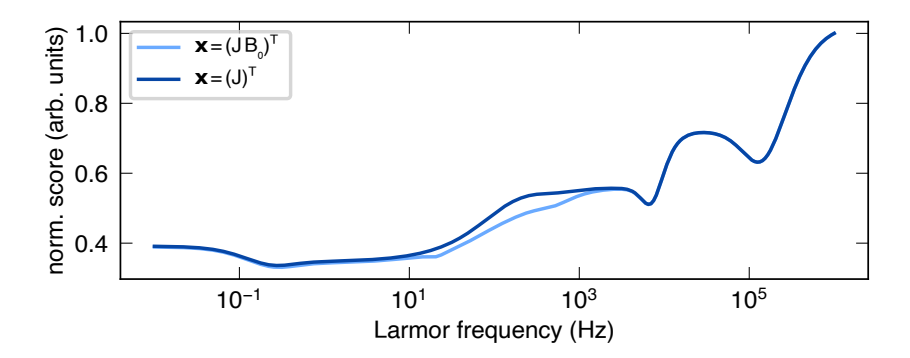


Figure 5.7: Field dependent J-score as a function of the ¹H LARMOR frequency for ¹³CH₃OH. In contrast to the previous example (CHOOH) and similar to CF₃CH₂OH, there is only a small difference depending on whether B₀ is a free fitting parameter at VLFs and below. Without inhomogeneous broadening, the highest J-score is reached in the high-field regime. However, this is another example where the ULF to VLF regime performs better than the zero-field regime.

NUCLEAR MAGNETIC RELAXATION DISPERSION

The last chapter (Chapter 5) described field-dependent relaxation rates due to long-lived coherences where the relaxation rates depended on the coupling regime. However, even for spin systems without scalar coupling, the relaxation rate can be highly dependent on the bias magnetic field strength. The random fluctuations of the spin Hamiltonian cause relaxation, but on short timescales, the fluctuations can be correlated. The ratio of the correlation time $\tau_{\rm c}$ and Larmor frequency determines the speed at which the fluctuations can relax the nuclear spin state.

The extreme narrowing limit was considered in the previous chapter, which describes the scenarios of correlation times $\tau_c \ll 2\pi/(|B|\,\gamma_{nucl})$ that are much shorter than a Larmor period, and it is often a valid assumption for ZULF conditions since molecular rotations or vibrations occur on much shorter timescales. However, nano-scale dynamic processes can occur on longer timescales ranging from milliseconds to microseconds, including protein folding, aqueous complexation, and surface adsorption phenomena. Under these conditions, the extreme narrowing approximation is not valid at ultralow field and relaxation rates can be highly dependent on the magnetic field. To gain insight into the molecular dynamics of the system, NMRD enables direct measurement of these field-dependent relaxation rates and extraction of correlation times of these slow processes.

This section summarizes the main result of Bodenstedt et al. [27] and Bodenstedt [103], where a new technique is introduced that extends the parameter space of NMR to extremely low frequencies combined with high relaxation rates. In this chapter only ¹H nuclear spins are considered. All relaxation rates are concerning the relaxation of ¹H.

6.1 INTRODUCTION TO FAST-FIELD-CYCLING NUCLEAR RELAX-ATION DISPERSION

NMRD is a method that uses the relaxation rates of nuclear spins, which are dependent on the magnetic field strength, to deduce cor-

relation times for molecular reorientation and diffusive transport. The information obtained from NMRD is not only of interest to fundamental science but can also have practical applications in fields such as industrial catalysis and petrology. In these fields, molecular diffusion can be restricted by surface geometry and adsorption, particularly in liquids that are confined within porous solids. Furthermore, NMRD can be useful in the medical field to design molecular agents for relaxation-contrast MRI. By combining spectroscopic dispersion using chemical shifts or spin-spin couplings, the dynamics can be linked to specific molecular functional groups, which makes it possible to analyze chemical mixtures and biological specimens.

To accurately measure correlation times τ_c of nuclear spin relaxation, a range of Larmor frequencies must be considered from $|B| \gamma_{nucl} \ll \tau_c$ to $\tau_c \ll |B| \gamma_{nucl}$, where |B| denotes the field strength and γ_{nucl} represents the nuclear gyromagnetic ratio. For extremely slow correlations, measurements must be conducted at ultralow magnetic fields, within shielded enclosures like a mu-metal chamber. The current NMRD technique mainly employs FFC electromagnets with a strength of around 1T for efficient inductive NMR signal detection. However, these electromagnets are used without shielding and require active cancellation of ambient fields to access the range below the geomagnetic field. Alternatively, samples can be transported between persistent high- and ultralow-field locations, but slow transport times limit the observable τ_c at the high end. Figure 6.1 depicts the limits of the existing NMRD techniques, with the orange- and green-shaded regions representing the current limitations.

6.2 BROWNIAN MOTION, RELAXATION AND CORRELATION

The scientific investigation of nuclear magnetic relaxation has been ongoing for almost as long as the development of NMR itself. While closely connected, the theory of relaxation can be significantly more complex. Numerous interactions between nuclear spins within a bulk liquid get averaged out when examined as an ensemble, which usually does not permit direct detection within the coherent nuclear spin evolution spectrum. Nonetheless, these interactions play a vital role in nuclear spin relaxation. The BPP theory, named after NICO-

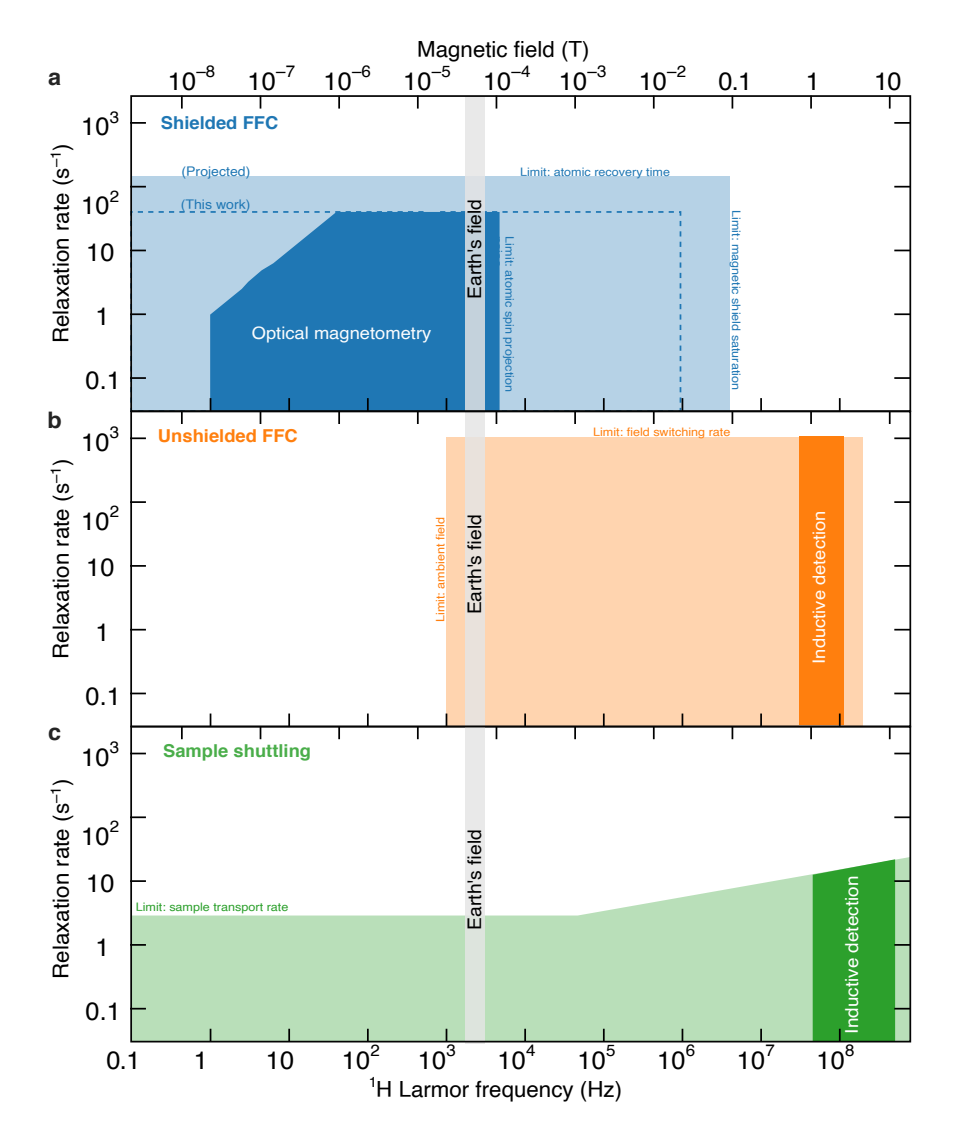


Figure 6.1: Overview of three different techniques to measure field-dependent relaxation rates. **a**, Boundaries of the faded colored zones in the horizontal dimension indicate upper limits of longitudinal nuclear relaxation rate, $T_{\mathrm{nucl},1}^{-1}$ imposed by signal receiver dead time and/or speed of field-switching events. Boundaries in the vertical dimension indicate limits to the range of magnetic fields achievable by electromagnetic sources. Dark colored zone indicates Larmor frequencies where NMR signals are detected and correspond to measurable transverse relaxation rates $T_{\mathrm{nucl},2}^{-1}$. The diagonal of slope 1 corresponds to the spectroscopic resolution limit where rates of Larmor precession and transverse relaxation are equal: $|\mathbf{B}| \gamma_{\mathrm{nucl}}/(2\pi) = T_{\mathrm{nucl},2} \approx T_{\mathrm{nucl},1}$.

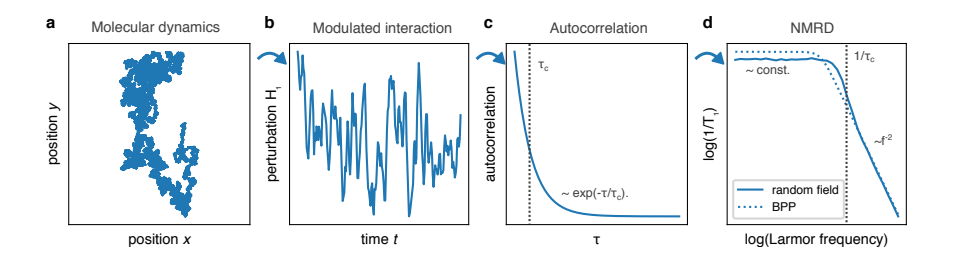


Figure 6.2: Illustration of spin relaxation using numerical simulation to demonstrate how the longitudinal relaxation rate $1/T_1$ varies with frequency in NMR: The random motion of particles (Brownian motion) (a), affects the system's quantum properties, like its Hamiltonian \hat{H}_1 , through a random magnetic field (b). Each component of the magnetic field is generated such that it shares the same exponential auto-correlation function (c) as the Brownian motion itself. By integrating the Schödinger¹ equation the relaxation rate can be estimated for different magnetic fields (d). The resulting dispersion curve exhibits similar characteristics to the more complex Bloembergen-Purcell-Pound (BPP) theory in cases involving dipolar relaxation.

LAAS BLOEMBERGEN², EDWARD MILLS PURCELL³, and ROBERT POUND⁴, was introduced in 1948 [15] and remains one of the most prevalent frameworks for explaining nuclear spin relaxation. This theory treats relaxation as a problem within second-order time-dependent perturbation theory. Other pioneering contributions were made by Felix Bloch, Anatole Abragam⁵, and Alfred Redfield⁶.

² Nicolaas Bloembergen (1920–2017) was a Dutch-American physicist who made pioneering contributions to the field of nonlinear optics and spectroscopy, and was awarded the Nobel Prize in Physics in 1981 for his work on laser spectroscopy and the development of new techniques for studying matter at the molecular level.

³ Edward Mills Purcell (1912–1997) was an American physicist who co–discovered nuclear magnetic resonance (NMR) and made pioneering contributions to the field of nuclear physics, for which he was awarded the Nobel Prize in Physics in 1952.

⁴ Robert Pound (1919–2010) was an American physicist who, along with his colleague Henry Rebka Jr., conducted a groundbreaking experiment in 1959 that confirmed the gravitational redshift predicted by Einstein's general theory of relativity, providing direct evidence for the gravitational time dilation effect.

⁵ Anatole Abragam (1914–2011) was a French physicist who made significant contributions to the field of nuclear magnetic resonance (NMR) spectroscopy and the study of condensed matter, and his book "The Principles of Nuclear Magnetism" became a seminal reference in the field.

⁶ BLOEMBERGEN, PURCELL, and BLOCH later received the Nobel Prize in Physics with BLOCH and PURCELL awarded for their NMR and BLOEMBERGEN recognized for his advancements in laser spectroscopy.

The longitudinal relaxation time T_1 is an important measure to quantify the relaxation of a nuclear spin system. It indicates the time it takes for the magnetization ($\propto \gamma_S \langle \hat{S}_z \rangle$) thermalization

$$\langle \hat{S}_z \rangle (t) = \langle \hat{S}_z \rangle_{\text{eq}} - \left(\langle \hat{S}_z \rangle_{\text{eq}} - \langle \hat{S}_z \rangle (0) \right) \exp(-t/T_1)$$
 (6.1)

aligned with a magnetic field B_0 along the z-axis to reach equilibrium.

A key outcome of the BPP establishes a link between the relaxation rate

$$R_1(\omega_{\text{nucl}}) = 1/T_1(\omega_{\text{nucl}}) \propto j(\omega_{\text{nucl}}) \tag{6.2}$$

and a spectral density function $j(\omega_{\rm nucl})$. This function is connected to the correlation function $G(\tau)$ of the fundamental relaxation process through a Fourier transform

$$j(\omega) = \int_0^\infty G(\tau) \cos(\omega \tau) d\tau . \qquad (6.3)$$

The details of nuclear magnetic relaxation for a given physical mechanism can quickly become complicated. Nonetheless, a straightforward model proves adequate for illustrating several key aspects. To this end, an ensemble of identical spin-1/2 nuclei and a time-dependent spin Hamiltonian

$$\hat{H}(t) = \hat{H}_0 + \hat{H}_1(t) \tag{6.4}$$

is assumed. The first term $\hat{H}_0 = \gamma_{\text{nucl}} B_0 \hat{S}_z$ describes the coupling of the nuclei to a constant magnetic field parallel to the z-axis. The second term $\hat{H}_1(t)$ characterizes the relaxation process. Assuming that $\hat{H}_1(t)$ is modulated by rotational Brownian motion, first described by Peter Debye⁷ within his investigation of polar molecules [104], the probability $P(\phi,\theta,t)$ of finding a molecule at time t in an orientation (ϕ,θ) follows a linear diffusion equation

Here, ϕ and θ are spherical coordinates.

$$\frac{\partial P(\phi, \theta, t)}{\partial t} = k \cdot \Delta P(\phi, \theta, t) \tag{6.5}$$

where Δ is the Laplace⁸ operator on the surface of a sphere⁹.

- 7 Peter Debye (1884–1966) was a Dutch-American physicist and chemist who made significant contributions to understanding molecular dipole moments, X-ray diffraction, and the Debye model of specific heat capacity.
- 8 Pierre-Simon Laplace (1749–1827) was an influential French mathematician, physicist, and astronomer known for his profound contributions to celestial mechanics, probability theory, and the development of the Laplace transform.
- 9 This assumes that the molecule can be described as a rigid rotor without any modulation of intra-molecular distances. However, there are situations where this assumption does not hold.

In reality, $\hat{H}_1(t)$ characterizes interactions between spins, such as scalar (1st and 2nd kind), dipolar, and quadrupolar interactions, modulated by the molecule's translational and/or rotational motion, and having various levels of spherical tensor rank. These interactions can span between molecules or occur within the same molecule, involving nuclear and/or electronic spins. These interactions can be represented using spherical tensor operators of rank k, denoted as $\hat{T}_q^{(k)}$ for instance, k=2 for dipolar or quadrupolar interactions), which transform similarly to spherical harmonics $Y_{lm}(\phi,\theta)$ (with l=k) under rotations. It can be shown that the auto-correlation function of a first- and second-degree spherical harmonic is linked to an exponential function [105]

$$G(\tau) \propto \exp(-\tau/\tau_{\rm c})$$
 , (6.6)

under the condition that the rotational diffusion conforms to the linear diffusion equation Equation 6.5.

In the framework of this model, the interaction can be approximated by substituting the precise (sometimes involving multiple spins) coupling operators with a single-spin random field represented as the Zeeman term $\hat{H}_1(t) = \gamma_{\text{nucl}} \mathbf{B}(t) \cdot \hat{\mathbf{S}}$ where $B_i(t)$ comprises of three time-dependent magnetic field components. Each of these components is constructed such that its auto-correlation over time

$$G(\tau) = \lim_{T \to \infty} \frac{1}{T} \int_0^T B_i(t+\tau) B_i(t) dt \propto \exp(-\tau/\tau_c)$$
 (6.7)

is proportional to the correlation function outlined in Equation 6.6.

In Figure 6.2a a simulated random trajectory is presented for a single particle, while in Figure 6.2b a corresponding magnetic field component is depicted. This field component possesses correlation properties as defined by Equation 6.7. By numerically integrating the Schödinger equation, calculating $\langle \hat{S}_z \rangle$, and fitting it to Equation 6.1, it becomes possible to estimate $1/T_1$ at a specific magnetic field. This sequence can be iterated across various magnetic fields B_0 , resulting in the creation of the NMRD curve, as shown in Figure 6.2d.

Even within this greatly simplified relaxation model, certain noticeable characteristics similar to those observed in actual experimental data become evident. The relaxation rate is proportional to a LORENTZIAN function

$$R_1(f_{\text{nucl}}) = \frac{1}{T_1(f_{\text{nucl}})} \propto \frac{1}{1 + 4\pi^2 f_{\text{nucl}}^2 \tau_c^2}$$
(6.8)

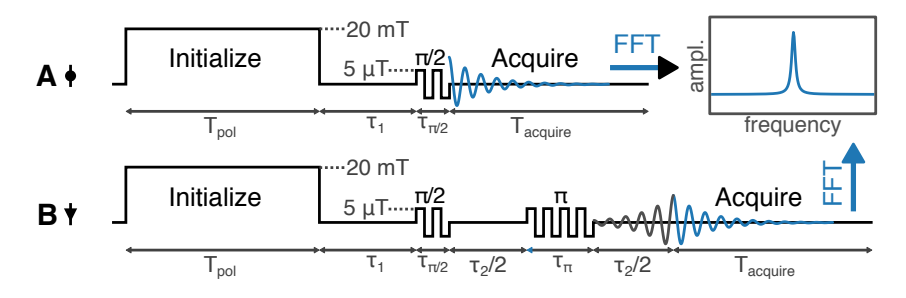


Figure 6.3: Sequences to measure longitudinal (A) and transverse relaxation rates (B). The vertical axis (not to scale) shows field strength with the polarization field along z and the $\pi/2$ and π pulses along y.

with a cutoff frequency $f_{\rm cutoff} = 1/(2\pi\tau_{\rm c})$. For higher frequencies, the tail of the profile can be roughly approximated by a power-law relationship $T_1(f_{\rm Larmor}) \propto f_{\rm Larmor}^2$.

It can be shown, that the exponent of 2 is distinctive for relaxation induced by typical rotational motion resembling Brownian rotational motion in bulk liquids with a linear diffusion equation. Any other exponent might suggest anomalous diffusion or a relaxation mechanism unrelated to diffusion, potentially giving rise to a correlation function with a stretched exponential behavior [106]

$$G(\tau) = \exp\left(-(\tau/\tau_{\rm c})^{\beta}\right) . \tag{6.9}$$

6.3 FAST FIELD CYCLING AT ULTRALOW FIELDS

The OPM described in Chapter 2 allows the direct observation of NMRD over a broad range of magnetic fields down to a few nanoteslas. Many single-component liquids and simple solutions are characterized by an exponential correlation function for molecular tumbling, with a time constant τ_c in the low ps range. As long as much slower additional motion processes do not exist, the NMR relaxation times T_1 and T_2 are independent of magnetic field below $B_z \ll (\gamma_I \tau_c)^{-1}) \approx 0.1 \, \text{T}$, even in ultralow fields.

Here, the dependence of relaxation in aqueous solutions of the paramagnetic compound TEMPOL is investigated, which is being studied elsewhere for its potential therapeutic properties [107] and as a source of nuclear spin hyperpolarization [108, 109] that can enhance

In other words, the system is in the extreme narrowing limit

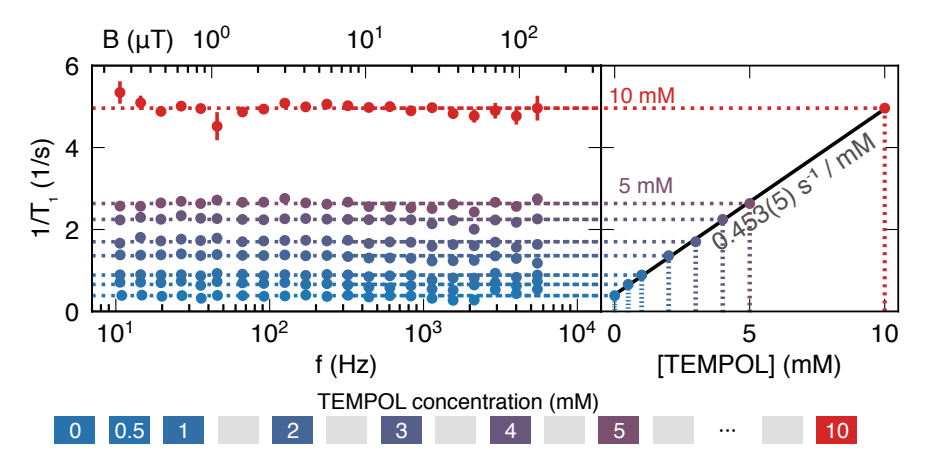


Figure 6.4: Ultralow-field NMR relaxation of ^1H in aqueous 4-hydroxy-2,2,6,6-tetramethylpiperidin-1-oxyl (TEMPOL) solutions at 30 °C: Field dependence of rates T_1^{-1} across 25 nT $< B_z < 130\,\mu\text{T}$, 1.8 mL sample volume. Rates are linearly proportional to TEMPOL concentration.

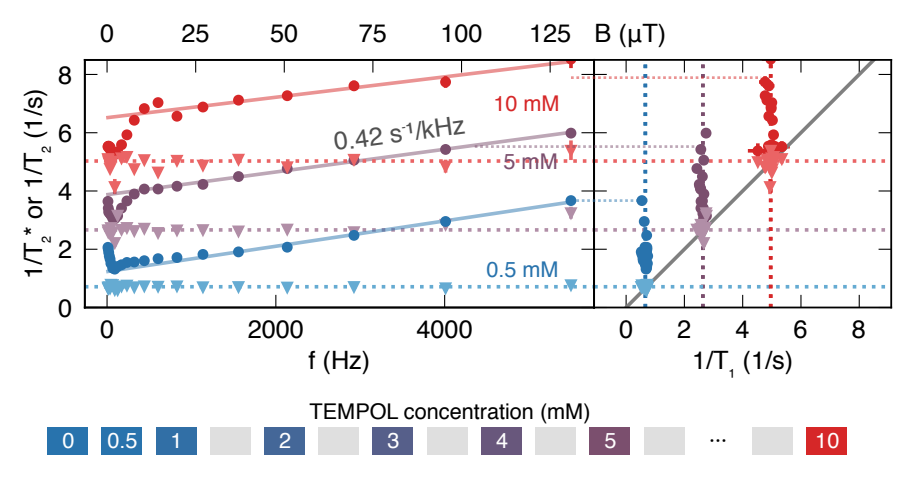


Figure 6.5: Ultralow-field NMR relaxation of ¹H in aqueous TEMPOL solutions at 30 °C: Field dependence of $(T_2^*)^{-1}$ and $(T_2)^{-1}$. $(T_2^*)^{-1}$ depends weakly on field due to instrument-specific gradients in B_z , while $T_2^{-1} \approx T_1^{-1}$.

sensitivity in NMR. Sequences A and B are used to measure ${}^{1}H$ T_{1} and T_{2} , respectively (Figure 6.3).

Sequence A involves pre-polarization of nuclear spin at 20 mT, followed by switching to a lower magnetic field for a duration of τ_1 , after which a dc $\pi/2$ pulse induces free nuclear precession about the z axis, resulting in NMR signal amplitudes, s_A , which fit well with the function $s_A \propto \exp(-\tau_1/T_1)$. The relaxation rates observed exhibit linear scaling with concentration of the paramagnetic dopant, with

$$T_1^{-1} = (T_1^{(0)})^{-1} + k_1[\text{TEMPOL}] ,$$
 (6.10)

where $T_1^{(0)}$ is the relaxation time at zero solute, as shown in Figure 6.4. The relaxivity parameter, k_1 , has a value of $0.453(5) \, \mathrm{s}^{-1} \, \mathrm{mmol}^{-1} \, \mathrm{dm}^3$, which agrees well with literature values at the high-field end [108, 109], thus providing confidence in the method used.

In Sequence B, the initial $\pi/2$ pulse is succeeded by a Hahn¹⁰-echo that refocuses transverse magnetization after time τ_2 . The amplitudes of the NMR signal, fitted using the function $\exp(-\tau_1/T_1 - \tau_2/T_2)$, yield a transverse relaxivity parameter, k_2 , defined by

$$T_{2,I}^{-1}(B_{z,I},[\text{TEMPOL}]) = T_2^{-1}(B_z,0) + k_2(B_z)[\text{TEMPOL}]$$
, (6.11)

as depicted in Figure 6.5 using triangle plot markers. The result $k_2 = k_1$ remains consistent even at ultralow fields, indicating the absence of slow motional correlations and isotropic molecular tumbling in the fast motion limit.

The decay rates in the transverse direction can also be estimated by using the full width at half maximum (FWHM) obtained from the Fourier-transformed NMR spectra of sequence A, since the inhomogeneity in B_z is relatively low. The coils introduce field gradients $\mathrm{d}B_z/\mathrm{d}z$, as well as smaller components along the x and y directions due to imperfections in the coil windings. This results in a linear dependence of $(\mathrm{d}/\mathrm{d}B_z)(T_2^*)^{-1} = 0.01\,\mathrm{s}^{-1}\,\mu\mathrm{T}^{-1}$ above 500 Hz $^1\mathrm{H}$ frequency.

The magnetic fields are superposition of the fields from different coils. Some are centered on the ⁸⁷Rb cell whereas others are centered on the NMR sample. Therefore, the gradients may cancel out at some Larmor frequencies, which is responsible for the line narrowing at around 200 Hz. The overall results indicate that the NMR line

¹⁰ Erwin Hahn (1921–2016) was an American physicist who pioneered the field of spin echoes and made significant contributions to nuclear magnetic resonance (NMR), leading to advancements in medical imaging and spectroscopy.

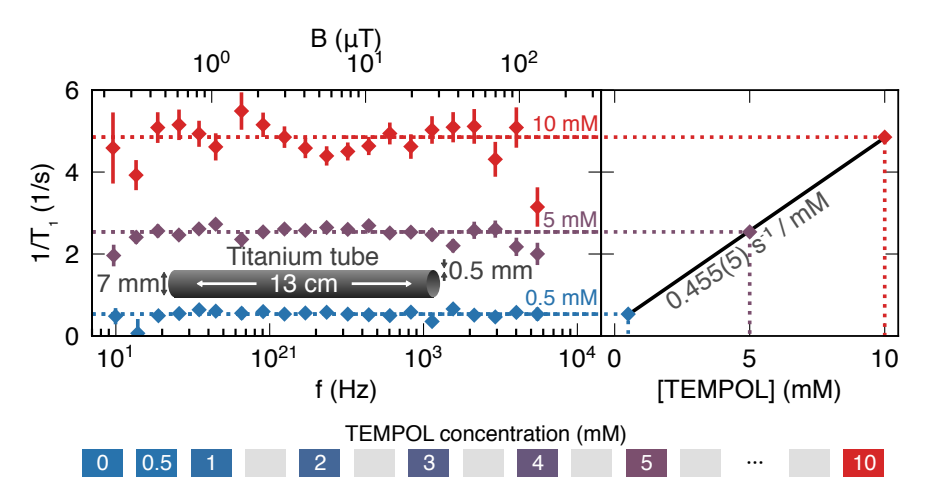


Figure 6.6: Relaxation rates for TEMPOL solutions encased in 0.5 mm thick titanium tube, 0.1 mL sample volume. All vertical error bars represent estimated standard deviation errors obtained from least-squares regression analysis.

width remains below 1 Hz even at geomagnetic fields and that the addition of TEMPOL does not affect the spectroscopic resolution in the zero/ultralow-field range.

6.4 FFC NMRD IN METAL CONTAINERS

To demonstrate the versatility of this technique, it can be shown that it can be applied to metal sample enclosures without any amplitude loss of NMR signals up to Larmor frequencies of few kHz. A titanium alloy tube with an outer diameter of 8 mm, inner diameter of 7 mm, and pressure rating of 13 MPa can contain 0.1 mL of TEMPOL solution, which exhibits identical relaxation rates $1/T_1$ as those in Figure 6.4, as shown in Figure 6.6. Although the smaller sample volume results in larger error bars due to lower SNR, this measurement is unattainable using conventional fast-field cycling NMR techniques due to eddy currents in metal that strongly attenuate the amplitude of high-frequency NMR signals and limit the rate of field switching. The transverse relaxation rates are also unaffected by the presence of the metal tube, indicating that eddy currents are negligible over the relatively small (mT) range of field switching. Hence, this approach can enable the study of relaxation in previously unexplored contexts, such as high-pressure fluids (e.g. supercritical fluids), flow in

pipes, foil-sealed products (e.g. foods, pharmaceuticals), and sealed radioactive samples (e.g. lead, tungsten).

6.5 LIQUIDS CONFINED IN POROUS MATERIALS

The ¹H spin relaxation of n-alkane hydrocarbons confined within matrices of alumina (γ polymorph, 9 nm mean pore diameter) and titania (anatase polymorph, 7 nm to 10 nm mean pore diameter) is studied to gain insight into molecular motion near pore surfaces. Catalytic features are possessed by these simple inorganic oxides in their mesoporous form due to their high specific surface area, Lewis¹¹ acidic sites, and the option of chemical treatments including metalization to activate the pore surface. However, due to the frequency range of conventional NMRD techniques, limited understanding of how molecular dynamics and surface site properties relate to long- τ_c relaxation processes exists, even without surface functionalization [110].

The ¹H relaxation rates at 30 °C for imbibed n-alkanes, measured between 1 Hz and 5.5 kHz Larmor frequency using the sequence shown in Figure 6.8a, are shown in Figure 6.7. Fast field switching between relaxation and detection events is preferred to probe the lowest fields due to excess noise in the magnetometer below 100 Hz (including mains electricity noise and 1/f noise, see Figure 6.8b). At frequency above 100 Hz Larmor frequency, NMR signals are detectable at the relaxation field without switching since the noise floor is low enough. The measurable NMR relaxation is limited in principle to rates $T_1^{-1} < R_{\rm op}^{-1}$, where the latter is of order $300 \, {\rm s}^{-1}$. However, in practice, the limit is $T_1^{-1} < T_{2,\rm atom}^{-1}$ or around $100 \, {\rm s}^{-1}$ since the atomic precession signal causes a 10 ms dead time following the $\pi/2$ pulse (see Figure 6.8c).

The weak dispersion in T_1^{-1} for each alkane, as well as between the two porous materials, across the conventional FFC-NMR frequency range 10 kHz to 1 MHz, is the main feature of Figure 6.7 and was reported by Ward-Williams et al. [110]. The relaxation rate for each alkane is only slightly dependent on the porous material, indicating that the relaxation process is dominated by bulk effects in this frequency range. In contrast, relaxation rates below 10 kHz strongly

¹¹ Gilbert N. Lewis (1875–1946) was an influential American physical chemist known for his groundbreaking work on chemical bonding, the Lewis dot structure, and the Lewis acids and bases theory, significantly advancing our understanding of molecular interactions.

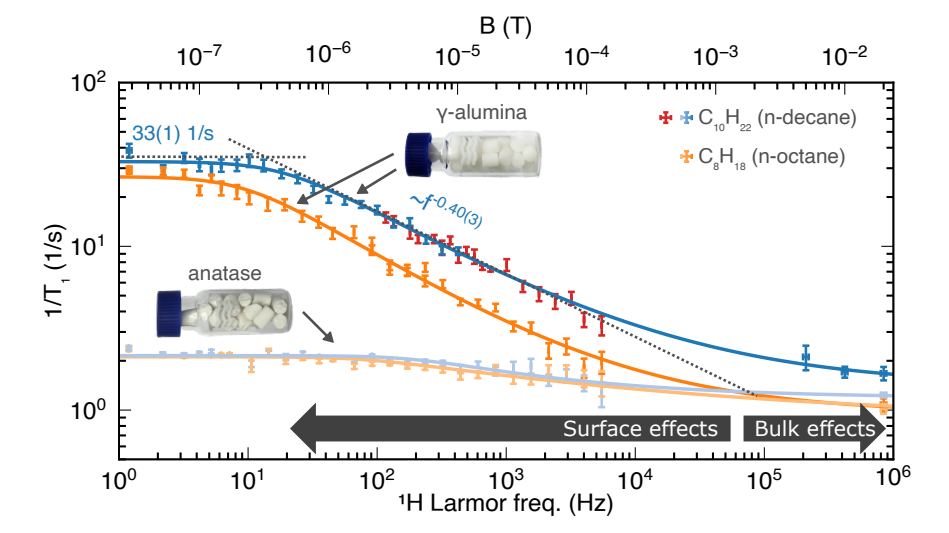


Figure 6.7: Ultralow-field FFC NMR of pore-confined fluids: **a**, Magnetization decay rates for n-octane and n-decane in porous γ -alumina and anatase titania. For n-decane in γ -alumina, colors indicate the NMR detection field, as discussed in the main text and represented in the rest of the figure. Data above 100 kHz correspond to magnetization buildup rates in the magnetic field; vertical error bars represent estimated standard deviation errors obtained from least-squares regression analysis.

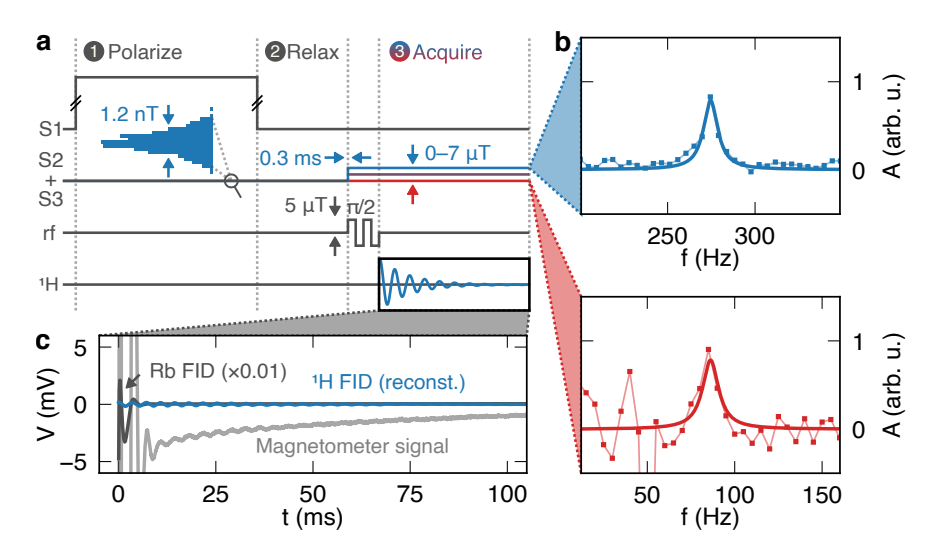


Figure 6.8: Ultralow-field FFC NMR techniques: **a** FFC sequence used to measure $T_{1,I}$ decay at ultralow field; **b** frequency- and **c** time-domain NMR signal of n-decane in γ -alumina after relaxation at $\omega_I/(2\pi)=85$ Hz. In **b**, the NMR SNR illustrate the FFC requirement below 100 Hz: poor snr at $\omega_I/(2\pi)=85$ Hz is due to 1/f and 50 Hz noise of the OPM; FFC switching to $\omega_I/(2\pi)=275$ Hz between relaxation and detection events is optimal for high SNR and short dead time. The blue and red color coding also serves to indicate the method used to measure $T_{1,I}$ for n-decane in γ -alumina, in Figure 6.7. The reconstructed time-domain signal in (**c**, blue curve) equates to the Lorentzian line shape fitted in **b**.

depend on the material, and mechanisms related to the surface become prominent, with higher values observed towards zero field. The T_1 dispersion in titania is much weaker than in γ -alumina, with T_1^{-1} reaching only around $2\,\mathrm{s}^{-1}$ below 200 Hz, compared to $30\,\mathrm{s}^{-1}$ for alumina, although the two materials have similar mean pore diameter and surface area/volume ratio. The first material's surfaceinduced relaxation is not as active, likely due to a lower concentration of paramagnetic impurities ([Fe³+] $\approx 2 \times 10^{16}\,\mathrm{g}^{-1}$ in alumina vs. $2 \times 10^{15}\,\mathrm{g}^{-1}$ in titania), as determined by electron spin resonance spectroscopy [111]. These results suggest that the lower-frequency relaxation mechanism involves dipole-dipole coupling between ¹H and the surface spins, rather than surface-induced modulation of intra-molecular ¹H-¹H spin couplings.

A power-law frequency dependence is obeyed by the longitudinal relaxation in γ -alumina between $\omega/(2\pi)=50\,\mathrm{Hz}$ and $5000\,\mathrm{Hz}$: $T_1 \propto \omega^\xi$. Exponents $\xi=0.50(3)$ for octane and $\xi=0.45(3)$ for decane are given by fitted slopes $-\mathrm{d}(\log,T_1^{-1})/\mathrm{d}(\log,\omega)$. Such values are consistent with simple numerical simulations in which imbibed molecules randomly walk within a dilute matrix of non-mobile spins – such as surface paramagnets – where the strength of dipole-dipole interactions between the two spin species scales with the inverse cube of their instantaneous separation [112]. This nonlinear dependence results in an example of Lévy¹² walk statistics. A detailed characterization of these effects in the alumina system is ongoing work.

To analyze the correlation time, the measured relaxation rates are fitted with a stretched LORENTZIAN function

$$\frac{1}{T_{1,\text{fit}}(\omega)} = \frac{1}{T_1(0)(1+\tau_c^2\omega^2)^{\beta}} + \frac{1}{T_1(\infty)} , \qquad (6.12)$$

which has four independent fit parameters: $T_1(0)$, $T_1(\infty)$, τ_c , and β . The solid lines in Figure 6.7 represent the fitted curves. For $\omega \tau_c \gg 1$ and $T_{1,\mathrm{fit}}(\omega) \ll T_1(\infty)$, the function is approximated by a power law with $\xi = 2\beta$. The correlation time parameter τ_c for alkanes in alumina is determined by examining the relaxation behavior below 50 Hz, where $T_1(\omega)$ changes from a power law frequency dependence to a constant, indicating a plateau at $T_1(0)$. Using the analysis presented

¹² Paul Lévy (1886–1971) was a French mathematician who made significant contributions to the fields of probability theory and stochastic processes, particularly his work on Levy processes and Levy flights, which have applications in diverse areas such as finance, physics, and biology.

earlier, this indicates a maximum correlation time ($\tau_c = \tau_{c,max}$) of around 20 ms to 30 ms, which is at least two orders of magnitude longer than the maximum correlation time of more polar molecules in porous confinement, such as water. The plateau for decane extends to a higher Larmor frequency than that for octane, indicating a shorter $\tau_{c,max}$ despite octane having a higher self-diffusion coefficient as a bulk liquid. However, at this point, τ_c is of similar magnitude to the longitudinal relaxation time. Under such conditions, the assumptions of standard NMR relaxation theories, such as the Wangsness-Bloch-Redfield theory, are not strictly justified as valid, particularly the coarse graining of time. This is because spin diffusion may be part of the relaxation mechanism or set an upper limit for the relaxation rate in the plateau. To determine if this is true, more information on the physical process responsible for spin relaxation is needed.

6.6 CHEMICALLY INDUCED DYNAMIC NUCLEAR POLARIZATION

The same experimental setup was also used to perform *in-situ* low-field photo-chemically induced dynamic nuclear polarization (CIDNP) (see Figure 6.9 from [99]). With the details explained in Chuchkova et al. [99], the FFC approach was used to measure directly the photo-CIDNP signal of 1,4-benzoquinone (BQ) at polarization fields between few nT up to 100 mT. The lifetime of the sample as well as relaxation rates were studied.

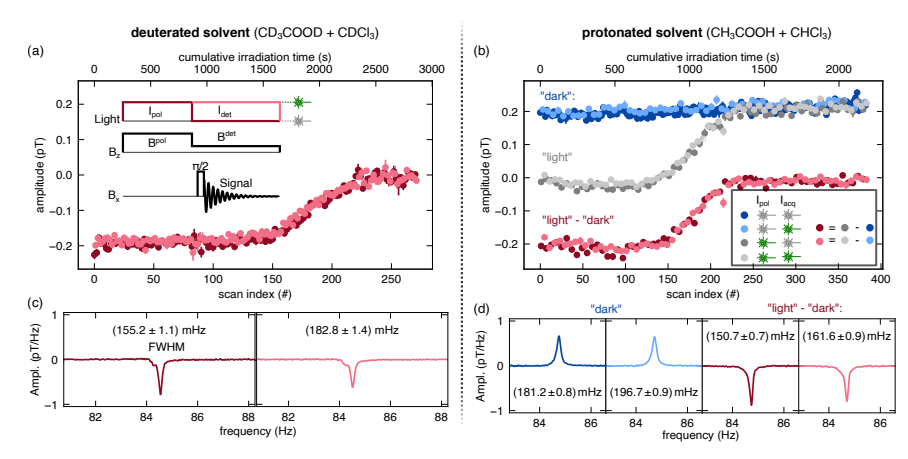
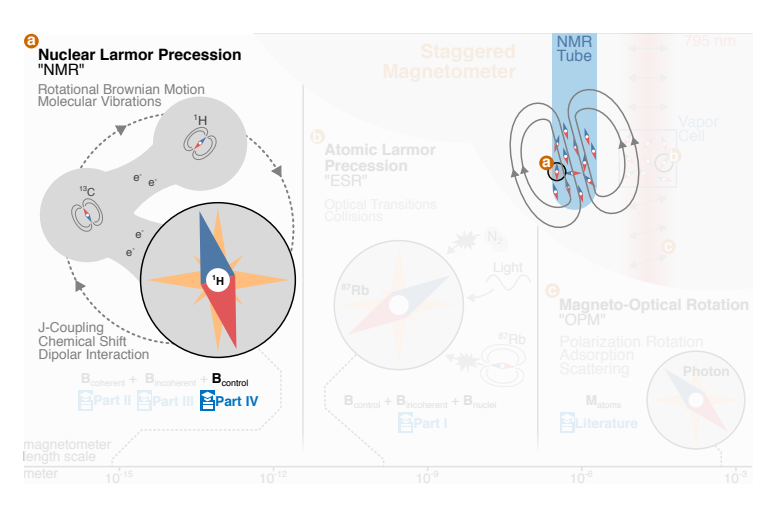


Figure 6.9: Magnetometer-detected photo-CIDNP measurements. (a) The amplitude of ¹H-precession signals from BQ in the CDCl₃/CD₃COOD solvent mixture following 4s of irradiation at 520 nm through the immersed optical fiber. Each point corresponds to the integral signal intensity of a single pulse-acquire measurement. Each data point corresponds to the integrated signal intensity of an individual pulse-acquire measurement. The signals colored in dark red and light red correspond to detection under dark and light conditions, respectively. (b) Overall ¹H precession signal arising from the BQ solute and CHCl₃/CH₃COOH solvent mixture is shown, utilizing the same irradiation parameters as in panel (a). Four sets of experiments were conducted, varying conditions of light and dark during polarization and detection stages. (c) Accumulated photo-CIDNP signals obtained with or without irradiation during detection in the deuterated sample. The left spectrum is the average of 29 transients acquired "in the dark" (light off), while the spectrum to the right was acquired with the light kept on. The FWHM as determined by LORENTZIAN fitting is marginally larger in the case of acquisition with the light on. (d) Accumulated NMR signals similar to panel c but for the case of protonated solvents. Note that the solvent signals that are seen for the "dark" prepolarization conditions are from the solvent with a concentration 3 orders of magnitude higher than that of BQ.

Part IV

NUCLEAR SPIN CONTROL



The behavior of a thermodynamic system is influenced by its internal degrees of freedom, which are determined by chemical and physical properties such as inter-particle couplings and symmetry. While these internal properties may be difficult to change, it is important to recognize that the dynamics of the system can be controlled by manipulating the symmetry of the external environment. Techniques such as dynamical decoupling, spin locking, and magnetic field cycling can alter the rates at which a spin ensemble reaches thermodynamic equilibrium. By using these methods, it is possible to investigate internal variables despite the presence of local, random interactions that fluctuate rapidly compared to coherent time scales.

In the next two chapters, this will be investigated: First, Chapter 7 discusses techniques to perform robust, selective/collective spin control at ultralow fields. Chapter 8 applies these techniques to manipulate the symmetry of the system to influence relaxation to thermal equilibrium.

These chapters follow closely the three publications Bodenstedt et al. [113], Bodenstedt et al. [114], as well as Mouloudakis et al. [115].

ROBUST SPIN-SELECTIVE INVERSION AT ULTRALOW FIELDS

One of the key elements of NMR is the ability to manipulate the nuclear spin states through magnetic field pulses by applying a series of precisely timed and positioned magnetic fields to the sample. By varying the amplitude, duration, spectral composition, timing, and gradient of these pulses, one can manipulate the spin states of the nuclei in the sample, which in turn affects the detectable NMR signal.

Controlling quantum states in a robust and precise way is a fundamental challenge in many fields, including quantum computation [116, 117], quantum sensing [118, 119] and medical imaging [120]. Quantum optimal control theory [121] tries to find the optimal way to achieve a quantum operation with a limited set of control mechanisms. To improve the robustness quantum gates can be developed that tolerate tiny errors in the control parameters to achieve acceptable results.

Conventional spin-resonance experiments take place within strong magnets (such as superconducting magnets) that have a fixed magnitude and direction of the magnetic field. As a result, spin control is limited to only the amplitude and phase degrees of freedom. Nevertheless, other strategies are theoretically possible: Error-compensated pulse design can be traced back to a set of fundamental principles, including the Magnus¹ expansion [122], impulse-response theory [123], recursive iteration, and other considerations related to time symmetry [124]. When the restriction of a strong magnetic field is removed, new pulse strategies become available, and existing pulse strategies can be implemented using different degrees of freedom.

In the context of NMR, over the last decades, numerous techniques have been developed to create error-tolerant pulses, utilizing phase modulation [125–130], amplitude modulation [131–133], or both phase and amplitude modulation [134–136] of the ac fields. This chapter discusses the main results of Bodenstedt et al. [113] and

¹ Wilhelm Magnus (1907–1990) was a German–American mathematician known for his contributions to combinatorial group theory and his work on the Magnus expansion, which provides a powerful tool for studying group presentations and their applications in various branches of mathematics and theoretical physics.

Bodenstedt et al. [114] that translates methods for pulse optimization from high-field into the ZULF regime.

Of special interest in NMR is the ability to collectively or selectively address different spin species in a way that is robust to experimental imperfections. Here, the example of selective/collective spin inversion at low and high field will be discussed which will be of utter importance in the context of dynamical decoupling (see Chapter 8).

7.1 SPIN INVERSION USING ORDINARY DC AND AC PULSES

In the simplified scenario of a single species of uncoupled nuclear spin the spin evolution can be described by the classical, phenomenological Вьосн equations

$$\frac{\mathrm{d}\mathbf{S}}{\mathrm{d}t} = \gamma \mathbf{S} \times \mathbf{B} \tag{7.1}$$

(here relaxation is neglected; compare Equation 1.2a to Equation 1.2c).

Rabi Oscillations

In a high-field NMR scenario, a strong constant field $\mathbf{B}_0 = (0, 0, B_0)$ (typically in z direction) is applied, and a weaker, rotating, orthogonal field

$$\mathbf{B}_{1} = \begin{pmatrix} B_{1}\cos(\omega t) \\ B_{1}\sin(\omega t) \\ 0 \end{pmatrix} \tag{7.2}$$

is applied for a short time to change the spin state.

These kinds of oscillations can be very well described by the RABI² effect, which is based on two-state model systems and occurs, besides NMR, in many quantum mechanical systems from atom-light interaction to quantum computing.

The resulting oscillations

$$S_z(t) = S_z(0) \cdot \left(1 - \frac{2\Omega^2}{\Omega^2 + \delta^2} \sin^2 \left(\frac{\sqrt{\Omega^2 + \delta^2}t}{2} \right) \right) \tag{7.3}$$

² Isidor Isaac Rabi (1898–1988) was an American physicist who won the Nobel Prize in Physics in 1944 for his discovery of nuclear magnetic resonance (NMR), which has become a fundamental tool in many areas of science and technology, including magnetic resonance imaging (MRI).

are consequently called Rabi oscillations. Here, $\delta = |\omega - \omega_{Larmor}|$ is the detuning between the AC field (oscillating with angular frequency ω) and the nuclear Larmor frequency $\omega_{Larmor} = \gamma B_0$. It is assumed the initial state is given by $\mathbf{S}(0) = (0,0,S_0)$ and it is $\Omega = \gamma B_1$.

Full inversion, i.e. $S_z(t_\pi) = -S_z(0)$, can be achieved by using resonant pulses by using the same frequency for the driving field and the Larmor frequency, effectively setting the detuning to zero ($\delta=0$). In the rotating frame, such pulses produce a spin rotation of $\hat{R}(\psi,\mathbf{n})$, where the spin rotation angle ψ is proportional to the strength B_1 and duration of the pulse. The rotation axis \mathbf{n} is determined by the phase of the pulse.

The resonance condition ensures that only spins with the same gyromagnetic ratio are affected by the driving field, since according to Equation 7.1 large detunings δ drastically lower the efficiency³ of the driving field. This allows good selectivity at high fields.

The simplicity of the pulses comes with the cost of them not being very robust regarding errors in phase, amplitude, or frequency. Good calibration and control of the driving fields is therefore crucial for accurate results.

Square Wave Pulses

At low field $B_0 \ll B_1$, ω in Equation 7.2 is so small, that \mathbf{B}_1 can be approximated

$$\mathbf{B}_{1} \approx \begin{pmatrix} B_{1} - B_{1}\omega t \\ 0 + B_{1}\omega t \\ 0 \end{pmatrix} \stackrel{\omega \to 0}{\approx} \begin{pmatrix} B_{1} \\ 0 \\ 0 \end{pmatrix}$$
 (7.4)

using small-angle approximations, which is effectively a DC pulse. In low-field NMR, it is possible to directly implement a rotation $\hat{R}(\psi,\mathbf{n})$ about a (laboratory frame) axis \mathbf{n} , by applying a DC field of strength B_1 along \mathbf{n} for a time τ , to generate rotation by an angle $\psi = \gamma B \tau$. Rotations with arbitrary \mathbf{n} and ψ can in principle be produced with three-axis control of $\mathbf{B}(t)$. In this way, any simple rotation $\hat{R}(\psi,\mathbf{n})$ used in high-field about a (laboratory frame) axis \mathbf{n} can be implemented.

³ In the rotating frame, detunings effectively change the rotation axis. The lower the angle between the \mathbf{B}_0 and \mathbf{n} is, the lower the efficiency of the pulse.

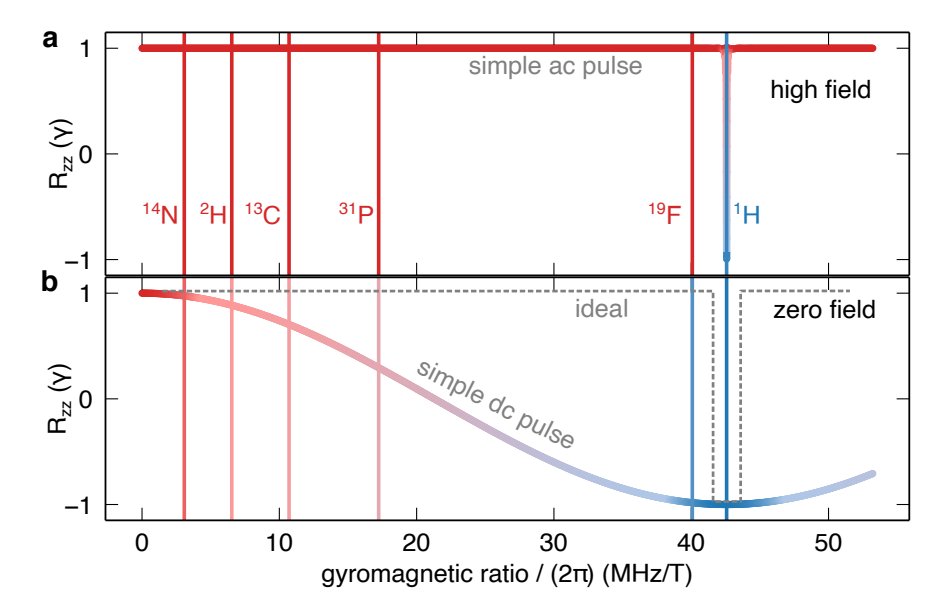


Figure 7.1: Spin inversion profiles for 1H resonant pulses at high-field (1 T) and zero-field (0 T). Red signifies no net rotation while blue signifies complete spin inversion. At high field, ordinary pulses offer great spin species selectivity, whereas at zero field a simple, ordinary DC pulse does not feature an attractive pass-/stopband characteristic. \hat{R}_{zz} represents the z-projection of the unit vector \mathbf{e}_z after the rotation. $\hat{R}_{zz} = -1$ indicates complete inversion, while $\hat{R}_{zz} = 1$ signifies no net rotation.

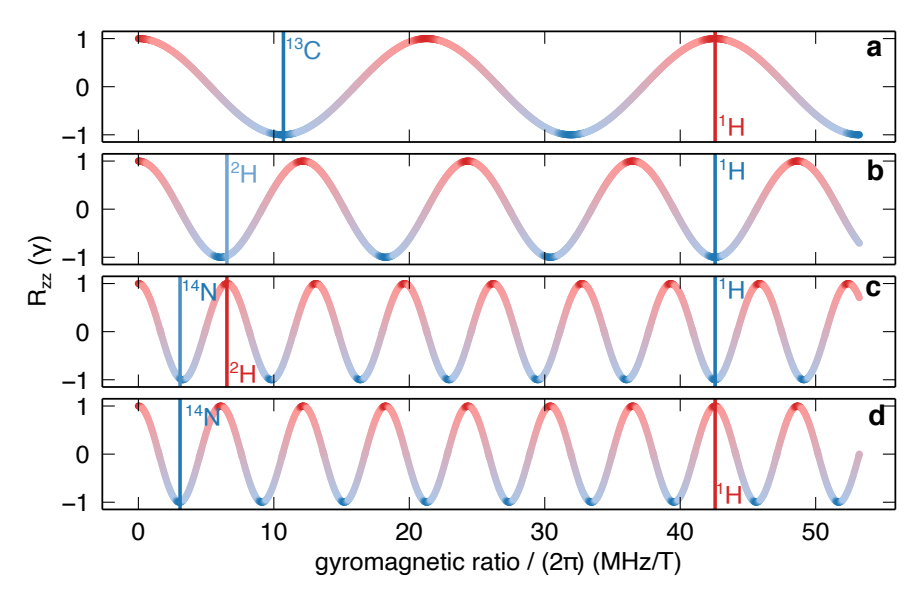


Figure 7.2: Spin inversion using ordinary DC pulses with different pulse durations (top to bottom: 2π , 7π , 13π and 14π on 1 H). Again, red signifies no net rotation while blue signifies complete spin inversion. The vertical lines represent sets of nuclear spin species for which good collective/selective inversion can be achieved.

However, setting both $\omega=0$ and $B_0=0$ automatically leads $\omega_{\rm Larmor}=0$ for all spin species. This also sets the detuning $\delta=0$ which takes away most of the spin selectivity.

Magic Ratios

Since γ differs for different spin species, the Rabi frequency $\Omega = \gamma B_1$ also differs and some magic ratios for pair of nuclear spins exist, that allow some selectivity even with simple DC pulses. Some examples are shown in Figure 7.1: Here the Rabi oscillation of ¹H nuclear spin is plotted. Exploiting the proximity of the relative ratio of nuclear spin gyromagnetic ratios to rational numbers allows the flipping of spins of one species but barely affecting another.

Limitations

At near-zero magnetic fields, conventional RF pulses are inadequate for performing spin-selective rotations due to the small differences in Larmor frequencies compared to the bandwidth of the RF pulses [137]⁴. In ultralow fields, where the magnitude of the static magnetic field B_0 is comparable to the pulse field $B_{\rm rf}$, the final state of the spin system becomes highly dependent on the strength of the B_0 field. This necessitates extensive calibration and adjustments to achieve consistent rotations across different bias fields. Moreover, low-frequency and DC components can introduce increased noise due to the 1/f noise spectrum of electronic components, leading to pulse errors that undermine the reproducibility and reliability of NMR experiments.

7.2 COMPOSITE 90X-180Y-90X INVERSION PULSES

Composite pulses [126, 128] consist of trains of simple pulses that collectively achieve a desired rotation, offering advantages over individual pulses. They can be designed to maintain consistent performance across a range of parameter values, such as γ or B_0 , making them robust against experimental imperfections. Furthermore, composite pulses allow for the application of different rotations to different γ values, enabling species-specific manipulations. However, the direct translation of composite pulses from high-field to low-field techniques is not straightforward due to the diverse effects of parameter variations on the rotation. In resonant rotations, the rotation axis $\bf n$ depends on the detuning and, consequently, on γ , whereas in dc rotations, it is ψ that varies with γ .

High Field Comparison

In contrast to high-field NMR, where phase/frequency offsets and flip-angle offsets originate in distinct imperfections of the experimental system and have different effects on the generated spin rotations, in low-field NMR flip angle and axis are both determined by the dc field strengths. As shown, this allows a single composite pulse strategy to be robust against variations of each, something that is uncommon in high-field composite pulses.

Composite pulses are used intensively in high-field NMR to compensate for pulse imperfections and improve their robustness. For instance, in a high field, a $90_x180_y90_x$ pulse is often a first choice for

⁴ Although certain combinations of spin species with specific gyromagnetic ratios (e.g. $\gamma_{^{1}H} \approx 4\gamma_{^{13}C}$) offer limited spin selectivity, this approach is unsatisfactory and does not provide a general solution.

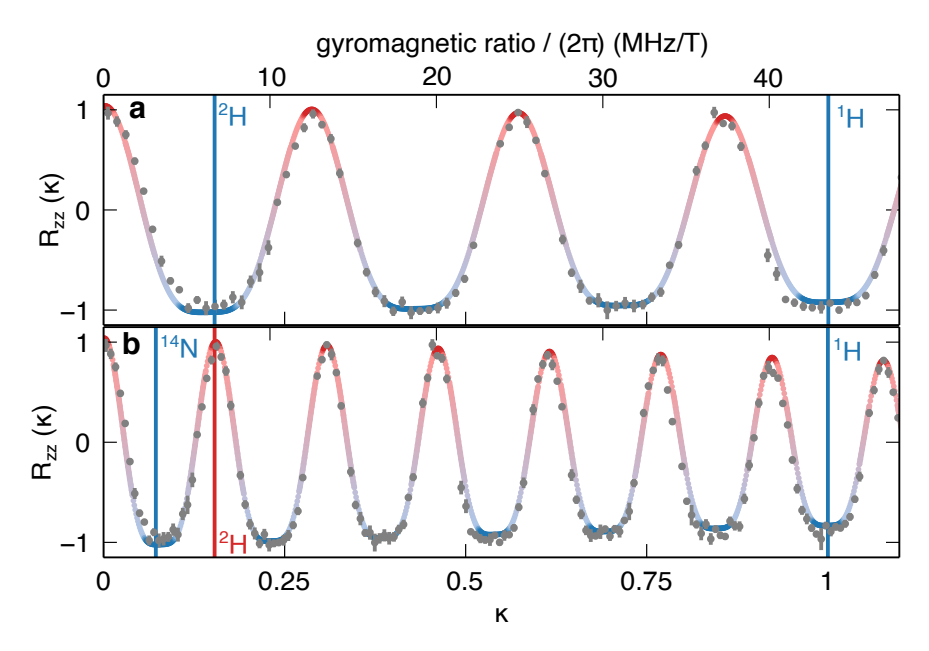


Figure 7.3: Spin inversion using DC 90x-180y-90x pulses for v=7 (top) and v=13 (bottom). The colored plot represents the theoretical simulation (red signifies no net rotation while blue signifies complete spin inversion). The grey data points show experimental data. Here, the values for different values of $\kappa\cong\gamma/\gamma_{^1H}$ were experimentally simulated by varying the pulse lengths, i.e. $\tau\to\kappa\tau$ [114]. The vertical lines represent sets of nuclear spin species for which good collective/selective inversion can be achieved.

tolerance to errors in RABI frequency and thus pulse length. The same technique can also be applied for DC pulses under ZULF conditions:

Selective and Collective 1H/2H Spin Inversion

This will be exemplarily demonstrated for a spin system of $I_1 = {}^1\mathrm{H}$ and $I_2 = {}^2\mathrm{H}$. The nominal operation $R_1(\pi, \mathbf{e}_x)R_2(0, \mathbf{e}_x)$ is approximated using a composite of three dc pulses (Figure 7.3) that rotates the $I_1 = {}^1\mathrm{H}$ spin first by $\pi/2$ about the x axis, then π about y and finally $\pi/2$ about x, since for the ratio $u = \gamma_{^2\mathrm{H}}/\gamma_{^1\mathrm{H}} \approx 0.154$ in this case it is found that

$$\hat{R}_1\left(\frac{\pi}{2}, \mathbf{e}_x\right) \hat{R}_1(\pi, \mathbf{e}_y) \hat{R}_1\left(\frac{\pi}{2}, \mathbf{e}_x\right) = \hat{R}_1(\pi, \mathbf{e}_x)$$
(7.5)

and

$$\hat{R}_2\left(\frac{u\pi}{2}, \mathbf{e}_x\right) \hat{R}_2(u\pi, \mathbf{e}_y) \hat{R}_2\left(\frac{u\pi}{2}, \mathbf{e}_x\right) \approx \hat{R}_2(0, \mathbf{e}_x) . \tag{7.6}$$

If pulse flip angles are multiplied by v to approximate $\pi/2$ and π rotations on the $I_2 = {}^2\mathrm{H}$ spin, the same DC pulse sequence can be used to produce $R_1(\pi, \mathbf{e}_x)R_2(\pi, \mathbf{e}_x)$ transformations, provided that v is odd and (1-|vu|) is less than the error-compensation bandwidth of the overall rotation [128]. Here v=7 yields

$$\hat{R}_1\left(\frac{v\pi}{2}, \mathbf{e}_x\right) \hat{R}_1(v\pi, \mathbf{e}_y) \hat{R}_1\left(\frac{v\pi}{2}, \mathbf{e}_x\right) = \hat{R}_1(\pi, \mathbf{e}_x) \tag{7.7}$$

and

$$\hat{R}_2\left(\frac{vu\pi}{2},\mathbf{e}_x\right)\hat{R}_2(vu\pi,\mathbf{e}_y)\hat{R}_2\left(\frac{vu\pi}{2},\mathbf{e}_x\right)\approx\hat{R}_2(\pi,\mathbf{e}_x)$$
 (7.8)

These types of pulses can be used to implement XY4 pulse sequence (only on ¹H, and on ¹H and ²H simultaneously) using DC pulse (see Chapter 8).

7.3 ROTATION ALGEBRA IN THE MERIDIONAL PLANE

Direct translation of composite pulses from the AC (high-field) to DC (low-field) domain is not always straightforward. Whereas, in a high field, a 90_x180_y90_x pulse is often a first choice for tolerance to errors in RABI frequency and thus pulse length, in low-field, the pulse length tolerance of a DC composite pulse can be achieved using analogs of AC pulses that compensate for offset in the AC carrier frequency – a different source of error.

As a proof of principle, this concept shall be illustrated for DC composite pulses where fields are confined to a single meridional plane of the BLOCH sphere (e.g., *x-z* plane, where *z* defines the bias axis). This follows closely the description of Bodenstedt et al. [113] where the term *meridional composite pulses* was first introduced and it will be shown that they are considerably more selective than traditional composite pulses, including $90_x 180_y 90_x$ where magnetic field is kept in the equatorial plane of the Bloch sphere (*x-y* plane).

As a basis for designing meridional composite pulses, one can utilize the theorem stating that successive rotation of a 3D object by π radians around a pair of unit vectors \mathbf{n}' and \mathbf{n}'' is mathematically equivalent to a single rotation by an angle ϕ around the

perpendicular unit vector \mathbf{n} , which is parallel to $\mathbf{n}' \times \mathbf{n}''$. The angle $\phi/2$ corresponds to the angle between \mathbf{n}' and \mathbf{n}'' , expressed as $\mathbf{n}' \cdot \mathbf{n}'' = |\mathbf{n}'| |\mathbf{n}''| \cos(\phi/2)$:

$$\hat{R}(\pi, \mathbf{n}'')\hat{R}(\pi, \mathbf{n}') = \hat{R}(\phi, \mathbf{n}) . \tag{7.9}$$

Here, $\hat{R}(\phi, \mathbf{n})$ describes a rotation⁵ by an angle ϕ about the vector \mathbf{n} . By extension, an equation follows for the cumulative effect of 2N rotations-by- π about axes $\mathbf{n}_1', \mathbf{n}_1'', \mathbf{n}_2', \mathbf{n}_2'', \ldots, \mathbf{n}_N', \mathbf{n}_N''$ in a common plane normal to \mathbf{n} :

$$\prod_{j=1}^{N} \hat{R}(\pi, \mathbf{n}_{j}^{"}) \hat{R}(\pi, \mathbf{n}_{j}^{"}) \equiv \hat{R}\left(\sum_{j=1}^{N} \phi_{j}, \mathbf{n}\right). \tag{7.10}$$

For instance, if all of the \mathbf{n}' and \mathbf{n}'' vectors lie within the Cartesian⁶ x-z plane as defined by vectors $\mathbf{e}_x = (1,0,0)^{\mathsf{T}}$ and $\mathbf{e}_z = (0,0,1)^{\mathsf{T}}$, then the overall rotation is produced about the y axis, defined $\mathbf{n} = \mathbf{e}_y = (0,1,0)^{\mathsf{T}}$. A graphical representation of Equation 7.9 is shown in Figure 7.4.

The problem of interest for robust, spin-selective pulse generation is the approximate implementation of Equation 7.10, where a sequence of 2N rotations by $\kappa\pi$ is applied about axes $\mathbf{n}_1', \mathbf{n}_1'', \dots, \mathbf{n}_N', \mathbf{n}_N''$. If, as above, the angle between \mathbf{n}_i' and \mathbf{n}_i'' is $\phi_i/2$, the objective is to find a sequence of angles $\phi_1, \phi_2, \dots, \phi_N$ such that the resulting rotation is

$$\hat{R}(\kappa, \mathbf{n}_1', \dots, \mathbf{n}_N', \mathbf{n}_1'', \dots, \mathbf{n}_N'') \equiv \prod_{j=1}^N \hat{R}(\kappa \pi, \mathbf{n}_j'') \hat{R}(\kappa \pi, \mathbf{n}_j') \approx \hat{R}(\beta, \mathbf{n})$$
(7.11)

for some detuned range of κ , (and therefore gyromagnetic ratio, $\gamma \propto \kappa$), say ($\kappa \mod 2$) = $(1 + \delta)$, where δ is the detuning. Here β is the target rotation angle.

⁵ Strictly speaking, this equation is not correct for half-integer spinors. These systems would accumulate an additional phase of π , i.e. $\hat{R}(\pi, \mathbf{n''})\hat{R}(\pi, \mathbf{n'}) = (-1)^{2S}\hat{R}(\phi, \mathbf{n})$. However, this additional phase does not affect the analysis outlined here as long as an even number of rotations is performed.

⁶ René Descartes (1596–1650) was a French philosopher, mathematician, and scientist who is widely regarded as the founder of modern philosophy and analytic geometry, and is best known for his famous statement, "I think, therefore I am."

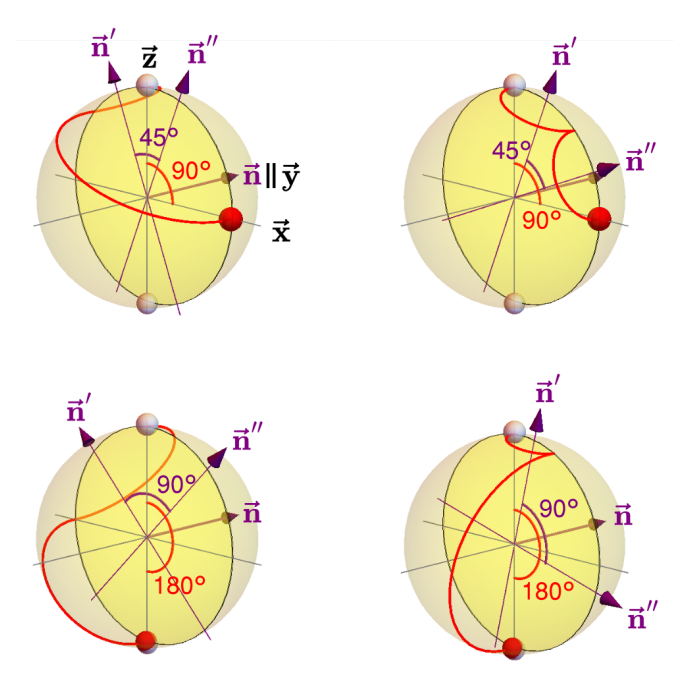


Figure 7.4: The top row presents graphical illustrations of Equation 7.9 for $\phi = 90^{\circ}$, while the bottom row showcases examples for $\phi = 180^{\circ}$. The solid red curves depict the trajectory followed by a particle starting at the point $\mathbf{e}_z = (0,0,1)$ as it undergoes successive 180° rotations around the pair of axes \mathbf{n}' and \mathbf{n}'' . These axes, indicated by purple arrows, lie within the x-z plane and form an angle of $\phi/2$.

7.4 BAND-SELECTIVE, UNIFORM RESPONSE, PURE-PHASE PULSES

One route to a solution is to recognize that for $\kappa = (1 + \delta)$ one can cast Equation 7.11 (see appendix in [113]) into a form

$$\hat{R}(\kappa, \phi_1, \dots, \phi_N)
\equiv \prod_{j=1}^N \hat{R}\left(\frac{\phi_j}{2}, \mathbf{e}_y\right) \hat{R}\left((1+\delta)\pi, \mathbf{e}_z\right) \hat{R}\left(-\frac{\phi_j}{2}, \mathbf{e}_y\right) \hat{R}\left((1+\delta)\pi, \mathbf{e}_z\right)
= \prod_{j=1}^N \left(\hat{R}_z^{2j}(\delta)\hat{R}\left(\frac{\phi_j}{2}, \mathbf{e}_y\right)\right) \left(\hat{R}_z^{2j-1}(\delta)\hat{R}\left(-\frac{\phi_j}{2}, \mathbf{e}_y\right)\right),$$
(7.12)

where $\hat{R}_z^d(\delta)$ is the dth power of the right-acting superoperator $\hat{R}_z(\delta)$, which rotates operators $\hat{R}(\phi, \mathbf{n})$ by an angle $\pi(1 + \delta)$ about \mathbf{e}_z , as defined by [138]

$$\hat{R}_z(\delta)\hat{R}(\phi,\mathbf{n}) \equiv \hat{R}\left(-\pi(1+\delta),\mathbf{e}_z\right)\hat{R}(\phi,\mathbf{n})\hat{R}\left(\pi[1+\delta],\mathbf{e}_z\right) . \tag{7.13}$$

The form of Equation 7.12 indicates that relative to the ideal transformation ($\kappa=1$), the error δ has the effect of shifting the spins' frame of reference by an offset 2δ about \mathbf{e}_z between each ϕ_j rotation. Consequently, the task of determining suitable values for ϕ_j can be reframed as the challenge of compensating for this frame offset. Frame-offset compensation represents a widely explored subject within the field of physics and holds significant importance in the realms of NMR, MRI, and quantum information processing.

Frame-Offset Compensation

One previously used approach involves the utilization of broadband uniform-rotation pure-phase (BURP) [133] pulses, originally developed [134] by Geen and Freeman⁷. A BURP pulse is an amplitude-modulated ac pulse with a duration of τ_p , where the carrier frequency is resonant with the nominal Larmor frequency. The shape of the carrier-envelope is designed in such a way that it yields a (rotating

⁷ Raymond Freeman (1932–2022) was a distinguished British chemist and professor at Jesus College, Cambridge, recognized for his significant contributions to the field of NMR spectroscopy.

frame) rotation of $\hat{R}(\beta(t), \mathbf{e}_y)$ for $\delta = 0$, where the accumulated flip angle within the interval $0 \le t \le \tau_p$ is given by

$$\beta(t) = a_0 \frac{t}{\tau_p} + b_0 + \sum_{k=1}^{n_{\text{cut}}} \left(a_k \sin\left(\frac{2\pi kt}{\tau_p}\right) + b_k \cos\left(\frac{2\pi kt}{\tau_p}\right) \right). \tag{7.14}$$

The expression can be interpreted as a truncated Fourier series, where a cutoff of $n_{\rm cut} \sim 6$ is typically sufficient for achieving desired precision [133, 134]. The numerical values for a_k and b_k can be found in the Supplemental Material provided by Bodenstedt et al. [113]. BURP pulses exhibit a generous tolerance for the mismatch between the carrier and Larmor precession frequencies, with an excitation pass-band inversely proportional to the pulse length of the BURP pulse.

Discretization

Using dc pulse pairs as described in Equation 7.10, a pointwise approximation of $\beta(t)$ can be made: Intermediate rotation angles

$$\phi_j = \beta\left(\frac{\tau_p j}{N}\right) - \beta\left(\frac{\tau_p (j-1)}{N}\right) ,$$
 (7.15)

are defined and then a sequence of nominally- π rotations

$$\hat{R}(\kappa, \mathbf{n}_1', \dots, \mathbf{n}_N', \mathbf{n}_1'', \dots, \mathbf{n}_N'') \equiv \prod_{j=1}^N \hat{R}(\kappa \pi, \mathbf{n}_j'') \hat{R}(\kappa \pi, \mathbf{n}_j')$$
(7.16)

is constructed with

$$\mathbf{n}_{j}' = \begin{pmatrix} +\sin(\phi_{j}/4) \\ 0 \\ \cos(\phi_{j}/4) \end{pmatrix} \text{ and } \mathbf{n}_{j}'' = \begin{pmatrix} -\sin(\phi_{j}/4) \\ 0 \\ \cos(\phi_{j}/4) \end{pmatrix} . \tag{7.17}$$

This defines a *meridional composite pulse*, i.e., a series of $\kappa\pi$ rotations about pairs of axes in the *x-z* plane, separated by angles $\phi_j/2^8$. The values of ϕ_j ranging from N=10 to N=40 are provided in the Supplemental Material [113].

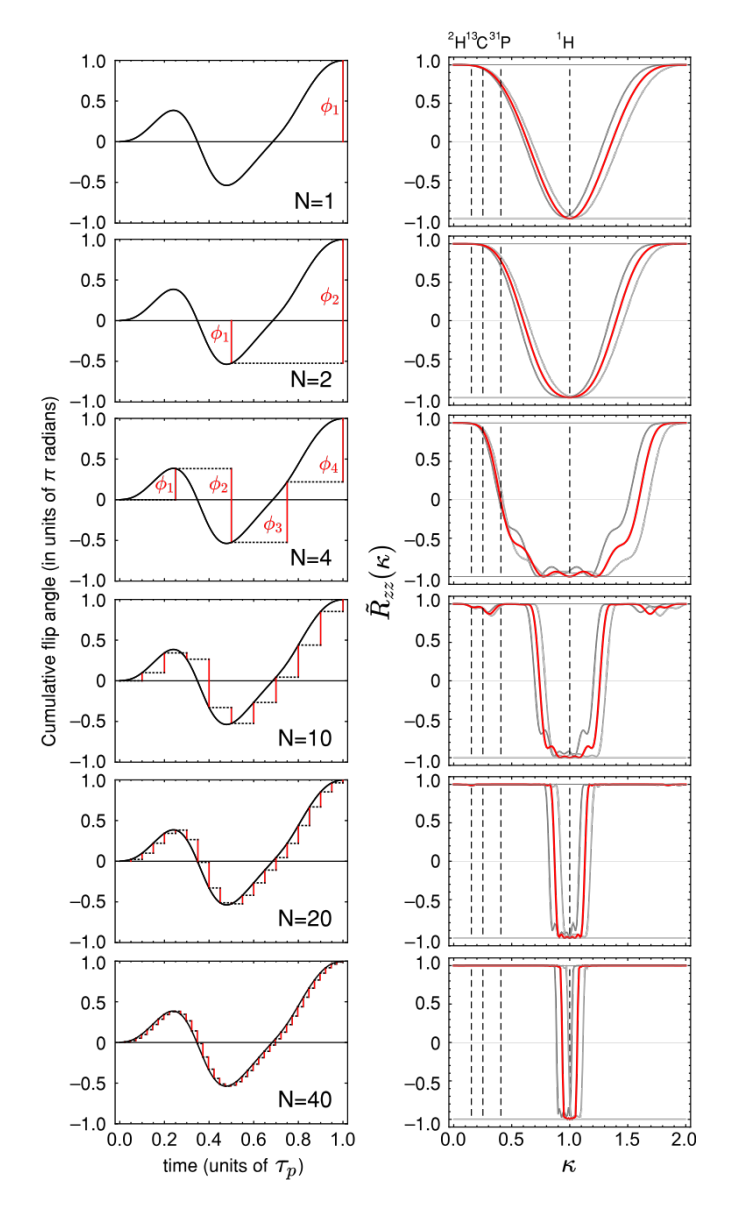


Figure 7.5: Band-pass spin inversion using dc pulses derived from I-BURP-1 [133]. The time profiles of flip angle accumulated in the x-z plane are displayed in the left column for the conventional pulse (β , black) and discretized pulses (ϕ_j , red) with different values of N: 1, 2, 4, 10, 20, and 40. On the right, the plot illustrates the inversion performance $\hat{R}_{zz}(\kappa)$ of the discretized pulse (red). The gray and light gray plots show the inversion profile for the same parameters but with a mis-calibrated z-coil by $\pm 10\%$ [113]. The dashed vertical lines correspond to the values of $\kappa_I/\kappa_{^1H} \equiv \gamma_I/\gamma_{^1H}$ when $\kappa_{^1H}$ is equal to 1 for $I=^2H$, ^{13}C , ^{31}P .

Numerical Simulations

The performance of the discretized BURP pulses can be analyzed by numerical simulation. This will be done with the example of inversion pulse I-BURP-1 [113, 133], as shown in Figure 7.5. Continuous and pointwise $\beta(t)$ values agree closely with one another for $N \gtrsim n_{\rm max}$. For instance, for N > 10, the fractional difference between $\beta(t)$ and the connecting line between sampling points $\beta(j\tau_p/N)$ is below 0.05 for all time points.

The inversion can be quantified by

$$\hat{R}_{zz}(\kappa) \equiv \mathbf{e}_z \cdot \hat{R}(\kappa, \mathbf{n}_1', \dots, \mathbf{n}_N', \mathbf{n}_1'', \dots, \mathbf{n}_N'') \mathbf{e}_z . \tag{7.18}$$

A value of $\hat{R}zz(\kappa) = -1$ signifies complete spin inversion, while $\hat{R}zz(\kappa) = +1$ indicates no net rotation of the spin away from \mathbf{e}_z . As observed from the plots on the right-hand side of Figure 7.5, $\hat{R}_{zz}(\kappa)$ exhibits an inversion passband with a full width at half-maximum of $2\delta \approx 5/N$. For moderate values of N (around 20), this width should be sufficiently broad to allow for generous error tolerance (e.g., $2\delta \sim 0.25$), while maintaining selectivity in γ .

Experimental Performance

The band-pass profiles of the pulses depicted in Figure 7.5 can be measured by employing a sample consisting solely of a single spin species, such as 1H in water (1H_2O). In low-field conditions, the rotation axes \mathbf{n}' and \mathbf{n}'' remain independent of γ , while κ is directly proportional to γ and the pulse duration. Therefore, the impact of a change in γ can be simulated by an equivalent alteration in the pulse duration.

The performance of the spin-selective inversion pulses is evaluated by applying a composite pulse, immediately followed by a DC pulse with a flip angle of 90° along $+\mathbf{e}_x$. The peak field of the composite pulse is adjusted to ensure that the lengths of I-BURP-1 pulses are comparable for different values of N, approximately $(\tau_p/\kappa) \sim 8\,\mathrm{ms}$ for $^1\mathrm{H}$. Subsequently, the resulting FID is detected by the magnetometer situated adjacent to the flow cell.

The amplitude of the observed FID for composite pulses of duration $\kappa \tau_p$ is represented by S_{κ} , while the FID amplitude in the absence

⁸ While the BURP pulse has a duration τ_p , the pointwise approximation does not. This is because the actual rotation sequence is not dependent on the absolute value of τ_p , as demonstrated by Equation 7.14.

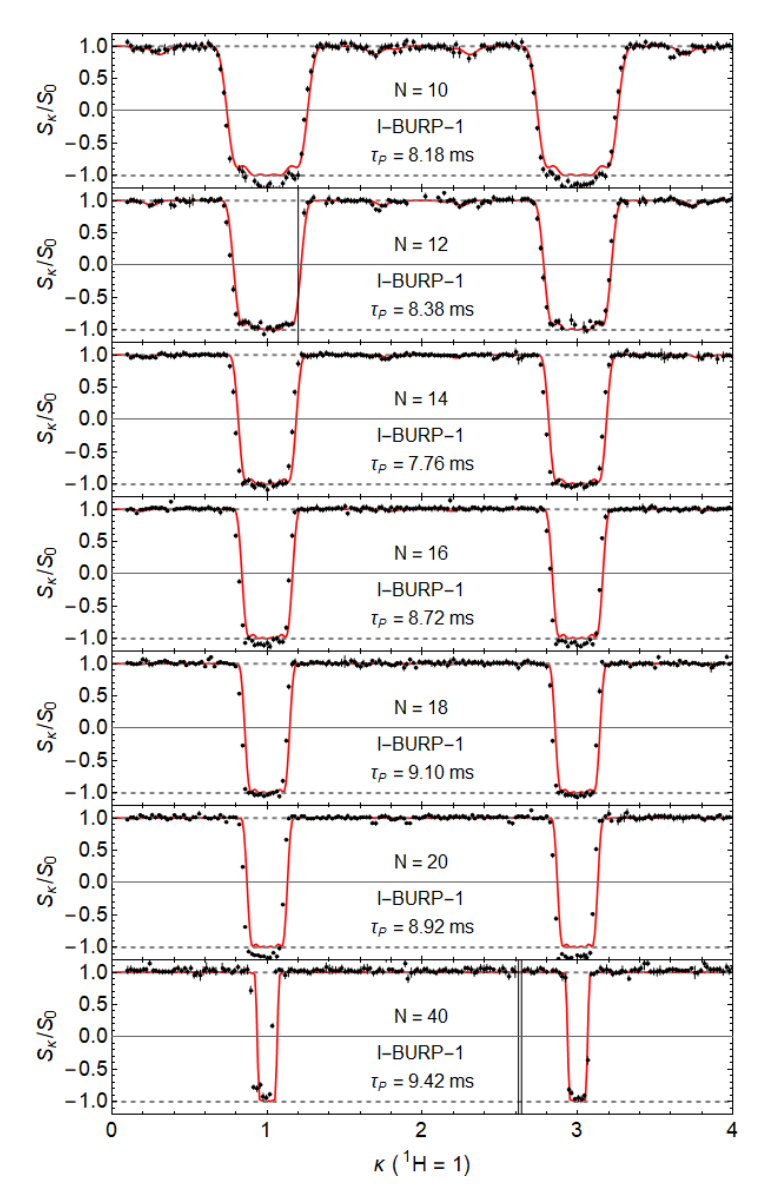


Figure 7.6: The experimental (black circles) versus simulated (solid red curves) band-pass inversion profiles for discrete I-BURP-1 pulses with N = 10, 12, 14, 16, 18, 20 and 40. Each data point represents the mean signal amplitude of approximately 10 NMR transients.

of any applied composite pulse is denoted as S_0 . The ratio S_{κ}/S_0 corresponds to $\hat{R}_{zz}(\kappa)$, which takes values ranging from -1 (indicating complete spin inversion) to +1 (indicating no spin inversion). These values are plotted for various pulses up to $\kappa=4$ in Figure 7.6.

The experimental and simulated profiles exhibit a close agreement, with residuals falling within the margins of experimental error. This outcome confirms the feasibility of designing spin-selective pulses using the approach described in Equation 7.10. Furthermore, it suggests that any imperfections present in the pulses are negligible compared to the compensation limits, which is remarkable considering the simplicity of the electronic drive circuitry.

7.5 PHASE ALTERNATING COMPOSITE PULSES

Another result of this approach is the development of DC counterparts of wide-offset-tolerant AC composite pulses. In the context of high-field NMR, these pulses are commonly referred to as *phase-alternating composite pulses* [131, 132, 139–141], due to the alternating sign of the flip angle in the AC frame (e.g. $\beta_1 = 59^\circ$, $\beta_2 = -298^\circ$, and $\beta_3 = 59^\circ$ [132]). These angles can be directly mapped to a meridional composite pulse using $\phi_j = \beta_j$. By employing the same concept of DC pulse pairs, the required flip angles can be generated in the DC regime.

Optimized Parameters

Table 7.1 presents a selection of phase-alternating composite pulses for inversion along with the corresponding passband widths. Remarkably, highly uniform inversion can be achieved using only a few pulses (N < 10), offering a level of selectivity comparable to or even better than I-BURP-1.

It is important to note that the passband widths may vary across different studies due to variations in optimization criteria. Typically, achieving uniform excitation within the passband receives the highest priority, followed by effective rejection in the stopband. However, in certain low-field NMR applications, both of these criteria may hold equal importance. Hence, the present work encompasses additional solutions to cater to these diverse requirements.

The original sequences reported in Table 7.1 were found in a few minutes with a standard desktop computer, by randomly sam-

N	angles (degree)		Stopband	Passband	Reference	
	ϕ_1	ϕ_2	ϕ_3	$(\tilde{R}_{zz}(\kappa)$	$(\hat{R}_{zz}(\kappa)$	
	ϕ_4	ϕ_5	ϕ_6	> 0.99)	< -0.95)	
	ϕ_7	ϕ_8	Ф9			
2	60	-24 0		$ \kappa < 0.20$	$0.83 < \kappa < 1.17$	here [113]
3	59	-298	59	$ \kappa < 0.36$	$0.93 < \kappa < 1.07$	[132]
3	24	-97	253	$ \kappa < 0.24$	$0.75 < \kappa < 1.25$	here [113]
4	-34 289	123	-198	$ \kappa < 0.29$	$0.86 < \kappa < 1.14$	[131], [139]
4	27 -30	-81	263	$ \kappa < 0.29$	$0.75 < \kappa < 1.25$	here [113]
5	325 -263	_	56	$ \kappa < 0.41$	$0.95 < \kappa < 1.05$	[132]
9	_	-238 276 -238		$ \kappa < 0.55$	$0.89 < \kappa < 1.11$	here [113]

Table 7.1: Composite pulses for the inversion operation ${\bf e}_z \to -{\bf e}_z$. All angles ϕ_j are given in degrees.

pling ~ 50000 points in a N-1 dimensional space of ϕ values $\phi_1, \phi_2, \ldots, \phi_{N-1}$, with resolution $0.02 \times \pi$ rad. The final angle is constrained to be

$$\phi_N = \pi - \sum_{j=1}^{N-1} \phi_j \quad , \tag{7.19}$$

so that $\beta = \pi$. Our merit function is $l_1 + l_2$, where l_1 is the mean value of $(1 + \hat{R}_{zz}(\kappa))^2$ over the range $0.8 < \kappa < 1$ and l_2 is the mean of $(1 - \hat{R}_{zz}(\kappa))^2$ for $|\kappa| < 0.5$.

Trajectories

The table in Table 7.1 presents angle sets with lengths up to N=9, which offer the widest passband and stopband widths. In general, these sequences demonstrate a broader passband compared to phase-alternating composite pulses of the same length N. Achieving an increased width of the stopband is more challenging and necessitates higher values of N. The performance of these pulses is depicted in Figure 7.7, while the Supplemental Material [113] includes a collection of animations that facilitate visualizing the spin vector trajectories during the pulses.

Experimental Performance

Figure 7.8 shows the band-pass profiles of the phase alternating composite pulses in a similar way as in Figure 7.6. The performance of the spin-selective inversion pulses is evaluated again by applying a composite pulse, immediately followed by a DC pulse with a flip angle of 90° along $+\mathbf{e}_{x}$. The experimental and simulated profiles exhibit a close agreement, with residuals falling within the margins of experimental error.

7.6 OUTLOOK

Contrary to high-field NMR, where phase/frequency offsets and flipangle offsets arise from separate imperfections in the experimental setup and produce distinct effects on the resulting spin rotations, low-field NMR exhibits different behavior. In low-field NMR, both the flip angle and axis are determined by the strengths of the dc fields. As illustrated, this characteristic enables a single composite

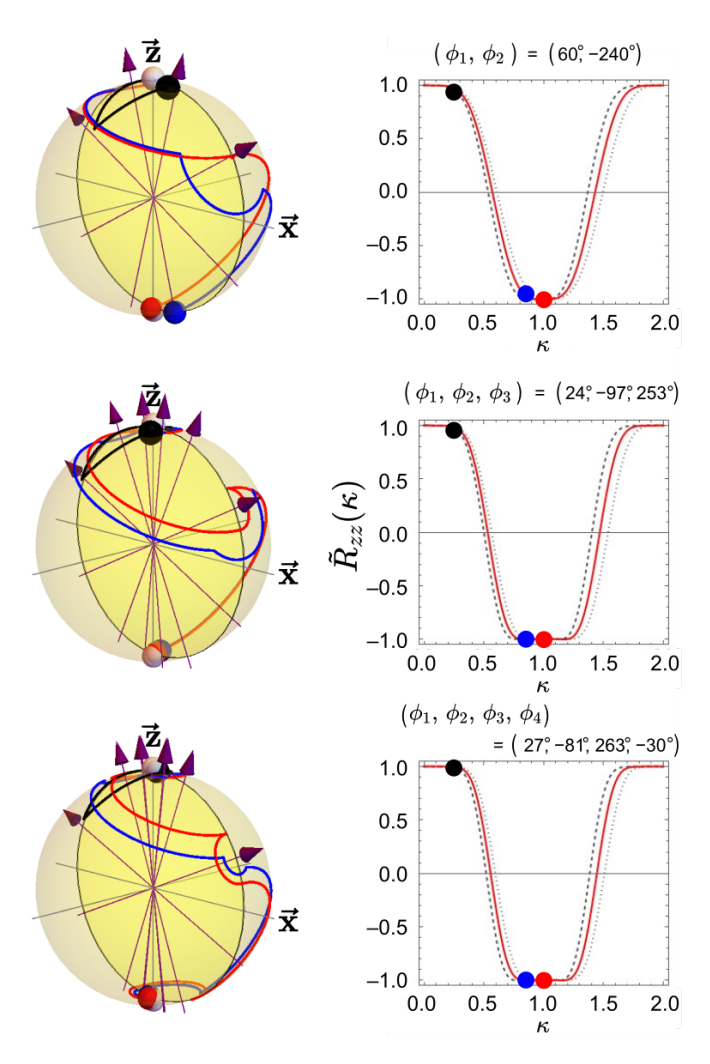


Figure 7.7: The Bloch sphere spin vector trajectories and band-pass inversion profiles are depicted for the selected composite pulses listed in Table 7.1. The trajectories represented by black, blue, and red curves correspond to values of $\kappa=0.25$, $\kappa=0.85$, and $\kappa=1.0$ respectively. The rotation axes, indicated by purple arrows, are symmetrically displaced about \mathbf{e}_z within the x-z plane. The solid red curve illustrates the band-pass profile $\mathbf{e}_z \to -\mathbf{e}_z$ for a perfectly calibrated set of coils, while the dashed and dotted gray curves correspond to profiles where the z coil is mis-calibrated by $\pm 10\,\%$ respectively.

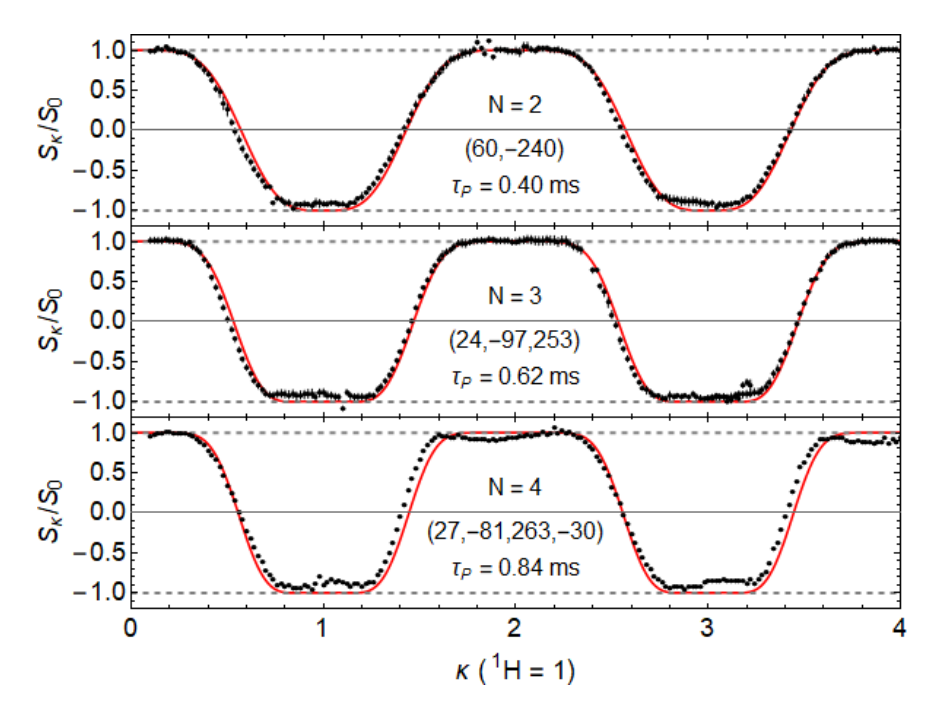


Figure 7.8: Just like in Figure 7.6, the experimental data for the phase-alternating composite pulses is represented by black circles, while the simulated data is depicted by solid red curves. The plots illustrate the band-pass inversion profiles for meridional composite pulses with N=2, 3, and 4, as listed under "this work" in Table 7.1. Each data point corresponds to the average signal amplitude of around 10 NMR transients.

pulse strategy to withstand variations in both factors, which is not typically observed in high-field composite pulses.

Also, unlike many high-field NMR composite pulses, the criterion that determines the total flip angle of a meridional composite pulse (Equation 7.10) is not restricted to specific angles (e.g., 90° or 180°). As a result, it enables the generation of pulses with arbitrary flip angles. This general design approach, in combination with the aforementioned error compensation properties, holds significant value in spin resonance applications at low fields, where robust and selective control is required. The duration of these pulses is considerably shorter compared to high-frequency AC pulses with equivalent compensation bandwidth, such as swept-frequency adiabatic inversion pulses [142]. Moreover, these pulses can be performed without the need for tuned high-frequency circuitry [143]. The anticipated applications encompass sub-MHz NMR spectroscopy and MRI, field-cycling relaxation measurements, nuclear spin polarimetry, as well as portable NMR spectrometers for usage beyond research laboratories.

The pulse durations τ_p demonstrated here and in Bodenstedt et al. [113, 114] are constrained by the hardware timer resolution (2 µs) and the field-to-current ratio of the x coil. Higher clock speeds and stronger fields, considering the electrical inductance of the coils, could potentially reduce pulse lengths by at least one order of magnitude, resulting in τ_p ranging from 10 µs to 100 µs. These durations are significantly shorter than the periods of the spin-spin scalar couplings between common nuclear spin species, making them suitable for heteronuclear quantum control in low-field NMR applications. In such cases, the pulses selectively rotate one or more spins in a multi-species system. The selectivity and error tolerance of these pulses should complement existing control methods that rely on equatorial composite pulses [114, 144].

DECOUPLING OF SPIN DECOHERENCE PATHS

This chapter focuses on the examination of nuclear spin relaxation close to zero magnetic fields and explores its manipulation through dynamical decoupling pulse sequences. The discussion closely follows the content presented in the publication Bodenstedt et al. [114].

The thermodynamic behavior of a system is typically determined by its internal degrees of freedom, which rely on chemical and physical properties like inter-particle couplings and symmetry. While these properties may not be easily altered, it is widely recognized that the effect of internal properties on system dynamics can be controlled by manipulating the symmetry of the external environment. For instance, dynamical decoupling [145–148], spin locking [149, 150], magnetic field cycling [17, 150, 151] and other symmetry switching techniques [152] can influence the rates at which a spin ensemble relaxes to thermodynamic equilibrium. These techniques allow the internal variables (such as spin dipole-dipole or spin-rotation couplings) to be probed, even though relaxation is characterized by local, random interactions that fluctuate extremely rapidly relative to coherent time scales.

For a given spin system, the near-zero-field regime is characterized by inter-spin couplings that are significantly larger in magnitude than couplings with external magnetic fields. One appeal of zero field is the efficiency of nuclear spin hyperpolarization techniques close to zero field, such as ¹³C polarization via parahydrogen [153–155]. However, interference of other nuclei, especially those that possess a quadrupolar moment, has been shown to tremendously reduce polarization lifetimes and polarization transfer efficiency [156–158].

8.1 COHERENT AVERAGING THEORY

Average Hamiltonian theory is a useful approximation technique in quantum physics and especially in NMR to get analytical insight into time-dependent Hamiltonians. Here the same concept is applied to analyze the effect of a decoupling sequence on a simple model system close to zero-field.

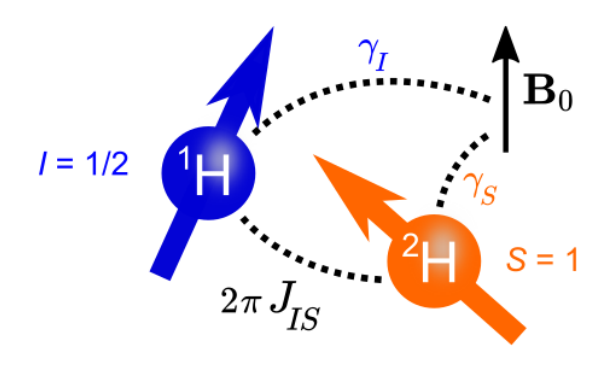


Figure 8.1: Model spin system consisting of two coupled hydrogen nuclei $I = {}^{1}\text{H}$ and $S = {}^{2}\text{H}$ in a constant magnetic field \mathbf{B}_{0} .

Model System

The analysis focuses on a dual-species system (see Figure 8.1), denoted as IS, where the relaxation of the I species is comparatively slow in comparison to the strength of couplings with the S species and the self-relaxation of S. The polarization lifetime of I is thus limited by S, however, the limit may be overcome by dynamically decoupling either spin from the other. The scenario is experimentally applied to I nuclei of spin quantum number 1/2 (hydrogen-1) that couple to S nuclei with nonzero electric quadrupole moment (spin ≥ 1 , namely nitrogen-14 or deuterium).

Hamiltonian

The *IS* pair evolves freely via spin-spin and spin-field couplings (se Figure 8.1) given by a Hamiltonian

$$\hat{H}(J_{IS}, \mathbf{B}) = \frac{2\pi J_{IS}}{\hbar} \cdot \hat{\mathbf{S}} \cdot \hat{\mathbf{I}} - \gamma_I \cdot \hat{\mathbf{I}} \cdot \mathbf{B} - \gamma_S \cdot \hat{\mathbf{S}} \cdot \mathbf{B} , \qquad (8.1)$$

where J_{IS} is the strength of the coupling, $\mathbf{B} = \{B_x, B_y, B_z\}$ denotes the magnetic field vector, γ_I and γ_S are the gyromagnetic ratios.

Discrete Time Evolution

The system is assumed to experience pulsed magnetic fields at regular time intervals τ to rotate the spin state instantaneously and periodically, such that

$$\mathbf{B}(t) = \mathbf{B}_0 + \sum_{j=1}^{n} \mathbf{B}_j \delta(t/\tau - j) ,$$
 (8.2)

where δ is the DIRAC¹ function, \mathbf{B}_0 is the constant bias field and $\{\mathbf{B}_j\}$ are the field pulse amplitudes. The spin density operator $\hat{\rho}$ after n pulse-delay events is expressed mathematically as

$$\hat{\rho}(n\tau) = \prod_{j=1}^{n} \hat{R}_{j} \exp\left(\hat{\mathcal{L}}_{0}\tau\right) \hat{\rho}(0). \tag{8.3}$$

Here superoperators $\{\hat{R}_j\}^2$ denote each transformation under the pulsed fields, $\hat{\mathcal{L}}_0$ is the Liouvillian superoperator defined by the master equation

$$\frac{\mathrm{d}\hat{\rho}}{\mathrm{d}t} = \hat{\mathcal{L}}_0 \hat{\rho} = \hat{H} \hat{\rho} - \hat{\Gamma} \hat{\rho} \tag{8.4}$$

with

$$\hat{H}\hat{\rho} = -\frac{\mathrm{i}}{\hbar} [\hat{H}(J_{IS}, \mathbf{B}_0)\hat{\rho} - \hat{\rho}\hat{H}(J_{IS}, \mathbf{B}_0)]$$
(8.5)

and $\hat{\Gamma}$ is the relaxation superoperator. For simplicity – and because in the experiments later described the equilibrium polarization of the spin system is negligible compared to that of the initially prepared state – the thermal equilibrium density operator is ignored.

Coherent Averaging

Coherent averaging theory is used to transform the right-hand side of Equation 8.3 into a simple form

$$\hat{\rho}(n\tau) = \exp\left(\overline{\mathcal{L}}n\tau\right)\hat{\rho}(0) , \qquad (8.6)$$

where $\overline{\mathcal{L}}$ is the *average Liouvillian*. The lowest-order terms of $\overline{\mathcal{L}}$

- 1 Paul Dirac (1902–1984) was a British theoretical physicist who made groundbreaking contributions to quantum mechanics and quantum field theory, including the formulation of the Dirac equation and the prediction of the existence of antimatter, and he was awarded the Nobel Prize in Physics in 1933.
- 2 The rotation superoperators \hat{R} can be derived from rotation operators \hat{R} via $\hat{R}\hat{\rho} = \hat{R}\hat{\rho}\hat{R}^{-1}$.

Note that $\overline{\mathcal{L}}$ still has the dimensions of a superoperator. For improved readability, the double-hat $\hat{\cdot}$ notation is omitted.

$$\overline{\mathcal{L}} = \hat{\mathcal{L}}^{(0)} + \hat{\mathcal{L}}^{(1)} + \dots$$
 (8.7a)

$$\hat{\mathcal{L}}^{(0)} = \frac{1}{n} \sum_{i=1} \hat{\mathcal{L}}'_{i}$$
 (8.7b)

$$\hat{\mathcal{L}}^{(1)} = \frac{1}{2n} \sum_{j=1,k < j} [\hat{\mathcal{L}}'_j, \hat{\mathcal{L}}'_k], \tag{8.7c}$$

with

$$\hat{\mathcal{L}}'_{j} = \hat{R}_{n} \hat{R}_{n-1} \dots \hat{R}_{j} \hat{\mathcal{L}}_{0} \hat{R}_{j}^{-1} \dots \hat{R}_{n-1}^{-1} \hat{R}_{n}^{-1}, \tag{8.7d}$$

are the most important to consider, but if τ^{-1} is fast compared to both J_{IS} and $\gamma |\mathbf{B}|$ then $\overline{\mathcal{L}} = \hat{\mathcal{L}}^{(0)}$ is a good approximation. In this form the combined dynamic effects of \hat{H} and $\hat{\Gamma}$ may be analyzed.

Decoupling under Selective and Collective XY4 Pulse Sequences

Three distinct scenarios for $\{\hat{R}_j\}$ are considered: For sake of reference, the *first* is where all transformations

$$\hat{\hat{R}}_{j} = \hat{\hat{\mathbb{I}}} \tag{8.8}$$

equal an identity operation (no pulses i.e. $\mathbf{B}_{i>0} = \mathbf{0}$).

The *second* is where pulses rotate the I spin vector by π radians alternately about x and y axes, leaving the S spin vector unchanged:

$$\hat{\hat{R}}_1 = \hat{R}_x^{(I)}(\pi)\hat{R}_x^{(S)}(0) \tag{8.9a}$$

$$\hat{R}_2 = \hat{R}_y^{(I)}(\pi)\hat{R}_y^{(S)}(0) \tag{8.9b}$$

$$\hat{R}_3 = \hat{R}_x^{(I)}(\pi)\hat{R}_x^{(S)}(0) \tag{8.9c}$$

$$\hat{R}_4 = \hat{R}_y^{(I)}(\pi)\hat{R}_y^{(S)}(0) \tag{8.9d}$$

This repeated unit of the pulse sequence is denoted as $XY_4(I)$ and is the zero-field analog of the CARR³-PURCELL sequence for I [159].

³ Herman Carr (1924–2008) was an American physicists and pioneer of magnetic resonance imaging.

Thirdly, both I and S are rotated by π alternately about the x and y axes, which is denoted as XY4(I+S):

$$\hat{\hat{R}}_1 = \hat{R}_x^{(I)}(\pi)\hat{R}_x^{(S)}(\pi) \tag{8.10a}$$

$$\hat{\hat{R}}_2 = \hat{R}_y^{(I)}(\pi)\hat{R}_y^{(S)}(\pi) \tag{8.10b}$$

$$\hat{\hat{R}}_3 = \hat{R}_x^{(I)}(\pi)\hat{R}_x^{(S)}(\pi) \tag{8.10c}$$

$$\hat{\hat{R}}_4 = \hat{\hat{R}}_y^{(I)}(\pi)\hat{\hat{R}}_y^{(S)}(\pi)$$
 (8.10d)

:

It can be shown in the latter scenarios that $\hat{\mathcal{L}}^{(0)}$ does not contain any terms that are linear in the spin operator of the spin that is rotated. As an example, $XY_4(I+S)$ eliminates all \mathbf{B}_0 terms from $\hat{\mathcal{L}}^{(0)}$ meaning that the system behaves as if the field is zero. In contrast, $XY_4(I)$ averages $\hat{I}_x\hat{S}_x$, $\hat{I}_y\hat{S}_y$ and $\hat{I}_z\hat{S}_z$ to zero, so that the coupling between the spins appears to vanish.

Figure 8.2 shows the effect of XY4 through matrix representations of contributions to $\hat{\mathcal{L}}^{(0)}$. Nonzero matrix elements are shaded corresponding to $\operatorname{tr}(\hat{q}^{\dagger}\hat{\mathcal{L}}^{(0)}\hat{p})\neq 0$ for spherical tensor operators $\hat{p},\hat{q}\in\{\hat{T}_{l,m}\}$; this basis is chosen for the representation since both $\hat{\Gamma}$ and $\hat{\mathcal{H}}$ matrices are block diagonal in the projection quantum number m. The first three columns represent each line of Equation 8.1 and confirm the behavior described above, wherein Figure 8.2b spin coupling terms are absent and in Figure 8.2c the field \mathbf{B}_0 is averaged to zero.

Figure 8.2 highlights the different spherical symmetry of the spin-spin and spin-field couplings. The J_{IS} coupling is invariant to the global rotation of the quantization axis and therefore overall angular momentum cannot be changed, so in the first column, only basis operators with $l_p = l_q$ and $m_p = m_q$ are connected. The Zeeman interaction, however, may connect operators with $m_p = m_q$ or $m_p = m_q \pm 1$. Matrices for dipole-dipole relaxation and cross-correlated [148] random field relaxation in the motional narrowing limit represented in the two right-hand columns are also diagonal in l and m, except for dipole-dipole relaxation under XY4(l) where rotation symmetry is broken slightly. Due to the different symmetries, contributions to $\hat{\mathcal{L}}^{(0)}$ do not share a common eigenbasis. This means that eigenvalues of $\hat{\Gamma}$ generally do not equate to overall relaxation rates, and, moreover, that overall relaxation of the system depends

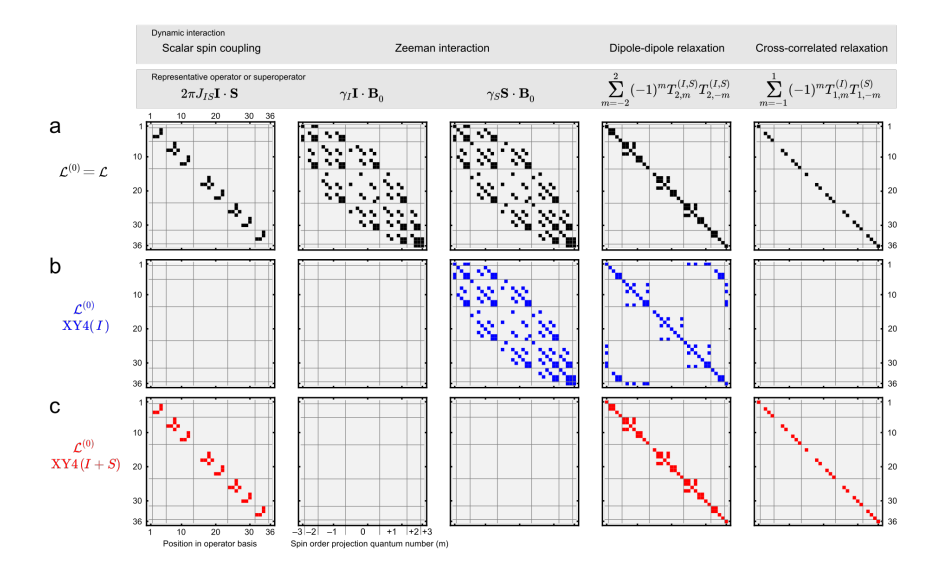


Figure 8.2: Symbolic matrix representations of $\hat{\mathcal{L}}^{(0)}$ for interactions within a two-particle system comprising spin-1/2 (I) and spin-1 (S) species. The representation is made in the spherical tensor operator basis sorted by projection index m to illustrate block diagonal properties, where gray lines demarcate blocks of different m. Shading corresponds to a nonzero matrix element of $\hat{\mathcal{L}}^{(0)}$ between two basis operators, and the matrix dimension equals the number of basis operators $(2I+1)^2(2S+1)^2=36$. Three scenarios are presented: **a** free evolution, i.e. $\hat{\mathcal{L}}^{(0)}=\hat{\mathcal{L}}_0$, **b** XY4 applied to the I spin, **c** XY4 applied to both I and S. Analytical expressions for all matrix elements are provided in the Supporting Information of Bodenstedt et al. [114].

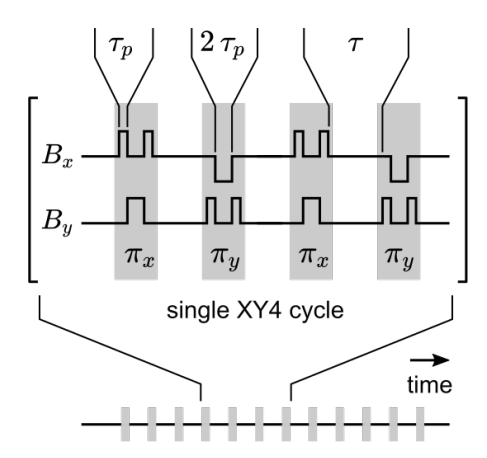


Figure 8.3: Pulse sequence comprising a periodic train of dc rotation pulses of duration $4\tau_p$ and effective flip angle π , which are separated by a time delay τ . Alternate pulses are applied along the x and y axes.

on the pulse sequence used. In this example, XY₄(*I*) averages out cross-correlated relaxation.

8.2 ZERO-FIELD IMPLEMENTATION OF THE XY4 PULSE SEQUENCE

The results of the previous chapter (see Chapter 7) can be directly applied to realize the XY4 pulse sequence at ultralow fields. Here, composite π pulses in combination with magic ratios will be used to apply selective and collective spin inversions on hydrogen-1, deuterium, and nitrogen-14.

Selective and Collective Spin Inversion

For $I={}^{1}\mathrm{H}$ and $S={}^{2}\mathrm{H}$ the nominal operation $\hat{R}_{x}^{(I)}(\pi)\hat{R}_{x}^{(S)}(0)$ is approximated using a composite of three dc pulses (Figure 8.3 that rotates the I spin first by $\pi/2$ about the x axis, then π about y and finally $\pi/2$ about x, since for the ratio $u=\gamma_{S}/\gamma_{I}\approx 0.154$ in this case it is found that

$$\hat{\hat{R}}_{x}^{(I)}(\pi/2)\hat{\hat{R}}_{y}^{(I)}(\pi)\hat{\hat{R}}_{x}^{(I)}(\pi/2) = \hat{\hat{R}}_{x}^{(I)}(\pi)$$
(8.11a)

$$\hat{R}_{x}^{(S)}(u\pi/2)\hat{R}_{y}^{(S)}(u\pi)\hat{R}_{x}^{(S)}(u\pi/2) \approx \hat{R}_{x}^{(S)}(0).$$
 (8.11b)

If pulse flip angles are multiplied by v to approximate $\pi/2$ and π rotations on the S spin, the same dc pulse sequence can be used

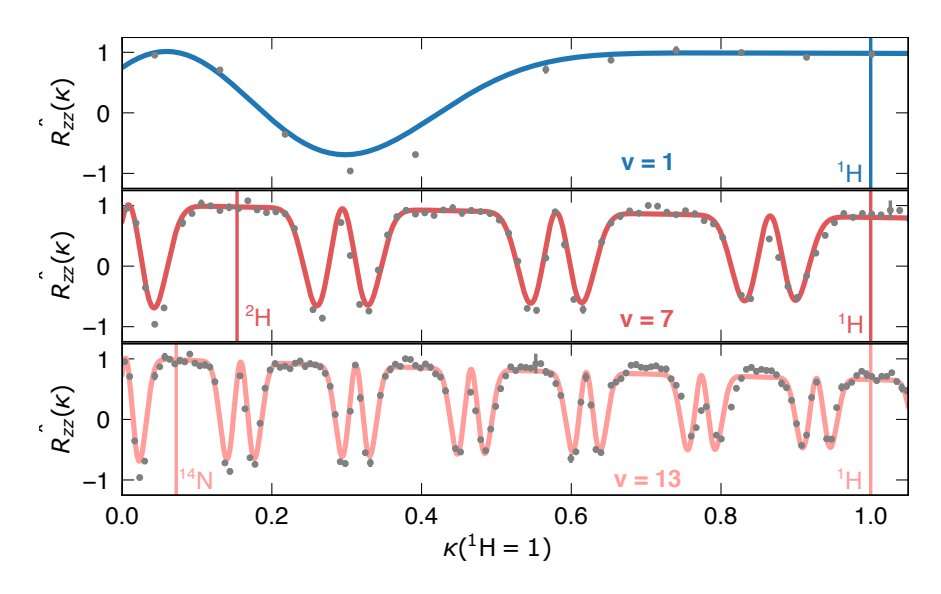


Figure 8.4: Experimental benchmark of XY4. Data points show amplitudes of the *z*-magnetization following four phase-cycled composite pulses κ . The solid line gives the fit to the analytical model $\hat{R}_{zz}(\kappa) = [1091 - 1232\cos(2\theta) + 88\cos(4\theta) + 848\cos(6\theta) + 764\cos(8\theta) + 368\cos(10\theta) + 104\cos(12\theta) + 16\cos(14\theta) + \cos(16\theta)]/2048$ using $\theta = 2\pi v \kappa$.

to produce $R_x^{(I)}(\pi)R_x^{(S)}(\pi)$ transformations, provided that v is odd and (1-|vu|) is less than the error-compensation bandwidth of the overall rotation [128]. Here v=7 yields

$$\hat{R}_{x}^{(I)}(v\pi/2)\hat{R}_{y}^{(I)}(v\pi)\hat{R}_{x}^{(I)}(v\pi/2) = \hat{R}_{x}^{(I)}(\pi)$$
(8.12a)

$$\hat{R}_{r}^{(S)}(vu\pi/2)\hat{R}_{v}^{(S)}(vu\pi)\hat{R}_{r}^{(S)}(vu\pi/2) \approx \hat{R}_{r}^{(S)}(\pi) . \tag{8.12b}$$

Consequently, $XY_4(I)$ and $XY_4(I+S)$ can be implemented using dc pulses.

Figure 8.4 shows the spin inversion profile for the two scenarios (Figure 8.4a and Figure 8.4b) for a full XY4 pulse cycle. Figure 8.4c shows that for v = 13 collective spin inversion can also be achieved for the $I = {}^{1}\text{H}$ and $S = {}^{14}\text{N}$ spin pair (here ${}^{2}\text{H}$ spins are almost not affected by the pulse sequence).

Numerical Simulations

Numerical simulations demonstrate that both versions of XY4 are highly accurate when applied using DC pulses of finite length. For

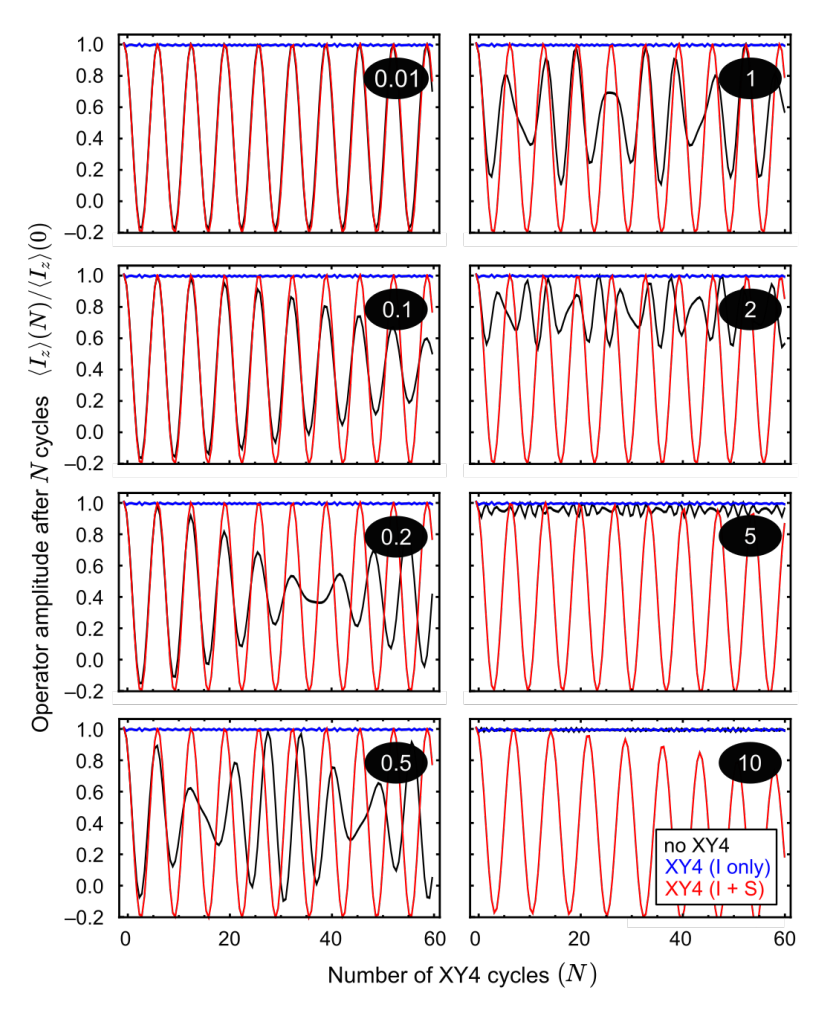


Figure 8.5: Numerically simulated trajectories of I-spin polarization along the z axis during the sequence shown in Figure 8.3. Representative values $J=2.5\,\mathrm{Hz}$, and $\tau=0.01\,\mathrm{s}$ are used. Each plot shows trajectories for a different dimensionless magnetic field $\mathbf{B}_0'\equiv\{0,0,|(\gamma_I-\gamma_S)B_z/(2\pi J_{IS})|\}$ in the crossover regime between strong and weak internuclear coupling, where the z component is marked in the black ovals. Three curves are shown, which correspond to cases of (black, $\tau_p=0\,\mathrm{s}$) no applied pulses, where a clear change in dynamics is observed through the crossover, (blue, $\tau_p=46\,\mathrm{\mu s}$) XY4 pulses on the I spin only, resulting in decoupling and a stationary I-spin polarization, plus (red, $\tau_p=7\times46\,\mathrm{\mu s}$) XY4 pulses on both spins to impose zero-field conditions, resulting in polarization oscillations.

Note that the thermal equilibrium density operator is ignored here. example, Figure 8.5 shows the evolution of a ${}^{1}\text{H}$ - ${}^{2}\text{H}$ spin pair starting from $\hat{\rho}(0) = \hat{I}_z/\hbar$ versus the number of XY4 cycles applied. Each panel shows a different condition of a dimensionless magnetic field

$$\mathbf{B}_0' \equiv \begin{pmatrix} 0 \\ 0 \\ \left| (\gamma_I - \gamma_S) \cdot \frac{B_z}{2\pi J_{IS}} \right| \end{pmatrix} \tag{8.13}$$

between strong and weak coupling regimes. The strong coupling regime is marked by $|\mathbf{B}_0'| < 1$ and corresponds to the plots in the left-hand column, while weak coupling is marked by $|\mathbf{B}_0'| \gg 1$. In the simulation, $J_{IS} = 2.5$ Hz is chosen as a typical coupling between $^1\mathrm{H}$ and $^2\mathrm{H}$ nuclei attached to adjacent carbon atoms in an aliphatic chain, thus the range of B_z is nT to $700\,\mathrm{nT}$, and the interval between pulse centers, $\tau = 0.01\,\mathrm{s}$ is much shorter than $1/J_{IS} = 0.4\,\mathrm{s}$. Differences between the curves are immediately seen. In the case of free evolution nearest to zero fields (black curves, $|\mathbf{B}_0'| = 0.1$), the expectation value of \hat{I}_z oscillates at a frequency J_{IS} corresponding to polarization exchange back and forth with S. At the high-field end, the expectation value is roughly constant because the secular part of the Hamiltonian commutes with \hat{I}_z .

In agreement with the analysis presented earlier, all $XY_4(I)$ and $XY_4(I+S)$ trajectories are invariant across the range of B_z and converge to the free-evolution system behavior in the high- and zero-field limits. The simulations therefore confirm that the error

$$\left(1 - \frac{\gamma_{1_{\rm H}}}{7\gamma_{2_{\rm H}}}\right) \approx 0.06 \tag{8.14}$$

lies within the inversion bandwidth of the pulses (see Figure 8.4) and that the phase cycle compensates for residual imperfections.

Pulsed Induced Relaxation

The long-term fidelity of composite π -pulse trains in combination with XY4 phase cycling was also validated. Figure 8.6 shows fitted phases and amplitudes of the $\pi/2$ ¹H precession signal in water following the sequence shown in Figure 3a of the main text. Pulse lengths τ_p were set equal to v=1 (blue), v=7 (orange) and v=13 (green) times the $\pi/2$ dc pulse length for ¹H, corresponding to coincident π rotations on ²H or ¹⁴N.

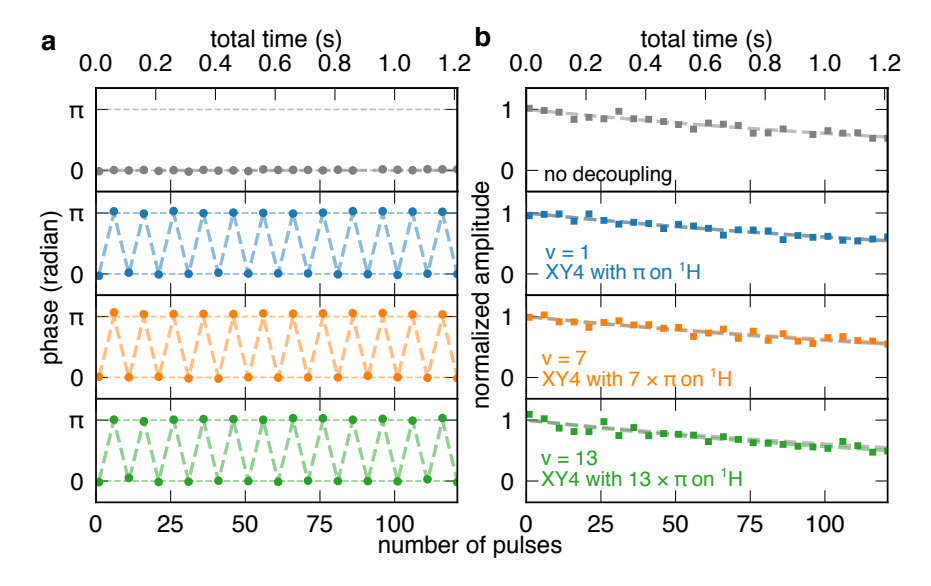


Figure 8.6: Phase (a) and normalized amplitude (b) of a proton precession signal after a variable number of XY4 pulses.

The time between two composite π -pulses was fixed to $\tau=10\,\mathrm{ms}$, resulting in an overall delay between pre-polarization and acquisition of between $\tau=0\,\mathrm{ms}$ and $\tau=1200\,\mathrm{ms}$. The signal amplitudes were fit to an exponential decay function $\propto \exp(-N_{\mathrm{pulses}}\tau/T_1')$ shown by the dashed gray lines in Figure 8.6b, where the plotting curves all have the same time constant $T_1'=2.0(1)\,\mathrm{s}$. These data indicate that Within experimental error the relaxation rate does not depend on v, and from here it is concluded that no additional decoherence is introduced by the DC pulses.

Shimming Procedure

In the absence of decoupling pulse sequences, it is challenging to impose a truly zero field at the location of the NMR sample. On our experimental setup, the sample is placed in a four-layer MuMetal and ferrite shield to screen out Earth's field by a factor of $\sim 10 \times 10^3$, leaving residual fields on the order of 1 nT to 10 nT. These residual fields can be partially compensated for in the x, y, and z direction by applying direct current to coils located inside the shield. The compensation field along each axis is typically determined from shifts in the nuclear Larmor frequency as a function of applied compensation current during the measurement period. However, the

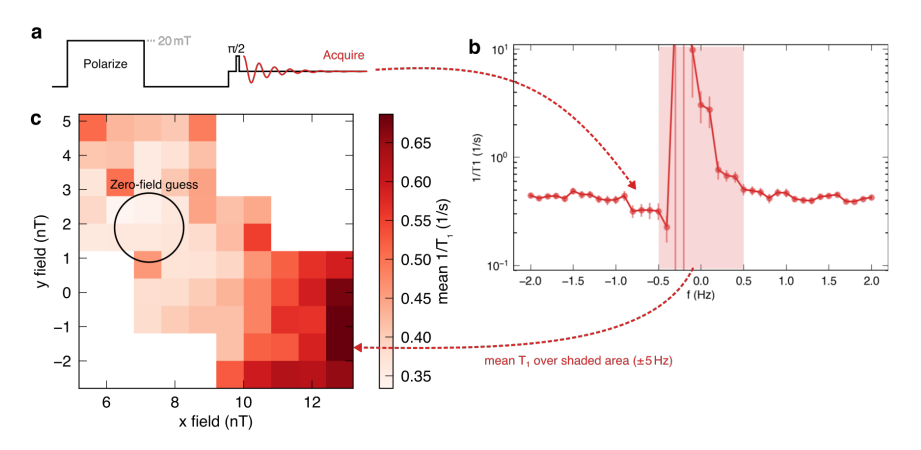


Figure 8.7: Zero-field shimming via effective $1/T_1$ relaxation rate. (a) fast-field-cycling pulse sequence to measure effective decay rate near zero field, for the water sample; (b) fitted monoexponential relaxation rates vs bias field along the z axis; (c) variation in average relaxation rate across the central resonance feature in (b) vs x and y bias magnetic fields. The lightest-shaded pixels indicate the best estimate of zero field.

precision of the correction field is limited by the spin relaxation time T_2^* .

An alternative method is through indirect probing of near-zero-field Rabi oscillations as shown in Figure 8.7. The amplitude of the NMR signal after switching to a high field for detection (Figure 8.7a exhibits approximately monoexponential decay behavior as a function of the time delay between polarization and detection events. The decay rate is equal to the sum of the intrinsic T_1 relaxation rate of the sample as well as an additional, effective, contribution due to residual fields orthogonal to the polarization and detection magnetic fields. As shown in Figure 8.7b, the contribution of the perpendicular field is significant at 1 H Larmor frequencies below 0.5 Hz (consistent with residual fields being on the order of $10\,\mathrm{nT}$) resulting in the central or "zero-field resonance" feature seen in the plot.

Point-by-point adjustment of the perpendicular field can reduce the magnitude of the zero-field resonance feature as shown in Figure 8.7c. Each pixel in the two-dimensional plot represents the mean effective relaxation rate across the region $\gamma_{\rm H}B_z$ between ± 0.5 Hz, corresponding to the region shaded in Figure 8.7b; this mean should be minimized at exactly zero field. The data indicate that the best estimate of zero field is obtainable within an uncertainty of 1 nT to 2 nT. However, while precise, the procedure is extremely time-consuming

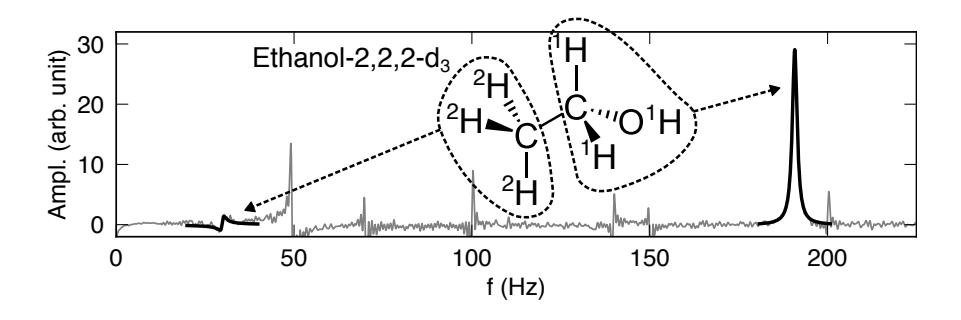


Figure 8.8: Optical-magnetometer-detected NMR spectra of the CH₂OH and CD₃ subsystems at 4.46 μT showing single unresolved resonances for 1 H and 2 H. Respective Larmor frequencies are 191 Hz and 29 Hz and full-widths-at-half-maximum are 1.63(4) Hz and 1.05(23) Hz. Other peaks including 50 Hz and harmonics are due to background technical noise in the laboratory.

and must be repeated every time the magnetic shield is opened (for instance, to perform maintenance or to change the sample).

8.3 SCALAR RELAXATION EFFECTS DUE TO DEUTERIUM

Experimental – anhydrous trideuterated ethanol (CD₃CH₂OH, 99.9 % pure liquid) is chosen as a material to experimentally investigate scalar relaxation near zero field, albeit a more challenging system to analyze than the IS spin pair since it contains six spins in total. The two 1 H nuclei in the CH₂ group are scalar coupled to 2 H spins in the CD₃ with a coupling constant of $^{3}J_{\text{HD}} = 1.2\,\text{Hz}\,[158]$ and are also coupled with the third 1 H nucleus (OH) with $^{2}J_{\text{HH}} = 5.4\,\text{Hz}\,[160]$. In the high-field limit, therefore, all 1 H spins are regarded as coupling strongly to one another and weakly to 2 H. The resulting NMR spectrum contains one broad unresolved line per spin species (Figure 8.9a) [158].

Since ¹H spins couple to one another strongly, the relaxation of their total magnetization $\propto T_{10}^{(I)}$ is quantified by a single exponential time constant, $T_1(^1\text{H})$. The dependence of $T_1(^1\text{H})$ on B_z is measured using a fast-field cycling protocol and presented in Figure 8.9b. The method involves first pre-magnetizing the spins in a $B_z = 20\,\text{mT}$ magnetic field, allowing them to relax for a time τ_{relax} near $B_z = 0$, and finally returning to $B_z = 4.46\,\mu\text{T}$ where a free-precession signal is detected, of amplitude proportional to $\exp(-\tau_{\text{relax}}/T_1(^1\text{H}))$.

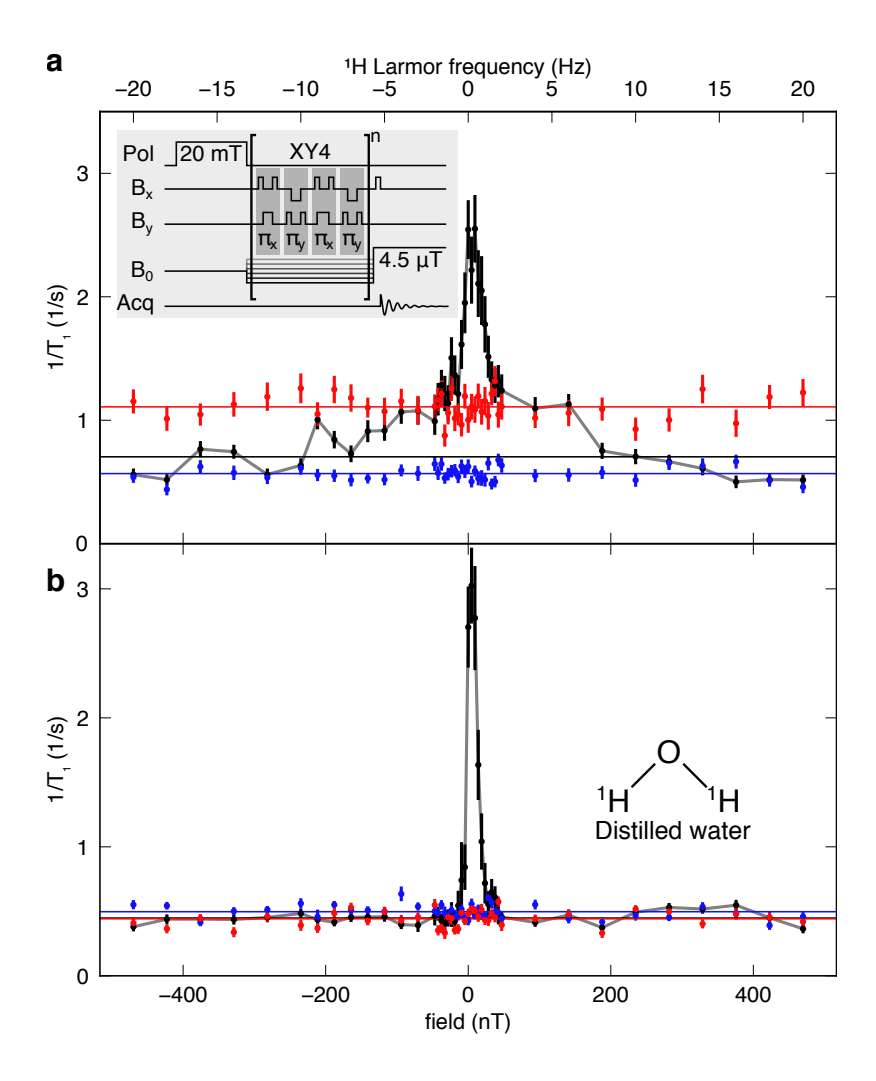


Figure 8.9: Manipulation of 1H nuclear spin evolution near zero fields in pure CD_3CH_2OH and pure H_2O : (b) Fitted monoexponential relaxation rates for the 1H signal in CD_3CH_2OH versus B_z under conditions of (black) free evolution, (blue) $XY_4(^1H)$ and (red) $XY_4(^1H+^2H)$ using v=7; (c) Fitted monoexponential relaxation rates for the 1H signal in H_2O . The same color coding denotes the pulse sequence.

During $\tau_{\rm relax}$ spins may evolve freely or under the constraint of XY4 pulse trains ($\tau_p=46\,\mu {\rm s}$ for I, $\tau_p=324\,\mu {\rm s}$ for I+S using v=7, $\tau=0.01\,{\rm s}$). Qualitatively the dispersion of relaxation rates in Figure 8.9b is consistent with coherent averaging theory where for both XY4(I) (blue) and XY4(I+S) (red) curves the rate is constant across the range $-0.5\,\mu {\rm T} < B_z < 0.5\,\mu {\rm T}$, where $\mathcal{L}^{(0)}$ should not depend on ${\bf B}_0$. The rate difference between XY4(I) and XY4(I+S) is then attributed to scalar relaxation and amounts to $0.5(1)\,{\rm s}^{-1}$ in the ethanol system – in other words, that the $^1{\rm H}$ relaxation time is almost doubled when the coupling to $^2{\rm H}$ is the dominant coherent interaction. For comparison, Figure 8.9cc shows relaxation rates for $^1{\rm H}$ in a sample of pure water ($^1{\rm H}_2{\rm O}$). As ${\rm H}_2{\rm O}$ contains only $^1{\rm H}$ spins, XY4(I) and XY4(I+S) dynamical decoupling sequences are effectively the same, and no rate differences are observed.

There also occurs below $|B_z| = 50\,\mathrm{nT}$ a large increase in the apparent relaxation rate for both CD₃CH₂OH and H₂O in the case of free evolution (black curves in Figure 8.9b and Figure 8.9c). The behavior is attributed to non-secular components B_x and B_y of the background field of order 10 nT, which switches the axis of LARMOR precession away from B_z during $\tau_{\rm relax}$. This hypothesis is confirmed by manual adjustment of the background field to set $B_x = B_y = 0$ and eliminate the feature (see Supporting Information Figure 8.7). However, such a process is extremely time-consuming and due to field drifts must be performed regularly. The absence of the feature for XY4 data indicates that dynamical decoupling is a faster and more reliable method to obviate the effects of residual fields, and is consistent with the absence of \mathbf{B}_0 terms from the lowest-order average Liouvillian.

8.4 SCALAR RELAXATION DUE TO NITROGEN-14

Finally, nitrogen-14 is another spin-1 species abundant in organic compounds such as amines, peptides, and ammonium salts. In many of these compounds, it is found that protic exchange at the nitrogen atom provides efficient pathways for spin decoherence[161–163]. However, in non-exchanging systems the decoherence mechanisms due to $^{14}N^{-1}H$ couplings appear to be much weaker, even negligible. This is shown by the ^{1}H relaxation dispersions plotted in Figure 8.11a-d where for a selection of ^{14}N -containing compounds in D_2O solution ($\approx 2\,\mathrm{M}$), there is no measurable difference between the free evolution, XY4(^{1}H) or XY4($^{1}H^{+14}N$) scenarios despite heteronuclear J couplings of a few Hz [164–166], similar in magnitude to those

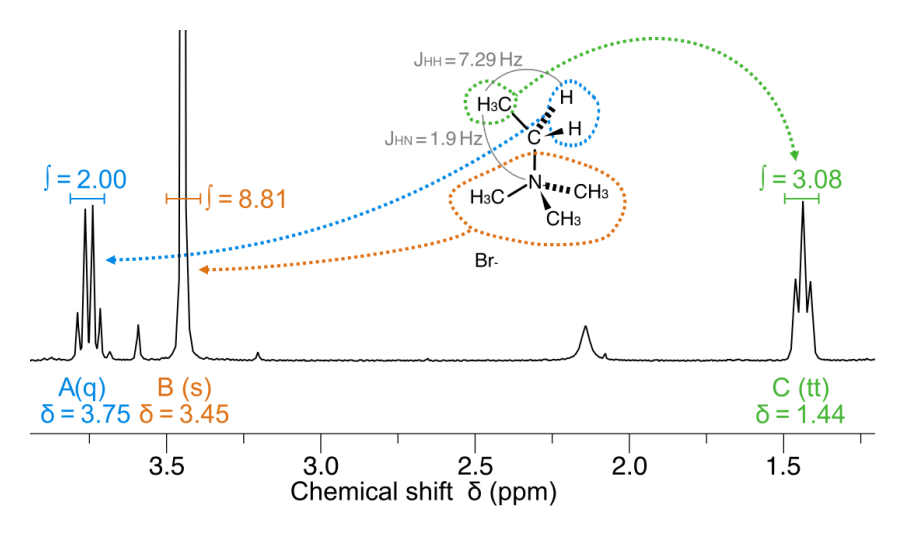


Figure 8.10: ¹H NMR spectrum of ¹⁴NEtMe₃Br at 7.0 T, with horizontal axis in units of ¹H chemical shift (frequency 300 Hz/ppm)

found in [2,2,2-d₃]-ethanol. The hypothesis of weak heteronuclear coupling is supported by a lack of dependence on the point symmetry of the nitrogen atom, which influences the magnitude of the ¹⁴N nuclear quadrupole moment and thus ¹⁴N relaxation rate. It could be argued that the lower number of spin states to which ¹H nuclei may couple, (2S+1)=3 in mono-¹⁴N compounds (Figure 8.11a-c) compared with $(2S+1)^3=27$ in [2,2,2-d₃]-ethanol, limits heteronuclear decoherence effects to below 100 nT total field. Yet, even in this central region, the XY4 sequences should distinguish the ¹⁴N-induced decoherence from effects of residual B_x and B_y components, and neither curve in Figure 8.11 shows significant field dependence.

8.5 REAL-TIME POLARIMETRY OF HYPERPOLARIZED NUCLEAR SPINS

The same XY4 pulse sequence was also used to monitor the polarization level of a hyperpolarized solution non-destructively and in real-time (see Figure 8.12). As described in detail in Mouloudakis et al. [75], the continuous flipping of the 13 C nuclear spins in pyruvate does any measurable increase in relaxation allowing the monitoring of the relaxation decay with T_1 . Previously the sample was hyperpolarized via dissolution DNP.

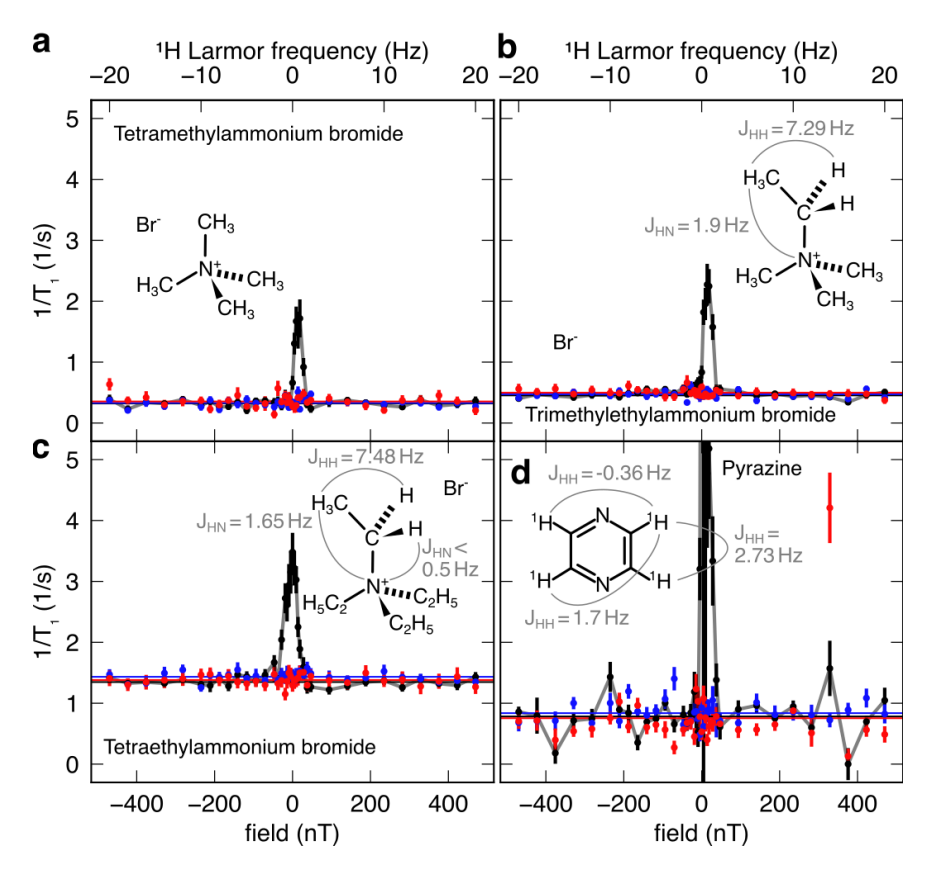


Figure 8.11: Fitted monoexponential relaxation rates for the 1H signal of ^{14}N compounds solvated in D_2O : (a) tetramethylammonium bromide, $N(CH_3)_4Br$; (b) ethyltrimethylammonium bromide, $N(CH_3)_3(CH_2CH_3)Br$; (c) tetraethylammonium bromide, $N(CH_2CH_3)_4Br$; (d) pyrazine, C_4HN_2 . Colors represent the dynamical decoupling conditions: (black) no pulses, free evolution; (blue) $XY4(^1H)$; (red) $XY4(^1H+^{14}N)$ using v=13.

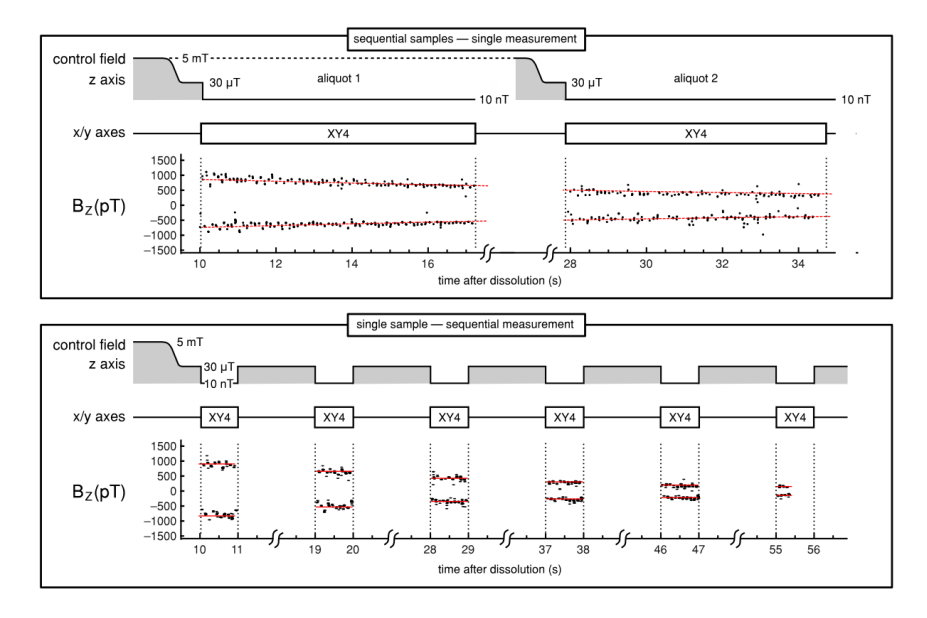


Figure 8.12: The NMR signals recorded for 0.08 M hyperpolarized [1- 13 C]-pyruvate under 13 C XY4, $\tau=50$ ms. Upper panel B_z data are obtained after portioning the hyperpolarized solution into two $1.0\,\mathrm{cm}^3$ aliquots, each stored at 5 mT and then placed sequentially next to the zero-field OPM. Red curves show monoexponential decays with fitted decay time constant $T_1(\text{zero field})=24(1)\,\mathrm{s}$. The lower panel data were obtained with a single aliquot, by alternating 1-s acquisition periods at zero field with 8-s storage periods at 30 μ T. Signal loss in between acquisition periods is attributed to natural decay, fitted by the red curve to $T_1(30\,\mu\text{T})=24(1)\,\mathrm{s}$, which within error is equal to $T_1(\text{zero field})$.

In this thesis, nuclear spin dynamics and relaxation phenomena were investigated in unconventional magnetic field regimes, i.e. at field strengths both above and significantly below that of EARTH's magnetic field, using detection methods based on OPMs. Prior to this work, the unique magnetic field characteristics of this regime posed a challenge: it was too weak for inductive detection but too strong for zero-field magnetometers, limiting its exploration to techniques relying on SQUIDs. In this thesis, nuclear spin dynamics and relaxation phenomena were observed in unconventional magnetic field regimes, i.e. at field strengths above and far below that of the EARTH's field, using detection based on OPMs. The research described in this thesis expands the applicability of OPMs to this specific magnetic field regime. By combining different OPM sensor strategies, it demonstrates continuous optical NMR detection across the entire spectrum, ranging from zero-field to fields measuring hundreds of microtesla. This sensor strategy is then combined with the versatile fast-fieldcycling toolset, paving the way for a new category of experiments within the field of NMR.

THESIS SUMMARY

The obstacle of not having a suitable sensor was solved in this thesis by combining different magnetometer strategies (Chapter 1). Whereas most applications require the magnetometer to be sensitive in a fixed frequency regime for which it can be optimized, the experiments of this thesis required the magnetometer to be sensitive at frequencies from 0 Hz to few kHz. Whereas concepts for realizing magnetometers operating well on either end of this range existed (SERF and RF magnetometers), a main contribution of this thesis (Chapter 2) was finding operating conditions where acceptable sensitivity could be achieved over a broad range of frequencies via rapidly tuning the magnetometers resonance frequency. Further modifications, mostly in the form of coils and temperature control, allowed the magnetometer to be used for NMR.

High-field NMR incorporates well-established techniques and offers some advantages compared to ZULF NMR, such as high chem-

ical specificity due to relatively strong signals and the ability to resolve small chemical shifts. However, it comes with certain drawbacks, including a larger size, greater weight, higher power consumption, and increased cost. Furthermore, high-field NMR is limited to samples that can be placed inside a high-field magnet. While the high magnetic field strength is arguably the most significant asset of high-field NMR, it can also be its greatest weakness for certain applications. This includes scenarios such as NMR within metal containers, liquids embedded in porous materials, or samples containing magnetic impurities or other broadening/damping mechanisms. In these circumstances, ZULF NMR methods may compete with and even outperform their high-field counterparts, which is the primary focus of Chapter 3 to Chapter 5.

Using high-resolution spectroscopy as an example, as detailed in Chapter 4, this thesis explores the potential of the ULF regime for estimating the J-coupling constant, a parameter closely tied to a molecule's chemical structure. By making certain assumptions, including equal initial polarization, uniform sensitivity, and high-field limitations due to gradient broadening, the thesis demonstrates that the ULF regime may represent the optimal field strength, minimizing statistical uncertainty, for estimating the J-coupling constant in heteronuclear spin systems like CF₃CH₂OH or ¹³CH₂OH with long-lived coherences (see Chapter 5).

Another significant application and one of the primary motivations behind developing the tunable magnetometer were the measurements of NMRD in systems characterized by random molecular Brownian motion with long coherence times, such as it is expected for, e.g., surface adsorption phenomena in porous materials. As detailed in Chapter 6, the combination of FFC with a tunable OPM field sensor has successfully enabled the measurement of longitudinal relaxation rates up to tens per second, spanning from nanotesla to millitesla field strengths. Importantly, this approach marked the first instance where the low-frequency plateau of longitudinal relaxation rates could be directly measured for systems exhibiting correlation times as long as tens of milliseconds.

The thesis concludes with two chapters that discuss and demonstrate approaches to enhance nuclear spin control in the ZULF regime. DC pulses, which logically correspond to resonant RF pulses at high-field NMR, lack not only selectivity and precision but also the error tolerance crucial for complex dynamical decoupling sequences. To address these challenges, several methods are developed as outlined

in Chapter 7. These pulses find application in tasks such as decoupling small residual magnetic fields and play an essential role in the successful implementation of the real-time polarimetry method, as elaborated in Chapter 8.

OPERATING REGIMES AND THE VALIDITY OF APPROXIMATIONS IN PHYSICAL MODELS

While a large part of the thesis is dedicated to practical applications of ZULF NMR, the thesis also studies the pure physics of spin systems (both atomic and nuclear) in these unconventional regimes. This provides examples of some fundamental concepts in physics, notably the importance of approximations in physical models, their validity, and their limits.

In high-field NMR, the secular approximation of the J-coupling Hamiltonian often allows for a robust approximation of eigenstates using the angular momentum operators parallel to the magnetic field. This results in a diagonal Hamiltonian that simplifies the prediction of resonance properties such as amplitude and frequency through the application of quantum numbers and transition rules.

In ZULF NMR, similar approaches and approximations can be employed, at least for spin systems like A_nX_m . However, these methods become less reliable when the magnitudes of the J-coupling and Zeeman interactions become comparable. In such cases, the resulting eigenstates can be challenging to associate with quantum numbers, and it may be difficult, or even impossible, to determine transition rules. Low-order perturbation theory fails to predict the system's eigenstates under these conditions.

This thesis explores the implications of pushing the limits of these approximations and their impact on spectroscopy, with a particular focus on Chapter 4 and Chapter 5. These chapters investigate the transition from the strong coupling to the weak coupling regime and shed light on the consequences of this shift.

In addition to the approximations that impact the system's Hamiltonian, this thesis also explores the impact of ULF NMR on the secular approximation of the relaxation super-operator. Because of the distinct symmetry and the possibility that resonance frequencies may be comparable to the relaxation terms, the typical assumptions regarding simplifying the relaxation super-operator do not apply in the ULF regime. This topic is briefly addressed in Chapter 5 and serves as a motivation for further research in this area.

The atomic physics component of the thesis also highlights significant changes in the system's behavior under various operating conditions. While certain aspects of physics can be accurately described under extreme conditions, such as extremely low or high polarization and low or high magnetic fields, the thesis delves into the system's behavior in intermediate regimes where analytical solutions have not been established to date. This constitutes one of the central topics of Chapter 1.

ANALOGIES BETWEEN ATOMIC AND NUCLEAR SPIN PHYSICS

Another significant finding in this thesis centers on the numerous parallels between the fields of NMR and atomic physics. Atomic and nuclear spin physics share intrinsic similarities, as both domains revolve around the concept of spin and its interactions. However, in recent decades, these two fields have seemingly diverged, mainly due to their distinct focuses on different applications. NMR has achieved notable success in chemistry, structural biology, and chemical imaging, while atomic physics is primarily employed to investigate fundamental quantum mechanics and explore light-matter interactions, leading to applications in quantum sensing, computing, and communication.

This divergence often obscures the many similarities between both fields. For instance, the SERF effect, as discussed in Chapter 1, can be analogously understood as akin to the motional narrowing phenomenon, also known as extreme narrowing in NMR, explored in Chapter 5 and Chapter 6. Both phenomena result in a reduction of resonance linewidth due to the random motion of particles.

Additionally, the scalar coupling in NMR, as discussed in Chapter 3, has a mathematical equivalence to the hyperfine coupling between electronic and nuclear spins within atoms, as covered in Chapter 1. In this sense, the strong and weak coupling regimes, as detailed in Chapter 4, are direct consequences of the ZEEMAN and PASCHEN⁴-BACK⁵ effects. These intriguing similarities give rise to selection rules for zero-field spectra that mirror magnetic dipole transitions in atoms, as discussed in Appendix D.

⁴ Friedrich Paschen (1865–1947) was a German physicist who made significant contributions to the understanding of atomic spectra and the Paschen series of spectral lines.

⁵ Ernst Emil Alexander Back (1881–1959) was a German physicist who is most notably know for his contribution in discovering the Paschen-Back effect and measuring.

Analogously, SR2K (as discussed in Chapter 8) exhibits similarities to the relaxation of nuclear spins in atoms influenced by spin-exchange collisions, as discussed in Chapter 1. To delve further into the specifics, the relaxation description originally developed to elucidate the SERF effect [30] (Chapter 1), which relies on superoperators, Liouville brackets, and a spherical operator basis, closely parallels the relaxation description employed in NMR [167] (Chapter 5).

OUTLOOK

High-field NMR methods have enjoyed a substantial head start over several decades, and they undoubtedly bring numerous advantages to the table for a wide range of applications. ZULF NMR methods, although relatively newer in comparison, have made remarkable strides in recent years. While high-field NMR continues to dominate in many areas, these emerging techniques may find their unique niches, expanding and complementing established high-field methods. Addressing the challenges that lie ahead will be crucial to establishing these innovative approaches and enable them to become increasingly competitive alternatives for applications currently unavailable or dominated by other NMR methods.

The most pressing issue in this regard is the improvement of SNR, achieved through both sensor optimization and signal amplification. Estimations for the theoretical sensitivity limit of OPM based magnetometers appear promising when directly compared to inductive detection. They suggest that current realizations of OPMs are still far from reaching these quantum-limited sensitivities, potentially outperforming inductive detection across a broader frequency range.

Regarding signal amplification, promising approaches are found in the field of nuclear spin hyperpolarization. Specifically, methods based on parahydrogen [153–155] emerge as strong candidates due to their efficiency at fields close to zero, eliminating the drawback of low thermal polarization at low fields.

In spectroscopy, an unresolved challenge is the complexity of ZULF spectra, particularly for larger spin systems. Because they are insensitive to chemical shifts, zero-field spectra often prove difficult to analyze due to the substantial potential for resonance overlap. Advanced spectroscopy methods, such as spectral filtering or two-dimensional spectroscopy techniques, are being developed and may have the potential to solve some of these issues in a similar way as two-dimensional NMR revolutionized chemical structure analysis.

In the field of NMRD, the magnetometer's dead time currently poses a limitation on the utilization of chemical systems characterized by stronger molecular interactions and interfaces with hydrogen bonding, which exhibit faster relaxation rates. Theoretically, employing Q-switching of the optical pumping beam, as demonstrated in Cooper et al. [57], represents a technique to accelerate and control the magnetometer's recovery following magnetic field pulses, thereby diminishing the dead time to less than the field switching time, which is well below 1 ms, all while maintaining sensitivity [55].

Finally, there is also the prospect of completely new applications involving ZULF NMR experiments in combination with OPMs in the field of magnetometry or fundamental research.

APPENDIX



MATHEMATICAL NOTATION, DEFINITIONS AND DERIVATIONS

This chapter contains information about the mathematical notation and some additional definitions and derivations that are used within the thesis.

A.1 EINSTEIN NOTATION

The EINSTEIN¹ summation convention is assumed within this thesis, i.e. $a_ib_i = \sum_i a_ib_i$, where the sum is over all valid indices that appear twice (here only i).

A.2 NOTATION FOR FIELDS

Let $c = a + bi \in \mathbb{C}$ be an element in the field of complex number \mathbb{C} . The asterisk \cdot^* is used to describe the complex conjugate

In other words, the overline notation \bar{c} will not be used to indicate complex conjugation.

$$c^* = a - bi \tag{A.1}$$

of a complex number.

A.3 NOTATION FOR VECTOR SPACES

In this thesis, this will mainly be the 3D vector space \mathbb{R}^3 or \mathbb{C}^3 .

¹ Albert Einstein (1879–1955) was a renowned theoretical physicist whose revolutionary theory of relativity transformed our understanding of space, time, and the nature of the universe.

Vectors

Upright boldface type as in $\mathbf{v} = (v_1 \dots v_n)$. Unit vectors along the coordinate axis x, y and z are indicated by \mathbf{e}_x , \mathbf{e}_y and \mathbf{e}_z . Within standalone equations

$$\mathbf{v} \equiv |v\rangle \equiv \begin{pmatrix} v_1 \\ \vdots \\ v_n \end{pmatrix} \tag{A.2}$$

vectors may sometimes be alternatively represented by column matrices of length n.

If the vector space is equipped with an inner product $\langle \cdot, \cdot \rangle$, it is represented by the dot operator $\mathbf{a} \cdot \mathbf{b} = \langle a, b \rangle$.

Matrices

Italic type with a "hat" as in \hat{A} . Matrix elements

$$\hat{A} \equiv \begin{pmatrix} A_{11} & A_{12} & \cdots & A_{1n} \\ A_{21} & A_{22} & \cdots & A_{2n} \\ \vdots & \vdots & \ddots & \vdots \\ A_{m1} & A_{m2} & \cdots & A_{mn} \end{pmatrix}$$
(A.3)

are indicated by A_{ji} . The identity matrix is $\hat{1}$. For matrices, the dot operator \cdot represents matrix multiplication.

The \cdot^{T} symbol is used to describe the transpose of a matrix

$$(\hat{A}^{\dagger})_{ii} = A_{ii} \tag{A.4}$$

and the \cdot^* asterisk for the complex conjugate

$$(\hat{A}^*)_{ij} = A^*_{ij} . \tag{A.5}$$

Sometimes also known as Hermitian transpose. Finally, ·† describes the conjugate transpose

$$(\hat{A}^{\dagger})_{ij} = ((\hat{A}^*)^{\dagger})_{ij} = ((\hat{A}^{\dagger})^*)_{ij} = A_{ij}^*$$
(A.6)

of a matrix \hat{A} .

A.4 NOTATION FOR HILBERT SPACES

A Hilbert space \mathcal{H} is a vector space equipped with an inner product $\langle \cdot, \cdot \rangle$.

Operators

For operators, i.e. linear maps within a HILBERT space, the same notation as for matrices will be used. For operators \hat{A} and \hat{B} the dot operator represents composition $\hat{A} \cdot \hat{B} \equiv \hat{A} \circ \hat{B}$.

Tensor Operators

Tensor operators borrow the notation of mathematical tensors (here called *pure tensors*), which describe multilinear relationships between algebraic objects. However, in contrast to pure tensors, the strict distinction between contra- and covariant vectors/indices is often diluted and there is no generally established notation regarding the position of indices over different subfields in physics². Additionally, pure tensors are defined as multilinear maps into a field $\mathbb F$ i.e. the function value is a scalar, whereas tensor operators are used as multilinear maps into a Hilbert space $\mathcal H$ i.e. the function value is an operator.

Within this thesis, mainly three different types of tensor operators are used. Simple operators \hat{A} can be seen as scalar tensor operators with rank zero .

Vector operators

$$\hat{\mathbf{B}} \equiv (\hat{B}_0 \dots \hat{B}_n) \tag{A.7}$$

are often called rank one tensor operators. Most vectors will be in 3D, i.e. $\hat{\mathbf{B}} = (\hat{B}_x \, \hat{B}_y \, \hat{B}_z)$. A dot product between two vector operators $\hat{\mathbf{a}}$ and $\hat{\mathbf{B}}$ should be interpreted according to the definition of the inner product

$$\hat{\mathbf{A}} \cdot \hat{\mathbf{B}} = \hat{A}_1 \cdot \hat{B}_1 + \dots + \hat{A}_n \cdot \hat{B}_n = \hat{A}_i \cdot \hat{B}_i . \tag{A.8}$$

sometimes the term "order" is preferred over the term "rank" to avoid confusion with the rank of a matrix

² To be consistent with the literature, in most parts of this thesis, there will be no distinction between co- and contravariant vectors/indices. Their difference is manifested mainly during basis transformations which will not occur very often in this thesis. In contrast to other fields of physics, quantum mechanics often prefers orthonormal basis vectors with basis transformations given by unitary operators which eliminates some of the differences between contra- and covariant vectors. However, there would be some advantages in using them even in quantum mechanics, e.g. it would provide an intrinsic explanation of why coordinates (= contravariant tensors) transform differently than the basis tensors (= covariant tensors) (see Equation B.22).

Rank two tensor operators

$$\hat{\mathbf{A}} \equiv \begin{pmatrix} \hat{A}_{11} & \hat{A}_{12} & \cdots & \hat{A}_{1n} \\ \hat{A}_{21} & \hat{A}_{22} & \cdots & \hat{A}_{2n} \\ \vdots & \vdots & \ddots & \vdots \\ \hat{A}_{m1} & \hat{A}_{m2} & \cdots & \hat{A}_{mn} \end{pmatrix}$$
(A.9)

can be expressed as a matrix of operators \hat{A}_{ij} . In most cases, this will be an element of the product space of two 3D spaces i.e.

$$\hat{\mathbf{A}} \equiv \begin{pmatrix} \hat{A}_{xx} & \hat{A}_{xy} & \hat{A}_{xz} \\ \hat{A}_{yx} & \hat{A}_{yy} & \hat{A}_{yz} \\ \hat{A}_{zx} & \hat{A}_{zy} & \hat{A}_{zz} \end{pmatrix} .$$
(A.10)

Spin Operators

All spin operators are defined in units of angular momentum (i.e. they are defined with \hbar). For Spin-1/2 the following conventions are used:

$$\hat{\mathbf{S}} = (\hat{S}_x \, \hat{S}_y \, \hat{S}_z) \tag{A.11}$$

$$\hat{S}_x = \frac{\hbar}{2}\hat{\sigma}_x$$
 $\hat{S}_y = \frac{\hbar}{2}\hat{\sigma}_y$ $\hat{S}_z = \frac{\hbar}{2}\hat{\sigma}_z$ (A.12)

$$\hat{S}_{x} = \frac{\hbar}{2}\hat{\sigma}_{x} \qquad \qquad \hat{S}_{y} = \frac{\hbar}{2}\hat{\sigma}_{y} \qquad \qquad \hat{S}_{z} = \frac{\hbar}{2}\hat{\sigma}_{z} \qquad \qquad (A.12)$$

$$\hat{\sigma}_{x} = \begin{pmatrix} 0 & 1 \\ 1 & 0 \end{pmatrix} \qquad \hat{\sigma}_{y} = \begin{pmatrix} 0 & -i \\ i & 0 \end{pmatrix} \qquad \hat{\sigma}_{z} = \begin{pmatrix} 1 & 0 \\ 0 & -1 \end{pmatrix} \qquad (A.13)$$

Raising \hat{S}_{+} and lowering \hat{S}_{-} operators are defined as

$$\hat{S}_{\pm} = \hat{S}_x \pm i\hat{S}_y . \tag{A.14}$$

Rotation Operators

Spatial or spin rotations about the vector **n** by the angle ϕ are described by the 3D rotation group (SO(3)) and special unitary group (SU(2)) and can represented by rotation operators $\hat{R}(\phi, \mathbf{n})$. Rotation about the coordinate axis may be written as $\hat{R}_x(\phi)$, $\hat{R}_y(\phi)$ and $\hat{R}_z(\phi)$. Spin rotations

$$\hat{R}(\phi, \mathbf{n}) = e^{-i\phi\frac{\mathbf{n}\cdot\hat{\mathbf{S}}}{\hbar}} \tag{A.15}$$

can be expressed via the spin operators \hat{S} .

In contrast, spatial rotations

$$\hat{R}(\phi, \mathbf{n}) = e^{-i\phi \frac{\mathbf{n} \cdot \hat{\mathbf{L}}}{\hbar}} \tag{A.16}$$

can be expressed via orbital angular momentum operators L.

A.5 NOTATION FOR PRODUCT SPACES

For $\hat{\mathcal{B}}_{\mathcal{B}} \in \mathcal{B}$ and $\hat{\mathcal{C}}_{\mathcal{C}} \in \mathcal{C}$ the product

$$\hat{A} = \hat{B}_{\mathcal{B}} \otimes \hat{C}_{\mathcal{C}} = \begin{pmatrix} B_{11} \hat{C} & \cdots & B_{1n} \hat{C} \\ \vdots & \ddots & \vdots \\ B_{n1} \hat{C} & \cdots & B_{nn} \hat{C} \end{pmatrix}$$

$$= \begin{pmatrix} B_{11} C_{11} & \cdots & B_{11} C_{1m} & \cdots & B_{1n} C_{11} & \cdots & B_{1n} C_{1m} \\ \vdots & \ddots & \vdots & \ddots & \vdots & \ddots & \vdots \\ B_{11} C_{m1} & \cdots & B_{11} C_{mm} & \cdots & B_{1n} C_{m1} & \cdots & B_{1n} C_{mm} \\ \vdots & \ddots & \vdots & \ddots & \vdots & \ddots & \vdots \\ B_{n1} C_{11} & \cdots & B_{n1} C_{1m} & \cdots & B_{nn} C_{11} & \cdots & B_{nn} C_{1m} \\ \vdots & \ddots & \vdots & \ddots & \vdots & \ddots & \vdots \\ B_{n1} C_{m1} & \cdots & B_{n1} C_{mm} & \cdots & B_{nn} C_{m1} & \cdots & B_{nn} C_{mm} \end{pmatrix}$$

$$= \begin{pmatrix} A_{11,11} & \cdots & A_{11,1m} & \cdots & A_{1n,11} & \cdots & A_{1n,1m} \\ \vdots & \ddots & \vdots & \ddots & \vdots & \ddots & \vdots \\ A_{11,m1} & \cdots & A_{11,mm} & \cdots & A_{1n,m1} & \cdots & A_{1n,mm} \\ \vdots & \ddots & \vdots & \ddots & \vdots & \ddots & \vdots \\ A_{n1,11} & \cdots & A_{n1,1m} & \cdots & A_{mn,11} & \cdots & A_{mn,1m} \\ \vdots & \ddots & \vdots & \ddots & \vdots & \ddots & \vdots \\ A_{n1,m1} & \cdots & A_{n1,mm} & \cdots & A_{mn,m1} & \cdots & A_{nn,mm} \end{pmatrix}$$

$$= \begin{pmatrix} A_{11} & \cdots & A_{1(nm)} \\ \vdots & \ddots & \vdots \\ A_{(nm)1} & \cdots & A_{(nm)(nm)} \end{pmatrix}$$

represent an element of the product space $\mathcal{B}\otimes\mathcal{C}$. Here, $\cdot\otimes\cdot$ represents the Kronecker³ product. The matrix is expressed in the product basis.

³ Leopold Kronecker (1823–1891) was a German mathematician known for his foundational contributions to number theory and his advocacy for a rigorous and axiomatic approach to mathematical reasoning.

Matrix indices may be written as $A_{kl,ij}$ where (k,i) refers to subspace \mathcal{B} and (l,j) refers to subspace \mathcal{C} .

If the subscript is already used (e.g. to indicate the coordinate axis for rotation or spin operators like $\hat{R}_x(\phi)$) the operator only acting on the subspace may alternatively be written as $\hat{R}_x^{(\mathcal{B})}(\phi)$.

If an operator \hat{a} , that is part of a product space $\mathcal{B} \otimes \mathcal{C}$, only acts on the subspace \mathcal{B} , the following notation is used

$$\hat{A} = \hat{A}_{\mathcal{B}} \otimes \hat{\mathbb{1}}_{\mathcal{C}} = \begin{pmatrix} A_{11} & \cdots & 0 & \cdots & A_{1n} & \cdots & 0 \\ \vdots & \ddots & \vdots & \ddots & \vdots & \ddots & \vdots \\ 0 & \cdots & A_{11} & \cdots & 0 & \cdots & A_{1n} \\ \vdots & \ddots & \vdots & \ddots & \vdots & \ddots & \vdots \\ A_{n1} & \cdots & 0 & \cdots & A_{nn} & \cdots & 0 \\ \vdots & \ddots & \vdots & \ddots & \vdots & \ddots & \vdots \\ 0 & \cdots & A_{n1} & \cdots & 0 & \cdots & A_{nn} \end{pmatrix} . (A.18)$$

An operator

$$\hat{B} = \hat{1}_{\mathcal{A}} \otimes \hat{B}_{\mathcal{B}} = \begin{pmatrix} B_{11} & \cdots & B_{1n} & \cdots & 0 & \cdots & 0 \\ \vdots & \ddots & \vdots & \ddots & \vdots & \ddots & \vdots \\ B_{n1} & \cdots & B_{nn} & \cdots & 0 & \cdots & 0 \\ \vdots & \ddots & \vdots & \ddots & \vdots & \ddots & \vdots \\ 0 & \cdots & 0 & \cdots & B_{11} & \cdots & B_{n1} \\ \vdots & \ddots & \vdots & \ddots & \vdots & \ddots & \vdots \\ 0 & \cdots & 0 & \cdots & B_{n1} & \cdots & B_{nn} \end{pmatrix} . (A.19)$$

only acting on the ${\cal B}$ system can be defined analogously.

A.6 NOTATION FOR LIOUVILLE SPACES

A space of operators called a Liouville space $\mathcal{A}_{\mathcal{L}}$, is a Hilbert space itself under the Frobenius/Hilbert-Schmidt inner product.

Vectors

An operator, i.e. an element $\hat{A} \in \mathcal{A}_{\mathcal{L}}$ of this space, may be written as

$$\hat{A} \equiv \begin{pmatrix} A_{11} & \cdots & A_{1n} \\ \vdots & \ddots & \vdots \\ A_{n1} & \cdots & A_{nn} \end{pmatrix} \equiv |\hat{A}\rangle_{\mathcal{L}} \equiv \begin{pmatrix} A_{11} \\ \vdots \\ A_{1n} \\ \vdots \\ A_{n1} \\ \vdots \\ A_{nn} \end{pmatrix}_{\mathcal{L}} \equiv \begin{pmatrix} A_{1} \\ \vdots \\ A_{n} \\ \vdots \\ A_{(n-1)\times n+1} \\ \vdots \\ A_{n\times n} \end{pmatrix}_{\mathcal{L}}$$
(A.20)

The dimension dim $\mathcal{A}_{\mathcal{L}} = n^2$ of the Liouville space is the squared value of the dimension dim $\mathcal{A} = n$ of its corresponding Hilbert space.

Inner Product

For matrices/operators \hat{A} and \hat{B} the Frobenius/Hilbert-Schmidt inner product

$$\langle \hat{A}, \hat{B} \rangle = \operatorname{Tr} \hat{A}^{\dagger} \hat{B} = A_{ij}^* B_{ij}$$
 (A.21)

is used.

Superoperators

A superoperator [168] $\hat{\mathcal{C}}$ is a linear operator that acts on elements/vectors of a Liouville space. Let $\hat{A} \in \mathcal{A}_{\mathcal{L}}$ be an operator. The matrix elements for $\hat{\mathcal{C}}_{ji}$

$$\begin{pmatrix}
B_{1} \\
\vdots \\
B_{n\times n}
\end{pmatrix}_{\mathcal{L}} = \begin{pmatrix}
C_{11}A_{1} + \dots + C_{1(n\times n)}A_{n\times n} \\
\vdots \\
C_{(n\times n)1}A_{n\times n} + \dots + C_{(n\times n)(n\times n)}A_{n\times n}
\end{pmatrix}_{\mathcal{L}}$$

$$= \begin{pmatrix}
C_{11} & \dots & C_{1,n\times n} \\
\vdots & \ddots & \vdots \\
C_{(n\times n)1} & \dots & C_{(n\times n)(n\times n)}
\end{pmatrix}_{\mathcal{L}\otimes\mathcal{L}} \cdot \begin{pmatrix}
A_{1} \\
\vdots \\
A_{n\times n}
\end{pmatrix}_{A_{\mathcal{L}}}$$
(A.22)

define how the superoperator \hat{C} acts on \hat{A} . Here $\hat{B} \in \mathcal{A}_{\mathcal{L}}$ is also an operator in the same Liouville space. If $\dim \mathcal{A}_{\mathcal{L}} = \dim^2 \mathcal{A} = n^2$ then the corresponding superoperator has $(n^2)^2 = n^4$ elements.

Whereas any linear operator over a finite vector space can be expressed as a matrix once a basis is defined, some superoperators can be described in an even more compact way. For every operator $\hat{B} \in \mathcal{A}_{\mathcal{L}}$ the following linear maps fulfill the definition of a superoperator:

$$\hat{\mathcal{L}}^{(\hat{B})}:\mathcal{A}_{\mathcal{L}}
ightarrow\mathcal{A}_{\mathcal{L}};\qquad \hat{A}\mapsto\hat{B}\hat{A}$$
 (A.23)

$$\hat{\mathcal{R}}^{(\hat{B})}:\mathcal{A}_{\mathcal{L}}
ightarrow\mathcal{A}_{\mathcal{L}}; \qquad \hat{A}\mapsto\hat{A}\hat{B} \qquad \qquad (A.24)$$

$$\hat{\mathcal{B}}: \mathcal{A}_{\mathcal{L}} \to \mathcal{A}_{\mathcal{L}}; \qquad \hat{A} \mapsto [\hat{B}, \hat{A}] = \hat{B}\hat{A} - \hat{A}\hat{B}$$
 (A.25)

A.7 REDUCED DENSITY OPERATORS

The following derivations make use of the *completeness relation* for the Pauli⁴ matrices that can be written as follows

$$\hat{\sigma}_{\alpha\beta} \cdot \hat{\sigma}_{\gamma\delta} \equiv \hat{\sigma}_{x,\alpha\beta} \hat{\sigma}_{x,\gamma\delta} + \hat{\sigma}_{y,\alpha\beta} \hat{\sigma}_{y,\gamma\delta} + \hat{\sigma}_{z,\alpha\beta} \hat{\sigma}_{z,\gamma\delta} = 2\delta_{\alpha\delta}\delta_{\beta\gamma} - \delta_{\alpha\beta}\delta_{\gamma\delta}$$
(A.26)

and the definition of matrix multiplication

$$(\hat{a}\cdot\hat{b})_{ij} = a_{ik}b_{kj} . \tag{A.27}$$

The partial trace $\operatorname{Tr}_{\mathcal{B}} \hat{a}$ is over \mathcal{B} for an operator \hat{a} within a product space $\mathcal{A} \otimes \mathcal{B}$ is given by

$$(\operatorname{Tr}_{\mathcal{B}}\hat{a})_{i,j} = a_{ik,jk} . \tag{A.28}$$

⁴ Wolfgang Pauli (1900–1958) was an Austrian–Swiss physicist and one of the pioneers of quantum mechanics, known for his exclusion principle and his contributions to the development of the theory of elementary particles and quantum field theory.

With this Equation 1.15b can be derived as follows:

$$\varphi_{kl,ij} \equiv \left(\frac{\hat{\rho}}{4}\right)_{kl,ij} + \left(\frac{\hat{\mathbf{S}} \cdot \hat{\rho} \hat{\mathbf{S}}}{\hbar^{2}}\right)_{kl,ij} \\
= \frac{\hat{\rho}_{kl,ij}}{4} + \frac{(\hat{S}_{x}\hat{\rho} \hat{S}_{x})_{kl,ij} + (\hat{S}_{y}\hat{\rho} \hat{S}_{y})_{kl,ij} + (\hat{S}_{z}\hat{\rho} \hat{S}_{z})_{kl,ij}}{\hbar^{2}} \\
\stackrel{A.27}{=} \frac{1}{4} \left(\hat{\rho}_{kl,ij} + \hat{\sigma}_{x,lo}\hat{\rho}_{ko,im}\hat{\sigma}_{x,mj} + \hat{\sigma}_{y,lo}\hat{\rho}_{ko,im}\hat{\sigma}_{y,mj} + \hat{\sigma}_{z,lo}\hat{\rho}_{ko,im}\hat{\sigma}_{z,mj}\right) \\
= \frac{1}{4} \left(\hat{\rho}_{kl,ij} + \hat{\sigma}_{x,lo}\hat{\sigma}_{x,mj}\hat{\rho}_{ko,im} + \hat{\sigma}_{y,lo}\hat{\sigma}_{y,mj}\hat{\rho}_{ko,im} + \hat{\sigma}_{z,lo}\hat{\sigma}_{z,mj}\hat{\rho}_{ko,im}\right) \\
\stackrel{A.26}{=} \frac{1}{4} \left(\hat{\rho}_{kl,ij} + (2\delta_{lj}\delta_{om} - \delta_{lo}\delta_{mj})\hat{\rho}_{ko,im}\right) \\
= \frac{1}{4} \left(\hat{\rho}_{kl,ij} + 2\hat{\rho}_{km,im}\delta_{lj} - \hat{\rho}_{kl,ij}\right) \\
= \frac{\hat{\rho}_{km,im}\delta_{lj}}{2} \\
\stackrel{A.28}{=} \left(\operatorname{Tr}_{S}\hat{\rho}\right)_{k,i} \otimes \left(\frac{\hat{\mathbb{I}}_{S}}{2}\right)_{lj} \\
= \left(\hat{\rho}_{I} \otimes \frac{\hat{\mathbb{I}}_{S}}{2}\right)_{kl,ij} \quad \text{q.e.d.} \tag{A.29}$$

The expectation value of an operator \hat{a} for a system described by the density operator $\hat{\rho}$ is given by

$$\langle \hat{a} \rangle = \text{Tr} \left(\hat{\rho} \hat{a} \right) \ .$$
 (A.30)

In addition, the trace of the density operator is

$$\operatorname{Tr} \hat{\rho} = 1 . \tag{A.31}$$

For a product space $S \otimes I$ of two particles with spin S = 1/2 and I, the spin operator \hat{S}_x is given by

$$\hat{S}_{x,kl,ij} = (\hat{S}_x)_{kl,ij} = (\mathbb{1}_I \otimes \hat{S}_x^{(S)})_{kl,ij}
= (\mathbb{1}_I \otimes \frac{\hbar}{2} \sigma_x)_{kl,ij} = \mathbb{1}_{I,ki} \frac{\hbar}{2} \sigma_{x,ij} = \delta_{ki} \frac{\hbar}{2} \sigma_{x,ij} .$$
(A.32)

Similar identities can be derived for \hat{S}_y and \hat{S}_y . With this, Equation 1.15a can be derived in the following way:

$$\begin{split} \hat{\mathbb{I}}_{kl,ij} + \frac{4}{\hbar^2} \cdot (\langle \hat{\mathbf{S}} \rangle \cdot \hat{\mathbf{S}})_{kl,ij} \\ = & \delta_{ki} \delta_{lj} + 4 \cdot (\langle \hat{S}_x \rangle \hat{S}_x + \langle \hat{S}_y \rangle \hat{S}_y + \langle \hat{S}_z \rangle \hat{S}_z)_{kl,ij} \\ \frac{A_{=0}^{30}}{\delta_{ki}} \delta_{lj} + \frac{4}{\hbar^2} \cdot ((\operatorname{Tr} \rho \hat{S}_x) \hat{S}_{x,kl,ij} + (\operatorname{Tr} \rho \hat{S}_y) \hat{S}_{y,kl,ij} + (\operatorname{Tr} \rho \hat{S}_z) \hat{S}_{z,kl,ij}) \\ = & \delta_{ki} \delta_{lj} + \frac{4}{\hbar^2} \cdot ((\rho \hat{S}_x)_{mn,mn}) \hat{S}_{x,kl,ij} \\ + (\rho \hat{S}_y)_{mn,mn}) \hat{S}_{y,kl,ij} + (\rho \hat{S}_z)_{mn,mn}) \hat{S}_{z,kl,ij}) \\ = & \delta_{ki} \delta_{lj} + \frac{4}{\hbar^2} \cdot (\rho_{mn,op} \hat{S}_{x,op,mn} \hat{S}_{x,kl,ij} \\ + \rho_{mn,op} \hat{S}_{y,op,mn} \hat{S}_{y,kl,ij} + \rho_{mn,op} \hat{S}_{z,op,mn} \hat{S}_{z,kl,ij}) \\ & \hat{S}_{ki} \delta_{lj} + (\rho_{mn,mp} \hat{\sigma}_{x,pn} \hat{\sigma}_{x,lj} \delta_{ki} \\ + \rho_{mn,mp} \hat{\sigma}_{y,pn} \hat{\sigma}_{y,lj} \delta_{ki} + \rho_{mn,mp} \hat{\sigma}_{z,pn} \hat{\sigma}_{z,lj} \delta_{ki}) \\ = & \delta_{ki} \delta_{lj} + \rho_{mn,mp} \delta_{ki} (\hat{\sigma}_{x,pn} \hat{\sigma}_{x,lj} + \hat{\sigma}_{y,pn} \hat{\sigma}_{y,lj} + \hat{\sigma}_{z,pn} \hat{\sigma}_{z,lj}) \\ \hat{S}_{ki} \hat{\delta}_{lj} + \rho_{mn,mp} \delta_{ki} (2\delta_{pj} \delta_{nl} - \delta_{pn} \delta_{lj}) \\ = & \delta_{ki} \delta_{lj} + 2\rho_{ml,mj} \delta_{ki} - \rho_{mn,mn} \delta_{lj} \delta_{ki} \\ = & \delta_{ki} (\delta_{lj} + 2\rho_{ml,mj} - \operatorname{Tr} \rho \delta_{lj}) \\ \hat{S}_{ki} \hat{\delta}_{lj} + 2\rho_{ml,mj} - \delta_{lj}) \\ \hat{S}_{ki} \hat{\delta}_{lj} \\ = & \delta_{ki} \delta_{lj} \hat{\delta}_{lj} \hat{\delta}_{lj}$$

A.8 COMMUTATORS

With $\mathbf{B} = \mathbf{0}$, the zero-field Hamiltonian from Equation 3.3 becomes

$$\hat{H} = \frac{2\pi}{\hbar} \sum_{i,j>i} J_{ij} \hat{\mathbf{I}}_i \cdot \hat{\mathbf{I}}_j \tag{A.34}$$

if the quadrupolar and dipolar terms are neglected. Each term of the sum can be alternatively expressed

$$\hat{\mathbf{I}}_i \cdot \hat{\mathbf{I}}_j = (\hat{\mathbf{I}}_i + \hat{\mathbf{I}}_j)^2 - \hat{\mathbf{I}}_i^2 - \hat{\mathbf{I}}_i^2 \tag{A.35}$$

in form of the total nuclear spin operators $\hat{\mathbf{I}}_i^2$ and $\hat{\mathbf{I}}_j^2$ combined with the coupled nuclear spin operator $\hat{\mathbf{I}}_{ij} = \hat{\mathbf{I}}_i + \hat{\mathbf{I}}_j$ of spin i and j with the following commutation relations

$$[\hat{A}, \hat{\mathbf{B}}] \equiv [\hat{A}, \hat{B}_x], \dots, [\hat{A}, \hat{B}_x]$$

$$[\hat{\mathbf{I}}_{i}^{2}, \hat{\mathbf{I}}_{i}^{2}] = [\hat{\mathbf{I}}_{i}^{2}, \hat{\mathbf{I}}_{ii}^{2}] = [\hat{\mathbf{I}}_{i}^{2}, \hat{\mathbf{I}}_{ii}^{2}] = 0$$
(A.36a)

$$[\hat{\mathbf{I}}_{ij}, \hat{\mathbf{I}}_{i}^{2}] = [\hat{\mathbf{I}}_{ij}, \hat{\mathbf{I}}_{i}^{2}] = [\hat{\mathbf{I}}_{ij}, \hat{\mathbf{I}}_{ij}^{2}] = \mathbf{0}$$
 (A.36b)

Similarly, the total angular momentum operator of all nuclear spins

$$\hat{\mathbf{f}}^{2} = (\sum_{k} \hat{\mathbf{I}}_{k})^{2} = (\hat{\mathbf{I}}_{ij} + \sum_{k \neq i, j \hat{\mathbf{I}}_{k}})^{2} = (\hat{\mathbf{I}}_{ij} + \hat{\mathbf{I}}_{\neg ij})^{2} = \hat{\mathbf{I}}_{ij}^{2} + \hat{\mathbf{I}}_{\neg ij}^{2} + 2\hat{\mathbf{I}}_{ij} \cdot \hat{\mathbf{I}}_{\neg ij}$$
(A.37)

can be expressed in terms of the previously defined $\hat{\mathbf{I}}_{ij}$ and new $\hat{\mathbf{I}}_{\neg ij}$ operator, which also commute

$$[\hat{\mathbf{I}}_{\neg ij}^2, \hat{\mathbf{I}}_i^2] = [\hat{\mathbf{I}}_{\neg ij}^2, \hat{\mathbf{I}}_i^2] = [\hat{\mathbf{I}}_{\neg ij}^2, \hat{\mathbf{I}}_{ii}^2] = 0$$
(A.38a)

$$[\hat{\mathbf{1}}_{\neg ij}, \hat{\mathbf{1}}_{\neg ij}^2] = [\hat{\mathbf{1}}_{\neg ij}, \hat{\mathbf{1}}_i^2] = [\hat{\mathbf{1}}_{ij}, \hat{\mathbf{1}}_j^2] = [\hat{\mathbf{1}}_{ij}, \hat{\mathbf{1}}_{ij}^2] = \mathbf{0}$$
(A.38b)

$$[\hat{\mathbf{I}}_{ij}, \hat{\mathbf{I}}_{-ij}^2] = \mathbf{0}$$
 (A.38c)

with all the others. Combining all of the commutation relations it follows

$$[\hat{\mathbf{I}}_i \cdot \hat{\mathbf{I}}_j, \hat{\mathbf{F}}^2] = 0 \tag{A.39a}$$

$$[\hat{\mathbf{I}}_i \cdot \hat{\mathbf{I}}_{j,} \hat{\mathbf{F}}] = \mathbf{0} . \tag{A.39b}$$

A.9 SECULAR APPROXIMATIONS

Approximations play an important role in physics. Almost every model has a defined scope due to the limited validity of approximations necessary to derive the model. When changing the operating conditions of physical systems, the validity of some approximations has to be re-evaluated. Many experiments in this thesis are about parameter variation over several orders of magnitude.

Secular approximation is an umbrella term for a category of approximations employed in both physics and NMR that share the characteristic of disregarding certain off-diagonal terms of a linear operator. In physics, approximations are labeled secular if they are valid for long times, often involving the neglect of rapidly oscillating terms in combination with slowly changing dynamics, aligning with

from Latin saeculum "age, span of time"

the etymological roots of the word from Latin. In contrast, in the field of NMR, secular approximations cover a much broader set of approximations that may not be linked to rapid oscillations. The more interested reader might be referred to the book *Principles of nuclear magnetic resonance in one and two dimensions* by Ernst et al. [101] for more detailed information about secular approximations and their usage in the field of NMR.

Here three common examples will be discussed that appear in the thesis. The first example, discussing the approximation of a Hamiltonian may not be considered a secular approximation in physics, but very much in NMR. However, this difference in terminology is not a major concern since it does not affect the underlying math.

Hamiltonians

Here, perturbation theory is used to motivate secular approximations for Hamiltonians⁵ which is common practice in NMR but equally applicable in other quantum systems. Assuming a Hamiltonian of the form

$$\hat{H} = \hat{H}_0 + \hat{H}' \tag{A.40}$$

with a dominating term \hat{H}_0 and a small perturbation \hat{H}' the eigenbasis $\{|n\,i\rangle\}$ of the unperturbed Hamiltonian \hat{H}_0

$$\hat{H}_{(0)} |ni\rangle = E_n^{(0)} |ni\rangle$$
 (A.41)

can be defined, with $i = 1, ..., d_n$ if d_n represents the degeneracy of the states with eigenenergy $E_n^{(0)}$. The first-order eigenstates

$$|n i^{(0)}\rangle = \sum_{j} a_{ij} |n j\rangle \tag{A.42}$$

as a superposition of states with the same eigenvalue. If an eigenvalue E_m is non-degenerate it is just $|m i^{(0)}\rangle = |m i\rangle$. For the degenerate eigenvalues there are procedures⁶ to determine the zero-order eigenbasis $|n i^{(0)}\rangle$, but the details are not relevant for further discussion.

$$\langle n i'^{(0)} | \hat{H}' | n i^0 \rangle \tag{A.43}$$

are diagonal for each eigenenergy E_n .

⁵ However, secular approximations can also be motivated in other ways, e.g. transformations to the interaction picture.

⁶ If some E_n are degenerate, the eigenstates $|ni\rangle^0$ are constructed by requiring that the matrices

First-order energy corrections are then given by

$$E_{ni}^{(1)} = \langle n i^{(0)} | \hat{H}' | n i^{(0)} \rangle$$
 (A.44)

If

$$\hat{H}' = \sum_{n,n',i,i'} h_{n'i'}^{ni} |n'i'\rangle \langle ni|$$
(A.45)

is given in the product basis first order energy corrections are given by

$$E_{ni}^{(1)} = \langle n i^{(0)} | \hat{H}' | n i^{(0)} \rangle$$

$$= \sum_{m,m',k,k',j,j'} a_{ij}^* \langle n j | h_{m'k'}^{mk} | m'k' \rangle \langle m k | a_{ij'} | n j' \rangle$$

$$= \sum_{j,j'} a_{ij}^* a_{ij'} h_{nj'}^{nj} . \tag{A.46}$$

Only terms $h_{nj'}^{nj}$ of \hat{H}' that connect states with the same eigenvalue $E_n^{(0)}$ are relevant. In other words, terms in \hat{H}' that connect different eigenvalues (i.e. $h_{n'j'}^{nj}$ with $n \neq n'$) may be ignored in first order. Neglecting these terms in the perturbation Hamiltonian is called the *secular approximation* [38] in NMR7. This is also illustrated in Figure A.2.

Neglecting terms in a linear operator, i.e. increasing the sparseness of the matrix, may significantly reduce the computational work related to matrix operations such as multiplication or inversion. Especially matrix diagonalization benefits from sparse matrices for high dimensions.

Whereas this approach is well defined for completely degenerate or non-degenerate states, issues arise with nearly degenerate states or scenarios with terms with similar order of magnitude, where it is not clear which term is to be considered as a perturbation. Here, the decision to neglect certain terms could be made by defining a threshold and neglecting terms that connect eigenvalues with an energy difference above that threshold.

⁷ As mentioned above, this approximation may not fulfill the requirement for being labeled a secular approximation in physics, due to the absence of oscillating terms. It should, however, not be confused with taking perturbation theory to first order, which describes the calculation of eigenenergies and eigenstates without applying any approximation to the underlying system Hamiltonian.

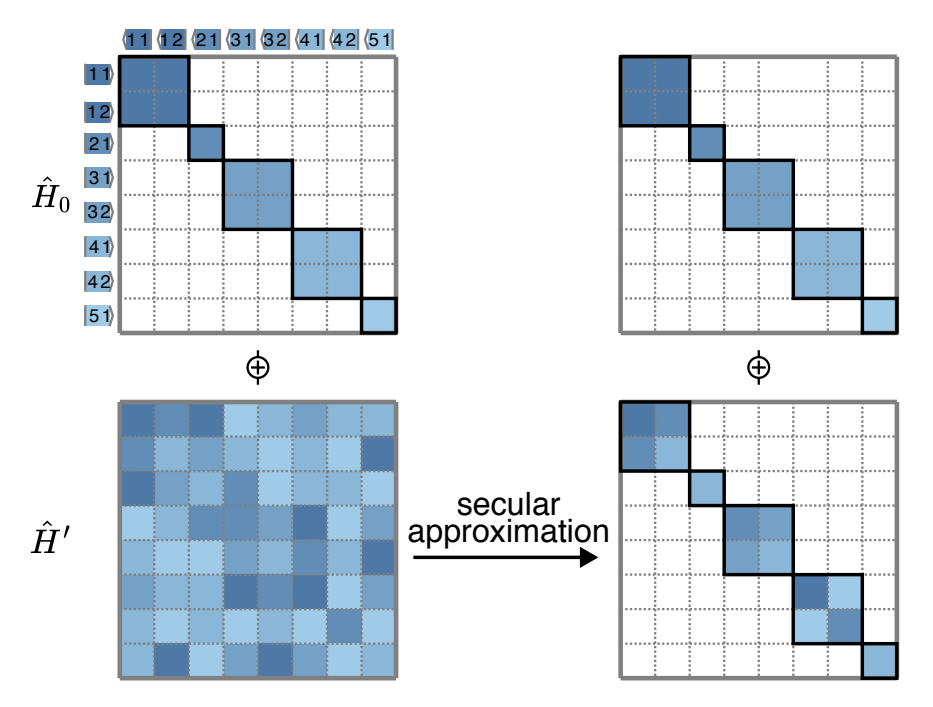


Figure A.1: Graphical illustration of the secular approximation of a perturbation Hamiltonian \hat{H}' . Off-diagonal terms between non-degenerate states are here ignored due to their vanishing effect on first-order energy corrections.

Superoperators

The secular approximation can also be applied to the space of operators on vectors within the Liouville space. Ideally, first the full Hamiltonian \hat{H} is sufficiently simplified to be able to diagonalize it

$$\hat{H} |ni\rangle = E_n |ni\rangle \tag{A.47}$$

with eigenvalues E_n and eigenvectors $|ni\rangle$.

A suitable basis for the LIOUVILLE space is then given by the product basis

$$|i\rangle_{\mathcal{L}} = |n\,k\rangle\,\langle n'\,k'|$$
 (A.48)

The time evolution of a density operator $\hat{\rho}(t)$ with $\hat{\rho}(0)=|i\rangle_{\mathcal{L}}$ is given by the von Neumann equation

$$\hat{\rho}(t) = e^{-i\hat{H}t/\hbar} |n\,k\rangle \langle n'\,k'| \, e^{i\hat{H}t/\hbar} = e^{i\omega_i t} |i\rangle_{\mathcal{L}} = e^{i\omega_i t} \hat{\rho}(0) \quad (A.49)$$

where $\omega_i = (E_{k'} - E_k)/\hbar$ is the oscillation frequency.

A real-valued relaxation superoperator $\hat{\Gamma}$ may be written in the product basis

$$\hat{\Gamma} = \sum_{ij} \Gamma_{ij} |i\rangle_{\mathcal{L}} \langle j|_{\mathcal{L}} . \tag{A.50}$$

A relaxation superoperator is symmetric (i.e. $\Gamma_{ij} = \Gamma_{ji}$). The diagonal terms describe auto-relaxation, and the off-diagonal terms describe cross-relaxation.

In order to understand when terms Γ_{ij} can be neglected, an artificial two-dimensional Liouville space $\{|0\rangle_{\mathcal{L}},|1\rangle_{\mathcal{L}}\}^8$ can be considered. Let $\Delta\omega=\omega_1-\omega_0$ be the difference in oscillating frequencies.

For a system with only cross-relaxation $\Gamma_{ij} = -\Gamma$ evolution of these two states could be described by the matrix equation

$$\frac{\mathrm{d}}{\mathrm{d}t} \left| \hat{\rho}(t) \right\rangle_{\mathcal{L}} = \begin{pmatrix} -\Gamma - \mathrm{i}\Delta\omega/2 & -\Gamma \\ -\Gamma & -\Gamma + \mathrm{i}\Delta\omega/2 \end{pmatrix} \left| \hat{\rho}(t) \right\rangle_{\mathcal{L}} . \quad (A.51)$$

This matrix differential equation can easily be solved by diagonalizing the matrix. The eigenvalues are given by

$$\lambda_{\pm} = -\Gamma \pm \frac{1}{2} \sqrt{4\Gamma - \Delta\omega^2} \ . \tag{A.52}$$

The underscore \mathcal{L} in $|\cdot\rangle_{\mathcal{L}}$ indicates elements of a LIOUVILLE space (see Equation A.20).

Here, the density operator $\hat{\rho}(t)$ is expressed as a vector $|\hat{\rho}(t)\rangle_{\mathcal{L}}$ in the LIOUVILLE space (see Equation A.20) using the basis defined in Equation A.48.

⁸ Note that this cannot represent a real system. The smallest, non-trivial LIOUVILLE space has four dimensions. However, block-diagonal subspaces with two dimensions are possible and this is how this example should be interpreted.

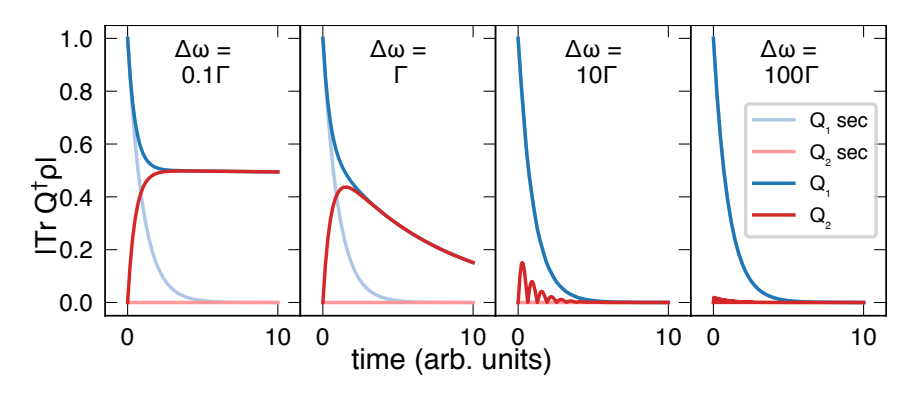


Figure A.2: Validity of the secular approximation for superoperators for different ratios of $\Delta\omega/\Gamma$. Starting from an initial state $\hat{\rho}=|1\rangle_{\mathcal{L}}$ the evolution of the projections $|\langle \rho(t)\,|\,i\rangle|=|\mathrm{Tr}\,\hat{\rho}\,|i\rangle_{L}|$ is plotted as a function of time t. The saturated curves show the evolution of the full superoperator whereas the pale curves show the evolution where the off-diagonal terms are neglected, i.e. the secular approximation is applied. As can be seen, only in the case of $\Delta\omega\ll\Gamma$ the secular approximation leads to results close to the exact solution. Under these conditions, cross-relaxation is quenched due to fast oscillations.

For $|\Delta\omega|\gg |\Gamma|$, i.e. fast oscillation of the off-diagonal terms with respect to the relaxation rate, the eigenvalues can be approximated as

$$\lambda_{\pm}^{\text{secular}} \approx -\Gamma \pm i\Delta\omega/2$$
 (A.53)

which leads to the same results as if the off-diagonal terms were neglected. This is called the *secular approximation* [101]. In contrast, for vanishing $\Delta\omega\approx0$ the eigenvalues are given by

$$\lambda_{+}^{\text{degenerate}} \approx 0$$
 (A.54a)

$$\lambda_{-}^{\text{degenerate}} \approx -2\Gamma$$
 (A.54b)

leading to a long lived coherence $|+\rangle_{\mathcal{L}}=(|0\rangle_{\mathcal{L}}-|1\rangle_{\mathcal{L}})/\sqrt{2}$ and a fast decaying coherence $|-\rangle_{\mathcal{L}}=(|0\rangle_{\mathcal{L}}+|1\rangle_{\mathcal{L}})/\sqrt{2}$. This is also illustrated in Figure A.2.

Figure A.3 provides a graphical illustration for two larger, five-level system. Depending on the level structure, the secular approximations eliminate more or less off-diagonal elements of the relaxation superoperator.

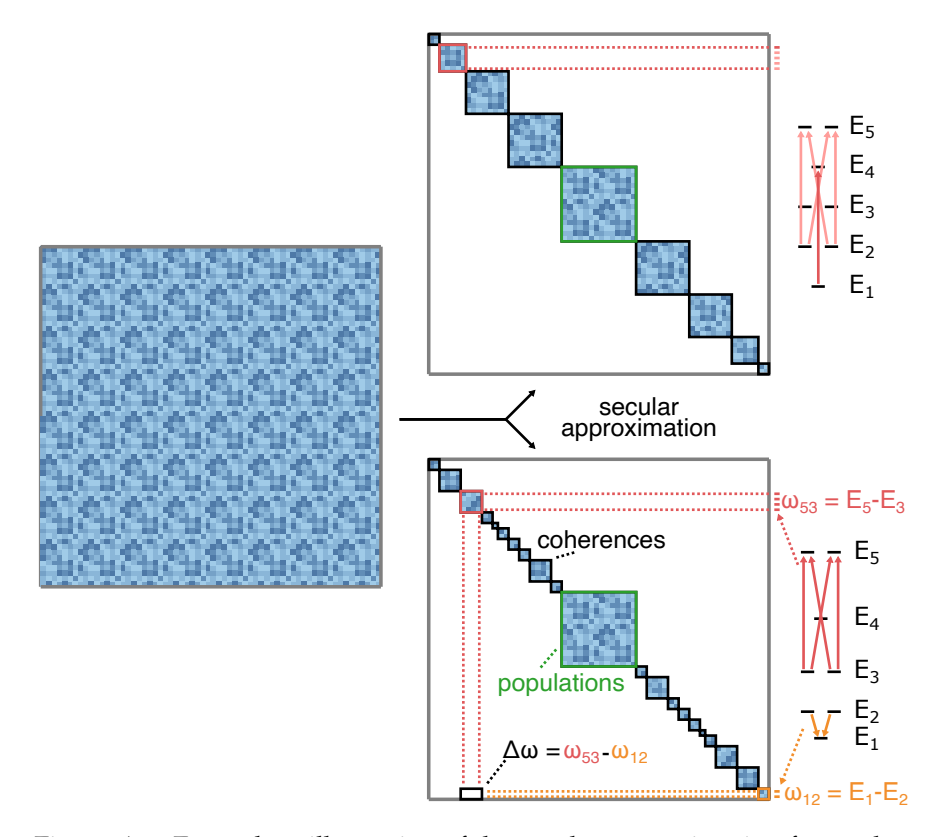


Figure A.3: Exemplary illustration of the secular approximation for a relaxation superoperator for two eight-dimensional, five-level systems. It is assumed that in both cases the off-diagonal terms are much smaller than the energy gaps. In this case, cross-relaxation can only be observed between populations and coherences between degenerate states. The energy levels are equidistantly spaced for the example at the top and unevenly for the bottom example.

Decomposition of Liouville Space Under Time Evolution

Assuming a time-independent, perturbed Hamiltonian of the form

$$\hat{H} = \hat{H}_0 + \hat{H}' \tag{A.55}$$

the secular approximation removes off-diagonal terms of the Hamiltonian that connect states with different zero-order eigenenergies $|n\,i\rangle$. A basis of the Liouville space is given by the product basis $|n'\,i'\rangle\,\langle n,i|$ which implies a general density operator can be expressed as

$$\hat{\rho} = \rho_{n'i'}^{ni} |n'i'\rangle \langle n, i| . \tag{A.56}$$

The time evolution of any of these basis states under \hat{H} can be calculated by the solving the Liouville-von Neumann-equation

$$\begin{split} i\hbar\frac{\partial}{\partial t}\hat{\rho}(t) &= [\hat{H},\hat{\rho}(t)] \\ &= [\hat{H}_{0} + \hat{H}',\rho_{n'i}^{ni}(t) | n'i'\rangle \langle ni|] \\ &= [\hat{H}_{0},\rho_{n'i'}^{ni}(t) | n'i'\rangle \langle ni|] + [\hat{H}',\rho_{n'i'}^{ni}(t) | n'i'\rangle \langle ni|] \\ &= [E_{n'} - E_{n})\rho_{n'i'}^{ni}(t) | n'i'\rangle \langle ni| \\ &+ [h_{mj'}^{mj} | nj'\rangle \langle nj|,\rho_{n'i'}^{ni}(t) | n'i'\rangle \langle n,i|] \\ &= (E_{n'} - E_{n})\rho_{n'i'}^{ni}(t) | n'i'\rangle \langle ni| \\ &+ \rho_{n'i'}^{ni}(t)h_{mj'}^{mj} | mj'\rangle \langle mj | n'i'\rangle \langle ni| \\ &- \rho_{n'i'}^{ni}(t)h_{mj'}^{mj} | n'i'\rangle \langle n,i | mj'\rangle \langle mj|) \\ &= (E_{n'} - E_{n})\rho_{n'i'}^{ni}(t) | n'i'\rangle \langle n,i| \\ &+ \rho_{n'i'}^{ni}(t)h_{n'j'}^{n'i'} | n'j'\rangle \langle n,i| \\ &- \rho_{n'i'}^{ni}(t)h_{n'j'}^{n'i'} | n'i'\rangle \langle n,i| \end{split}$$

As can be seen, due to the secular approximation no term mixes basis states with different main quantum numbers n' and n. Terms with n' = n can therefore be investigated separately from terms with $n' \neq n$.

The same is sometimes true if the secular approximation is applied to the relaxation super-operator $\hat{\Gamma}$: If the secular approximation is applied to Hamiltonian the first order states $|n\,i^{(0)}\rangle=a_{ij}\,|n\,j\rangle$ form an eigenbasis of the Liouville space

$$|n i^{(0)}\rangle \langle n' i'^{(0)}|$$
 (A.58)

The secular approximation removes off-diagonal elements of the superoperator for which $\Delta \omega = \omega_i - \omega_j \gg \Gamma_i j$. The oscillation frequency $\omega_{ni}^{n'i'}$ for $|n\,i^{(0)}\rangle\,\langle n'\,i'^{(0)}|$ is given by

$$\omega_{ni}^{n'i'} = E_{n'}^{(0)} + E_{n'i'}^{(1)} - E_{n}^{(0)} - E_{ni}^{(1)} , \qquad (A.59)$$

The difference

$$\Delta\omega = \omega_{ni}^{n'i'} - \omega_{mj}^{m'j'}$$

$$= E_{n'}^{(0)} + E_{n'i'}^{(1)} - E_{n}^{(0)} - E_{ni}^{(1)} - E_{m'}^{(0)} - E_{m'j'}^{(1)} + E_{mj}^{(0)} + E_{mj}^{(1)}$$
(A.60)

between two states $|n\,i^{(0)}\rangle\,\langle n'\,i'^{(0)}|$ and $|m\,j^{(0)}\rangle\,\langle m'\,j'^{(0)}|$ determines if the relaxation is quenched for this coherence. If one of the two basis states (e.g. the second) describes a coherence between states with the same main quantum number m=m', $\Delta\omega$ can be simplified to

$$\Delta\omega = \omega_{ni}^{n'i'} - \omega_{mj}^{mj'}$$

$$= E_{n'}^{(0)} - E_{n}^{(0)} + E_{n'i'}^{(1)} - E_{ni}^{(1)} - E_{m'j'}^{(1)} + E_{mj}^{(1)} . \qquad (A.61)$$

$$\approx E_{n'}^{(0)} - E_{n}^{(0)}$$

In the last step, it was assumed that the zeroth order eigenenergies are much larger than the first-order corrections. If the splitting is also much larger than the cross-relaxation term between these two coherences⁹, the approximated relaxation superoperator does not contain any term mixing coherences with n' = n and $n' \neq n$. Since

$$|n i^{(0)}\rangle = \sum_{j} a_{ij} |n j\rangle \tag{A.62}$$

this is also true for any choice of eigenbasis $|nj\rangle$ of \hat{H}_0 . As a consequence, the time evolution of terms with n'=n and $n'\neq n$ can be discussed independently of each other. In other words, under time-evolution, the LIOUVILLE space can be decomposed into two invariant subspaces, one containing terms with n'=n and the other one with $n'\neq n$. This is illustrated in Figure A.4.

⁹ For example, the hyperfine coupling is typically much larger than the spinexchange/destruction collision relaxation rates

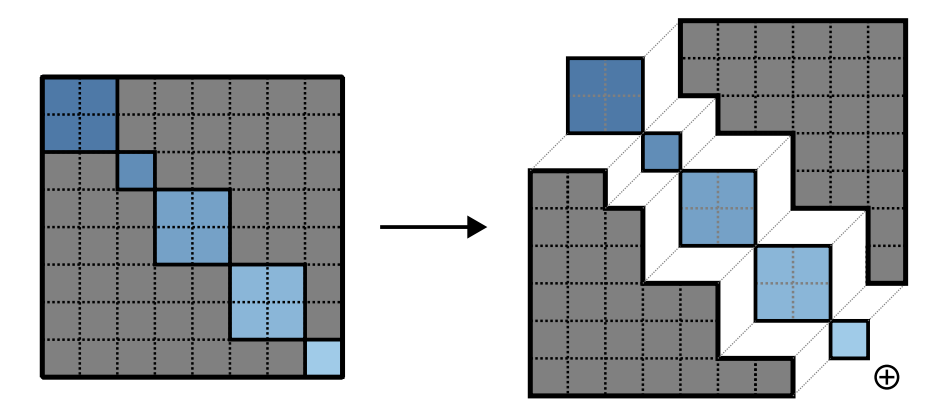


Figure A.4: Graphical illustration of the Liouville space decomposition. If an Hamiltonian (left) is in a block-diagonal form, the time evolution of terms in the Liouville space is completely decoupled (right). If the difference in eigenenergies is much larger than the cross-relaxation this decoupling persists even under the influence of a relaxation superoperator. The Liouville space can be decomposed into invariant subspaces under time evolution.

B

ROTATION ALGEBRA AND REPRESENTATION THEORY

See Noether's theorem

Rotations and rotational symmetry belong to the most important concepts in physics. They appear in many physical systems that show some sort of rotational symmetry which often leads to a conservation law (i.e. the conservation of angular momentum).

This section will discuss briefly the concepts without going into mathematical detail. The interested reader might be referred to a deeper introduction to the representation theory of LIE groups and algebras [169].

In contrast to the rest of the thesis, this chapter is consistently using tensor notation (e.g. covariant tensors are written as $v^i \mathbf{e}_i$ and contravariant tensor as $v_i \mathbf{e}^i$) since it simplifies the notation and is consistent with tensor algebra literature.

B.1 ALGEBRAIC DESCRIPTION OF ROTATIONS

Rotations are mathematically described by the rotation group SU(2) and SO(3). The two groups each form a Lie group which gives rise to the same Lie algebra $\mathfrak{su}(2)/\mathfrak{so}(3)$.

Rotation Groups

Mathematically, rotations form a group which in practice means that applying two random rotations to the same object has the same effect as applying a single, simple rotation along a specific axis by a specific angle.

In quantum physics mainly two types of rotations are important: *Spatial* rotations are described by SO(3) and describe rotations within an Cartesian¹ vector space. These types of rotations are applied whenever something "physical" is rotated, e.g. the laboratory or part of scientific equipment. In contrast, rotations of spinor, here called

¹ Euclid was an ancient Greek mathematician often referred to as the "father of geometry" for his influential work "Elements," which laid the foundation for the study of geometry and served as a standard mathematical text for over two millennia.

intrinsic rotations, are described by the SU(2). Mathematically, there is no difference between spatial and intrinsic rotations as long as the rotations are infinitesimal. However, they differ for macroscopic rotations which becomes clear when realizing that a 360° rotation of a spinor transforms to its negative whereas it is an identity transformation for spatial objects.

Lie Algebra

Instead of studying random rotations of SO(3) or SU(2) it is often useful to look at infinitesimal rotations (here along x as an example)

$$\hat{L}_{x}^{\mathfrak{g}} = \lim_{\phi \to 0} \frac{\hat{R}(\phi, \mathbf{e}_{x}) - \hat{R}(0, \mathbf{e}_{x})}{\phi}$$
(B.1)

instead. Mathematically this can be done by looking at the tangent space at the group identity. For SO(3) the corresponding Lie algebra $\mathfrak{so}(3)$ can be represented by the span of the three matrices $\hat{L}_x^{\mathfrak{g}}$, $\hat{L}_y^{\mathfrak{g}}$ and $\hat{L}_z^{\mathfrak{g}}$ which correspond to infinitesimal rotations around the x, y and z axis. The Lie algebra is also equipped with a Lie bracket, which is an alternating bilinear map

$$\mathfrak{so}(3) \times \mathfrak{so}(3) \to \mathfrak{so}(3) : x \times y \mapsto [x, y] = xy - yx$$
 (B.2)

and is here given by the commutator. Calculating it explicitly leads to

$$[\hat{L}_x^{\mathfrak{g}}, \hat{L}_y^{\mathfrak{g}}] = \hat{L}_z^{\mathfrak{g}}, \quad [\hat{L}_z^{\mathfrak{g}}, \hat{L}_x^{\mathfrak{g}}] = \hat{L}_y^{\mathfrak{g}} \text{ and } [\hat{L}_y^{\mathfrak{g}}, \hat{L}_z^{\mathfrak{g}}] = \hat{L}_x^{\mathfrak{g}}.$$
 (B.3)

The same can be done with SU(2) to construct the corresponding Lie algebra $\mathfrak{su}(2)$. It can be shown that $\mathfrak{su}(2)$ and $\mathfrak{so}(3)$ are isomorph, i.e. it is not required to discuss them separately and from now on they will be simply referred by \mathfrak{g} .

B.2 IRREDUCIBLE REPRESENTATIONS OF LIE ALGEBRAS

Representation theory enables the translation of mathematical conclusions from groups and algebras to mathematical objects that are kind of similar in structure.

Lie Algebra Representation

Representation theory is a useful tool for studying the rotation of objects by exploiting properties of the underlying group or algebra. Mathematically, a representation

$$\rho: \mathfrak{g} \to \operatorname{End}(V) \tag{B.4}$$

of a Lie algebra $\mathfrak g$ on a vector space V is a Lie algebra homomorphism from the algebra $\mathfrak g$ to the space of all linear maps $\operatorname{End}(V)$ of V to itself.

The structure-maintaining feature of the Lie algebra, the Lie bracket, can be defined with a commutator

$$\rho([x,y]) = \rho(x)\rho(y) - \rho(y)\rho(x) \tag{B.5}$$

and must hold for all $x, y \in \mathfrak{g}$.

In quantum mechanics, the vector space V will usually be a HILBERT space for intrinsic rotations and a 3D CARTESIAN space for spatial rotations. For intrinsic rotations $\operatorname{End}(V)$ can be interpreted as the LIOUVILLE space.

Reducible and Irreducible Representations

Assuming $\rho : \mathfrak{g} \to \operatorname{End}(V)$ is a representation of LIE algebra \mathfrak{g} then a subspace $W \subset V$ is called invariant if $\rho(x)w \in W$ for all $w \in W$ and $x \in \mathfrak{g}$. A (non-zero) representation is called irreducible if the only invariant subspaces are V and the zero space $\{0\}$.

Decomposition into a Direct Sum of Irreducible Sub-Representations

One of the main reasons to study representations of Lie algebras is the fact, that the corresponding vector space V can always be expressed

$$V = V_1^{\otimes a_1} \otimes \dots \otimes V_k^{\otimes a_k} \tag{B.6}$$

as a direct sum of subspaces V_i where each of them forms an irreducible representation with the co-restricted map ρ . The number of factors as well as the multiplicities are unique.

If the exact structure of the vector space associated with an irreducible representation is not important, the bold number notation will be used e.g. $W \equiv 3$ represents an irreducible representation of $\}$ with dim W = 3.

B.3 SPHERICAL BASIS STATES OF IRREDUCIBLE REPRESENTA-TION

The three basis vectors \hat{L}_x , \hat{L}_y and \hat{L}_z (see Equation B.1) form a basis of the Lie algebra \mathfrak{g} and are defined as the infinitesimal rotations around the coordinate axis \mathbf{e}_x , \mathbf{e}_y and \mathbf{e}_z .

In quantum mechanics a slightly modified basis

$$\hat{L}_x^{\mathfrak{g}} \mapsto i\hbar \hat{L}_x^{\mathfrak{g}}, \quad \hat{L}_y^{\mathfrak{g}} \mapsto i\hbar \hat{L}_y^{\mathfrak{g}} \text{ and } \hat{L}_z^{\mathfrak{g}} \mapsto i\hbar \hat{L}_z^{\mathfrak{g}}$$
 (B.7)

will be used. These new matrices are Hermitian² and can be more easily compared with angular momentum operators. The commutator relations in this new basis are given by

$$[\hat{L}_{x}^{\mathfrak{g}}, \hat{L}_{y}^{\mathfrak{g}}] = i\hbar \hat{L}_{z}^{\mathfrak{g}}, \quad [\hat{L}_{z}^{\mathfrak{g}}, \hat{L}_{x}^{\mathfrak{g}}] = i\hbar \hat{L}_{x}^{\mathfrak{g}} \text{ and } [\hat{L}_{y}^{\mathfrak{g}}, \hat{L}_{z}^{\mathfrak{g}}] = i\hbar \hat{L}_{x}^{\mathfrak{g}}$$
(B.8)

In addition, the lowering and raising operators

$$\hat{L}_{\pm}^{\mathfrak{g}} = \hat{L}_{x}^{\mathfrak{g}} + i\hat{L}_{y}^{\mathfrak{g}} \tag{B.9}$$

as well as the total angular momentum operator

$$\hat{\mathbf{L}}_{\mathfrak{g}}^{2} = \hat{L}_{x}^{\mathfrak{g}} \hat{L}_{x}^{\mathfrak{g}} + \hat{L}_{y}^{\mathfrak{g}} \hat{L}_{y}^{\mathfrak{g}} + \hat{L}_{z}^{\mathfrak{g}} \hat{L}_{z}^{\mathfrak{g}} \tag{B.10}$$

can be defined for the Lie algebra \mathfrak{g} . For an n-dimensional irreducible representation it can be shown, that the eigenvalue equation

$$\hat{\mathbf{L}}_{\mathfrak{g}}^{2} | l \, m \rangle = \frac{n}{2} \left(\frac{n}{2} - 1 \right) \hbar^{2} | l \, m \rangle = l(l+1) \hbar^{2} | l \, m \rangle \tag{B.11}$$

only allows solutions with $l \in 0, 1/2, 1, 3/2, ...$, i.e. l can only take integer or half-integer³ values, since the dimension n is always an integer. Here, $|l m\rangle$ is an eigenvector with l = n/2 - 1.

The other operators, e.g. $\hat{L}_z^{\mathfrak{g}}$, lead to an eigenvalue equation

$$\hat{L}_{7}^{\mathfrak{g}} | l m \rangle = m \hbar | l m \rangle \tag{B.12}$$

that only allows the eigenvalues $m \in -l, -l+1, ..., l$. In total, this leads to an eigenbasis made of n orthonormal basis vectors.

² Charles Hermite (1822–1901) was a French mathematician known for his pioneering contributions to number theory, algebra, and mathematical analysis, and for his discovery of the transcendental number e, and his work in mathematical physics.

³ Often the spherical basis is associated with spherical harmonics, which is a good analogy for integer values. However, it ignores that the concept of spherical basis also works for half-integer values which have no counterpart in the theory of spherical harmonics.

The relative phase of these vectors can be defined by requiring

$$\hat{L}_{\pm}^{\mathfrak{g}} |l \, m\rangle = \hbar \sqrt{(l \mp m)(l \pm m + 1)} |l \, m \pm 1\rangle \quad . \tag{B.13}$$

A basis whose vectors fulfill all these equations is called a *spherical* basis.

3D Euclidian Vector Space

Elements of SO(3) describe rotations in a 3D CARTESIAN and therefore the operators (here in CARTESIAN coordinates)

$$\hat{L}_{x}^{\mathfrak{g}} = i\hbar \lim_{\phi \to 0} \frac{\hat{R}(\phi, \mathbf{e}_{x}) - \hat{R}(0, \mathbf{e}_{x})}{\phi} = i\hbar \begin{pmatrix} 0 & 0 & 0 \\ 0 & 0 & -1 \\ 0 & 1 & 0 \end{pmatrix}$$
(B.14a)

$$\hat{L}_{y}^{\mathfrak{g}} = i\hbar \begin{pmatrix} 0 & 0 & 1\\ 0 & 0 & 0\\ -1 & 0 & 0 \end{pmatrix}$$
 (B.14b)

$$\hat{L}_{z}^{\mathfrak{g}} = i\hbar \begin{pmatrix} 0 & -1 & 0 \\ 1 & 0 & 0 \\ 0 & 0 & 0 \end{pmatrix} \tag{B.14c}$$

are exactly the ones defined above and fulfill, by construction, the commutator equations (see Equation B.8).

In addition, the spherical Cartesian basis vectors \mathbf{e}_{-} , \mathbf{e}_{0} and \mathbf{e}_{+} fulfill Equation B.11–Equation B.13, i.e.

$$\hat{\mathbf{L}}_{\mathfrak{g}}^{2}\mathbf{e}_{i} = 1(1+1)\hbar^{2}\mathbf{e}_{i} \tag{B.15}$$

$$\hat{L}_{z}^{\mathfrak{g}}\mathbf{e}_{i}=i\hbar\mathbf{e}_{i}\tag{B.16}$$

$$\hat{L}_{\pm}^{\mathfrak{g}} \mathbf{e}_{i} = \hbar \sqrt{(1 \mp i)(1 \pm i + 1)} \mathbf{e}_{i \pm 1} . \tag{B.17}$$

The spherical basis vectors are therefore a spherical basis with respect to the above definition for the LIE algebra g.

Spin Hilbert Space

Let \mathcal{H}_S be a Hilbert space for a spin S particle. It is an irreducible representation of \mathfrak{g} by defining

$$\rho: \mathfrak{su}(2) \to \operatorname{End}(\mathcal{H}_{S}): v^{i}\hat{L}_{i}^{\mathfrak{g}} \mapsto v^{i}\hat{S}_{i}$$
(B.18)

These operators fulfill all commutators relations and the $|S m_S\rangle$ states are constructed in the same way as the example above. The usual basis states are therefore in the spherical basis and the Hilbert space is an irreducible representation of \mathfrak{g} .

Dual Vector Space

Here, only a vector space *V* over a field *F* equipped with an inner product

$$\langle \cdot, \cdot \rangle : V \otimes V \to F : \mathbf{v}, \mathbf{w} \mapsto \langle \mathbf{v}, \mathbf{w} \rangle$$
 (B.19)

is considered, since it defines a canonical isomorphism

$$V \to V^* : \mathbf{v} \mapsto \mathbf{v}^* = \langle \mathbf{v}, \cdot \rangle$$
 (B.20)

that maps a vector $\mathbf{v} \in V$ to its dual vector $\mathbf{v}^* \in V*$.

Let V be an n-dimensional Cartesian vector space V over \mathbb{C} with Cartesian basis $\{\mathbf{e}_i\}$. The inner product for such a vector space is typically⁴ defined as

$$\langle v^i \mathbf{e}_i, w^i \mathbf{e}_i \rangle = (v^i)^* w^i \tag{B.21}$$

where $\mathbf{v} = v^i \mathbf{e}_i \in V$ and $\mathbf{w} = w^i \mathbf{e}_i \in V$ are two vectors. If V is over \mathbb{R} instead, the complex conjugate $(w^i)^* \mapsto w^i$ is ignored.

The spherical basis of 3D Cartesian vector spaces is defined as

$$\mathbf{e}_0 = \mathbf{e}_z$$
 and $\mathbf{e}_{\pm} = \mp \frac{1}{\sqrt{2}} \mathbf{e}_x - \frac{\mathrm{i}}{\sqrt{2}} \mathbf{e}_y$ (B.22)

The corresponding dual basis is given by

$$\mathbf{e}^{0} = \mathbf{e}^{z} \text{ and } \mathbf{e}^{\pm} = \mp \frac{1}{\sqrt{2}} \mathbf{e}^{x} + \frac{i}{\sqrt{2}} \mathbf{e}^{y}$$
 (B.23)

which ensures

$$\mathbf{e}^{i}(\mathbf{e}_{j}) = \delta^{i}_{j} \tag{B.24}$$

with the Kronecker delta δ_i^i .

One could naively assume that the dual basis of a spherical basis is a spherical basis itself. However, with usual conventions, this is

The same can be done for any n-dimensional Cartesian vector space.

⁴ This is the definition typically used by physicists. Mathematicians usually prefer the inner product to be linear in the first argument instead of the second.

often not the case. The rotation $\hat{R}^*(v^*)$ of a dual vector v^* is defined via the natural isomorphism Equation B.20

$$\hat{R}^* v^* \equiv \langle \hat{R} v, \cdot \rangle = \langle v, \hat{R}^\dagger \cdot \rangle = v^* \circ \hat{R}^\dagger . \tag{B.25}$$

The dual angular momentum operators are defined via infinitesimal rotations

$$\hat{L}_{x}^{*}v^{*} = i\hbar \lim_{\phi \to 0} \frac{\hat{R}^{*}(\phi, \mathbf{e}_{x}) - \hat{R}^{*}(0, \mathbf{e}_{x})}{\phi} v^{*}$$

$$= v^{*} \circ i\hbar \lim_{\phi \to 0} \frac{\hat{R}(\phi, \mathbf{e}_{x})^{\dagger} - \mathbb{1}^{\dagger}}{\phi}$$

$$= v^{*} \circ i\hbar \left(\lim_{\phi \to 0} \frac{\hat{R}(\phi, \mathbf{e}_{x}) - \mathbb{1}}{\phi}\right)^{\dagger}$$

$$\stackrel{B.1}{=} v^{*} \circ i\hbar \left(\frac{\hat{L}_{x}}{i\hbar}\right)^{\dagger}$$

$$= v^{*} \circ i\hbar \left(\frac{\hat{L}_{x}}{i\hbar}\right)^{\dagger}$$

$$= v^{*} \circ i\hbar \left(\frac{\hat{L}_{x}}{i\hbar}\right)$$

$$= v^{*} \circ i\hbar \left(\frac{\hat{L}_{x}}{i\hbar}\right)$$

$$= v^{*} \circ -\hat{L}_{x}$$
(B.26)

and therefore the representation maps

$$\hat{L}_{x}^{\mathfrak{g}} \mapsto \cdot \circ - \hat{L}_{x} . \tag{B.27}$$

In the same way, the maps of the other angular momentum operators

$$\hat{L}_{\nu}^{\mathfrak{g}} \mapsto \cdot \circ \hat{L}_{\nu}$$
 (B.28a)

$$\hat{L}_z^{\mathfrak{g}} \mapsto \cdot \circ - \hat{L}_z \tag{B.28b}$$

$$\hat{L}_{\pm} = \hat{L}_x \pm i\hat{L}_y \mapsto \cdot \circ (-\hat{L}_x \mp i\hat{L}_y) = \cdot \circ (-\hat{L}_{\pm})$$
(B.28c)

can be derived.

Investigating the effect of the raising and lowering operators $\cdot \circ -\hat{L}_{\pm}$ to the dual basis vectors \mathbf{e}^{i}

$$\mathbf{e}^{i} \circ -\hat{\mathbf{L}}_{\pm} = -\sqrt{(j \mp m)(j \pm m + 1)}\mathbf{e}^{i \mp 1} \neq \sqrt{(j \pm m)(j \mp m + 1)}\mathbf{e}^{i \pm 1}$$
(B.29)

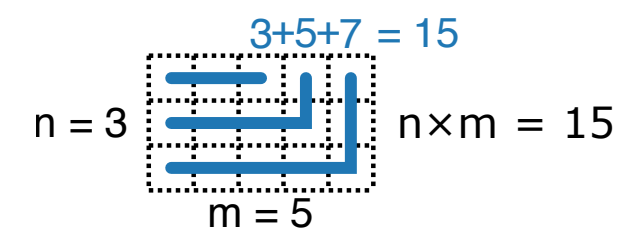


Figure B.1: Graphical representation of the dimensions of the vector space decomposition for irreducible representations of $\mathfrak{so}(3)$ and $\mathfrak{su}(2)$.

shows that the dual basis does not fulfill Equation B.13 and, as mentioned before, is therefore not a spherical basis of the dual space.

The correct spherical basis of the dual space is given by

$$\mathbf{e}_{\text{spherical}}^{m} = (-1)^{-m-J} \mathbf{e}^{-m} \tag{B.30}$$

and can be constructed from the dual basis of the spherical basis of the vector space.

Dual Hilbert Space

The same can be done for a Hilbert space. If $|l \, m\rangle$ is a spherical basis of the Hilbert space \mathcal{H} , a spherical basis of the dual Hilbert space is given by

$$\langle l m |_{\text{spherical}} = (-1)^{-m-l} \langle l - m |$$
 (B.31)

B.4 PRODUCT SPACE OF IRREDUCIBLE REPRESENTATIONS

The true power of representations theory reveals itself when the product space of two irreducible representations of the same Lie algebra g is investigated.

Or dual vector space

Let ρ be an irreducible representation of a Lie algebra $\mathfrak g$ with a vector space V of dimension dim V=n=2l+1. As mentioned before, such a vector space will be denoted by $\mathbf n$ which is called the bold number notation. For example, $\mathbf 3_{\mathfrak g}$ represents a three-dimensional vector space of an irreducible representation of a Lie algebra $\mathfrak g$. Furthermore, let $|l\ m\rangle$ be a spherical basis of such a vector space.

The product space ($m \ge n$ assumed)

$$\begin{split} \mathbf{n} \otimes \mathbf{m} &= \\ &= \bigoplus_{i=1}^n \mathbf{m} - \mathbf{n} - \mathbf{1} + 2\mathbf{i} \\ &= (\mathbf{m} + \mathbf{n} - \mathbf{1}) \oplus (\mathbf{m} + \mathbf{n} - \mathbf{3}) \oplus \cdots \oplus (\mathbf{m} - \mathbf{n} + \mathbf{3}) \oplus (\mathbf{m} - \mathbf{n} + \mathbf{1}) \\ &\qquad \qquad (B.32) \end{split}$$

can be decomposed into irreducible subspaces. Hereby, the representations

$$\rho: \mathfrak{g} \to \operatorname{End}(\mathbf{n} \otimes \mathbf{m}): x \mapsto \rho_{\mathbf{n}}(x) \otimes \rho_{\mathbf{m}}(x)$$
(B.33)

are defined via their original representations ρ_n and ρ_m . Counting the dimensions leads to

$$\sum_{i=1}^{n} m - n - 1 + 2i = mn - nn - n + 2\frac{n(n+1)}{2} = m \times n \quad (B.34)$$

the expected result of the dimension of the product space. This is also graphically visualized in Figure B.1.

An often-occurring scenario is

$$\mathbf{n} \otimes \mathbf{n} = \bigoplus_{i=1}^{n} -\mathbf{1} + 2\mathbf{i}$$

$$= (2\mathbf{n} - \mathbf{1}) \oplus (2\mathbf{n} - \mathbf{3}) \oplus \cdots \oplus (\mathbf{3}) \oplus (\mathbf{1})$$
(B.35)

the product space of two vector spaces with the same dimensions.

Assuming $|l_1 m_1\rangle$ and $|l_2 m_2\rangle$ are spherical basis states in ρ_n and ρ_m then the spherical basis of the product space

$$|LM\rangle = \sum_{m_1, m_2} |l_1 m_1\rangle \otimes |l_2 m_2\rangle C_{l_1 m_1 l_2 m_2}^{LM}$$
 (B.36)

can be derived using the Clebsch⁵-Gordan⁶ coefficients $C_{l_1 \, m_1 \, l_2 \, m_2}^{L\, M}$. The spherical quantum numbers have to fulfill the triangular condition

$$|l_1 - l_2| \le L \le l_1 + l_2 \tag{B.37}$$

⁵ Alfred Clebsch (1833–1872) was a German mathematician known for his pioneering work in algebraic geometry and his development of Clebsch–Gordan coefficients, which are fundamental to the study of angular momentum and quantum mechanics.

⁶ Paul Gordan (1837–1912) was a German mathematician who made significant contributions to algebraic geometry, invariant theory, and the theory of algebraic equations, and is particularly known for his work on geometric and algebraic aspects of determinants.

as well as

$$m_1 + m_2 = M$$
 (B.38)

to lead to non-zero Clebsch-Gordan coefficients.

This is an extremely powerful technique that works as long as the original vector spaces are already irreducible representations (or a direct sum of irreducible representations). It works for vector spaces, dual spaces, combinations of them, and even tensor operators.

Coupling Angular Momentum

A common case in quantum physics is the product space of two Hilbert spaces describing a spin \mathcal{H}_1 and \in_2 . Let l_1 , l_2 , m_1 , and m_2 be the corresponding quantum numbers. Each Hilbert space forms an irreducible representation of the Lie algebra \mathfrak{g} with the spherical basis $|l_1 m_1\rangle$ and $|l_2 m_2\rangle$. From Equation B.36 the spherical basis $|L M\rangle$ of the product space $\mathcal{H}_1 \otimes \mathcal{H}_2$ is given by

$$|L, M\rangle = \sum_{m_1, m_2} |l_1 m_1\rangle \otimes |l_2 m_2\rangle C_{l_1 m_1 l_2 m_2}^{LM}$$
 (B.39)

Vector Space Endomorphisms

An endomorphisms \hat{A} is a linear map

$$\hat{A}: V \to V: \mathbf{v} \mapsto \hat{A}(\mathbf{v}) \equiv \hat{A}\mathbf{v}$$
 (B.40)

from a vector space V over a field F into itself. If \mathbf{e}_i is a basis of V and \mathbf{e}^i it holds for a vector $\mathbf{v} = v^i \mathbf{e}_i$

$$\hat{A}\mathbf{v} = \hat{A}v^{i}\mathbf{e}_{i} = (\mathbf{A}_{k}\mathbf{e}^{k})v^{i}\mathbf{e}_{i} = (\mathbf{e}_{i}A_{k}^{j}\mathbf{e}^{k})v^{i}\mathbf{e}_{i} . \tag{B.41}$$

with $\mathbf{A}_k = \hat{A}\mathbf{e}_k$ (i.e. $\mathbf{A}_k\mathbf{e}^k = \hat{A}$) and $A_k^j = \mathbf{e}^j\mathbf{A}_k$ (i.e. $\mathbf{e}_jA_k^j = \mathbf{A}_k$). $\mathbf{e}_jA_k^j\mathbf{e}^k$ can be interpreted as an element of the product space of $V \otimes V^*$ and therefore, a spherical basis for this tensor can be constructed from the spherical basis of the underlying (dual) vector space.

If \mathbf{e}_i is a 2l+1 dimensional spherical basis of V and \mathbf{e}^j is the corresponding dual basis, then a spherical basis of the product space is given by

$$\mathbf{e}_{L,M} = \sum_{i,j} (-1)^{j-l} \mathbf{e}_i \mathbf{e}^{-j} C_{l,i,l,j}^{LM} . \tag{B.42}$$

A spherical basis can also be constructed for linear maps between two different vector spaces (even with different dimensions $l_1 \neq l_2$), as long as both of them are irreducible representations of the same Lie algebra \mathfrak{g} .

Spherical Operator Basis

An operator \hat{A} is an endomorphism from a Hilbert space \mathcal{H} into itself

$$\hat{A}: \mathcal{H} \to \mathcal{H}: |\varphi\rangle \mapsto \hat{A} |\varphi\rangle$$
 (B.43)

In the same way as the vector space endomorphism, it can be interpreted as an element of the product space of \mathcal{H} with its dual space \mathcal{H}^* . In that way, taking the spherical basis $(-1)^{m_2-l_2} \langle l_2 m_2 |$, a spherical operator basis \hat{T}_{LM} can be defined by⁷

$$\hat{T}_{LM}^{l_1 l_2} = \sum_{m_1, m_2} |l_1 m_1\rangle \langle l_2 - m_2| (-1)^{-m_2 - j_2} C_{l_1 m_1 l_2 m_2}^{LM} .$$
 (B.44)

As for vector space endomorphisms, a spherical basis can also be constructed for linear maps between two different Hilbert spaces, that are both irreducible representations of the same Lie algebra g.

In Mathematica the SpinDynamica⁸ [170, 171] packages automatically generate a spherical operator basis⁹ with the

SphericalTensorOperatorBasis[]

command.

Commutator Equation of Spherical Operators

Alternatively, to constructing spherical operators from the spherical basis of the underlying vector spaces, the defining equations can also be directly formulated in the form of a commutator equation.

The spherical basis operators \hat{T}_{LM} should not be confused with the matrix elements T_{ij} of an operator \hat{T} .

⁷ In the context of operators, the quantum numbers *L* and *M* are often referred to as the *spherical rank*. To avoid confusion with the tensor rank of an operator, this terminology is avoided in this thesis.

⁸ SpinDynamica is a software package developed for the analysis and simulation of nuclear magnetic resonance (NMR) spectroscopy, providing a comprehensive set of tools and methods for studying spin dynamics in complex systems.

⁹ In contrast to the conventions used in this these, SpinDynamica's spin operators are defined with \hbar and are therefore not in units of angular momentum.

Let $\hat{A} = A_j^i |i\rangle \langle j|$ be an operator with a random basis $|i\rangle \langle j|$. The \hat{L}_x operator can be found by looking at infinitesimal rotations

$$i\hbar \lim_{\phi \to 0} \frac{\hat{R}(\phi, \mathbf{e}_{x}) \hat{A} \hat{R}(\phi, \mathbf{e}_{x})^{\dagger} - \hat{R}(0, \mathbf{e}_{x}) \hat{A} \hat{R}(0, \mathbf{e}_{x})^{\dagger}}{\phi}$$

$$= i\hbar \lim_{\phi \to 0} \frac{\hat{R}(\phi, \mathbf{e}_{x}) \hat{A} \hat{R}(\phi, \mathbf{e}_{x})^{\dagger} - \hat{A} \hat{R}(\phi, \mathbf{e}_{x})^{\dagger}}{\phi}$$

$$+ i\hbar \lim_{\phi \to 0} \frac{\hat{A} \hat{R}(\phi, \mathbf{e}_{x})^{\dagger} - \hat{A}}{\phi}$$

$$= i\hbar \left(\lim_{\phi \to 0} \frac{\hat{R}(\phi, \mathbf{e}_{x}) - \mathbb{1}}{\phi}\right) \hat{A} \left(\lim_{\phi \to 0} \hat{R}(\phi, \mathbf{e}_{x})^{\dagger}\right)$$

$$+ i\hbar \hat{A} \lim_{\phi \to 0} \frac{\hat{R}(\phi, \mathbf{e}_{x}) - \mathbb{1}}{\phi}$$

$$= \hat{L}_{x} \hat{A} - \hat{A} \hat{L}_{x}$$

$$= [\hat{L}_{x}, \hat{A}]$$
(B.45)

which leads to

$$\hat{L}_x \mapsto [\hat{L}_x, \hat{A}]$$
 (B.46)

In the same way, it can be shown that

$$\hat{L}_y \mapsto [\hat{L}_y, \hat{A}] \text{ and } \hat{L}_z \mapsto [\hat{L}_z, \hat{A}]$$
 (B.47)

The equations for a spherical basis are then given by

$$[\hat{L}_z, \hat{T}_{L,M}] = \hbar m \hat{T}_{lm} \tag{B.48a}$$

$$[\hat{L}_{\pm}, \hat{T}_{LM}] = \hbar \sqrt{(l \mp m)(j \pm m + 1)} \hat{T}_{l m \pm 1}$$
 (B.48b)

This is sometimes the only given definition for spherical tensors but has the disadvantage, that it only works for this specific type of operator. In addition, it may generate confusion if compared to the spherical tensor operators introduced in the next section that do not fulfill this commutator equation, since the commutator may not even be defined for elements of the product space $V \otimes V$.

Second Rank Spherical Tensors

Some physical effects are described by second-rank tensors of the form

$$\hat{Q} = Q_{ij} \mathbf{e}^i \mathbf{e}^j \tag{B.49}$$

where \hat{Q} is a second rank contravariant coordinate tensor over the vector space $V^* \otimes V^*$. This tensor maps two vectors $\mathbf{v} = v^i \mathbf{e}_i \in V$ and $\mathbf{v} = v^i \mathbf{e}_i \in V$ to an element of the field \mathbb{F} of the vector space 2l+1 dimensional vector space V.

The vectors \mathbf{v} and \mathbf{w} can be interpreted as an element of the product space $V \otimes V$. Assuming each \mathbf{e}_i is a spherical basis, the spherical basis of the product space is simply given by

$$\mathbf{e}_{LM} = \sum_{m_1, m_2} \mathbf{e}_{m_1} \otimes \mathbf{e}_{m_2} C_{lm_1 lm_2}^{LM} . \tag{B.50}$$

This also defines a dual basis $V^* \otimes V^*$

$$\mathbf{e}^{LM} = \sum_{m_1, m_2} \mathbf{e}^{m_1} \otimes \mathbf{e}^{m_2} C_{lm_1 lm_2}^{LM} . \tag{B.51}$$

however, as mentioned previously, this is not a spherical basis anymore. Instead, the spherical dual basis would be given by

$$\mathbf{e}_{\text{spherical}}^{LM} = \sum_{m_1, m_2} (-1)^{-m_1 - m_2 - 1 - 1} \mathbf{e}_{-m_1} \otimes \mathbf{e}_{-m_2} C_{lm_1 l m_2}^{LM}$$

$$= (-1)^m \mathbf{e}^{L - M}$$
(B.52)

and vice versa

$$\mathbf{e}^{LM} = (-1)^M \mathbf{e}_{\text{spherical}}^{L-M} . \tag{B.53}$$

Often in the literature, it is not specified if the tensor is given in the canonical dual basis or the spherical basis of the dual space.

In reality V is often a 3D Cartesian vector space (i.e.l = 1) over the real \mathbb{R} or complex \mathbb{C} numbers.

Spherical Tensor Operators

In quantum mechanics, the concept of tensors is also used in the form of tensor operators¹¹. However, in contrast to the example described above, vectors

$$V \ni \mathbf{v} = v^i \mathbf{e}_i \mapsto \hat{A}^i \mathbf{e}_i = \hat{\mathbf{A}} \in \tilde{V}$$
 (B.54)

This is due to $\mathbf{e}^{LM}\mathbf{e}_{L'M'} = \delta_{L'}^L \delta_{M'}^M$

¹¹ Operators themselves can be interpreted as tensors. To distinguish vector operators from normal operators, in this thesis, the term tensor operator will only be used in the context of tensors of operators and linear maps between them. However, other literature may have a different naming convention and may use the term tensor operator in a much broader scope.

are replaced by vector operators and dual vectors

$$V^* \ni \mathbf{w}^* = w_i \mathbf{e}^i \mapsto \hat{w}_i \tilde{\mathbf{e}}^i = \tilde{\mathbf{w}}^* = \in \tilde{V}^*$$
(B.55)

are replaced by linear maps

$$\tilde{\mathbf{w}}: \tilde{V} \to \mathcal{L}$$
 (B.56)

where \mathcal{L} is the linear span of $\{\hat{A}^i\}$.

 \tilde{V} is a vector space but \tilde{V}^* is not a dual vector space, since \mathcal{L} , the vector space of operators, is not a field. Mathematically, tensor operators are therefore not tensors by definition. However, representation theory does not require the linear maps to be dual vectors, so only the notation of tensors can still be applied while keeping the representation theoretical aspects untouched. This is often done in quantum mechanics.

In SpinDynamica, spherical tensors operators of the type

$$\hat{T}_{LM} \in \tilde{V}_i \otimes \tilde{V}_k$$
 , (B.57)

where \tilde{V}_i is the linear span¹² of $\{\mathbf{e}_x \hat{I}_x^i, \mathbf{e}_y \hat{I}_y^i, \mathbf{e}_z \hat{I}_z^i\}$ with $i \in \{j, k\}$) and spin operators \hat{S}_x , \hat{S}_y , \hat{S}_z for spin i can be obtained by the

command.

¹² Note that in SpinDynamica spin operators are defined dimensionless.

NUMERICAL SIMULATIONS AND CALCULATIONS

Two different approaches will be discussed to numerically calculate and simulate spin dynamics in hot vapors that experience spinexchange collisions.

The first approach extends the original publication from Happer and Tam [30] to highly polarized spin states by considering a local approximation of the right side of the density matrix equation.

The other approach directly numerically integrates the density matrix equation.

C.1 SPHERICAL OPERATOR BASIS FOR 87RB GROUND SPIN STATES

The use of irreducible tensors offers several advantages when dealing with systems that offer some kind of rotational symmetry. First suggested by Fano [172] it got later popularized for describing optical pumping phenomenon [173–175] and or spin-exchange collisions [30, 173, 174].

Let $\hat{\mathbf{F}}$ be the total spin of a system and let $|F, m_F\rangle$ be an eigenstate of the $\hat{\mathbf{F}}^2$ and \hat{F}_z with the eigenvalues $\hbar^2 s \cdot (F+1)$ and $\hbar m_F$. With these states, spherical tensor operators can be defined by

$$\hat{T}_{l,m}^{F,F'} = \sum_{m_F=-l}^{l} |F, m_F\rangle \langle F', m_F - m| (-1)^{m_F - M - F'} \cdot C_{F,m_F,F',M-m_F}^{l,m} , \text{ (C.1)}$$

where $C^{J,M}_{j_1,m_1,j_2,m_2}$ is the Clebsch-Gordan coefficient. If only states with F=F' are considered, the spherical tensor operators may be also written as $\hat{T}_{l,m}$.

Spherical tensors fulfill the following commutator identities

$$[\hat{F}_{\pm}, \hat{T}_{l,m}] = \hbar \sqrt{(l \mp m) \cdot (l \pm m + 1)} \hat{T}_{l,m\pm 1}$$
 (C.2)

$$\left[\hat{F}_{z},\hat{T}_{l,m}\right] = \hbar m \hat{T}_{l,m\pm 1} \tag{C.3}$$

and transform under rotations as

$$\hat{\mathcal{D}}(\hat{R})\hat{T}_{l,m}\hat{\mathcal{D}}^{\dagger}(\hat{R}) = \sum_{m'=-l}^{l} \hat{T}_{l,m'}\mathcal{D}_{m',m}^{l} , \qquad (C.4)$$

where $\hat{\mathcal{D}}$ is the Wigner D-matrix, whose elements are defined by

$$\mathcal{D}_{m',m}^{l} = \langle l, m' | \hat{R} | l, m \rangle . \tag{C.5}$$

C.2 LOCAL LINEARIZATION OF THE DENSITY MATRIX EQUATION

The right side of the density matrix equation $\mathcal{L}(\hat{\rho}(t),t)$ (see Equation 1.7) is non-linear in $\hat{\rho}$, due to the term that describes spin-exchange collisions (see Equation 1.12). However, it can be locally approximated around $\hat{\rho}_0$

$$\mathcal{L}(\hat{\rho}(t)) \approx \mathcal{L}(\hat{\rho}_0) + \hat{\hat{\mathcal{L}}}(\hat{\rho}(t) - \hat{\rho}_0)$$
, (C.6)

with a linear super-operator $\hat{\mathcal{L}}$ for sufficiently close operators $\hat{\rho}$. It is also assumed, that \hat{f} does not have an explicit time dependence.

Let $\{|i\rangle = \hat{T}_i\}$ be an orthonormal basis of the Liouville space, i.e.

$$\langle j|i\rangle = \delta_{ij}$$
 (C.7)

where

$$\langle j|i\rangle = \operatorname{Tr} T_j^{\dagger} T_i \tag{C.8}$$

is the Hilbert-Schmidt inner product.

To investigate the dynamics of the system the matrix elements $\langle j|\hat{\hat{\mathcal{L}}}|i\rangle$ are of great interest. It can be calculated

$$\hat{\mathcal{L}}|i\rangle = \frac{1}{\lambda}\hat{\mathcal{L}}(\lambda|i\rangle) = \frac{1}{\lambda}\hat{\mathcal{L}}(\rho_0 + \lambda|i\rangle - \rho_0)$$

$$\stackrel{\lambda \to 0}{=} \frac{1}{\lambda}\left(\hat{f}(\rho_0 + \lambda|i\rangle) - \hat{f}(\rho_0)\right)$$
(C.9)

by using Equation C.6 for sufficiently small λ .

A convenient basis for the Liouville space is the spherical tensor operators $|i\rangle=|l,m,F,F'\rangle=\hat{T}_{l,m}^{F,F'}$, which fulfill the orthonormality condition.

The density matrix equations will be analyzed around density operators

$$\hat{\rho}_0 = N_S N_I \times e^{\beta \cdot \hat{\mathbf{f}}} \tag{C.10}$$

This is sometimes called a Liouville bracket in the context of NMR e.g. in MATHEMATICA package SPINDYNAMICA

¹ Eugene Wigner (1902–1995) was a Hungarian–American physicist and mathematician who made significant contributions to quantum mechanics, nuclear physics, and group theory, and was awarded the Nobel Prize in Physics in 1963 for his work on the application of symmetry principles to quantum mechanics.

that are described by a spin temperature distribution $\beta = (0,0,\beta)$ (see Equation 1.20). Since the spin temperature is aligned with the z axis the operator is a superposition of spherical tensors with m = 0. In contrast, transversal magnetization is described by spherical tensors with $m = \pm 1$.

Spin exchange collisions do not mix operators with different *m* quantum numbers i.e.

$$\langle j|\mathcal{L}|j\rangle = \delta_{m,m'} \langle j|\mathcal{L}|j\rangle$$
 (C.11)

with $|i\rangle = |l, m, F1, F2\rangle$ and $|j\rangle = |l', m', F1', F2'\rangle$.

Since the $m = \pm 1$ states are of main interest, it is sufficient to just calculate matrix elements

$$\langle l', 1, F1', F2' | \mathcal{L} | l, 1, F1, F2 \rangle$$

$$= \frac{1}{\lambda} \left(\langle l', 1, F1', F2' | \hat{f}(\rho_0 + \lambda \hat{T}_{l,1}^{F1,F2}) \rangle - \langle l', 1, F1', F2' | \hat{f}(\rho_0) \rangle \right)$$

$$= \frac{1}{\lambda} \left(\langle l', 1, F1', F2' | \hat{f}(\rho_0 + \lambda \hat{T}_{l,1}^{F1,F2}) \rangle \right)$$
(C.12)

with m = 1 (or m = -1). In the last step the fact that $\hat{\rho}$ only contains $T_{0,0}^{F,F'}$ operators was used.

From here, the analysis is completely identical to the procedure described in Happer and Tam [30]. The so-calculated matrix can be diagonalized and the eigenvalues be interpreted in the form of a relaxation rate and LARMOR frequency.

In contrast to the original paper, all tensors with $m=\pm 1$ are being considered instead of just the ones with l=1. For ⁸⁷Rb (l=3/2 and S=1/2) this leads to 12-dimensional Liouville space for each quantum number m which is significantly larger compared to what Happer and Tam [30] originally discussed.

Generally, the eigenproblem may lead to 12 different eigenvalues and 12 different relaxation rates (see Figure C.1). Even if not all of the eigenvectors may have a significant oscillator strength or oscillate at frequencies as high as the hyperfine splitting, the observed FID may be highly non-mono-exponential. For many applications (e.g. magnetometry) only the slowest relaxation rate is of interest that may be labeled $1/T_2$. However, in the context of spin noise spectroscopy, the other relaxation rates may be important for the analysis of the spectrum (see Mouloudakis et al. [75]).

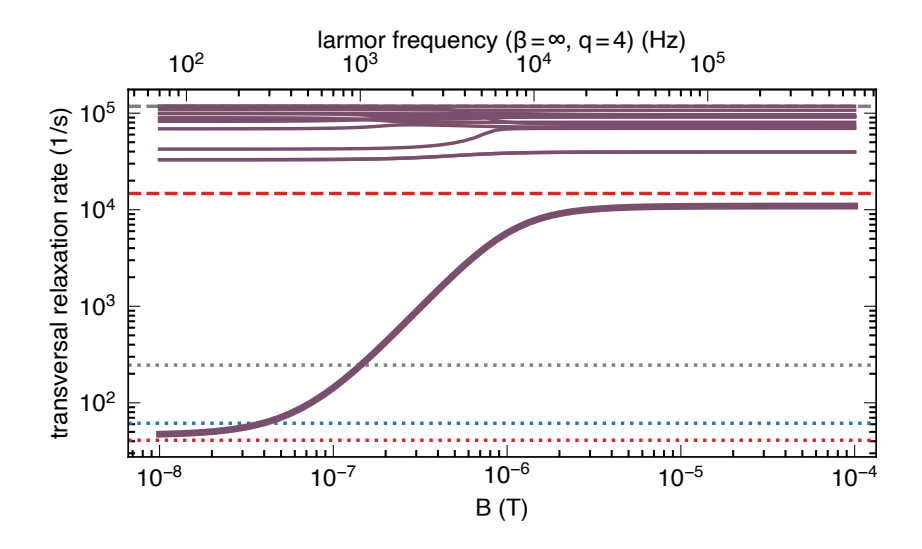


Figure C.1: Transverse relaxation rates of all LIOUVILLE eigenstates. Most of the coherences relax very quickly at a rate comparable to the spin-exchange rate. Whereas for magnetometry usually, only the slowest relaxation rate has to be considered, the other terms may measurably affect the spin evolution e.g. when studying spin-noise spectra.

C.3 NUMERICAL INTEGRATION OF THE DENSITY MATRIX EQUA-

An alternative approach is the numerical integration of the density matrix equation. Assuming the density matrix equation is of the form

$$\frac{\mathrm{d}\hat{\rho}}{\mathrm{d}t} = \frac{1}{\mathrm{i}\hbar} \left[\hat{H}, \hat{\rho} \right] + \mathcal{L}^{\mathrm{incoh}}(\hat{\rho}, t) \tag{C.13}$$

with a coherent and non-coherent part, the density operator's time evolution can be estimated. Assuming an density operator $\hat{\rho}_n = \hat{\rho}(n \times \Delta t)$, the density operator $\hat{\rho}_{n+1} = \hat{\rho}((n+1) \times \Delta t)$ will be estimated by using an iterative procedure

$$\hat{\rho}_{n+1} = e^{-i\hat{H}\Delta t/\hbar} \hat{\rho}_n e^{i\hat{H}\Delta t/\hbar} + \mathcal{L}^{incoh}(\hat{\rho}_n, n \times \Delta t) \Delta t$$
 (C.14)

which is a combination of the exact solution for the coherent term and an Euler² method for the incoherent one.

² Leonhard Euler (1707–1783) was a Swiss mathematician and physicist who made significant contributions to many areas of mathematics, including number theory, calculus, graph theory, and mathematical physics, and is regarded as one of the most prolific mathematicians in history.

Major challenges for numerical integration are fast oscillating terms since they require short integration time steps which can drastically increase the computational time. In the context of alkali atoms (especially 87 Rb the hyperfine coupling in the order of GHz creates fast oscillating terms between states of different total angular momentum quantum number F.

However, it has been shown [47], that as long as the hyperfine term greatly exceeds all other terms in the Hamiltonian (which is fulfilled for the parameter space discussed in this thesis) the density operator can be secularized

$$\hat{\rho}_{\text{sec}} = \hat{\rho}_{F=1} \oplus \hat{\rho}_{F=2} \tag{C.15}$$

which effectively removes all coherences between these states and therefore removes the fast oscillating terms.

Numerically, this secularization can be easily performed if the density matrix is expressed in a basis consisting of eigenstates of the total angular momentum $|F, m_F\rangle$.

This secularization

$$(\hat{\rho}_{n+1})_{ij} := \delta_{F,F'}(\hat{\rho}_{n+1})_{ij}$$
 (C.16)

is performed after each integration step. Here F and F' corresponds to the main quantum number of the i-th and j-th basis state.

After each integration step some further checks are performed to reduce accumulated numerical errors and ensure the new operator fulfills the requirements of a density operator. Firstly, it is ensured that the new density operator is still HERMITIAN by replacing the original density operator with

$$\hat{\rho}_{n+1} := \frac{\hat{\rho}_{n+1} + \hat{\rho}_{n+1}^{\dagger}}{2} , \qquad (C.17)$$

and secondly, negative values are removed from the diagonal

$$(\hat{\rho}_{n+1})_{ii} \stackrel{!}{\geq} 0$$
 . (C.18)

Thirdly, the populations on the diagonal are checked

$$\left| (\hat{\rho}_{n+1})_{ij} \right| \stackrel{!}{\leq} \sqrt{(\hat{\rho}_{n+1})_{ii}} \times \sqrt{(\hat{\rho}_{n+1})_{jj}} \tag{C.19}$$

to ensure the matrix is positive semi-definite

Note that the second and third corrections can be combined in one step.

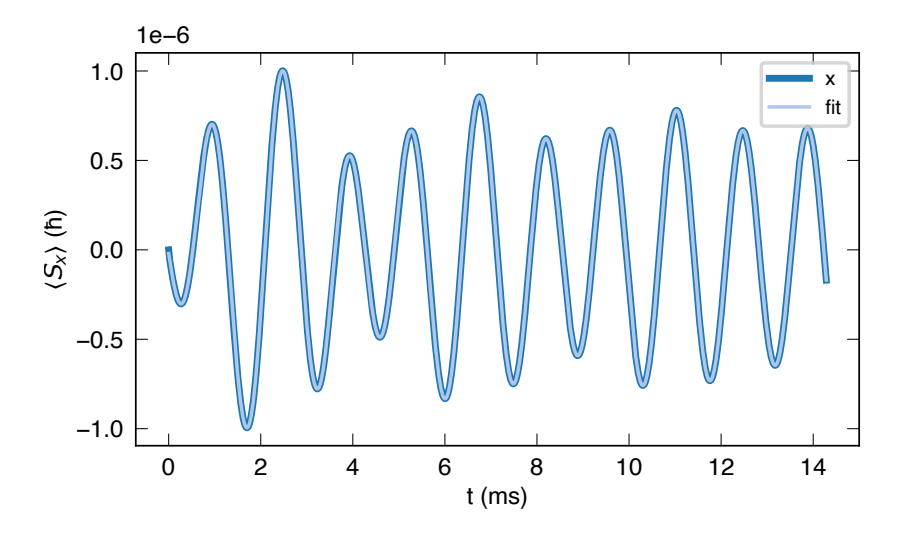


Figure C.2: Simulated and fitted time-domain signal showing the transient response of the magnetometer signal. At t=0 an oscillating magnetic field is turned on. There is excellent agreement between the fit and simulated data.

Lastly, the density operator is normalized

$$\hat{\rho}_{n+1} := \frac{\hat{\rho}_{n+1}}{\text{Tr}\,\hat{\rho}_{n+1}} \tag{C.20}$$

which ensures the probabilities add up to 1.

After the integration is performed, the observable can be calculated from the sequence of density operators which can be fitted using a suitable model. Figure C.2 shows an example of the transient response of the magnetometer signal driven by an oscillating magnetic field. It shows excellent agreement between the simulated data and the fitted model.



THEORETICAL DERIVATION OF ZERO FIELD NMR SPECTRA

This chapter contains some derivations that help to predict zero-field spectra. For the sake of simplicity, only A_nX_m spin systems are considered, where every spin is 1/2. The n A-spin are magnetically equivalent. The same holds for the m X-spins.

D.1 HAMILTONIAN

A simplified Hamiltonian

$$\begin{split} \hat{H} &= -\gamma_{\mathbf{A}} \mathbf{B} \cdot \sum_{i=1}^{n} \hat{\mathbf{I}}_{\mathbf{A},i} - \gamma_{\mathbf{X}} \mathbf{B} \cdot \sum_{i=1}^{m} \hat{\mathbf{I}}_{\mathbf{X},i} \\ &- \frac{\pi J_{\mathbf{A}\mathbf{X}}}{\hbar} \sum_{i=1}^{n} \sum_{j=1}^{m} \hat{\mathbf{I}}_{\mathbf{A},i} \cdot \hat{\mathbf{I}}_{\mathbf{X},j} \\ &- \frac{\pi J_{\mathbf{A}\mathbf{A}}}{\hbar} \sum_{i=1}^{n-1} \sum_{j=i+1}^{n} \hat{\mathbf{I}}_{\mathbf{A},i} \cdot \hat{\mathbf{I}}_{\mathbf{A},j} - \frac{\pi J_{\mathbf{X}\mathbf{X}}}{\hbar} \sum_{i=1}^{m-1} \sum_{j=i+1}^{m} \hat{\mathbf{I}}_{\mathbf{X},i} \cdot \hat{\mathbf{I}}_{\mathbf{X},j} \quad (D.1) \\ &= -\gamma_{\mathbf{A}} \mathbf{B} \cdot \hat{\mathbf{I}}_{\mathbf{A}} - \gamma_{\mathbf{X}} \mathbf{B} \cdot \hat{\mathbf{I}}_{\mathbf{X}} - \frac{\pi J_{\mathbf{A}\mathbf{X}}}{\hbar} \left(\hat{\mathbf{F}}^{2} - \hat{\mathbf{I}}_{\mathbf{A}}^{2} - \hat{\mathbf{I}}_{\mathbf{X}}^{2} \right) \\ &- \frac{\pi J_{\mathbf{A}\mathbf{A}}}{\hbar} \left(\hat{\mathbf{I}}_{\mathbf{A}}^{2} - \sum_{i=1}^{n} \hat{\mathbf{I}}_{\mathbf{A},i}^{2} \right) - \frac{\pi J_{\mathbf{X}\mathbf{X}}}{\hbar} \left(\hat{\mathbf{I}}_{\mathbf{X}}^{2} - \sum_{i=1}^{m} \hat{\mathbf{I}}_{\mathbf{X},i}^{2} \right) \end{split}$$

with

$$\hat{\mathbf{I}}_{A} = \sum_{i=1}^{n} \hat{\mathbf{I}}_{A,i}$$
 (D.2a)

$$\hat{\mathbf{I}}_{X} = \sum_{i=1}^{m} \hat{\mathbf{I}}_{X,i} \tag{D.2b}$$

$$\hat{\mathbf{f}} = \hat{\mathbf{I}}_A + \hat{\mathbf{I}}_X \ . \tag{D.2d}$$

At zero field (**B** = 0) the Hamiltonian commutes with $\hat{\mathbf{F}}^2$, $\hat{\mathbf{I}}_A^2$, $\hat{\mathbf{I}}_{A,i}^2$, $\hat{\mathbf{I}}_{X}^2$ and $\hat{\mathbf{I}}_{A}^2$ and there exists a orthogonal set of basis states that are eigenstates of these operators, that can be written as $|F, m_F, A, X\rangle$.

D.2 SELECTION RULES

Magnetometers are sensitive to the magnetic moment

$$\hat{\mu} = \gamma_{\mathcal{A}} \hat{\mathbf{I}}_{\mathcal{A}} + \gamma_{\mathcal{X}} \hat{\mathbf{I}}_{\mathcal{X}} \quad . \tag{D.3}$$

Assuming the eigenstates $|F, m_F, A, X\rangle$ are defined by

$$|F, m_F, A, X\rangle = C_{A, m_A, X, m_X}^{F, m_F} |A, m_A\rangle \otimes |X, m_X\rangle$$
 (D.4)

then, the spin operators¹

$$\hat{\mathbf{I}}_{X} = \hbar \sum_{N,F,F'} (-1)^{N} \mathbf{e}_{-N} \hat{T}_{1,N}(F,F') W(1,X,F,A;X,F')
\times \sqrt{\frac{X \cdot (2X+1)(F+1)(2F'+1)}{3}}
\hat{\mathbf{I}}_{A} = \hbar \sum_{N,F,F'} (-1)^{N-2A-2I-F-F'} \mathbf{e}_{-N} \hat{T}_{1,N}(F,F') W(1,A,F,X;A,F')
\sqrt{\frac{A \cdot (2A+1)(F+1)(2F'+1)}{3}}
(D.5b)$$

The spherical tensor operators $\hat{T}_{l,m}(F,F')$ (see Equation C.1 may contain matrix elements $|F,m_F\rangle \langle F',m_F'|$ that fulfill the triangular condition

$$|F - F'| \le l \le F + F' . \tag{D.6}$$

For l = 1 this can also be formulated in the form of a selection rule

$$\Delta F = F' - F = 0, \pm 1 \tag{D.7}$$

for the total spin quantum number F. In addition, it holds $\Delta A = 0$ and $\Delta I = 0$ since no term allows transitions between states of different A and I.

For F = F' = 0 the triangular condition

$$|F - F'| = 0 \le l = 1 \le 0 = F + F'$$
 (D.8)

is not fulfilled. Transitions between F = 0 and F' = 0 are therefore forbidden.

¹ Equation D.5b can be derived from Equation D.5a using the symmetry property $C^{J,m_J}_{j_1,m_1,j_2,m_2}=(-1)^{j_1+j_2-J}C^{J,m_J}_{j_2,m_2,j_1,m_1}$ of Clebsch-Gordan coefficients.

The magnetic moment operator can also be expressed in spherical coordinates

$$\hat{\boldsymbol{\mu}} = \left(-\frac{\hat{\mu}_x}{\sqrt{2}} + \frac{\mathrm{i}\hat{\mu}_y}{\sqrt{2}} \right) \mathbf{e}_+ + \left(\frac{\hat{\mu}_x}{\sqrt{2}} + \frac{\mathrm{i}\hat{\mu}_y}{\sqrt{2}} \right) \mathbf{e}_- + \hat{\mu}_z \mathbf{e}_0 . \tag{D.9}$$

The spherical tensor operators $\hat{T}_{l,m}(F,F')$ (see Equation C.1 may contain matrix elements $|F,m_F\rangle\langle F',m_F'|$ for which $m_F-m_F'=m$. Comparing Equation D.9 and Equation D.5a/Equation D.5b leads to another selection rule

$$\Delta m_F = m_F' - m_F = q \quad , \tag{D.10}$$

where q is the spherical coordinate.

D.3 EIGENENERGIES AND TRANSITION FREQUENCIES

The eigenenergies ϵ_{full} of states $|F, m_F, A, X\rangle$ at zero field (**B** = 0) are given by

$$\epsilon_{\text{full}} = \frac{hJ_{\text{AX}}}{2} \times (F(F+1) - A(A+1) - X(X+1)) + \frac{hJ_{\text{AA}}}{2} \times (A(A+1) - A_i(A_i+1)) + \frac{hJ_{\text{XX}}}{2} \times (X(X+1) - X_i(X_i+1))$$
(D.11)

Since the selection rules forbid transitions with $\Delta A \neq 0$ and $\Delta X \neq 0$ the last two summands can be ignored if only the transition frequencies are of interest.

The simplified transition energies

$$\epsilon = \frac{hJ_{AX}}{2} \times ((F+1)F - (A+1)A - (X+1)X)$$
 (D.12)

will be denoted as ϵ . Transition frequencies ν_{if} between a state $|i\rangle$ and $|f\rangle$ can then be calculated via

$$\nu_{if} = \left| \frac{\epsilon_i - \epsilon_f}{h} \right| . \tag{D.13}$$

D.4 EXAMPLES

The following section contains some examples of simple spin systems. In the following the bold-number notation is used, which means that **N** is a $2 \times N + 1$ dimensional irreducible representation of the $\mathfrak{so}(3)$ LIE algebra with weights $-N, -N+1, \ldots, N-1, N$.

dim	F	I_{A}	I_{X}	F(F+1)	$I_{A}(I_{A}+1)$	$I_X(I_X+1)$	ε/h
3	1	1/2	1/2	2	3/4	3/4	J/4
1	o	1/2	1/2	О	3/4	3/4	-3J/4

Table D.1: Possible spin quantum numbers and eigenenergies of the zero-field Hamiltonian of an AX spin system.

AX Spin System e.g. formic acid-13C



In this simple case, the total spin of A and X is just A = X = 1/2. The Hilbert spaces of the two systems is given by $\mathcal{H}_A = \mathcal{H}_X = \mathbf{2}$. The product space

formic acid-13C

$$\mathcal{H} = \mathcal{H}_{A} \otimes \mathcal{H}_{X} \qquad \dim \mathcal{H} = 4$$

$$= \overset{A=1/2}{\mathbf{2}} \otimes \overset{X=1/2}{\mathbf{2}} \qquad = 2 \times 2$$

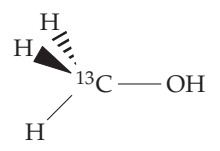
$$= \overset{F=0}{\mathbf{1}} \oplus \overset{F=3}{\mathbf{3}} \qquad = 1 + 3$$
(D.14)

can be decomposed into a one and three-dimensional subspace.

Table D.1 shows the possible eigenenergies of the eigenstates. The only possible transition between the two states fulfills the selection rules and, therefore, a resonance at the frequency

$$\nu = \frac{J_{\text{AX}}}{4} - \left(-\frac{3J_{\text{AX}}}{4}\right) = J_{\text{AX}} \tag{D.15}$$

is expected.



AX3 Spin System e.g. methanol-13C

The Hilbert space of the A spin is again simply $\mathcal{H}_A = \mathbf{2}$ with A = 1/2. In contrast, the Hilbert space of the X spin is given by

 $methanol-^{13}C$

$$\begin{split} \mathcal{H}_{X} &= \mathcal{H}_{X,1} \otimes \mathcal{H}_{X,2} \otimes \mathcal{H}_{X,3} & \text{dim } \mathcal{H}_{X} = 8 \\ &= \overset{X_{1}=1/2}{2} \otimes \overset{X_{2}=1/2}{2} \otimes \overset{X_{3}=1/2}{2} & = 2 \times 2 \times 2 \\ &= \begin{pmatrix} X_{12}=0 & X_{12}=1 \\ \mathbf{1} & \oplus & \mathbf{3} \end{pmatrix} \otimes \overset{X_{3}=1/2}{2} & = (1+3) \times 2 \\ &= \overset{X_{12}=0}{\mathbf{1}} \otimes \overset{X_{3}=1/2}{2} \oplus \overset{X_{12}=1}{\mathbf{3}} \otimes \overset{X_{3}=1/2}{2} & = 1 \times 2 + 3 \times 2 \\ &= \overset{X=1/2}{2} \oplus \overset{X=1/2}{2} \oplus \overset{X=3/2}{2} & = 2 + 2 + 4 \end{split}$$

dim	F	$I_{\mathbf{A}}$	I_{X}	F(F+1)	$I_A(I_A+1)$	$I_X(I_X+1)$	ε/h
5	2	1/2	3/2	6	3/4	15/4	₃ J/ ₄
3	1	1/2	3/2	2	3/4	15/4	-5J/4
2×3	1	1/2	1/2	2	3/4	3/4	J/4
2×3	o	1/2	1/2	2	3/4	3/4	-3J/4

Table D.2: Possible spin quantum numbers and eigenenergies of the zero-field Hamiltonian of an AX_3 spin system.

(D.16)

The full HILBERT space

$$\mathcal{H} = \mathcal{H}_{A} \otimes \mathcal{H}_{X}$$

$$= \overset{A=1/2}{2} \otimes \begin{pmatrix} \overset{X=1/2}{2} \oplus \overset{X=1/2}{2} \oplus \overset{X=3/2}{4} \end{pmatrix}$$

$$= 2 \otimes 2 \oplus 2 \otimes 2 \oplus 2 \otimes 4$$

$$= \overset{F=0}{1} \oplus \overset{F=1}{3} \oplus \overset{F=0}{1} \oplus \overset{F=1}{3} \oplus \overset{F=1}{3} \oplus \overset{F=1}{3} \oplus \overset{F=2}{5}$$
(D.17)

has

$$\dim \mathcal{H} = 16$$

$$= 2 \times (2 + 2 + 4)$$

$$= 2 \times 2 + 2 \times 2 + 2 \times 4$$

$$= 1 + 3 + 1 + 3 + 3 + 5$$
(D.18)

dimensions.

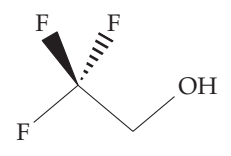
Table D.2 shows the possible eigenenergies of the eigenstates. There are two allowed transitions

$$\nu_1 = \frac{3J_{AX}}{4} - \left(-\frac{5J_{AX}}{4}\right) = 2J_{AX} \tag{D.19}$$

$$\nu_2 = \frac{J_{\text{AX}}}{4} - \left(-\frac{3J_{\text{AX}}}{4}\right) = J_{\text{AX}}$$
 (D.20)

at the J-coupling frequency and twice its value.

A2X3 Spin System e.g. 2,2,2-trifluoroethanol



2,2,2-trifluoroethanol

The two A spins are strongly coupled. The corresponding Hilbert space

$$\begin{split} \mathcal{H}_{A} &= \mathcal{H}_{A,1} \otimes \mathcal{H}_{A,2} & \dim \mathcal{H}_{A} = 2 \times 2 \\ &= 2 \otimes 2 & = 2 \times 2 \\ &= 1 \oplus 3 & = 1 + 3 \end{split} \tag{D.21}$$

can be decomposed into subspaces of spin-0 and spin-1 invariant which are invariant under rotations. The eigenstates linked to the \hat{J}_{H}^{2} operator are responsible for a 1-2-1-splitting of the fluorine resonance peak of 2,2,2-trifluoroethanol.

Accordingly, the HILBERT space

$$\begin{split} \mathcal{H}_X &= \mathcal{H}_{X,1} \otimes \mathcal{H}_{X,2} \otimes \mathcal{H}_{X,3} & \text{dim } \mathcal{H}_X = 8 \\ &= \mathbf{2} \otimes \mathbf{2} \otimes \mathbf{2} &= 2 \times 2 \times 2 \\ &= (\mathbf{1} \oplus \mathbf{3}) \otimes \mathbf{2} &= (1+3) \times 2 & \text{(D.22)} \\ &= (\mathbf{1} \otimes \mathbf{2}) \oplus (\mathbf{3} \otimes \mathbf{2}) &= (1 \times 2) + (3 \times 2) \\ &= \mathbf{2} \oplus \mathbf{2} \oplus \mathbf{4} &= 2 + 2 + 4 \end{split}$$

can be decomposed into three irreducible representation of $\mathfrak{so}(3)$, i.e. the elements are invariant under rotations. It leads to a 1-3-3-1-splitting of the hydrogen peak separated by J.

The total HILBERT space

$$\mathcal{H} = \mathcal{H}_{A} \otimes \mathcal{H}_{X}$$

$$= (\mathbf{1} \oplus \mathbf{3}) \times (\mathbf{2} \oplus \mathbf{2} \oplus \mathbf{4})$$

$$= \mathbf{2} \oplus \mathbf{2} \oplus \mathbf{4} \oplus \mathbf{2} \oplus \mathbf{4} \oplus \mathbf{2} \oplus \mathbf{4} \oplus \mathbf{2} \oplus \mathbf{4} \oplus \mathbf{6}$$
(D.23)

has

$$\begin{aligned} \dim \mathcal{H}_{total} &= \dim \mathcal{H}_{H} \times \dim \mathcal{H}_{F} = 4 \times 8 = 32 \\ &= 2 + 2 + 4 + 2 + 4 + 2 + 4 + 2 + 4 + 6 = 32 \end{aligned} \tag{D.24}$$

dimensions.

dim	F	$J_{\rm A}$	Jx	F(F+1)	$J_{A}(J_{A}+1)$	$J_X(J_X+1)$	ε/h
6	5/2	3/2	1	35/4	15/4	8/4	3J/2
4	3/2	3/2	1	15/4	15/4	8/4	-J
2	1/2	3/2	1	3/4	15/4	8/4	-5J/2
4	3/2	3/2	0	15/4	15/4	О	О
2×4	3/2	1/2	1	15/4	3/4	8/4	J/2
2×2	1/2	1/2	1	3/4	3/4	8/4	-J
2 × 2	1/2	1/2	О	3/4	3/4	О	О

Table D.3: Possible spin quantum numbers and eigenenergies of the zero-field Hamiltonian of an A_2X_3 spin system.

Table D.3 lists all the possible subspaces including their energy shifts due to the heteronuclear *J*-coupling. Applying the selection rules leads to expected transitions

$$v_1 = \frac{3J_{AX}}{2} - \left(-\frac{J_{AX}}{2}\right) = \frac{5J_{AX}}{2}$$
 (D.25)

$$v_2 = -J_{AX} - \left(-\frac{5J_{AX}}{2}\right) = \frac{3J_{AX}}{2}$$
 (D.26)

$$\nu_3 = \frac{J_{AX}}{2} - (-J_{AX}) = \frac{3J_{AX}}{2} \tag{D.27}$$

at two different resonance frequencies.

D.5 MORE COMPLEX SYSTEMS

Spin systems like $A_n X_m B_o$ with at least three magnetically nonequivalent spins are more difficult to handle. The Hamiltonian

$$\begin{split} \hat{H} &= -\gamma_{\mathrm{A}} \mathbf{B} \cdot \hat{\mathbf{I}}_{\mathrm{A}} - \gamma_{\mathrm{X}} \mathbf{B} \cdot \hat{\mathbf{I}}_{\mathrm{X}} - \gamma_{\mathrm{B}} \mathbf{B} \cdot \hat{\mathbf{I}}_{\mathrm{B}} \\ &- \frac{\pi J_{\mathrm{AX}}}{\hbar} \left(\hat{\mathbf{F}}_{\mathrm{AX}}^2 - \hat{\mathbf{I}}_{\mathrm{A}}^2 - \hat{\mathbf{I}}_{\mathrm{X}}^2 \right) - \frac{\pi J_{\mathrm{AB}}}{\hbar} \left(\hat{\mathbf{F}}_{\mathrm{AB}}^2 - \hat{\mathbf{I}}_{\mathrm{AB}}^2 - \hat{\mathbf{I}}_{\mathrm{B}}^2 \right) \\ &- \frac{\pi J_{\mathrm{XB}}}{\hbar} \left(\hat{\mathbf{F}}_{\mathrm{XB}}^2 - \hat{\mathbf{I}}_{\mathrm{X}}^2 - \hat{\mathbf{I}}_{\mathrm{B}}^2 \right) - \frac{\pi J_{\mathrm{AA}}}{\hbar} \left(\hat{\mathbf{I}}_{\mathrm{A}}^2 - \sum_{i=1}^n \hat{\mathbf{I}}_{\mathrm{A},i}^2 \right) \\ &- \frac{\pi J_{\mathrm{XX}}}{\hbar} \left(\hat{\mathbf{I}}_{\mathrm{X}}^2 - \sum_{i=1}^m \hat{\mathbf{I}}_{\mathrm{X},i}^2 \right) - \frac{\pi J_{\mathrm{BB}}}{\hbar} \left(\hat{\mathbf{I}}_{\mathrm{B}}^2 - \sum_{i=1}^o \hat{\mathbf{I}}_{\mathrm{B},i}^2 \right) \end{split}$$

contain the coupled spin operators $\hat{\mathbf{f}}_{AX}=\hat{\mathbf{I}}_A+\hat{\mathbf{I}}_X$, $\hat{\mathbf{f}}_{AB}=\hat{\mathbf{I}}_A+\hat{\mathbf{I}}_B$ and $\hat{\mathbf{f}}_{XB}=\hat{\mathbf{I}}_X+\hat{\mathbf{I}}_B$. The reason why these spin systems are difficult to analyze is the fact that these spin operators squared do not commute. For example

$$\begin{split} \left[\hat{\mathbf{f}}_{AX}^{2},\hat{\mathbf{f}}_{XB}^{2}\right] &= \left[(\hat{\mathbf{I}}_{A}+\hat{\mathbf{I}}_{X})(\hat{\mathbf{I}}_{A}+\hat{\mathbf{I}}_{X}),(\hat{\mathbf{I}}_{X}+\hat{\mathbf{I}}_{B})(\hat{\mathbf{I}}_{X}+\hat{\mathbf{I}}_{B})\right] \\ &= \left[\hat{\mathbf{I}}_{A}^{2}+\hat{\mathbf{I}}_{X}^{2}+2\hat{\mathbf{I}}_{A}\hat{\mathbf{I}}_{X},\hat{\mathbf{I}}_{X}^{2}+\hat{\mathbf{I}}_{B}^{2}+2\hat{\mathbf{I}}_{X}\hat{\mathbf{I}}_{B}\right] \\ &= \left[\hat{\mathbf{I}}_{A}^{2},\hat{\mathbf{I}}_{X}^{2}\right]+\left[\hat{\mathbf{I}}_{A}^{2},\hat{\mathbf{I}}_{B}^{2}\right]+\left[\hat{\mathbf{I}}_{X}^{2},\hat{\mathbf{I}}_{X}^{2}\right]+\left[\hat{\mathbf{I}}_{X}^{2},\hat{\mathbf{I}}_{B}^{2}\right] \\ &=0 &=0 \\ &+\left[2\hat{\mathbf{I}}_{A}\hat{\mathbf{I}}_{X},2\hat{\mathbf{I}}_{X}\hat{\mathbf{I}}_{B}\right]+\left[\hat{\mathbf{I}}_{X}^{2},2\hat{\mathbf{I}}_{X}\hat{\mathbf{I}}_{B}\right]+\left[\hat{\mathbf{I}}_{A}^{2},2\hat{\mathbf{I}}_{X}\hat{\mathbf{I}}_{B}\right] \\ &=0 &=0 \\ &+\left[2\hat{\mathbf{I}}_{A}\hat{\mathbf{I}}_{X},\hat{\mathbf{I}}_{X}^{2}\right]+\left[2\hat{\mathbf{I}}_{A}\hat{\mathbf{I}}_{X},\hat{\mathbf{I}}_{B}^{2}\right] \\ &=0 &=0 \\ &=4\left[\hat{I}_{i}^{(A)}\hat{I}_{i}^{(X)},\hat{I}_{j}^{(X)}\hat{I}_{j}^{(B)}\right]=4\hat{I}_{i}^{(A)}\hat{I}_{j}^{(B)}\left[\hat{I}_{i}^{(X)},\hat{I}_{j}^{(X)}\right] \\ &=4\mathrm{i}\hbar\epsilon_{ijk}\hat{I}_{i}^{(A)}\hat{I}_{i}^{(B)}\hat{I}_{k}^{(X)} \end{split}$$

is non-zero. In the same way, the commutators for the other coupled spin operators can be calculated. The eigenstates of the total Hamiltonian can therefore not simply be expressed in terms of angular momentum eigenstates.

In the scenario of one J-coupling constant being significantly larger than the others e.g. $J_{AX} \gg J_{AB}$, J_{XB} a perturbation approach can be tried, where the A and X spin still can be considered as strongly coupled.

In other cases, numerical simulations may be the most suitable approach that can be easily performed even for larger spin systems. In general, the number of resonances drastically increased the more spins are added to the systems, which makes zero field spectra difficult to interpret for larger molecules.

D.6 COMPARISON TO HIGH FIELD

At high field ($\mathbf{B} = (0,0,B_0)$) the ZEEMAN term is the dominant interaction by being orders of magnitude larger than the J-coupling constants. For the following discussion chemical shifts are ignored.

Assuming a $A_n X_m B_o$ spin system, the Zeeman term commutes with the spin operators $\hat{\mathbf{I}}_A^2$, $\hat{\mathbf{I}}_X^2$ and $\hat{\mathbf{I}}_B^2$. The Zeeman basis $|A\ m_A\ X\ m_X\ B\ m_B\rangle$ describes the eigenstates of the Zeeman as well as the J-coupling terms of magnetically equivalent spins. However, they are not eigenstates of the J-coupling terms of non-magnetically equivalent spins.

In the limit of weak coupling between spins e.g. $B_0 |\gamma_A - \gamma_X| \gg 2\pi \times J_{AX}$, the *secular approximation*

$$\hat{\mathbf{I}}_{A} \cdot \hat{\mathbf{I}}_{X} = \hat{I}_{x}^{(A)} \cdot \hat{I}_{x}^{(X)} + \hat{I}_{y}^{(A)} \cdot \hat{I}_{y}^{(X)} + \hat{I}_{z}^{(A)} \cdot \hat{I}_{z}^{(X)} \stackrel{\text{sec.approx.}}{\rightarrow} \hat{I}_{z}^{(A)} \cdot \hat{I}_{z}^{(X)} \quad (D.30)$$

allows the simplification of J-coupling terms of the HAMILTONIAN by removing non-commuting components of the interaction operator. It can be justified in many ways, e.g. by identifying and removing fast oscillating terms in the interaction picture or non-contributing terms in the perturbation theoretical approach.

With this approximation, the NMR spectra for molecules can be predicted as long as the underlying coupling constants are known.

D.7 J-COUPLING CONSTANT SENSITIVITY

In the context of J-coupling estimation, a value is the sensitivity of a resonance with respect to changes to the coupling constant. This can be conveniently described by the derivative

$$\frac{\mathrm{d}\nu}{\mathrm{d}I} \tag{D.31}$$

of the resonance frequency ν with respect to the coupling constant J.

Whereas at high-field the maximum of this value is given by half the multiplicity (n+1)/2, zero-field spectra sometimes allow even larger values. For the example of 2,2,2-trifluoroethanol, at high field, the largest J-sensitivity 3/2 can be observed on the outer peaks of the proton quartet. At zero field the highest observable resonance would have a sensitivity of 5/2.

N+1 rule in NMR

E

EXPERIMENTAL SETUP — NMRDUINO

In contrast to high-field NMR experiments, there are no commercial ZULF spectrometers. For the experiments presented in this thesis, a home-built spectrometer was used based on low-cost electronics and open-source software and hardware, which will be released as part of the NMRDUINO project. Further details can be found in Tayler, Bodenstedt, et al. [176].

E.1 NMRDUINO HARDWARE

The main circuit board of the NMRDUINO has the size of a credit card (see Figure E.1). It is powered by 5 V via USB. It works with a PC, MAC, and Linux (including RASPBERRY PI OS). Figure E.1 shows the size and components needed to assemble the NMRDUINO prototype. The high-voltage digital outputs require a separate voltage source that is electrically isolated from the rest of the board to prevent noise due to ground loops.

The total power consumption is very low. The full system (including a RASPBERRY PI, an NMRDUINO board, two current supplies, and a signal generator) can be operated with 96 Wh power bank for about 18 h which leads to a total power consumption of about 5.3 W. The option to operate the system on the battery was a major requirement when designing the system since it allows improved portability as well as noise reduction at utility frequencies.

Arduino Compatible Microcontroller

The heart of the NMRDUINO board is a Teensy USB development board. Whereas most of the experiments in this thesis were performed with a Teensy 3.5, the release version of NMRDUINO will be based on Teensy 4.0/4.1. The hardware was chosen mainly due to the higher clock speed (120 MHz for Teensy 3.5; 600 MHz for Teensy 4.0/4.1) compared to 16 MHz of the Arduino Uno.

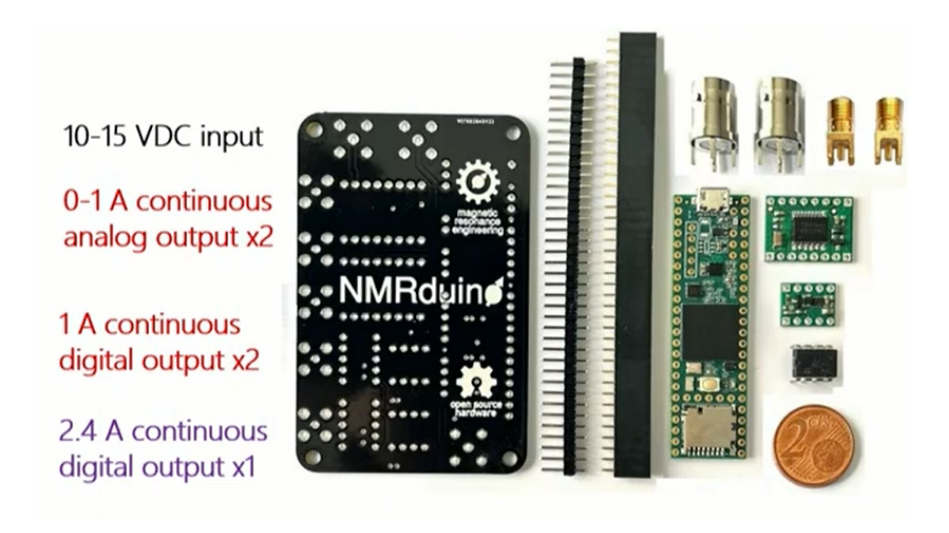


Figure E.1: Overview of the size and components of the NMRDUINO spectrometer. The whole circuit board is about the size of a credit card and can be powered by 5 V via universal serial bus (USB). Data communication is established by a serial protocol via USB as well.

Data Acquisition

The system allows data acquisition with 16-bit resolution within different voltage ranges up to $-10\,\mathrm{V}$ to $10\,\mathrm{V}$ at a maximum sampling rate of $100\,\mathrm{ksps}$. A maximum of $65\,536$ samples can be recorded per scan. In addition, supersampling can be used enabled on the spectrometer to increase the acquisition length while keeping the suppression of anti-aliasing at high sampling rates.

Output

In different configurations, the NMRDUINO can generate low noise current analog and digital current outputs up to 2.4 A. Figure E.2 a development version of the circuit used to amplify a low-current signal generated by an internal DAC with an operational amplifier followed by an H bridge to control the polarity of the signal. The system allows continuous current output. However, if coils are driven by these high currents some form of active or passive cooling might be needed.

A pulse sequence is handled on an event basis. Depending on the configuration a pulse sequence can handle up to 21000 events. On

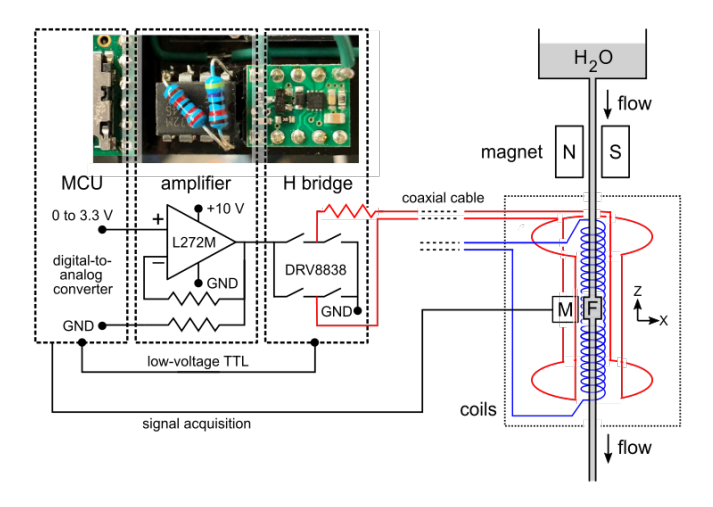


Figure E.2: Schematic of the circuit used for the analog high-current output channels. The internal unipolar digital to analog converter (DAC) signal gets amplified by an externally powered L272M operational amplified. Subsequently, the polarity of the signal is controlled via an integrated H-bridge circuit. As an example, this system was used to create fast magnetic field pulses to manipulate the state of nuclear spin in $\rm H_2O$.

each event, the value of a single or multiple channels can be altered. For the setup used in this thesis, the timing resolution was $2\,\mu s$. With an upgrade to Teensy 4.0/4.1 it is expected to improve this resolution even further.

E.2 NMRDUINO SOFTWARE

This section describes the software that controls the spectrometer. A detailed description of the firmware that is running on the microcontroller will be available in Tayler, Bodenstedt, et al. [176]. Figure E.3 shows the main elements of the graphical user interface.

System Requirements

The software is written in C++ and based on the QT framework (version 5.15 LTS). It runs on every platform that is compatible with QT and therefore natively on WINDOWS, MAC, and LINUX systems, including RASPBERRY PI 3B/4. Some functionality (especially to communicate with some devices) relies on libraries not available for

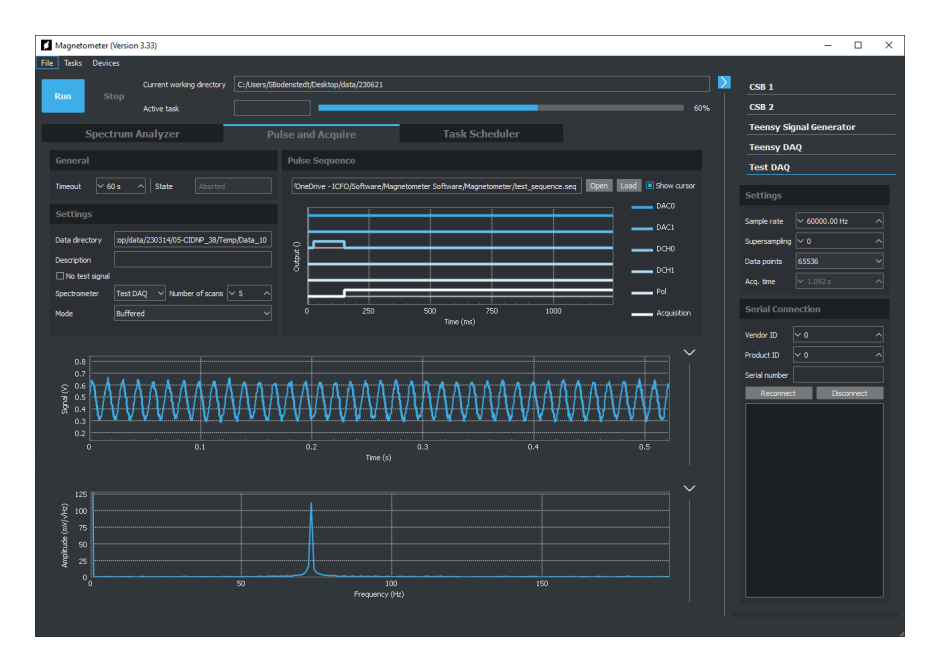


Figure E.3: Typical user interface of the NMRDUINO control software. The left side shows the active measurements whereas the connected devices are shown on the right panel. The software is highly modular and allows the simple inclusion of third-party devices or measurements. It is written in C++ and based on the QT framework.

all platforms and may not be supported. Also, some interfaces to optimize the rendering of plots are not supported on all platforms.

Measurement Modes

Natively the software comes with a real-time spectrum analyzer, and measurement allowing pulse-acquire sequences and a mode offering array-like operation. Each of these modes is highly customizable and allows a broad range of experiments.

Pulse Files

Pulse sequences are loaded via pulse-sequence files, which contain a simple, plain-text, tab-separated data structure. The following lines show a very simple example of such a file, that generates a four-second polarizing field followed by a short spin rotation pulse:

1	8#	Pol	DCH0	DCH1	DAC0	DAC1
2	0000000	0	0	0	0	0
3	25000	32767	0	0	0	32000
4	4000000	32767	0	0	0	0
5	4018000	0	0	0	0	0
6	4018020	0	32767	0	0	0
7	4018068	0	0	0	0	0
8	4038078	0	0	0	0	0

Figure E.4 shows a graphical representation of the sequence. The generation of these files can be automated with any scripting language (e.g. PYTHON). The top line describes four channels (two analog DACo and DAC1, and three digital Pol, DCHo, and DCH1).

Supported Devices

Natively the software runs with several versions of the NMRDUINO spectrometer as well as bipolar current supplys (CSBs) that support the TWINLEAF CSB command reference [177, 178]. In addition, several arbitrary waveform generators and smaller home-built devices (including temperature sensors and sine wave generators).

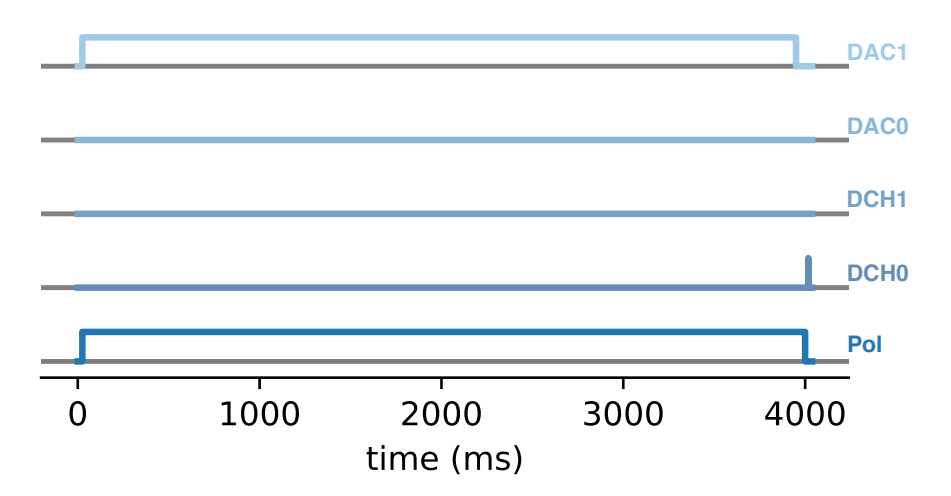


Figure E.4: Graphical representation of the pulse sequence described above. The sequence represents a 4 s polarization pulse (Pol) followed by a short digital pulse (DCHo) to apply a spin rotation. During the polarization, there is a constant output on one of the analog channels (DAC1) as well. The other channels are constant zero.

E.3 NUCLEAR SPIN POLARIZATION

Any kind of NMR experiment relies on some form of spin polarization. For the experiments performed in this thesis, several methods were developed. This section provides a brief summary. The detailed description can be found in the original publications.

Thermal Polarization in a High-Field Magnet

A relatively easy way to create a level of spin polarization sufficient for being detected is putting the sample inside the magnetic field of a magnet with a field strength of 1T or higher. This can be a simple Halbach magnet made from individual permanent magnets or using an electromagnet. In this thesis, experiments were performed with samples polarized in magnets between 1T (i.e. home-built Halbach magnet) and 14T (i.e. 600 MHz high field NMR magnet).

The main drawback of this technique is the need to subsequently shuttle the sample to an ultralow field environment to be detectable by an atomic magnetometer.

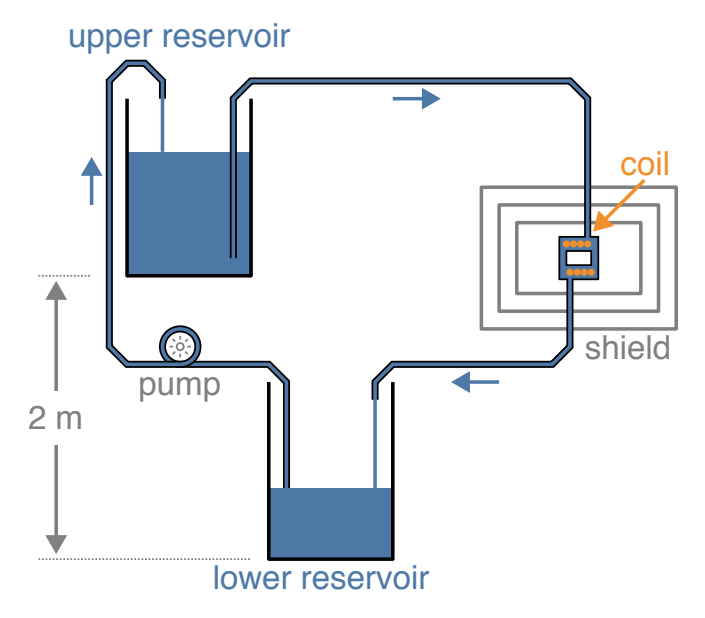


Figure E.5: Schematic of the semi-active cooling system for the polarization coil. Approximately every 30 min the pump has to repump the water from the lower to the upper reservoir. The water flow keeps the sample temperature below 35 °C if the polarizing current is run continuously.

Semi-Actively Cooled Electromagnet

As an alternative to mechanical sampling shuttling a system for thermal nuclear spin polarization via electromagnets was developed. This idea is shown in Figure 2.6 in Chapter 2. The coil is placed inside the shield and can generate a continuous field of up to 20 mT. The current is in order of 1 A to 2 A.

To prevent burning the coil and overheating of the sample the whole system is cooled by a continuous flow of deionized water (see Figure E.5). The cooling system is realized as a siphon and driven by gravity. Only re-pumping the water from the lower reservoir to the upper reservoir requires active pumping. This design was chosen to minimize the vibrational noise that may affect the sensitivity of the magnetometer.

The two reservoirs are vertically separated by a distance of 2 m. Approximately every half an hour the reservoir empties and needs to be repumped.

This polarization technique is especially suitable for samples with short coherence times. The coil ringdown is in the order of 20 ms

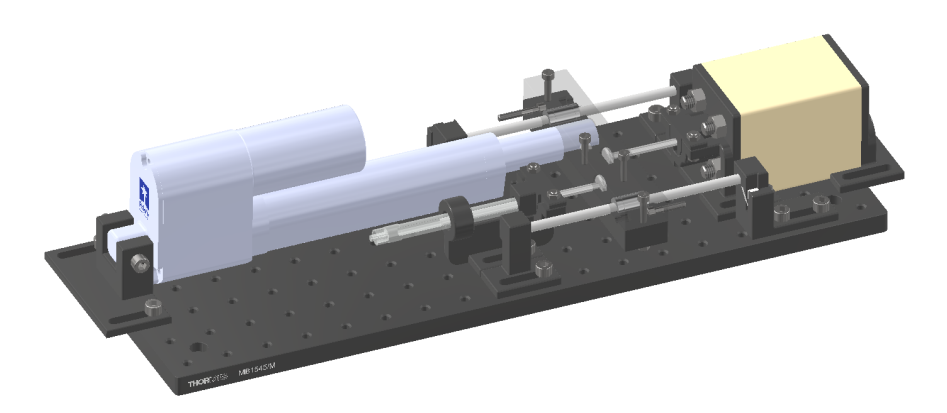


Figure E.6: Design of a home-built automated syringe pump to transfer a liquid sample within less than a second from a 1T permanent magnet towards a magnetically shielded environment. The design offers a cheap, reliable, and fast option for liquid samples. The used glass syringes equipped with polytetrafluoroethylene plungers are chemically compatible with many substances.

which is fast enough for most FFC experiments performed in this thesis.

Fast Liquid Sample Shuttling via Home-Built, High-Speed Syringe Pump

Liquid sample shuttling using a fast syringe pump is another alternative polarization method that is especially suitable for liquid samples with relaxation rates in the order of 1 s. Figure E.6 shows the 3D model used to design the pump. It is not as fast as mechanical sample shuttling but introduces less mechanical noise. It also faces less risk of breaking the sample mechanically.

Generation of Hyperpolarized Nuclear Spins

As an alternative to thermal polarization techniques, several hyperpolarization methods were applied to generate nuclear spin polarization. Photo-CIDNP is one of the techniques which is published in Chuchkova et al. [99]. Some results using dynamic nuclear polarization are published in [115].

F

DATA ANALYSIS — DFTTOOLS

This chapter described a toolset for the analysis of spectra obtained by a discrete Fourier transform (DFT) of a finite sequence of regularly sampled data. It summarizes the results of the manuscript Bodenstedt et al. [77] that is currently under preparation. Simultaneously to the publication, the release of the PYTHON package DFTTOOLS is planned.

F.1 MOTIVATION

FOURIER analysis is a toolbox used in many fields of research to get spectral information of data and mathematical functions. The discrete Fourier transform (DFT) is often used in digital data science since it can be applied to a finite set of non-continuous data. In contrast, the Fourier transform (FT) is often used to describe and investigate mathematical models since it requires continuous functions.

Often, the results obtained from the FT are directly compared to the results DFT to benchmark the quality of the model or to extract physical parameters from the measured data. Especially in NMR, spectra obtained from a DFT of a finite sequence of sampled data are fitted to mathematical model functions like LORENTZIANS that are motivated by the analysis of physical systems based on FTs.

This chapter explores the limitations of this approach. Figure F.1 and Figure F.2 show significant differences between different FOURIER analysis methods. The results show some similarities but the DFT features several artifacts that, if not taken care of, may drastically affect the quality of the results.

The Python package DFTTools was developed to handle these artifacts automatically to improve the performance of fits and, by that, reduce the uncertainties of the extracted physical parameters. It may be seen as an addition/replacement to the application of window functions that try to tackle these issues at the cost of distorting the spectrum. In general, there are many methods (e.g. artificial line broadening, signal truncation, zero-padding, windowing) frequently used, especially in the NMR community, that improve solely the aesthetics of spectra obtained from a DFT. However, these methods often do neither provide any additional insight into the system nor

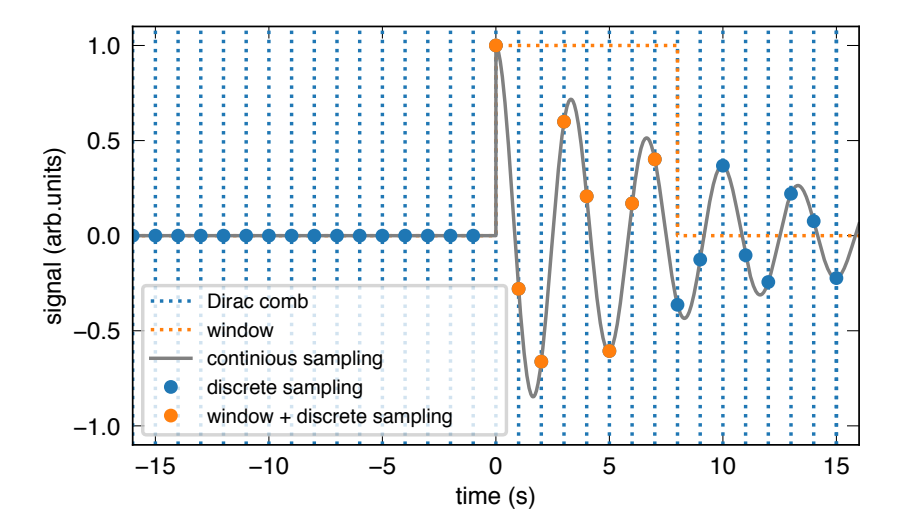


Figure F.1: Conceptual differences between the FT (grey), discrete-time Fourier transform (DTFT) (blue), and DFT (orange) in the time domain. It is assumed that the graph extends to $\pm\infty$ on the time axis. The vertical dotted lines represent discrete sampling. The sampling interval $T=1/f_{\rm s}=1\,{\rm s}$ is constant. The number of samples for the DTFT is infinite whereas only a finite number of samples N=8 is considered for the DFT.

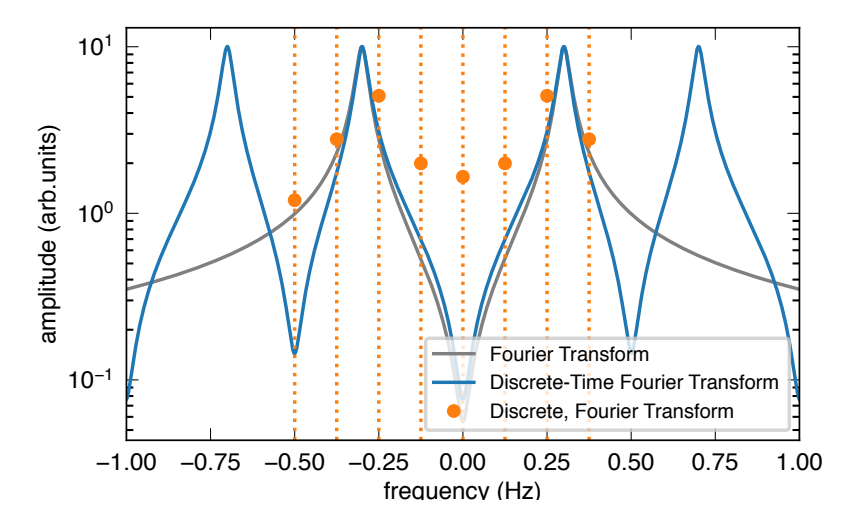


Figure F.2: Conceptual differences between the FT (grey), DTFT (blue), and DFT (orange) in the frequency domain. The frequency sampling is continuous for FT (grey) and DTFT (blue). For the DFT (orange) the frequency sampling is discrete (indicated by the vertical dotted lines) and separated $f_{\rm s}/N=1\,{\rm Hz}/8=125\,{\rm mHz}.$ It is assumed that the graph extends to $\pm\infty$ on the frequency axis. Even if the sampled signal is completely identical in the time domain, the transformed signals vary significantly in terms of amplitude, center frequency, linewidth, and phase. Extracting the original parameters of the damped sine curve from the DFT is a common, but non-trivial challenge.

do they reduce the uncertainty of the estimated parameters extracted from the spectra.

F.2 FOURIER ANALYSIS

In this section the differences between the FT, DTFT, and the DFT are explained and it will be derived how the results are mathematically connected.

Continuous Fourier Transform

The FT

$$a(f) = \mathcal{F}(s)(f) = \int_{-\infty}^{\infty} y(t) e^{-2\pi i f t} dt$$
 (F.1)

of a function $y: \mathbb{R} \to \mathbb{C}$ can in many cases be exactly calculated and is an important tool in many fields of physics and mathematics. However, it requires the function to be continuously defined for every real number. This requirement is often not fulfilled in practice, for digitally sampled time traces.

Discrete-time Fourier Transform

Often, a signal is sampled with a fixed frequency

$$f_{\rm s} = \frac{1}{T} \quad , \tag{F.2}$$

which is called the sampling frequency. Accordingly, *T* is called the sample interval/spacing.

The DTFT

$$a_{1/T}(y)(f) \equiv a_{f_{s}}(y)(f)$$

$$\equiv T \sum_{m=-\infty}^{\infty} y(mT) e^{-2\pi i f T m}$$

$$= \sum_{m=-\infty}^{\infty} \mathcal{F}(y)(f - mf_{s})$$
(F.3)

defines a Fourier transform where the function y is sampled at the sampling frequency. In the last step, the Poisson¹ summation formula was used to express the DTFT as an infinite sum of FTs.

Discrete Fourier Transform

The DTFT is already close to a real lab scenario except for the requirement for an infinite number of samples. This last issue is tackled by introducing the DFT

$$a_k \equiv T \sum_{m=0}^{N-1} y(mT) e^{-2\pi i km/N}$$
 (F.4)

that only requires a finite number of samples N. It may be convenient to introduce the function

$$g(t) = y(t)H(t) - y(t)H(t - NT)$$
 (F.5)

with the Heaviside² step function

$$H(t) = \begin{cases} 0, & \text{if } t < 0\\ 1/2, & \text{if } t = 0\\ 1, & \text{if } t > 0 \end{cases}$$
 (F.6)

The function g(t) has the convenient properties

$$g(mT) = \begin{cases} y(mT), & \text{if } 0 < m < N \\ 0, & \text{if } m < 0 \text{ or } N < m \\ y(mT)/2, & \text{if } m = 0 \text{ or } m = N \end{cases}$$
 (F.7)

¹ Siméon Denis Poisson (1781–1840) was a French mathematician and physicist who made significant contributions to various branches of mathematics, including his formulation of the Poisson equation in potential theory and his work on probability theory and statistics, with notable applications in physics and engineering.

² Oliver Heaviside (1850–1925) was an English mathematician and physicist who revolutionized the field of electrical engineering through his development of complex numbers, vector analysis, and his mathematical formalism known as Heaviside's operational calculus.

With the DFT in Equation F.4 can be expressed

$$a_{k} = a_{f_{s}}(g)(kf_{S}/N) + Tg(0)e^{-2\pi ik/N \times 0} - Tg(NT)e^{-2\pi ikN/N}$$

$$= \sum_{m=-\infty}^{\infty} \mathcal{F}(g)(kf_{s}/N - mf_{s}) + Tg(0) - Tg(NT)e^{-2\pi ik}$$

$$= \sum_{m=-\infty}^{\infty} \int_{-\infty}^{\infty} y(t)H(t)e^{-2\pi it(kf_{s}/N - mf_{s})}dt$$

$$- \sum_{m=-\infty}^{\infty} \int_{-\infty}^{\infty} y(t)H(t - NT)e^{-2\pi it(kf_{s}/N - mf_{s})}dt$$

$$+ Tg(0) + Tg(NT)e^{-2\pi ik}$$

$$= \sum_{m=-\infty}^{\infty} \int_{-\infty}^{\infty} y(t)H(t)e^{-2\pi it(f_{k} - mf_{s})}dt$$

$$- \sum_{m=-\infty}^{\infty} \int_{-\infty}^{\infty} y(t + NT)H(t)e^{-2\pi it(f_{k} - mf_{s})}dt$$

$$+ \frac{Ty(0)}{2} - \frac{Ty(NT)}{2}e^{-2\pi ik} ,$$
(F.8)

where in the last step the frequency

$$f_k = kf_s/N \tag{F.9}$$

was introduced.

As can be seen from Equation F.8, there are some significant differences between the DFT and the FT and results obtained from one transformation cannot be directly applied to the other.

F.3 EXAMPLES

The results from the last section will be applied to a exponentiallyand non-decaying sine function.

Exponentially Decaying Signal

In many physical systems, a signal

$$y(t) = a_0 e^{-\Gamma t} \cos \left(2\pi f_{\text{osc}} t + \varphi_0\right)$$

$$= a_0 e^{-\Gamma t} \frac{1}{2} \left(e^{i(2\pi f_{\text{osc}} t + \varphi_0)} + e^{-i(2\pi f_{\text{osc}} t + \varphi_0)} \right)$$

$$= \frac{a_0}{2} e^{-\Gamma t + i(2\pi f_{\text{osc}} t + \varphi_0)} + \frac{a_0}{2} e^{-\Gamma t - i(2\pi f_{\text{osc}} t + \varphi_0)}$$
(F.10)

is observed in the time domain t>=0 that can be described by an oscillating term $\cos{(\omega_0 t + \varphi_0)}$ that decays exponentially with a rate Γ . It is the step response of a freely oscillating damped harmonic oscillator, which can be found to some approximation in many physical systems in nature. It is assumed that y(t)=0 for t<0.

For $\Gamma \neq 0$ the FT of this signal can be easily calculated

$$\begin{split} \mathcal{F}(y)(f) &= \int_{-\infty}^{\infty} y(t) \mathrm{e}^{-2\pi \mathrm{i} f t} \mathrm{d} t \\ &= \int_{-\infty}^{\infty} y(t) H(t) \mathrm{e}^{-2\pi \mathrm{i} f t} \mathrm{d} t \\ &= \frac{a_0}{2} \left(\mathrm{e}^{\mathrm{i} \varphi_0} \int_0^{\infty} \mathrm{e}^{-(\Gamma + 2\pi \mathrm{i} (f - f_{\mathrm{osc}})) t} \mathrm{d} t \right. \\ &\quad + \mathrm{e}^{-\mathrm{i} \varphi_0} \int_0^{\infty} \mathrm{e}^{-(\Gamma + 2\pi \mathrm{i} (f + f_{\mathrm{osc}})) t} \mathrm{d} t \right) \\ &= \frac{a_0}{2} \left(\frac{\mathrm{e}^{\mathrm{i} \varphi_0}}{\Gamma + 2\pi \mathrm{i} (f - f_{\mathrm{osc}})} + \frac{\mathrm{e}^{-\mathrm{i} \varphi_0}}{\Gamma + 2\pi \mathrm{i} (f + f_{\mathrm{osc}})} \right) \\ &= \mathcal{L}(f, a_0/2, f_{\mathrm{osc}}, \Gamma, \varphi_0) \end{split}$$

where

$$\mathcal{L}(f, a, f_{\text{osc}}, \Gamma, \varphi) = a \times \left(\frac{e^{i\varphi}}{\Gamma + 2\pi i \cdot (f - f_{\text{osc}})} + \frac{e^{-i\varphi}}{\Gamma + 2\pi i \cdot (f + f_{\text{osc}})}\right)$$
(F.12)

is a double complex Lorentzian function. The Heaviside step function does not change the integral (since, by definition, it is assumed that y(t) = 0 for t < 0 anyway), but will be needed later.

For calculating the DFT of this signal, it is useful to introduce the parameters

$$t_n = n/f_s = nT (F.13a)$$

$$y_n = y(t_n) (F.13b)$$

$$\phi_n = \varphi_0 + 2\pi f_{\text{osc}} t_n \tag{F.13c}$$

$$a_n = a_0 e^{-t_n \Gamma} . ag{F.13d}$$

It also holds that

$$y(t+t_n) = a_0 e^{-\Gamma(t+t_n)} \cos(2\pi f_{\text{osc}}(t+t_n) + \varphi_0)$$

= $a_0 e^{-\Gamma t_n} e^{-\Gamma t} \cos(2\pi f_{\text{osc}}t_n + \varphi_0 + 2\pi f_0 t_n)$ (F.14)
= $a_n e^{-\Gamma t} \cos(2\pi f_{\text{osc}}t_n + \varphi_n)$,

which has the same form as Equation F.10 and only differs in the amplitude and phase.

With this, Equation F.8 can be calculated

$$a_{k} = \sum_{m=-\infty}^{\infty} \mathcal{L}(f_{k} - mf_{s}, a_{0}/2, f_{\text{osc}}, \Gamma, \varphi_{0})$$

$$- \sum_{m=-\infty}^{\infty} \mathcal{L}(f_{k} - mf_{s}, a_{N}/2, f_{\text{osc}}, \Gamma, \varphi_{N})$$

$$+ \frac{Ty_{0}}{2} - \frac{Ty_{N}e^{-2\pi ik}}{2}$$
(F.15)

for the signal described in Equation F.10. This result differs quite significantly from the solution of the FT in Equation F.11. However, often not all elements of the infinite summation have to be considered to achieve acceptable results since the LORENTZIAN decays asymptotically to zero at frequencies far away from resonance.

Non-Decaying Cosine Function

As another example a non-decaying cosine function

$$y(t) = a_0 \cos \left(2\pi f_{\text{osc}}t + \varphi_0\right)$$

$$= a_0 \frac{1}{2} \left(e^{i(2\pi f_{\text{osc}}t + \varphi_0)} + e^{-i(2\pi f_{\text{osc}}t + \varphi_0)} \right)$$

$$= \frac{a_0}{2} e^{i(2\pi f_{\text{osc}}t + \varphi_0)} + \frac{a_0}{2} e^{-i(2\pi f_{\text{osc}}t + \varphi_0)}$$
(F.16)

is considered. For the DFT the FT of

$$\int_{-\infty}^{\infty} y(t)H(t) - y(t)H(t - t_N)e^{-2\pi i f t} dt$$

$$= \int_{-\infty}^{\infty} y(t)\Pi\left(\frac{t - NT/2}{t_N}\right)e^{-2\pi i f t} dt \qquad (F.17)$$

$$= \int_{-\infty}^{\infty} y(t)e^{-2\pi i f t} dt * \int_{-\infty}^{\infty} \Pi\left(\frac{t - t_N/2}{t_N}\right)e^{-2\pi i f t} dt ,$$

where the convolution theorem

$$\mathcal{F}(f \cdot g) = \mathcal{F}(f) * \mathcal{F}(g) \tag{F.18}$$

was used in the last step. $\Pi(t)$ is the rectangular function or Heaviside Π function

$$\operatorname{rect}(t) \equiv \Pi(t) \equiv \begin{cases} 0, & \text{if } |t| > 1/2 \\ 1, & \text{if } |t| < 1/2 \\ 1/2, & \text{if } |t| = 1/2 \end{cases}$$
 (F.19)

The first integral is

$$\begin{split} & \int_{-\infty}^{\infty} y(t) \mathrm{e}^{-2\pi \mathrm{i} f t} \mathrm{d} t \\ & = \int_{-\infty}^{\infty} \frac{a_0}{2} \mathrm{e}^{\mathrm{i} (2\pi f_{\mathrm{osc}} t + \varphi_0)} + \frac{a_0}{2} \mathrm{e}^{-\mathrm{i} (2\pi f_{\mathrm{osc}} t + \varphi_0)} \mathrm{e}^{-2\pi \mathrm{i} f t} \mathrm{d} t \\ & = \frac{a_0}{2} \mathrm{e}^{\mathrm{i} \varphi_0} \int_{-\infty}^{\infty} \mathrm{e}^{2\pi \mathrm{i} f_{\mathrm{osc}} t} \mathrm{d} t + \frac{a_0}{2} \mathrm{e}^{-\mathrm{i} \varphi_0} \int_{-\infty}^{\infty} \mathrm{e}^{-2\pi \mathrm{i} f_{\mathrm{osc}}} \mathrm{e}^{-2\pi \mathrm{i} f t} \mathrm{d} t \\ & = \frac{a_0}{2} \mathrm{e}^{\mathrm{i} \varphi_0} \delta(f - f_{\mathrm{osc}}) + \frac{a_0}{2} \mathrm{e}^{-\mathrm{i} \varphi_0} \delta(f + f_{\mathrm{osc}}) \end{split}$$
 (F.20)

is just the sum of two DIRAC delta functions. The second integral

$$\int_{-\infty}^{\infty} \Pi\left(\frac{t - t_N/2}{t_N}\right) e^{-2\pi i f t} dt$$

$$= e^{-\pi i f t_N} \int_{-\infty}^{\infty} \Pi\left(\frac{t}{t_N}\right) e^{-2\pi i f t} dt$$

$$= e^{-\pi i f t_N} \operatorname{sinc}(f t_N) t_N$$
(F.21)

leads to the sinc function. Using the identity

$$S * \delta = S \tag{F.22}$$

Equation F.8 can be calculated

$$a_{k} = \sum_{m=-\infty}^{\infty} \int_{-\infty}^{\infty} y(t)H(t)e^{-2\pi i t(f_{k}-mf_{s})}dt$$

$$- \sum_{m=-\infty}^{\infty} \int_{-\infty}^{\infty} y(t+t_{N})H(t)e^{-2\pi i t(f_{k}-mf_{s})}dt$$

$$+ \frac{Ty(0)}{2} - \frac{Ty(t_{N})}{2}e^{-2\pi i k}$$

$$= \sum_{m=-\infty}^{\infty} \int_{-\infty}^{\infty} y(t)\Pi\left(\frac{t-t_{N}/2}{t_{N}}\right)e^{-2\pi i t(f_{k}-mf_{s})}dt$$

$$+ \frac{Ty(0)}{2} - \frac{Ty(t_{N})}{2}e^{-2\pi i k}$$

$$= \sum_{m=-\infty}^{\infty} e^{-\pi i(f_{k}-f_{osc}-mf_{s})t_{N}} \operatorname{sinc}((f_{k}-f_{osc}-mf_{s})t_{N})t_{N}$$

$$+ \sum_{m=-\infty}^{\infty} e^{-\pi i(f_{k}+f_{osc}-mf_{s})t_{N}} \operatorname{sinc}((f_{k}+f_{osc}-mf_{s})t_{N})t_{N}$$

$$+ \frac{Ty_{0}}{2} - \frac{Ty_{N}}{2}e^{-2\pi i k}$$
(F.23)

for the non-decaying signal. This result is again significantly different than the solution for the FT.

F.4 PYTHON PACKAGE

The DFTTOOLS PYTHON packaged was developed to simplify and automate the analysis of NMR spectra that occurred during this thesis. It is capable of fitting a larger number of resonances (> 1024) in a spectrum created by DFT of a finite, regularly sampled time domain signal. It was especially developed to automate the correction of DFT artifacts mentioned above and, by that, improve the accuracy of the fit results.

The tool will be released soon and accompanied by the publication Bodenstedt et al. [77].

Single Resonance Example

A mono-exponentially decaying cosine can be generated using the following syntax:

from which the DFT can be easily created

```
scan.calculate_fft(
norm="CFT",
window="rectangular",
)
```

Since often the frequency, amplitude, and phase are not known, the signal can then be fitted and plotted. Figure F.3 shows the spectrum as well as the fit error.

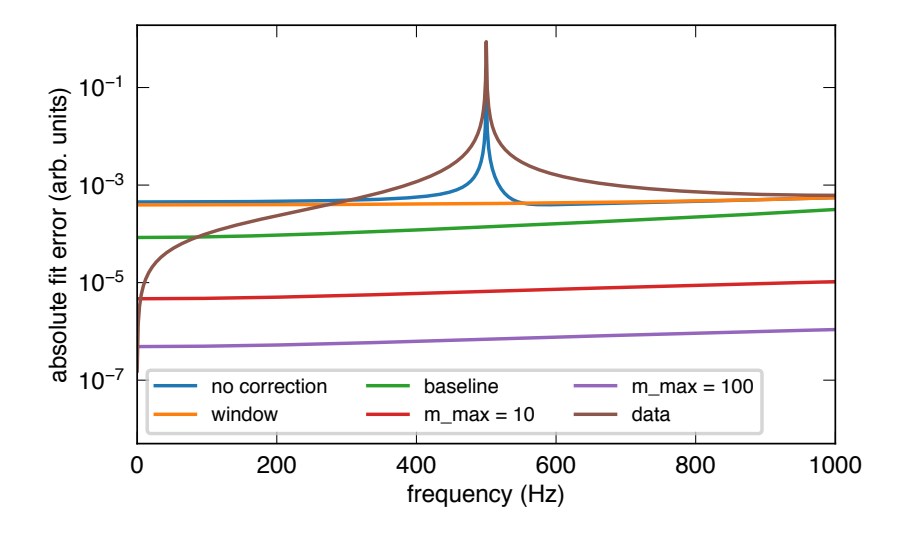


Figure F.3: Absolute fit error (the lower the better) for a single resonance at 500 Hz. The brown curve represents the absolute spectrum that is fitted. Even just correcting for the finite window (orange) and fixing the baseline (green) significantly reduces the fit error. Adding the corrections for the finite sample rate (red and purple) reduces the fit error even further. A quantitative analysis of the fit uncertainties is provided in Table F.1.

```
resonance = scan.fd.create_resonance(
       line_shape="lorentzian_complex",
       f0=f0,
3
       )
4
5
   resonance.fit_to_data()
6
   plt.figure()
   plt.xlabel("frequency (Hz)")
   plt.ylabel("absolute fit error (arb. units)")
10
   # fd stands for frequency-domain
   scan.fd.abs.plot(label="data")
   (scan.fd - resonance.data).abs.plot(label="no correction")
```

By default, no correction terms are considered, and the pure solution of the FT in Equation F.15

$$a_k^{\text{ft}} = \mathcal{L}(f_k, a_0/2, f_{\text{osc}}, \Gamma, \varphi_0) \tag{F.24}$$

is taken.

To correct the artifact that comes from using a finite window

$$a_k^{\text{window}} = -\mathcal{L}(f_k, a_N/2, f_{\text{osc}}, \Gamma, \varphi_N)$$
 (F.25)

via the correct_window() command

The infinite sum, that comes from the discrete sampling can be approximated by including terms up to m_{max}

$$a_k^{\text{sampling}} = \sum_{\substack{m = -m_{\text{max}} \\ m \neq 0}}^{m_{\text{max}}} \mathcal{L}(f_k - mf_s, a_0/2, f_{\text{osc}}, \Gamma, \varphi_0)$$

$$\sum_{\substack{m = -m_{\text{max}} \\ m \neq 0}}^{m_{\text{max}}} (f_k - mf_s, a_N/2, f_{\text{osc}}, \Gamma, \varphi_N)$$
(F.26)

via the correct_sample_rate_artifacts(m_max) command.

Finally, the baseline corrections

$$a_k^{\text{baseline}} = \frac{Ty_0}{2} - \frac{Ty_N}{2} e^{-2\pi ik} \tag{F.27}$$

can be included with the correct_baseline() command.

Combined the fully corrected DFT component up to m_{max} is given by

$$a_k^{\text{corrected}} = a_k^{\text{ft}} + a_k^{\text{window}} + a_k^{\text{sampling}} + a_k^{\text{baseline}}$$
 (F.28)

and can be applied to each resonance object via the following commands:

```
resonance.correct_window()

m_max = 10
resonance.correct_sample_rate_artifacts(m_max)
resonance.correct_baseline()
```

Figure F.3 shows the fit error for different correction terms for the example described above. The fit uncertainties are listed in Table F.1.

Fitting Multiple Resonances

Since the DFT, FT, and DTFT are linear transformations, the same procedure can be applied to a spectrum which is the sum of multiple resonances. The following example generates 512 resonances with random amplitude, phase, frequency, and linewidth at a low sampling rate and with only 4096 samples:

mode	$\sigma(f_{ m osc})$ in Hz	$\sigma(a_0)$	$\sigma(arphi_0)$ in rad	$\sigma(\Gamma)$ in ${ m s}^{-1}$
no correction	5.2×10^{-5}	1.3×10^{-1}	5.0×10^{-4}	5.2×10^{-5}
window	5.8×10^{-5}	2.4×10^{-4}	4.3×10^{-4}	7.8×10^{-5}
baseline	$6.5 imes 10^{-6}$	2.1×10^{-4}	2.9×10^{-5}	1.9×10^{-4}
$m_{\rm max} = 10$	1.2×10^{-6}	1.7×10^{-5}	4.9×10^{-6}	1.7×10^{-5}
$m_{\rm max} = 100$	1.2×10^{-7}	1.8×10^{-6}	5.2×10^{-7}	1.8×10^{-6}
$m_{\rm max}=1000$	1.2×10^{-8}	1.8×10^{-7}	5.2×10^{-8}	1.8×10^{-7}

Table F.1: Standard deviations of the fit parameters for different correction terms for the single resonance in the example shown in Figure F.3. The last two rows are only for academic purposes to highlight the scaling of the uncertainties with an increase of the number $m_{\rm max}$. For a single resonance, even an uncorrected fit provides quite good results except for the amplitude parameter.

```
n_res = 512 \# 512  resonances
  n = 2**12 # 4096 samples
  sample_rate = 2e3 # 2.0 kHz sample rate
   m_max = 10 # Number of summands in the infinite sum
  # Frequencies randomly distributed between 0Hz and 1000Hz
   np.random.seed(3)
   f0 = np.random.random(n_res) * 1000.0
   # Phases randomly distributed between 0 rad and 2 pi rad
   np.random.seed(4)
   phi = np.random.random(n_res) * 2 * np.pi
14
   # Amplitudes randomly distributed between 0.0 and 1.0
15
   np.random.seed(5)
   ampl = np.random.random(n_res)
18
   # Relaxation rates randomly distributed between 0.3 s^{-1}
19
   np.random.seed(6)
   gamma = np.random.random(n_res)*.1 + .2
21
22
   t = np.arange(0.0, n/sample_rate, 1/sample_rate)
23
24
scan = Scan()
26 scan.td.sample_rate = sample_rate
```

```
scan.td.x = t
   scan.td.y = np.zeros_like(t)
28
29
   # Generate time-domain signal
   for ampl_i, f0_i, gamma_i, phi_i in zip(ampl, f0, gamma, phi):
31
       scan.td.y += ampl_i * np.cos(2 * np.pi * f0_i * t + phi_i) *
32
            np.exp(-gamma_i * t)
33
   scan.calculate_fft(
34
       norm="CFT",
35
       window="rectangular",
36
37
38
   resonances = Resonances()
39
   for ampl_i, f0_i, gamma_i, phi_i in zip(ampl, f0, gamma, phi):
       resonance = scan.fd.create_resonance(
           fit_width=5.0,
42
           line_shape="lorentzian_complex",
43
           f0=f0 i
           )
45
46
       resonance.correct_window()
47
       resonance.correct_sample_rate_artifacts(m_max)
48
       resonance.correct_baseline()
49
50
      resonances += resonance # Simple syntax for adding resonance
51
           objects
```

Further Features

The DFTTools package features various line shapes (e.g. GAUSSIAN, symmetric/asymmetric LORENTZIAN, VOIGT³), normalization (e.g. FT-like, power/amplitude spectral density) and window functions (e.g. rectangular, Hamming⁴, Hahn). It also has convenient tools for background subtraction and filtering. The package will be released under an open-source license. The requirements are limited to a

³ Woldemar Voigt (1850–1919) was a German physicist who made important contributions to the understanding of the behavior of materials under stress, and is particularly known for his formulation of the Voigt notation used in tensor analysis and continuum mechanics.

⁴ Richard Hamming (1915–1998) was an American mathematician and computer scientist known for his significant contributions to information theory, error–correcting codes, and digital signal processing, and for the development of the Hamming codes used in computer memory systems.

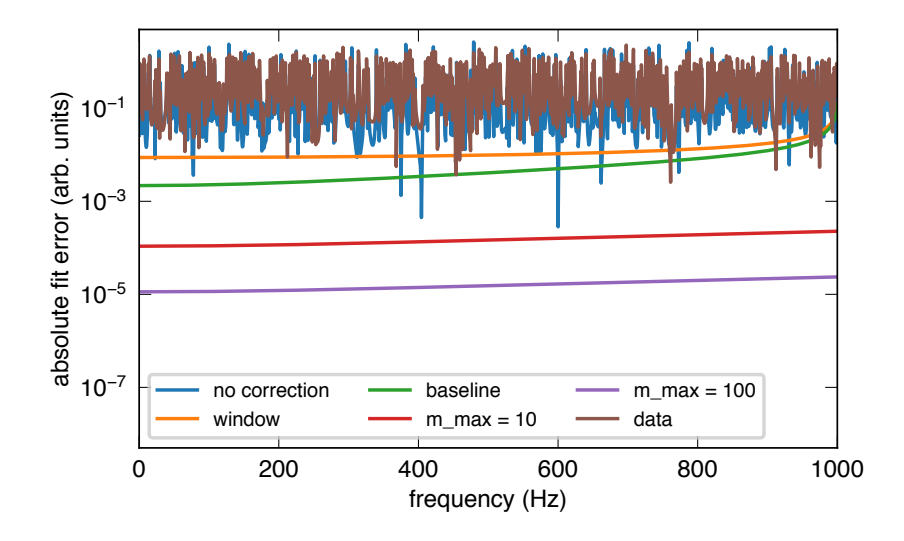


Figure F.4: Absolute fit error (the lower the better) for 512 resonances, randomly distributed over a 1 kHz frequency band. The brown curve represents the data that is fitted. Even just correcting for the finite window (orange) and fixing the baseline (green) significantly reduces the fit error. Adding the corrections for the finite sample rate (red and purple) reduces the fit error even further. A quantitative analysis of the fit uncertainties is provided in Table F.2.

mode	$\sigma(f_{ m osc})$	$\sigma(a_0)$	$\sigma(\varphi_0)$	$\sigma(\Gamma)$
	in Hz		in rad	in s ⁻¹
no correction	3.9×10^{-2}	3.2×10^{-1}	5.7×10^{-1}	1.6×10^{-1}
window	2.8×10^{-3}	8.5×10^{-3}	2.0×10^{-2}	1.7×10^{-2}
baseline	1.2×10^{-3}	3.3×10^{-3}	8.2×10^{-3}	6.8×10^{-3}
$m_{\text{max}} = 10$	3.5×10^{-5}	1.2×10^{-4}	2.6×10^{-4}	2.3×10^{-4}
$m_{\text{max}} = 100$	3.7×10^{-6}	1.2×10^{-5}	2.7×10^{-5}	2.4×10^{-5}
$m_{\rm max}=1000$	3.7×10^{-7}	1.2×10^{-6}	2.8×10^{-6}	2.5×10^{-6}

Table F.2: Median standard deviations of the fit parameters for different correction terms from the 512 resonances in the example shown in Figure F.4. The last two rows are only for academic purposes to highlight the scaling of the uncertainties with an increase of the number $m_{\rm max}$. Just correcting for the artifacts from the finite window length and correcting the baseline is often sufficient to improve the fit accuracy by an order of magnitude.

minimum (mostly numpy [179], scipy [180], pandas [181] and matplotlib [182]).

MAGNETOMETER CALIBRATION AND SENSITIVITY ESTIMATION

This chapter summarizes the calibration procedure to obtain the noise floor of the magnetometers and estimate its sensitivity.

G.1 POWER OF A TIME DOMAIN SIGNAL

Given an arbitrary, periodic (with period duration $T_{\rm period}$), time domain signal y(t) observed during the interval $t_0=0$ to $t_1=T$ its total power can be estimated by calculating

$$s_{\rm rms}^{\rm continious} = \sqrt{\frac{1}{T} \int_{t_0=0}^{t_1=T} y^2(t) dt} . \tag{G.1}$$

This root mean square (RMS) value is assumed to be constant and independent of the acquisition time T as long as $T \ll T_{\rm period}$. If the signal is not monitored continuously but sampled at the rate $f_{\rm s} = 1/T_{\rm s}$ the integral can be replaced

$$y_{\rm rms}^{\rm discrete} = \sqrt{\frac{1}{N} \sum_{i=0}^{N-1} y(t_i)^2} . \tag{G.2}$$

by a finite sum, where t_i is given by

$$t_i = \frac{i}{f_s} \tag{G.3}$$

and n is the number of samples. As long as the sampling rate and the signals frequency $\frac{1}{T_{\rm period}}$ have a non-rational ratio it can be shown

$$y_{\rm rms}^{\rm continious} \stackrel{\lim_{T \to \infty}}{=} y_{\rm rms}^{\rm discrete} = y_{\rm rms}$$
 (G.4)

and both values are identical for $T \to \infty$.

The "power" of the signal

$$P = y_{\rm rms}^2 \tag{G.5}$$

is then given by the squared RMS signal.

There are alternative ways to specify the strength of a signal alternatively to provide the RMS value. For a symmetrical signal, the *peak amplitude* describes the maximum signal

$$y_{\text{peak}} = \max_{t} |y(t)| \tag{G.6}$$

of the absolute signal. Alternatively, the peak-to-peak amplitude

$$y_{p-p} = \max_{t} y(t) - \min_{t} y(t)$$
 (G.7)

defines the difference between the highest or lowest signal value. These parameters are popular but, in contrast to the RMS value $s_{\rm rms}$, require the knowledge of the exact periodic signal profile to determine the signal power. However, the conversion factors are well-known for common signals. For example, for a sine signal

$$y(t) = y_{\text{peak}} \sin(2\pi f t) \tag{G.8}$$

it holds

$$y_{\text{peak}} = \frac{y_{\text{p-p}}}{2} = \sqrt{2}y_{\text{rms}}$$
 (G.9)

To prevent wrong calibration results, it is always important to be aware how the signal amplitude is specified. The same procedure can be applied to specify the noise power of the signal.

G.2 AMPLITUDE SPECTRAL DENSITY

Often not the total noise is of interest, but its spectral distribution. Fourier analysis is often the tool of choice to transform a time-domain signal into the frequency domain. In the field of signal processing, assuming a discretely sampled signal $y_i = y(t_i)$, the DFT is typically defined by

$$a_k = T_s \sum_{m=0}^{N-1} y_m e^{-2\pi i \frac{mk}{N}}$$
 (G.10)

Normalization

However, to provide any useful physical meaning it is required to normalize

$$a_k \mapsto na_k = a_k^{\text{norm}}$$
 (G.11)

the result obtained from the DFT. The most canonical normalization for amplitude spectral densities requires

NT_s is the sample spacing in the frequency domain.

$$y_{\rm rms}^2 \stackrel{!}{=} \sum_{k=0}^{N-1} \frac{|a_k^{\rm norm}|^2}{NT_{\rm s}}$$
 (G.12)

that the "integral" of the squared, absolute amplitude spectral density is equal to the RMS value of the signal. Once properly normalized, the elements a_k^{norm} are called the ASD, whereas the squared, absolute elements $|a_k^{\text{norm}}|$ are called PSD. If the signal is measured in the unit V, the amplitude spectral density (ASD) is given in units V/\sqrt{Hz} , whereas the power spectral density (PSD) is given in units of V^2/Hz .

Explicitly calculating Equation G.12

$$y_{\text{rms}}^{2} \stackrel{!}{=} \sum_{k=0}^{N-1} \frac{|a_{k}^{\text{norm}}|^{2}}{NT_{s}}$$

$$= \frac{n^{2} f_{s}}{N} \sum_{k=0}^{N-1} \left| T_{s} \sum_{m=0}^{N-1} y_{m} e^{-2\pi i \frac{mk}{N}} \right|^{2}$$

$$= \frac{n^{2} f_{s}}{N} \sum_{k,m,m'=0}^{N-1} y_{m} y_{m'} e^{-2\pi i \frac{(m-m')k}{N}}$$

$$= \frac{n^{2} f_{s}}{N} \sum_{m,m'=0}^{N-1} y_{m} y_{m'} \sum_{k=0}^{N-1} e^{-2\pi i \frac{(m-m')k}{N}}$$

$$= \frac{n^{2} f_{s}}{N} \sum_{m,m'=0}^{N-1} y_{m} y_{m'} N \delta_{mm'}$$

$$= n^{2} T_{s} \sum_{m}^{N-1} y_{m}^{2}$$

$$= n^{2} T_{s} \sum_{m}^{N-1} y_{m}^{2}$$

$$= n^{2} N T_{s} y_{rms}^{2}$$

$$= n^{2} N T_{s} y_{rms}^{2}$$

leads to a normalization factor

$$n = \frac{1}{\sqrt{NT_s}} . ag{G.14}$$

Figure G.1 summarizes the different normalization factors for single-sided spectra (see next section).

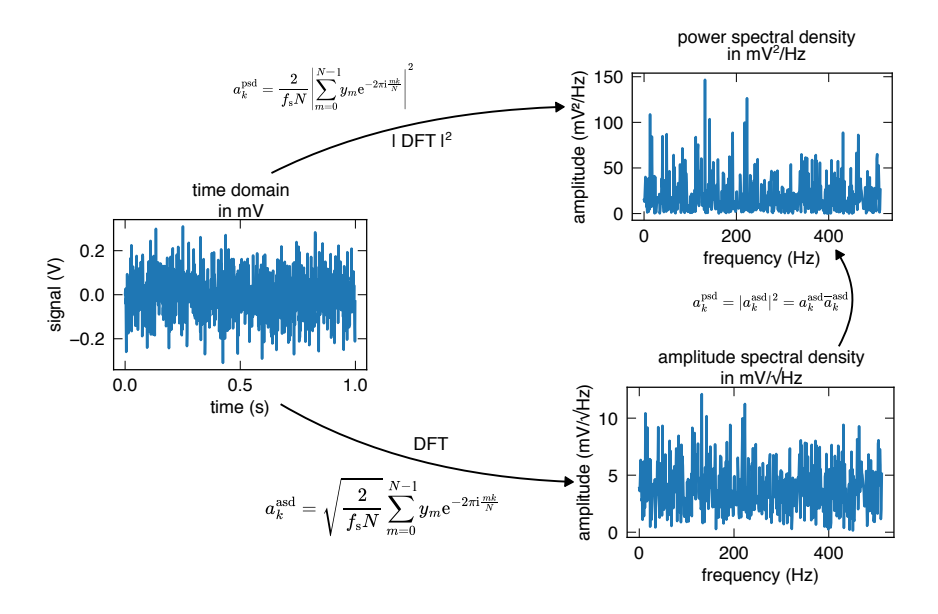


Figure G.1: Normalization factors for ASD and PSD for single sided spectra. Coming from a discretely sampled time domain signal, the PSD and ASD are obtained via DFT. The PSD is the squared, absolute ASD.

Single-Sided Spectrum

Many signals in physics are real-valued. In the context of FOURIER analysis, this implies that one side of the spectrum is redundant

$$a_{-k}^{\text{asd}} = a_{N-k}^{\text{asd}}$$

$$= \sqrt{2} f_{s} N \sum_{m=0}^{N-1} y_{m} e^{-2\pi i \frac{-mk}{N}}$$

$$= \sqrt{2} f_{s} N \sum_{m=0}^{N-1} y_{m}^{*} e^{-2\pi i \frac{mk}{N}}$$

$$= \sqrt{2} f_{s} N \sum_{m=0}^{N-1} y_{m} e^{-2\pi i \frac{mk}{N}}$$

$$= a_{k}^{\text{asd}}$$

$$(G.15)$$

since it can be reconstructed from the other side by complex conjugating. This is the reason that most of the time only the first N // 2+1 elements are given for the ASD and PSD.

The top line is for even N and the bottom for uneven N.

However, to ensure the integral still evaluates to the total RMS signal

$$y_{\text{rms}}^{2} = |na_{0}|^{2} + |na_{1}|^{2} \dots |na_{N//2+1}|^{2} \dots |na_{N-1}|^{2}$$

$$= n^{2} \times \begin{cases} |a_{0}|^{2} + |a_{1}|^{2} + |a_{N-1}|^{2} + \dots + |a_{N/2}|^{2} \\ |a_{0}|^{2} + |a_{1}|^{2} + |a_{N-1}|^{2} + \dots + |a_{N//2}|^{2} + |a_{N//2+1}|^{2} \end{cases}$$

$$= n^{2} \times \begin{cases} |a_{0}|^{2} + |a_{1}|^{2} + |a_{N-1}|^{2} + \dots + |a_{N//2}|^{2} \\ |a_{0}|^{2} + |a_{1}|^{2} + |a_{N-1}|^{2} + \dots + |a_{N//2}|^{2} + |a_{N//2+1}|^{2} \end{cases}$$

$$= n^{2} \times \begin{cases} |a_{0}|^{2} + 2|a_{1}|^{2} + \dots + |a_{N//2}|^{2} \\ |a_{0}|^{2} + 2|a_{1}|^{2} + \dots + 2|a_{N//2}|^{2} \end{cases}$$

$$= n^{2} \times \begin{cases} \frac{1}{\sqrt{2}} \left| \sqrt{2}a_{0} \right|^{2} + \left| \sqrt{2}a_{1} \right|^{2} + \dots + \frac{1}{\sqrt{2}} \left| \sqrt{2}a_{N//2} \right|^{2} \\ \frac{1}{\sqrt{2}} \left| \sqrt{2}a_{0} \right|^{2} + \left| \sqrt{2}a_{1} \right|^{2} + \dots + \left| \sqrt{2}a_{N//2} \right|^{2} \end{cases}$$

$$\equiv n^{2} \times \sum_{k=1}^{N//2} w_{k} \left| \sqrt{2}a_{k} \right|^{2}$$
(G.16)

the normalization factor

$$n \mapsto \sqrt{2}n = \sqrt{\frac{2}{NT_c}} \tag{G.17}$$

has to be adjusted and a weighting factor

$$w_i = \begin{cases} \frac{1}{\sqrt{2}}, & \text{if } i = 0 \text{ or } i = N/2\\ \frac{1}{\sqrt{2}}, & \text{otherwise} \end{cases}$$
 (G.18)

has to be introduced to avoid double-counting the first (and sometimes the last²) element. Table G.1 summarizes the normalization factors.

Windowing

Applying a window function

$$y_i \mapsto W_i y_i \tag{G.19}$$

¹ Forgetting this would lead to an overestimation of the sensitivity by a factor of $\sqrt{2}$.

² $a_{N/2}$ only exists if N is even.

ASD/PSD	single/double-sided	п	$nT_{\rm s}$
ASD	double-sided	$\frac{1}{\sqrt{T_{\rm s}N}}$	$\frac{1}{\sqrt{f_{\rm s}N}}$
ASD	single-sided	$\sqrt{\frac{2}{T_{\rm s}N}}$	$\sqrt{\frac{2}{f_s N}}$
PSD	double-sided	$\frac{1}{T_{\rm s}N}$	$\frac{1}{f_{\rm s}N}$
PSD	single-sided	$\frac{2}{T_{\rm s}N}$	$\frac{2}{f_{\rm s}N}$

Table G.1: Summary of the normalization factors. For pure real valued signals allow single-sided spectra. If the full, doubled-sided spectrum is considered, the normalization factor differs by a factor of $\sqrt{2}$ for the ASD and by a factor of 2 for the PSD.

to a time-domain signal is often used to reduce the effect *spectral leakage* in the frequency domain signal. As long as the window is power-normalized, i.e.

$$1 \stackrel{1}{=} \sum_{i=0}^{N-1} |W_i|^2 \tag{G.20}$$

the same normalization factors derived above can be used for the ASD and PSD.

G.3 TEST SIGNAL ESTIMATION

Often the ASD is required not in units of V/\sqrt{Hz} (or whatever unit the signal is measured in) but in a more meaningful unit like T/\sqrt{Hz} . In order to get the conversion correctly, a good way is to apply a test signal with well know rms-amplitude $B_{\text{test,rms}}$ (e.g. in T) and comparing it to response of the device.

The response is most conveniently quantified in the frequency domain. However, as Figure G.2, the signal amplitude cannot be just estimated by looking for the highest data point in the spectrum. In the figure, four time-domain signals with the same $B_{\rm test,rms}$ are Fourier transformed but they lead to very different peak amplitudes. A good way to extract the RMS-amplitude of the response $y_{\rm test,rms}$ is a fit of the exact line shape (see Appendix F) followed by integrating the signal in the way described above.

The ration of

$$\frac{y_{\text{test,rms}}}{B_{\text{test,rms}}} = b_{\text{response}} \tag{G.21}$$

The usual definitions of window functions are often not normalized!

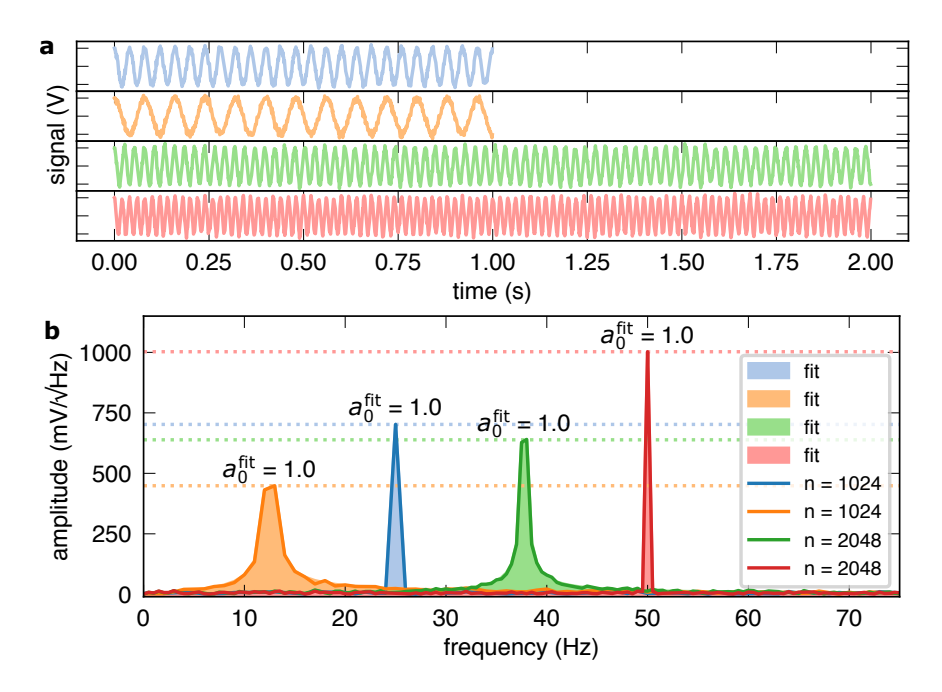


Figure G.2: Test signal rms-voltage estimation. **a** All four test signals in the time domain have the same rms-voltage. However, in the frequency domain **b** they show very different peak values. In contrast, fitting the resonance followed by integration leads to a consistent and accurate estimation for the rms-value in the frequency domain.

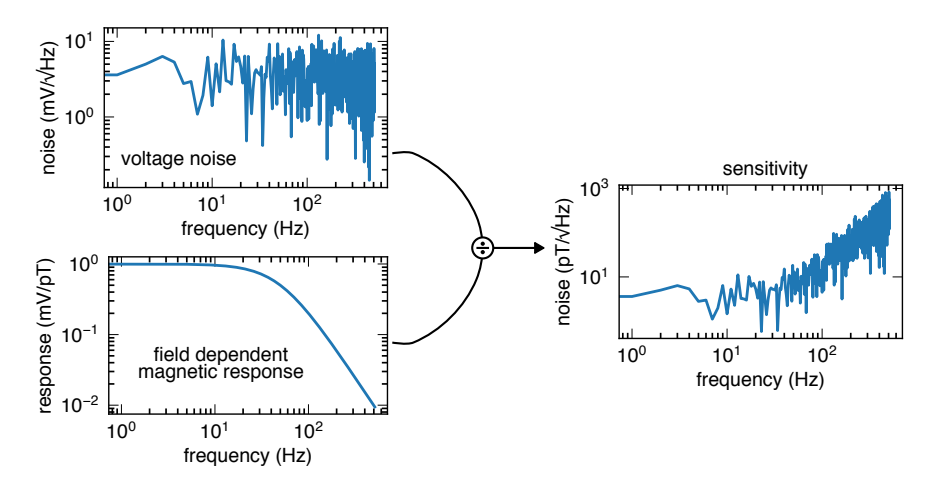


Figure G.3: Sensitivity estimation by dividing the voltage noise by the frequency-dependent magnetometer response. The magnetometer response also defines the bandwidth of the sensor which is typically defined as the frequency where the response drops by $\sqrt{2}$.

defines the response in units of VT^{-1} .

G.4 SENSITIVITY CALIBRATION

The response $b_{\rm response}(f)$ is usually frequency dependent. By measuring the response for all frequencies within the measurement bandwidth and interpolating the points in between, the full magnetometer response can be measured. The frequency-dependent sensitivity of the magnetometer is then simply given by

$$s_k = b^{-1} \left(\frac{kf_s}{N}\right) a_k^{\text{norm}} . \tag{G.22}$$

This is also graphically illustrated in Figure G.3.

- ¹Kong, L.-D., "Insight-HXMT discovery of the highest-energy CRSF from the first galactic ultraluminous x-ray pulsar swift jo243.6+6124," The Astrophysical Journal Letters 933, L3 (2022).
- ²Ge, M. Y., "Insight-HXMT firm detection of the highest-energy fundamental cyclotron resonance scattering feature in the spectrum of GRO j1008-57," The Astrophysical Journal 899, L19 (2020).
- ³Ramsey, N. F., Purcell, E. M., "Interactions between nuclear spins in molecules," Physical Review 85, 143–144 (1952).
- ⁴Gauss, K. F., "Intensitas vis magneticæ terrestris ad mensuram absolutam revocata," Abstracts of the Papers Printed in the Philosophical Transactions of the Royal Society of London 3, 166–174 (1837).
- ⁵Müller, C., "Nuclear magnetic resonance spectroscopy with single spin sensitivity," Nature Communications 5, 10.1038/ncomms5703 (2014).
- ⁶Pfender, M., "High-resolution spectroscopy of single nuclear spins via sequential weak measurements," Nature Communications **10**, 10.1038/s41467-019-08544-z (2019).
- ⁷Nagy, R., "High-fidelity spin and optical control of single siliconvacancy centres in silicon carbide," Nature Communications 10, 10.1038/s41467-019-09873-9 (2019).
- ⁸Larmor, J., "LXIII. on the theory of the magnetic influence on spectra; and on the radiation from moving ions," The London, Edinburgh, and Dublin Philosophical Magazine and Journal of Science 44, 503–512 (1897).
- ⁹Bielecki, A., Zax, D. B., Thayer, A. M., Millar, J. M., Pines, A., "Time domain zero field NMR and NQR," Zeitschrift für Naturforschung A 41, 440–444 (1986).
- ¹⁰Millar, J. M., Thayer, A. M., Bielecki, A., Zax, D. B., Pines, A., "Zero field NMR and NQR with selective pulses and indirect detection," The Journal of Chemical Physics **83**, 934–938 (1985).
- ¹¹Thayer, A., Millar, J., Pines, A., "Two-dimensional zero-field NMR and NQR," Chemical Physics Letters 129, 55–58 (1986).

- ¹²Weitekamp, D. P., Bielecki, A., Zax, D., Zilm, K., Pines, A., "Zerofield nuclear magnetic resonance," Physical Review Letters **50**, 1807–1810 (1983).
- ¹³Zax, D., Bielecki, A., Zilm, K., Pines, A., "Heteronuclear zero-field NMR," Chemical Physics Letters **106**, 550–553 (1984).
- ¹⁴Zax, D. B., Bielecki, A., Zilm, K. W., Pines, A., Weitekamp, D. P., "Zero field NMR and NQR," The Journal of Chemical Physics 83, 4877–4905 (1985).
- ¹⁵Bloembergen, N., Purcell, E. M., Pound, R. V., "Relaxation effects in nuclear magnetic resonance absorption," Physical Review 73, 679–712 (1948).
- ¹⁶Kimmich, R., Anoardo, E., "Field-cycling NMR relaxometry," Progress in Nuclear Magnetic Resonance Spectroscopy 44, 257–320 (2004).
- ¹⁷Kimmich, R., "Field cycling in NMR relaxation spectroscopy: applications in biological, chemical and polymer physics," Bull. of Magn. Reson. 1, 195–218 (1979).
- ¹⁸Peik, E, Tamm, C., "Nuclear laser spectroscopy of the 3.5 eV transition in th-229," Europhysics Letters (EPL) **61**, 181–186 (2003).
- ¹⁹Seiferle, B., "Energy of the 229th nuclear clock transition," Nature 573, 243–246 (2019).
- ²⁰Beeks, K., Sikorsky, T., Schumm, T., Thielking, J., Okhapkin, M. V., Peik, E., "The thorium-229 low-energy isomer and the nuclear clock," Nature Reviews Physics 3, 238–248 (2021).
- ²¹Cagnac, B, "Optical detection of nuclear magnetic resonance of mercury-201," Journal de Physique et le Radium (France) Changed to J. Phys. (Orsay, Fr.) **19** (1958).
- ²²Savukov, I., Seltzer, S., Romalis, M., "Detection of NMR signals with a radio-frequency atomic magnetometer," Journal of Magnetic Resonance 185, 214–220 (2007).
- ²³Seltzer, S. J., *Developments in alkali-metal atomic magnetometry* (Princeton University, 2008).
- ²⁴Purcell, E. M., Field, G. B., "Influence of collisions upon population of hyperfine states in hydrogen.," Astrophysical Journal, vol. 124, p. 542 124, 542 (1956).

- ²⁵Boehme, C., Lips, K., "Theory of time-domain measurement of spin-dependent recombination with pulsed electrically detected magnetic resonance," Physical Review B 68, 10.1103/physrevb. 68.245105 (2003).
- ²⁶Gruber, A., Dräbenstedt, A., Tietz, C., Fleury, L., Wrachtrup, J., Borczyskowski, C., "Scanning confocal optical microscopy and magnetic resonance on single defect centers," Science **276**, 2012–2014 (1997).
- ²⁷Bodenstedt, S., Mitchell, M. W., Tayler, M. C. D., "Fast-field-cycling ultralow-field nuclear magnetic relaxation dispersion," Nature Communications 12, 4041 (2021).
- ²⁸**Bodenstedt, S.**, Mitchell, M. W., Tayler, M. C. D., "Accounting for dq/dt in the Bloch equation," In preparation. (2023).
- ²⁹Mitchell, M. W., Palacios Alvarez, S., "Colloquium: quantum limits to the energy resolution of magnetic field sensors," Reviews of Modern Physics **92**, 10.1103/revmodphys.92.021001 (2020).
- ³⁰Happer, W., Tam, A. C., "Effect of rapid spin exchange on the magnetic-resonance spectrum of alkali vapors," Physical Review A **16**, 1877–1891 (1977).
- ³¹Grossetête, F., "Relaxation par collisions d'échange de spin," Journal de Physique **25**, 383–396 (1964).
- ³²Allred, J. C., Lyman, R. N., Kornack, T. W., Romalis, M. V., "High-sensitivity atomic magnetometer unaffected by spin-exchange relaxation," Physical Review Letters 89, 10.1103/physrevlett.89. 130801 (2002).
- ³³Ban, G., "Demonstration of sensitivity increase in mercury freespin-precession magnetometers due to laser-based readout for neutron electric dipole moment searches," Nuclear Instruments and Methods in Physics Research Section A: Accelerators, Spectrometers, Detectors and Associated Equipment 896, 129–138 (2018).
- ³⁴Fourcault, W., Romain, R., Gal, G. L., Bertrand, F., Josselin, V., Prado, M. L., Labyt, E., Palacios-Laloy, A., "Helium-4 magnetometers for room-temperature biomedical imaging: toward collective operation and photon-noise limited sensitivity," Optics Express 29, 14467 (2021).
- ³⁵Budker, D., Kimball, D. F. J., *Optical magnetometry* (Cambridge University Press, 2013).

- ³⁶**Bodenstedt, E.**, *Experimente der Kernphysik und ihre Deutung*, de, ISBN: 978-3-41-101401-9 (Bibliographisches Institut, 1972).
- ³⁷Traficante, D. D., "Relaxation. can T₂, be longer than T₁?" Concepts in Magnetic Resonance 3, 171–177 (1991).
- ³⁸Levitt, M. H., *Spin dynamics: basics of nuclear magnetic resonance* (John Wiley & Sons, 2013).
- ³⁹Sevian, H. M., Skinner, J. L., "T2 can be greater than 2T1," The Journal of Chemical Physics **91**, 1775–1782 (1989).
- ⁴⁰Budimir, J, Skinner, J., "On the relationship between T₁ and T₂ for stochastic relaxation models," Journal of statistical physics **49**, 1029–1042 (1987).
- ⁴¹Budker, D., Kozlov, M. G., Sensing: equation one, 2020.
- ⁴²Fabricant, A., Novikova, I., Bison, G., "How to build a magnetometer with thermal atomic vapor: a tutorial," New Journal of Physics **25**, 025001 (2023).
- ⁴³Auzinsh, M., Budker, D., Kimball, D. F., Rochester, S. M., Stalnaker, J. E., Sushkov, A. O., Yashchuk, V. V., "Can a quantum nondemolition measurement improve the sensitivity of an atomic magnetometer?" Physical Review Letters 93, 10.1103/physrevlett.93. 173002 (2004).
- ⁴⁴Budker, D., Romalis, M., "Optical magnetometry," Nature Physics 3, 227–234 (2007).
- ⁴⁵Jiménez-Martínez, R., Knappe, S., "Microfabricated optically pumped magnetometers," in *Smart sensors, measurement and instrumentation* (Springer International Publishing, Sept. 2016), pp. 523–551.
- ⁴⁶Ledbetter, M. P., Savukov, I. M., Acosta, V. M., Budker, D., Romalis, M. V., "Spin-exchange-relaxation-free magnetometry with cs vapor," Physical Review A 77, 033408 (2008).
- ⁴⁷Savukov, I. M., Seltzer, S. J., Romalis, M. V., Sauer, K. L., "Tunable atomic magnetometer for detection of radio-frequency magnetic fields," Physical Review Letters 95, 10.1103/physrevlett.95.063004 (2005).
- ⁴⁸Steck, D. A., *Rubidium 87 d line data*, (2021) https://steck.us/alkalidata/rubidium87numbers.pdf (visited on 10/04/2023).
- ⁴⁹Anderson, L. W., Pipkin, F. M., Baird, J. C., "Hyperfine structure of hydrogen, deuterium, and tritium," Physical Review 120, 1279–1289 (1960).

- ⁵⁰Appelt, S., Baranga, A. B.-A., Erickson, C. J., Romalis, M. V., Young, A. R., Happer, W., "Theory of spin-exchange optical pumping of 3He and 129Xe," Physical Review A 58, 1412–1439 (1998).
- ⁵¹Savukov, I. M., Romalis, M. V., "Effects of spin-exchange collisions in a high-density alkali-metal vapor in low magnetic fields," Physical Review A **71**, 10.1103/physreva.71.023405 (2005).
- ⁵²Katz, O., Dikopoltsev, M., Peleg, O., Shuker, M., Steinhauer, J., Katz, N., "Nonlinear elimination of spin-exchange relaxation of high magnetic moments," Physical Review Letters 110, 10.1103/physrevlett.110.263004 (2013).
- ⁵³Katz, O., Firstenberg, O., "Synchronization of strongly interacting alkali-metal spins," Physical Review A 98, 10.1103/physreva.98.012712 (2018).
- ⁵⁴Sheng, D., Li, S., Dural, N., Romalis, M. V., "Subfemtotesla scalar atomic magnetometry using multipass cells," Physical Review Letters 110, 160802 (2013).
- ⁵⁵Limes, M., Foley, E., Kornack, T., Caliga, S., McBride, S., Braun, A., Lee, W., Lucivero, V., Romalis, M., "Portable magnetometry for detection of biomagnetism in ambient environments," Physical Review Applied 14, 011002 (2020).
- ⁵⁶Dang, H. B., Maloof, A. C., Romalis, M. V., "Ultrahigh sensitivity magnetic field and magnetization measurements with an atomic magnetometer," Applied Physics Letters **97**, 151110 (2010).
- ⁵⁷Cooper, R. J., Prescott, D. W., Matz, P., Sauer, K. L., Dural, N., Romalis, M. V., Foley, E. L., Kornack, T. W., Monti, M., Okamitsu, J., "Atomic magnetometer multisensor array for rf interference mitigation and unshielded detection of nuclear quadrupole resonance," Physical Review Applied 6, 10.1103/physrevapplied.6.064014 (2016).
- ⁵⁸Keder, D. A., Prescott, D. W., Conovaloff, A. W., Sauer, K. L., "An unshielded radio-frequency atomic magnetometer with subfemtotesla sensitivity," AIP Advances 4, 10 . 1063 / 1 . 4905449 (2014).
- ⁵⁹Quiroz, D. R., Cooper, R. J., Foley, E. L., Kornack, T. W., Lee, G. J., Sauer, K. L., "Interleaved nqr detection using atomic magnetometers," Journal of Magnetic Resonance 343, 107288 (2022).

- ⁶⁰Lucivero, V., Lee, W., Limes, M., Foley, E., Kornack, T., Romalis, M., "Femtotesla nearly-quantum-noise-limited pulsed gradiometer at earth-scale fields," Physical Review Applied 18, 10.1103/physrev applied.18.1021001 (2022).
- ⁶¹Schultze, V., Schillig, B., IJsselsteijn, R., Scholtes, T., Woetzel, S., Stolz, R., "An optically pumped magnetometer working in the light-shift dispersed mz mode," Sensors 17, 561 (2017).
- ⁶²Groeger, S., Bison, G., Schenker, J.-L., Wynands, R., Weis, A., "A high-sensitivity laser-pumped mx magnetometer," The European Physical Journal D 38, 239–247 (2006).
- ⁶³Bevilacqua, G., Biancalana, V., Dancheva, Y., Vigilante, A., "Self-adaptive loop for external-disturbance reduction in a differential measurement setup," Physical Review Applied 11, 10.1103/phys revapplied.11.014029 (2019).
- ⁶⁴Grangier, P., Levenson, J. A., Poizat, J.-P., "Quantum non-demolition measurements in optics," Nature 396, 537–542 (1998).
- ⁶⁵Sewell, R. J., Napolitano, M., Behbood, N., Colangelo, G., Mitchell, M. W., "Certified quantum non-demolition measurement of a macroscopic material system," Nature Photonics 7, 517–520 (2013).
- ⁶⁶Vasilakis, G., Shen, H., Jensen, K., Balabas, M., Salart, D., Chen, B., Polzik, E. S., "Generation of a squeezed state of an oscillator by stroboscopic back-action-evading measurement," Nature Physics 11, 389–392 (2015).
- ⁶⁷Ciurana, F. M., Colangelo, G., Slodička, L., Sewell, R., Mitchell, M., "Entanglement-enhanced radio-frequency field detection and waveform sensing," Physical Review Letters 119, 10.1103/physre vlett.119.043603 (2017).
- ⁶⁸Kominis, I. K., Kornack, T. W., Allred, J. C., Romalis, M. V., "A subfemtotesla multichannel atomic magnetometer," Nature 422, 596–599 (2003).
- ⁶⁹macQsimal, Optical pumped magnetometers macQsimal, https://www.macqsimal.eu/macqsimal/optically-pumped-magnetometers/(visited on 28/04/2023).
- ⁷⁰Tayler, M. C. D., Mouloudakis, K., Zetter, R., Hunter, D., Lucivero, V. G., **Bodenstedt**, S., Parkkonen, L., Mitchell, M. W., "Miniature biplanar coils for alkali-metal-vapor magnetometry," Physical Review Applied 18, 014036 (2022).

- 7¹QuSpin, QZFM Gen-3, (2021) https://quspin.com/productsqzfm/ (visited on 28/04/2023).
- 72Twinleaf microSERF OPM, https://twinleaf.com/vector/microSERF/ (visited on 20/10/2023).
- ⁷³Inc. F., Magnetic sensing and imaging solutions, https://fieldlineinc.com/ (visited on 28/04/2023).
- ⁷⁴Savukov, I., Kim, Y. J., Schultz, G., "Detection of ultra-low field NMR signal with a commercial QuSpin single-beam atomic magnetometer," Journal of Magnetic Resonance 317, 106780 (2020).
- ⁷⁵Mouloudakis, K., Vasilakis, G., Lucivero, V. G., Kong, J., Kominis, I. K., Mitchell, M. W., "Effects of spin-exchange collisions on the fluctuation spectra of hot alkali-metal vapors," Physical Review A 106, 10.1103/physreva.106.023112 (2022).
- ⁷⁶**Bodenstedt, S.**, Mitchell, M. W., Tayler, M. C. D., "Resolution optimized NMR spectroscopy below Earth's field," In preparation. (2023).
- ⁷⁷**Bodenstedt, S.**, "DFTtools: a Python package for the analysis of low frequency free induction decays," In preparation. (2023).
- ⁷⁸Emondts, M., Ledbetter, M., Pustelny, S., Theis, T., Patton, B., Blanchard, J., Butler, M., Budker, D., Pines, A., "Long-lived heteronuclear spin-singlet states in liquids at a zero magnetic field," Physical Review Letters 112, 10.1103/physrevlett.112.077601 (2014).
- ⁷⁹Tayler, M. C., Ward-Williams, J., Gladden, L. F., "NMR relaxation in porous materials at zero and ultralow magnetic fields," Journal of Magnetic Resonance 297, 1–8 (2018).
- ⁸⁰Zhukov, I. V., Kiryutin, A. S., Yurkovskaya, A. V., Grishin, Y. A., Vieth, H.-M., Ivanov, K. L., "Field-cycling NMR experiments in an ultra-wide magnetic field range: relaxation and coherent polarization transfer," Phys. Chem. Chem. Phys. 20, 12396–12405 (2018).
- ⁸¹Kiryutin, A. S., Zhukov, I. V., Yurkovskaya, A. V., Budker, D., Ivanov, K. L., "Chapter 23. singlet order in heteronuclear spin systems," in *New developments in NMR* (Royal Society of Chemistry, 2020), pp. 418–433.
- ⁸²Blanchard, J. W., Budker, D., "Zero- to ultralow-field NMR," eMagRes, 1395–1410 (2016).

- ⁸³Blanchard, J. W., Ledbetter, M. P., Theis, T., Butler, M. C., Budker, D., Pines, A., "High-resolution zero-field NMR spectroscopy of aromatic compounds," Journal of the American Chemical Society 135, 3607–3612 (2013).
- ⁸⁴Tayler, M. C. D., Theis, T., Sjolander, T. F., Blanchard, J. W., Kentner, A., Pustelny, S., Pines, A., Budker, D., "Invited review article: Instrumentation for nuclear magnetic resonance in zero and ultralow magnetic field," Review of Scientific Instruments 88, 091101 (2017).
- ⁸⁵Hahn, E. L., Maxwell, D. E., "Spin echo measurements of nuclear spin coupling in molecules," Physical Review 88, 1070–1084 (1952).
- ⁸⁶Eills, J., A hitchhiker's guide to ZULF NMR, https://blog.zulf.eu/BP1.php (visited on 20/10/2023).
- ⁸⁷Appelt, S., Häsing, F. W., Sieling, U., Gordji-Nejad, A., Glöggler, S., Blümich, B., "Paths from weak to strong coupling in NMR," Physical Review A **81**, 023420 (2010).
- ⁸⁸Noether, E., "Invariant variation problems," Transport Theory and Statistical Physics 1, 186–207 (1971).
- ⁸⁹Ehrenfest, P., "Bemerkung über die angenäherte Gültigkeit der klassischen Mechanik innerhalb der Quantenmechanik," Zeitschrift für Physik 45, 455–457 (1927).
- ⁹⁰Dračínský, M., Bouř, P., "Computational analysis of solvent effects in NMR spectroscopy," Journal of Chemical Theory and Computation 6, 288–299 (2009).
- ⁹¹Garcon, A., "Constraints on bosonic dark matter from ultralow-field nuclear magnetic resonance," Science Advances 5, 10.1126/sciadv.aax4539 (2019).
- ⁹²Appelt, S., Kühn, H., Häsing, F. W., Blümich, B., "Chemical analysis by ultrahigh-resolution nuclear magnetic resonance in the earth's magnetic field," Nature Physics 2, 105–109 (2006).
- ⁹³Altenhof, A. R., Kaseman, D. C., Mason, H. E., Alvarez, M. A., Malone, M. W., Williams, R. F., "On the effects of quadrupolar relaxation in earth's field NMR spectra," Journal of Magnetic Resonance 355, 107540 (2023).
- ⁹⁴McDermott, R., Trabesinger, A. H., Mück, M., Hahn, E. L., Pines, A., Clarke, J., "Liquid-state NMR and scalar couplings in microtesla magnetic fields," Science 295, 2247–2249 (2002).

- ⁹⁵Appelt, S., Häsing, F. W., Kühn, H., Sieling, U., Blümich, B., "Analysis of molecular structures by homo- and hetero-nuclear j-coupled NMR in ultra-low field," Chemical Physics Letters 440, 308–312 (2007).
- ⁹⁶Gauss, C. F., Theoria motus corporum coelestium in sectionibus conicis solem ambientium, Vol. 7 (FA Perthes, 1877).
- ⁹⁷Cauchy, A., "Méthode générale pour la résolution des systemes d'équations simultanées," Comptes rendus de l'Académie des Sciences **25**, 536–538 (1847).
- ⁹⁸Björck, "Least squares methods," in , Vol. 1, Handbook of Numerical Analysis (Elsevier, 1990), pp. 465–652.
- ⁹⁹Chuchkova, L., "Magnetometer-detected nuclear magnetic resonance of photochemically hyperpolarized molecules," The Journal of Physical Chemistry Letters, 6814–6822 (2023).
- ¹⁰⁰Breuer, H.-P., Petruccione, F., *The theory of open quantum systems* (Oxford University PressOxford, Jan. 2007).
- ¹⁰¹Ernst, R. R., Bodenhausen, G., Wokaun, A., Redfield, A. G., *Principles of nuclear magnetic resonance in one and two dimensions*, 1989.
- io2Ernst, M., Relaxation: redfield theory, 4th NMR Meets Biology Meeting, (2008) \url{http://www.tifrh.res.in/~NMRTIFRH/presenta tions/Matthias_Ernst-Relaxation-Redfield.pdf}.
- ¹⁰³**Bodenstedt, S.**, "Optical magnetometry of nuclear spin relaxation dispersion in ultra-low fields," Thesis Proposal (2020).
- ¹⁰⁴Debye, P. J. W., *Polar molecules*, English (The Chemical Catalog Company, Inc., New York, 1929).
- ¹⁰⁵Abragam, A., *The principles of nuclear magnetism*, Comparative Pathobiology Studies in the Postmodern Theory of Education (Clarendon Press, 1961).
- ¹⁰⁶Klafter, J., Shlesinger, M. F., "On the relationship among three theories of relaxation in disordered systems," Proceedings of the National Academy of Sciences 83, 848–851 (1986).
- ¹⁰⁷Lewandowski, M., Gwozdzinski, K., "Nitroxides as antioxidants and anticancer drugs," <u>International Journal of Molecular Sciences</u> 18, 2490 (2017).
- Prandolini, M. J., Denysenkov, V. P., Gafurov, M., Endeward, B., Prisner, T. F., "High-field dynamic nuclear polarization in aqueous solutions," Journal of the American Chemical Society 131, 6090– 6092 (2009).

- ¹⁰⁹Neugebauer, P., Krummenacker, J. G., Denysenkov, V. P., Parigi, G., Luchinat, C., Prisner, T. F., "Liquid state DNP of water at 9.2 T: an experimental access to saturation," Physical Chemistry Chemical Physics 15, 6049 (2013).
- ¹¹⁰Ward-Williams, J., Korb, J.-P., Gladden, L. F., "Insights into functionality specific adsorption dynamics and stable reaction intermediates using fast field cycling NMR," The Journal of Physical Chemistry C 122, 20271–20278 (2018).
- ¹¹¹Ward-Williams, J., Korb, J.-P., Rozing, L., Sederman, A. J., Mantle, M. D., Gladden, L. F., "Characterizing solid–liquid interactions in a mesoporous catalyst support using variable-temperature fast field cycling NMR," The Journal of Physical Chemistry C 125, 8767–8778 (2021).
- ¹¹²Faux, D. A., McDonald, P. J., "Nuclear-magnetic-resonance relaxation rates for fluid confined to closed, channel, or planar pores," Physical Review E **98**, 10.1103/physreve.98.063110 (2018).
- ¹¹³**Bodenstedt, S.**, Mitchell, M. W., Tayler, M. C. D., "Meridional composite pulses for low-field magnetic resonance," Physical Review A 106, 10.1103/physreva.106.033102 (2022).
- ¹¹⁴Bodenstedt, S., Moll, D., Glöggler, S., Mitchell, M. W., Tayler, M. C. D., "Decoupling of spin decoherence paths near zero magnetic field," The Journal of Physical Chemistry Letters 13, 98–104 (2021).
- ¹¹⁵Mouloudakis, K., **Bodenstedt, S.**, Azagra, M., Mitchell, M. W., Marco-Rius, I., Tayler, M. C. D., "Real-time polarimetry of hyperpolarized 13C nuclear spins using an atomic magnetometer," The Journal of Physical Chemistry Letters 14, 1192–1197 (2023).
- ¹¹⁶Esteve, D., Raimond, J.-M., Dalibard, J., *Quantum entanglement and information processing*, École d'été de physique théorique, session LXXIX, Les Houches, ISBN: 978-0444517289 (Elsevier Science, London, England, 2003).
- ¹¹⁷Jones, J. A., "Quantum computing with NMR," Progress in Nuclear Magnetic Resonance Spectroscopy **59**, 91–120 (2011).
- ¹¹⁸Rembold, P., Oshnik, N., Müller, M. M., Montangero, S., Calarco, T., Neu, E., "Introduction to quantum optimal control for quantum sensing with nitrogen-vacancy centers in diamond," AVS Quantum Science 2, 024701 (2020).

- ¹¹⁹**Bodenstedt, S.**, Jakobi, I., Michl, J., Gerhardt, I., Neumann, P., Wrachtrup, J., "Nanoscale spin manipulation with pulsed magnetic gradient fields from a hard disc drive writer," Nano Letters **18**, 5389–5395 (2018).
- ¹²⁰Bernstein, M. A., King, K. F., Zhou, X. J., Handbook of MRI pulse sequences, ISBN: 978-0-12-092861-3 (Academic Press, San Diego, CA, 2004).
- ¹²¹Peirce, A. P., Dahleh, M. A., Rabitz, H., "Optimal control of quantum-mechanical systems: existence, numerical approximation, and applications," Physical Review A 37, 4950–4964 (1988).
- ¹²²Brinkmann, A., "Introduction to average Hamiltonian theory. I. Basics," Concepts in Magnetic Resonance Part A 45A, e21414 (2016).
- ¹²³Shinnar, M., Bolinger, L., Leigh, J. S., "The use of finite impulse response filters in pulse design," Magnetic Resonance in Medicine 12, 81–87 (1989).
- ¹²⁴Levitt, M. H., Ernst, R. R., "Composite pulses constructed by a recursive expansion procedure," Journal of Magnetic Resonance (1969) 55, 247–254 (1983).
- ¹²⁵Shaka, A., Freeman, R., "Composite pulses with dual compensation," Journal of Magnetic Resonance (1969) 55, 487–493 (1983).
- ¹²⁶Levitt, M. H., "Composite pulses," Progress in Nuclear Magnetic Resonance Spectroscopy **18**, 61–122 (1986).
- ¹²⁷Wimperis, S., "Broadband, narrowband, and passband composite pulses for use in advanced NMR experiments," Journal of Magnetic Resonance, Series A **109**, 221–231 (1994).
- ¹²⁸Levitt, M. H., "Composite pulses," eMagRes, 10.1002/978047003 4590.emrstm0086 (2007).
- ¹²⁹Demeter, G., "Composite pulses for high-fidelity population inversion in optically dense, inhomogeneously broadened atomic ensembles," Physical Review A 93, 023830 (2016).
- ¹³⁰Haller, J. D., Goodwin, D. L., Luy, B., "SORDOR pulses: expansion of the Böhlen-Bodenhausen scheme for low-power broadband magnetic resonance," Magnetic Resonance 3, 53–63 (2022).
- ¹³¹Shaka, A. J., "Composite pulses for ultra-broadband spin inversion," Chemical Physics Letters **120**, 201–205 (1985).

- ¹³²Shaka, A. J., Pines, A., "Symmetric phase-alternating composite pulses," Journal of Magnetic Resonance (1969) **71**, 495–503 (1987).
- ¹³³Geen, H., Freeman, R., "Band-selective radiofrequency pulses," Journal of Magnetic Resonance (1969) **93**, 93–141 (1991).
- ¹³⁴Freeman, R., "Shaped radiofrequency pulses in high resolution NMR," Progress in Nuclear Magnetic Resonance Spectroscopy 32, 59–106 (1998).
- ¹³⁵Khaneja, N., Reiss, T., Kehlet, C., Schulte-Herbrüggen, T., Glaser, S. J., "Optimal control of coupled spin dynamics: design of NMR pulse sequences by gradient ascent algorithms," Journal of Magnetic Resonance 172, 296–305 (2005).
- ¹³⁶Warren, W. S., Mayr, S. M., "Shaped pulses," eMagRes (2007).
- ¹³⁷Kreis, R., Thomas, A., Studer, W., Ernst, R. R., "Low frequency pulse excitation in zero field magnetic resonance," The Journal of Chemical Physics **89**, 6623–6635 (1988).
- ¹³⁸Jeener, J., "Superoperators in magnetic resonance," in *Advances in magnetic and optical resonance* (Elsevier, 1982), pp. 1–51.
- ¹³⁹Yang, X., Lui, J., Gao, B., Lu, L., Wang, X., Sanctuary, B. C., "Optimized phase-alternating composite pulse NMR," Spectroscopy Letters 28, 1191–1201 (1995).
- ¹⁴⁰Ramamoorthy, A., "Phase-alternated composite pulses for zero-field NMR spectroscopy of spin 1 systems," Molecular Physics 93, 757–766 (1998).
- ¹⁴¹Husain, S., Kawamura, M., Jones, J. A., "Further analysis of some symmetric and antisymmetric composite pulses for tackling pulse strength errors," Journal of Magnetic Resonance 230, 145–154 (2013).
- ¹⁴²Tayler, M. C. D., Sjolander, T. F., Pines, A., Budker, D., "Nuclear magnetic resonance at millitesla fields using a zero-field spectrometer," Journal of Magnetic Resonance 270, 35–39 (2016).
- ¹⁴³Michal, C. A., Dong, R. Y., "Two-pulse frequency-hopped excitation," Concepts Magn. Reson. Part A 45, 21416 (2018).
- ¹⁴⁴Bian, J., Jiang, M., Cui, J., Liu, X., Chen, B., Ji, Y., Zhang, B., Blanchard, J., Peng, X., Du, J., "Universal quantum control in zero-field nuclear magnetic resonance," Physical Review A 95, 052342 (2017).
- ¹⁴⁵Souza, A. M., Álvarez, G. A., Suter, D., "Robust dynamical decoupling," Philosophical Transactions of the Royal Society A: Mathematical, Physical and Engineering Sciences 370, 4748–4769 (2012).

- ¹⁴⁶Levitt, M. H., Bari, L. D., "Steady state in magnetic resonance pulse experiments," Physical Review Letters **69**, 3124–3127 (1992).
- ¹⁴⁷Levitt, M. H., Di Bari, L., "The homogeneous master equation and the manipulation of relaxation networks," Bulletin of Magnetic Resonance **16**, 94–114 (1994).
- ¹⁴⁸Ghose, R., Eykyn, T. R., Bodenhausen, G., "Average liouvillian theory revisited: cross-correlated relaxation between chemical shift anisotropy and dipolar couplings in the rotating frame in nuclear magnetic resonance," Molecular Physics 96, 1281–1288 (1999).
- ¹⁴⁹Carravetta, M., Levitt, M. H., "Long-lived nuclear spin states in high-field solution NMR," Journal of the American Chemical Society **126**, 6228–6229 (2004).
- ¹⁵⁰Kimmich, R., Field-cycling NMR relaxometry: instrumentation, model theories and applications (Royal Society of Chemistry, 2018).
- ¹⁵¹Kimmich, R., Anoardo, E., "Field-cycling NMR relaxometry," Progress in Nuclear Magnetic Resonance Spectroscopy **44**, 257–320 (2004).
- ¹⁵²Levitt, M. H., "Chapter 1. long-lived states in nuclear magnetic resonance: an overview," in *New developments in NMR* (Royal Society of Chemistry, 2020), pp. 1–32.
- ¹⁵³Goldman, M., Jóhannesson, H., Axelsson, O., Karlsson, M., "Design and implementation of 13C hyper polarization from parahydrogen, for new MRI contrast agents," Comptes Rendus Chimie 9, 357–363 (2006).
- ¹⁵⁴Cavallari, E., Carrera, C., Boi, T., Aime, S., Reineri, F., "Effects of magnetic field cycle on the polarization transfer from parahydrogen to heteronuclei through long-range j-couplings," The Journal of Physical Chemistry B 119, 10035–10041 (2015).
- ¹⁵⁵Stewart, N. J., Kumeta, H., Tomohiro, M., Hashimoto, T., Hatae, N., Matsumoto, S., "Long-range heteronuclear j-coupling constants in esters: implications for 13C metabolic MRI by side-arm parahydrogen-induced polarization," Journal of Magnetic Resonance 296, 85–92 (2018).
- ¹⁵⁶Hartwig, S., Voigt, J., Scheer, H.-J., Albrecht, H.-H., Burghoff, M., Trahms, L., "Nuclear magnetic relaxation in water revisited," The Journal of Chemical Physics 135, 054201 (2011).

- ¹⁵⁷Barskiy, D. A., Shchepin, R. V., Tanner, C. P. N., Colell, J. F. P., Goodson, B. M., Theis, T., Warren, W. S., Chekmenev, E. Y., "The absence of quadrupolar nuclei facilitates efficient 13C hyperpolarization via reversible exchange with parahydrogen," ChemPhysChem 18, 1493–1498 (2017).
- ¹⁵⁸Tayler, M. C., Gladden, L. F., "Scalar relaxation of NMR transitions at ultralow magnetic field," Journal of Magnetic Resonance 298, 101–106 (2019).
- ¹⁵⁹Lee, C., Suter, D, Pines, A, "Theory of multiple-pulse NMR at low and zero fields," Journal of Magnetic Resonance (1969) **75**, 110–124 (1987).
- ¹⁶⁰DeVience, S. J., Greer, M., Mandal, S., Rosen, M. S., "Homonuclear j-coupling spectroscopy at low magnetic fields using spin-lock induced crossing," ChemPhysChem 22, 2128–2137 (2021).
- ¹⁶¹Barskiy, D. A., Tayler, M. C. D., Marco-Rius, I., Kurhanewicz, J., Vigneron, D. B., Cikrikci, S., Aydogdu, A., Reh, M., Pravdivtsev, A. N., al., "Zero-field nuclear magnetic resonance of chemically exchanging systems," Nature Communications 10, 3002 (2019).
- ¹⁶²Birchall, J. R., "Quantifying the effects of quadrupolar via 15N relaxation dynamics in metronidazoles hyperpolarized via SABRE-SHEATH," Chemical Communications **56**, 9098–9101 (2020).
- ¹⁶³Shchepin, R. V., Jaigirdar, L., Chekmenev, E. Y., "Spin-lattice relaxation of hyperpolarized metronidazole in signal amplification by reversible exchange in micro-tesla fields," The Journal of Physical Chemistry C 122, 4984–4996 (2018).
- ¹⁶⁴Bullock, E., Tuck, D. G., Woodhouse, E. J., "Unusual spin-spin couplings in NMR spectra of alkyl ammonium salts," The Journal of Chemical Physics 38, 2318–2318 (1963).
- ¹⁶⁵Lehn, J.-M., Franck-Neunamm, M., "Nuclear spin-spin interactions. V. 1H-14N spin-spin coupling and quadrupolar relaxation in quaternary ammonium salts," The Journal of Chemical Physics 43, 1421–1422 (1965).
- ¹⁶⁶Porter, A., "Pyrazines and their benzo derivatives," in *Comprehensive heterocyclic chemistry* (Elsevier, 1984), pp. 157–197.
- ¹⁶⁷Refield, A. G., "The theory of relaxation processes," in *Advances in magnetic resonance* (Elsevier, 1965), pp. 1–32.
- ¹⁶⁸Primas, H., "Generalized perturbation theory in operator form," Reviews of Modern Physics **35**, 710–711 (1963).

- ¹⁶⁹Hall, B. C., Hall, B. C., *Lie groups, Lie algebras, and representations* (Springer, 2013).
- ¹⁷⁰Bengs, C., Levitt, M. H., "SpinDynamica: symbolic and numerical magnetic resonance in a Mathematica environment," Magnetic Resonance in Chemistry 56, 374–414 (2018).
- ¹⁷¹Bengs, C., *SpinDynamica NMR calculation and simulation in Mathematica*, (2023) https://www.spindynamica.soton.ac.uk (visited on 21/06/2023).
- ¹⁷²Fano, U., "Description of states in quantum mechanics by density matrix and operator techniques," Reviews of Modern Physics 29, 74–93 (1957).
- ¹⁷³D'Yakonov, M. I., Perel', V. I., "Coherence relaxation during diffusion of resonance radiation," Journal of Experimental and Theoretical Physics **20** (1965).
- ¹⁷⁴Omont, A., "Relaxation par collisions des états excités d'un atome," Journal de Physique **26**, 26–40 (1965).
- ¹⁷⁵Happer, W., Mathur, B. S., "Effective operator formalism in optical pumping," Physical Review **163**, 12–25 (1967).
- ¹⁷⁶Tayler, M. C. D., **Bodenstedt, S.,** "NMRduino: a modular, open-source, low-field magnetic resonance platform," In review. (2023).
- ¹⁷⁷Twinleaf, *Twinleaf CSB*, (2019) \url{https://twinleaf.com/current/CSB/} (visited on 29/06/2023).
- ¹⁷⁸Twinleaf, *Twinleaf VMR*, (2019) \url{https://twinleaf.com/current/CSB/reference/R10/} (visited on 29/06/2023).
- ¹⁷⁹Numpy, *Numpy*, (2023) https://numpy.org (visited on 21/06/2023).
- ¹⁸⁰SciPy, *Scipy*, (2023) https://scipy.org (visited on 21/06/2023).
- ¹⁸¹pandas, *Pandas python data analysis library*, (2023) https://pandas.pydata.org (visited on 21/06/2023).
- ¹⁸²Matplotlib, *Matplotlib visualization with python*, (2023) https://matplotlib.org (visited on 21/06/2023).